Numerical and Analytical Modelling of Nacre-Inspired Auxetic Mechanical Metamaterials

CWIERTKA, Klaudia Monika

Numerical and Analytical Modelling of Nacre-Inspired Auxetic Mechanical Metamaterials

Klaudia Monika Cwiertka

A thesis submitted in partial fulfilment of the requirements of
Sheffield Hallam University
for the degree of Doctor of Philosophy

July 2024

Abstract

Nacre, known for its brick-and-mortar structure consisting of 95% aragonite and 5% organic matrix, exhibits auxetic behaviour, as shown through experimental analyses. The auxeticity of nacre is still widely unexplored, with no conclusive answer as to the mechanism causing this unexpected property. This project aims to investigate the speculative theories on the mechanisms causing the auxeticity of nacre and further look into how the negative Poisson's ratio (NPR) can be enhanced.

This project utilises analytical and numerical modelling to create and optimise nacre-inspired mechanical metamaterial with negative Poisson's ratio. The focus of the models was to explore the mechanisms that could explain nacre's auxeticity but also to find the correlation between Poisson's ratio (PR) and the geometrical parameters.

Four different models were presented in the literature review, and three of them were further modelled. Focus was given to mechanism 1, which speculated on the role of the mortar in the nacre's auxeticity. Mechanisms 2 and 3 were explored and investigated the role of brick morphology and connectivity.

Analyses of mechanism 1 revealed dependencies of PR on volume ratio (the ratio of volume of bricks and mortar) and geometry, indicating that higher volume ratio models had lower PR but were prone to experienced yielding at lower strains. Combined bending and axial deformation of the struts in the X-shaped mortar was identified as a significant factor in the NPR of the 2D model of mechanism 1.

The 2D numerical model of mechanism 1 exhibited the same behaviour pattern as nacre but with lower PR, signifying the model's validity and making it a good contender for an explanation of nacre's auxetic behaviour.

Mechanism 1 was then explored as a 3D numerical model. The 3D models showed altered deformation mechanisms and NPR behaviour. It was recognised that the depth of the 3D models prevented the structures from showing the same behaviours as 2D models. The structure was not slender enough to experience the same type of deformation. The out-of-plane deformation was thought to be another contributing factor. To rectify this, a thin structure with beam elements was created. The beam 3D structure showed similar variability of PR as the 2D models, but no exact match was found.

The lowest PR achieved through numerical modelling of mechanism 1 was during the 2D analysis showing a PR of approximately -0.80 for the volume ratio of 0.91.

The project underscores the significance of understanding geometric properties and deformation behaviours in auxetic materials, providing insights into optimising NPR in nacre-inspired mechanical metamaterials.

Keywords: auxetic, negative Poisson's ratio, finite element analysis, ANSYS, nacre, bioinspired materials, mechanical metamaterials

I hereby declare that:

1. I have not been enrolled for another award of the University, or other academic or professional organisation, whilst undertaking my research degree.

2. None of the material contained in the thesis has been used in any other submission for an academic award.

3. I am aware of and understand the University's policy on plagiarism and certify that this thesis is my own work. The use of all published or other sources of material consulted have been properly and fully acknowledged.

4. The work undertaken towards the thesis has been conducted in accordance with the SHU Principles of Integrity in Research and the SHU Research Ethics Policy.

5. The word count of the thesis is 42,245

Name: Klaudia Monika Cwiertka

Date: Friday 26th July 2024

Award: Doctor of Philosophy

Director(s) of Studies: Prof Andy Alderson

Supervisor(s): Dr Emma Carter

Acknowledgement

The project has been funded by Sheffield Hallam University Faculty of Science, Technology and Arts Graduate Teaching Assistantship studentship, and it is a collaboration between the Materials and Engineering Research Institute and the Department of Engineering and Maths.

I want to thank my supervisors, Prof Andrew Alderson and Dr Emma Carter, for their consistent support and guidance while running this project. Their insight into the respective fields was incredibly valuable, and their patience was incomparable. I want to extend this thanks to the research support staff at the Materials and Engineering Research Institute for their support during this PhD.

To my partner, daughter, family, and friends, I am profoundly thankful for your constant support and encouragement. Your belief in me and your words of motivation has been a source of strength throughout this journey.

Table of Contents

Table of Figures

Table of Tables

Chapter 1 Introduction

Aims, Objectives and Original Contributions

Nacre has been studied thoroughly due to its great strength and fracture toughness, as well as a few other desirable properties, and it has inspired a number of biomimetic composites (Kakisawa & Sumitomo, 2011) (Ding, et al., 2017) (Sanderson, 2015). However, current studies of the nacre-inspired composites often omit its auxetic behaviour, which could further improve the properties of the metamaterials. Nacre is frequently mentioned within the auxetic research community (Duncan, et al., 2018). Therefore, it is essential to improve the understanding of the mechanisms that cause Negative Poisson's ratio (NPR) so that it can be exploited.

The original aspect of the project is to create a novel two-dimensional "brick-and-mortar" structure inspired by the nacre, exploring existing proposed mechanisms using the Finite Element Analysis (FEA). The models will allow a visualisation of the nacre's auxetic behaviour but using artificial materials, hence not replicating it exactly. This has the potential to create a link between a visual representation of the changes under the strain and allow a comparison to the behaviours observed in experimental results, hence bridging the theory and practice.

The resulting model is be used for further inspiration to integrate that mechanism into nacre-inspired metamaterials and allow for enhancement of the mechanical properties.

The main aims of this project are to investigate the fundamental principles and review the state-of-the-art research in auxetic materials and Finite Element Analysis, which should allow for the identification of the research gap concerning nacre-inspired auxetic mechanical metamaterials. Furthermore, the project will look into the developing and validation of analytical and numerical models to understand and replicate the auxetic behaviour observed in nacre, with the ultimate goal of finding the dependencies between Poisson's ratio and the different parameters.

These aims should be achieved by conducting a comprehensive review of existing literature on finite element methods and auxetics to establish a foundation of knowledge in both areas, with areas of focus including nacre and biomimetic metamaterials. Then, it is crucial to identify the key components of the nacre's structure and their roles and investigate the existing theories of the mechanism responsible for nacre's auxetic behaviour. The work carried out will be focused on developing analytical and numerical models of the most suitable mechanisms identified in the literature review to enable parametric studies.

Ultimately, the above aims and objectives should enable the identification of the most suitable mechanism, which will be developed into a 3D model exhibiting Negative Poisson's ratio.

By achieving these objectives, the project aims to advance the understanding of nacre-inspired auxetic mechanical metamaterials, contributing valuable insights to the field of finite element analysis of auxetics.

For the purpose of this project, the definitions of the metamaterial and metasurface are supported by the UK Metamaterials Network (UK Metamaterials Network, 2024).

Metamaterial: "A metamaterial is a 3D structure comprised of at least two different materials, with a response or function that is impossible to achieve with any individual constituent material."

Metasurface: "A metasurface is a 2D version of a metamaterial where the structural elements are confined to a 2D plane."

Chapter 2 Literature Review

Introduction

This chapter explores available literature on the topics directly relevant to this project, highlighting the most crucial and delving into areas where there are knowledge gaps and into how these can be used to benefit the original contributions of the project.

A number of themes recur throughout this chapter, with the most important being auxetics and finite element analysis.

The work within this chapter lays out the knowledge foundation for these topics and will be used to inform further the methodology and the corresponding set-up used within the analytical and finite element models found in later chapters.

Auxetics

Auxetics are defined as materials and structures characterised by a Negative Poisson's ratio (NPR). In comparison, what we refer to as conventional materials and structures have a positive Poisson's ratio (Nkansah, Evans, & Hutchinson, 1994) (Evans K. E., 1991).

Poisson's ratio (ν) can be defined as "the ratio of the change in the width per unit width (lateral strain, ε_y) of a material, to the change in its length per unit length (longitudinal strain, ε_x), as a result of stress in the lengthwise direction" (Evans K. E., 1991):

$$\upsilon = -\frac{lateral\ strain}{longitudinal\ strain} = -\frac{\varepsilon_y}{\varepsilon_x} \tag{1}$$

where longitudinal strain is in the same direction as the load applied, and lateral strain is perpendicular to the direction of the load.

In simple terms, when conventional materials are stretched, their cross-sectional area decreases, which tends to conserve their volume, Figure 1. On the contrary, the exact opposite occurs in auxetic materials, which usually have a unique internal structure that 'opens' in both the longitudinal and lateral directions when a tensile load is applied (Lakes, 1987) (Evans K. E., 1991).

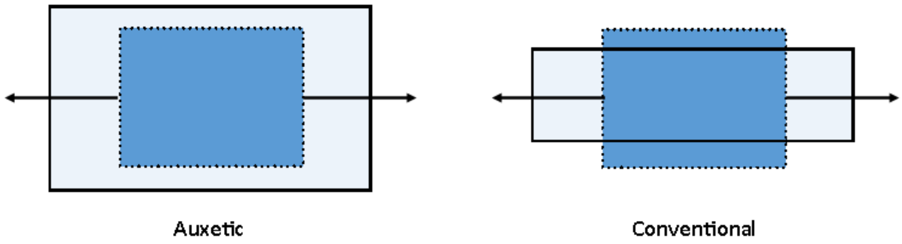

Figure 1: A comparison of deformation in an auxetic and conventional material. The arrows show tensile stress, which is applied along the length of the material. The darker shape represents the original shape, and the lighter shape represents the post-deformation area.

Most materials have a Poisson's ratio of between 0 and 0.5. Some examples are Metals such as stainless steel with an approximate Poisson's ratio of 0.30, Cork with a PR of 0, and rubber with a PR of 0.50.

The interest in auxetics has increased over the years, which can be seen in the number of auxetic-related patent applications, as shown in Figure 2 (Espacenet).

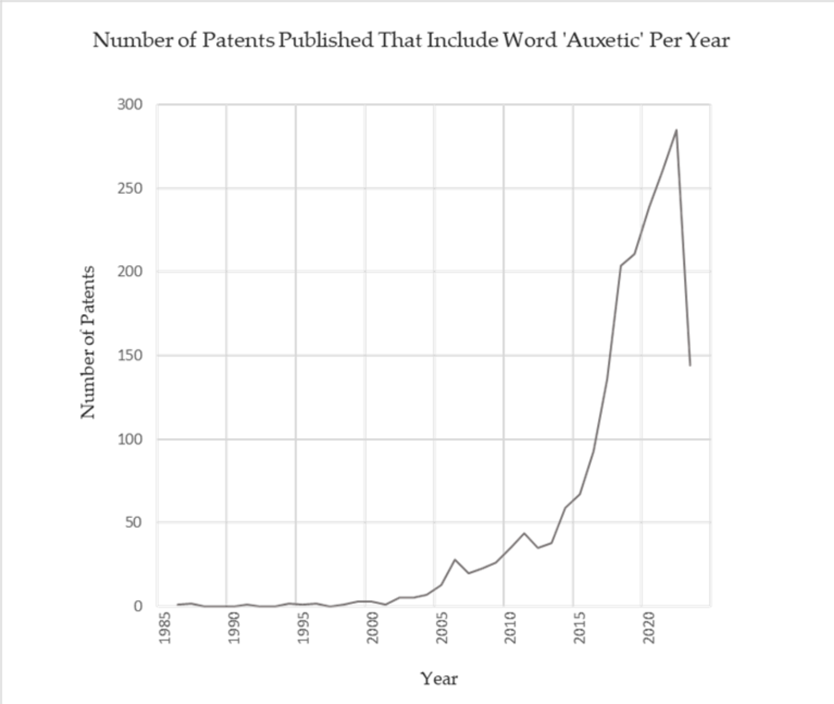

Figure 2: Number of patents published per year containing the term 'Auxetic' (Espacenet)

The growing interest in auxetics, as demonstrated by the increased number of applications, shows the broadening potential of this field. However, there are areas which are still widely unexplored. From the search on Espacenet, a free online patent search service, there are only three patents relating to bioinspired auxetic products, including ophthalmic devices, an artificial bone structure, and proliferation using tissue culture (Espacenet, 2021). This indicates that there is a scope for auxetics inspired by nature. One of the avenues of research opportunity is to explore naturally occurring auxetics, as found in the section 'Naturally Occurring Auxetics', of which nacre is one example. Understanding the auxetic behaviour of nacre could enable the development of synthetic composites that replicate the same behaviour. This area is shown to be under-researched and shows a potential for an original contribution to knowledge.

Characteristics of Auxetics

There are a number of properties known to be improved with a negative Poisson's ratio, such as higher material stiffness, indentation resistance, plane strain fracture toughness, shock and sound absorption, and higher energy absorption (Evans K. E., 1991). These are individually discussed in this section, with a focus on the relationship between the individual physical properties and the negative Poisson's ratio.

Shear Modulus And Bulk Modulus

Isotropic materials, materials that are uniform in all directions, are determined by four elastic constants: Young's, bulk, and shear moduli and Poisson's ratio. Young's modulus and Poisson's ratio are independent of each other, but they are related through the other elastic constants and they both correspond to the same loading condition. Young's modulus is defined as a measure of the stiffness of an elastic material, described as the ratio of stress to strain (Ma, Sobernheim, & Garzon, 2015).

$$Young's\ Modulus, E = \frac{\sigma}{\varepsilon} \tag{2}$$

Bulk modulus is defined as a measure of how resistant a material (solid or fluid) is to compression, described as the ratio of pressure increase to the relative decrease of the material volume (Horwood & Chockalingam, 2023). Bulk modulus is related to Poisson's ratio and Young's modulus by:

$$Bulk\ Modulus, K = \frac{E}{3(1-2v)} \tag{3}$$

Shear modulus is defined as a measure of the material stiffness, described as the ratio of shear stress to shear strain when the material is deformed by a force parallel to its surface within the limit of elastic deformation (Taraban, Li, Joyner, Stains, & Yu, 2016). . Shear modulus is related to Poisson's ratio and Young's modulus by

$$Shear\ Modulus, G = \frac{E}{2(1+v)} \tag{4}$$

The relation between these constants can be seen in Equations (3) and (4), and the knowledge of any two of the constants will enable the other two to be determined.

Equation (4) by (3) and re-arranging gives Equation (5).

$$Poisson's\ Ratio, v = \frac{(3K - 2G)}{2(3K + G)} \tag{5}$$

In other terms, $Young's\ modulus, E = 3K(1 - 2v) = 2G(1 + v)$

(6)

As per the first law of thermodynamics, all three of the moduli (Young's, bulk and shear) must be greater than 0. From Equation (5), when $K = \infty$ then $v = -1$, and if $G = \infty$ then $v = +0.5$ which provides an isotropic range of $-1 \le v \le 0.5$.

If $v = -1$, then from Equation (4), G tends to infinity, and from Equation (3), K decreases to minimum: $G \approx \infty\ and\ K \approx 0$.

When there's negative Poisson's ratio, there is a higher volume change within the structure whilst the structure is tending to maintain shape. This corresponds to the low bulk modulus and high shear modulus, observed in Figure 3 which was plotted using Equations (3) and (4),. The Young's modulus was assumed to remain unchanged at 100 Pa. It is seen that shear and bulk modulus have opposing behaviours in relation to the Poisson's ratio.

Higher shear modulus indicates that a material has higher resistance to shearing deformation, or in other words, the material is more rigid. The higher shear modulus brought on by the negative Poisson's ratio is more beneficial than the high bulk modulus when used in structures consisting of plates, shells, and beams, like structures for buildings, and body parts for cars, planes etc., where it is crucial that the structures do not distort.

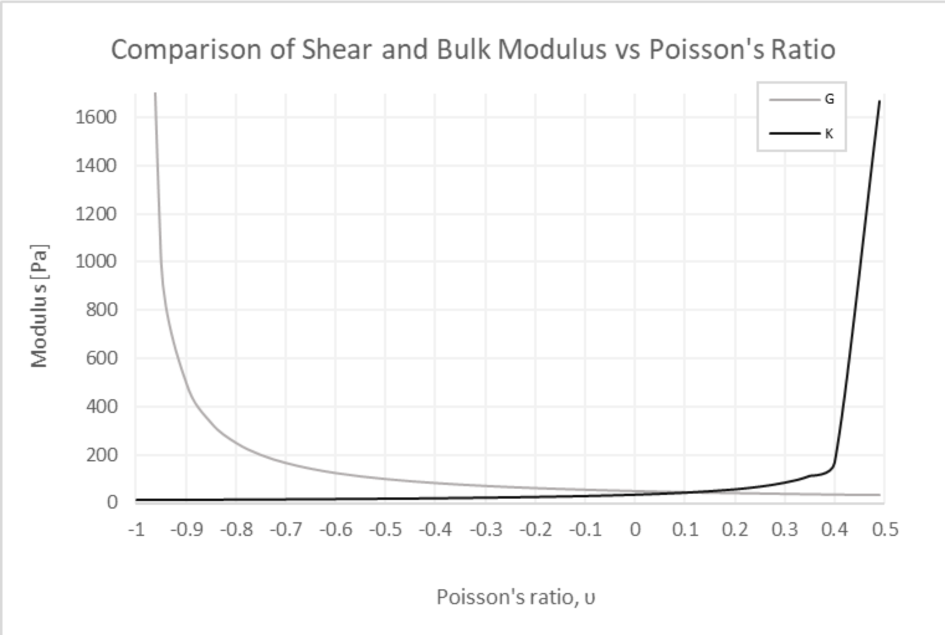

Figure 3: Comparison of shear and bulk modulus versus Poisson's ratio

Indentation Resistance

Indentation hardness measurement can be used to determine the material's resistance to deformation. Generally, to test indentation hardness, the material is indented until an impression is made. There are multiple testing methods for this purpose which are best used when comparing the experiments where the same testing methods and standards were used.

The Indentation Hardness, H, is proportional to the pressure required to produce the indentation depth (Alderson, Pickles, P.J, & Evans, 1994):

$$H \propto (1-\nu^{2})^{-1} \tag{7}$$

Using Hertzian approach which considers purely elastic behaviour, it can be determined that the hardness of the material is proportional to $(1-\nu^{2})^{-2/3}$ (Alderson, Pickles, P.J, & Evans, 1994):

$$H \propto (1-\nu^{2})^{-2/3} \tag{8}$$

The enhanced indentation resistance has been reported through experimental studies, for example, by Alderson et al. (1994), who confirmed this through the experimental study on the auxetic ultra-high molecular weight polyethene (UHMWPE), where the foams with NPR achieved double the hardness of the conventional UHMWPE (Alderson, Pickles, P.J, & Evans, 1994).

Other work showing increased indentation resistance is by Lim (2015), who suggested that the indentation resistance is higher within auxetic structures due to the densification of regions under stress, whereas, in conventional materials, there is a displacement away from the indent, which weakens the material. This can be observed in Figure 4.

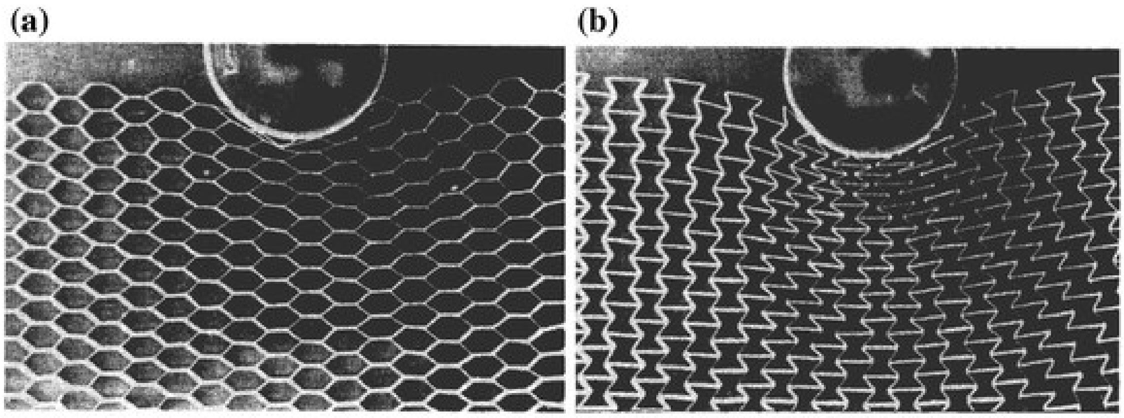

Figure 4: Compression by cylindrical indenter on (a) conventional honeycomb, (b) auxetic re-entrant honeycomb (Lim, 2015)

They were considering the limits of Poisson's ratio for isotropic material to be $\mathbf{-1 \leq \upsilon \leq 0.5}$, the lower the Poisson's ratio, the higher the indentation resistance, as can be found in Figure 5 where equations (7) and (8) were used to plot the relationship.

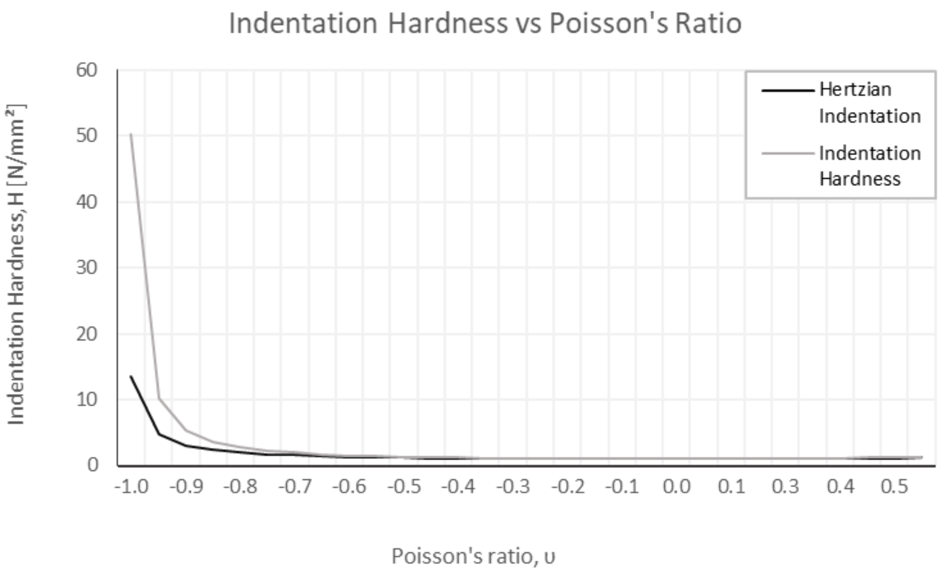

Figure 5: The plot shows the correlation between the Hertzian Indentation Hardness which is used for purely elastic behaviour and Indentation Hardness against varying Poisson's ratio

Energy and Shock Absorption

Energy absorption can be found from the load-displacement graphs of experimental data by finding the area below the curve (Jawaid, Thariq, & Saba, 2019).

In an experimental study by Ahmad & Rad (2014), the auxetics required a higher force for equal displacement than conventional material when tested under the impact of the falling weight. The author concluded that " *the auxetic foam may be advantageous to the conventional ones since it can mitigate higher impact energy with respect to the same volume of foam*" (Ahmad & Rad, 2014), but the results within the paper did not support this statement definitively as the highest energy absorption was for the sample with the positive PR, the data sample used was small with only five specimens tested, the results had slight variation within the range of 0.5 MJ/cm^3 between the highest and lowest energy absorption found. However, the correlation between NPR and higher energy absorption has been found in other studies, such as the Finite Element Analysis by Yang et al. Shock absorption, or damping, measures how much of the impact shock's kinetic energy has been dissipated, which can be seen as lower oscillations after the impact (Yang, Vora, & Chang, 2018). Figure 6 shows the results obtained by Yang et al., which show stress variations over time after the impact, which was a 1000N circular load applied at the top surface of the 4x 4x2inch cube for the time of 0.01s with another 0.04s period of 'relaxation' period post-impact to allow for the load transfer. The 'a' plot is a conventional structure, and 'b' and 'c' are auxetic structures. Graphs show that the auxetic structures have much lower oscillations after the impact than the conventional structure.

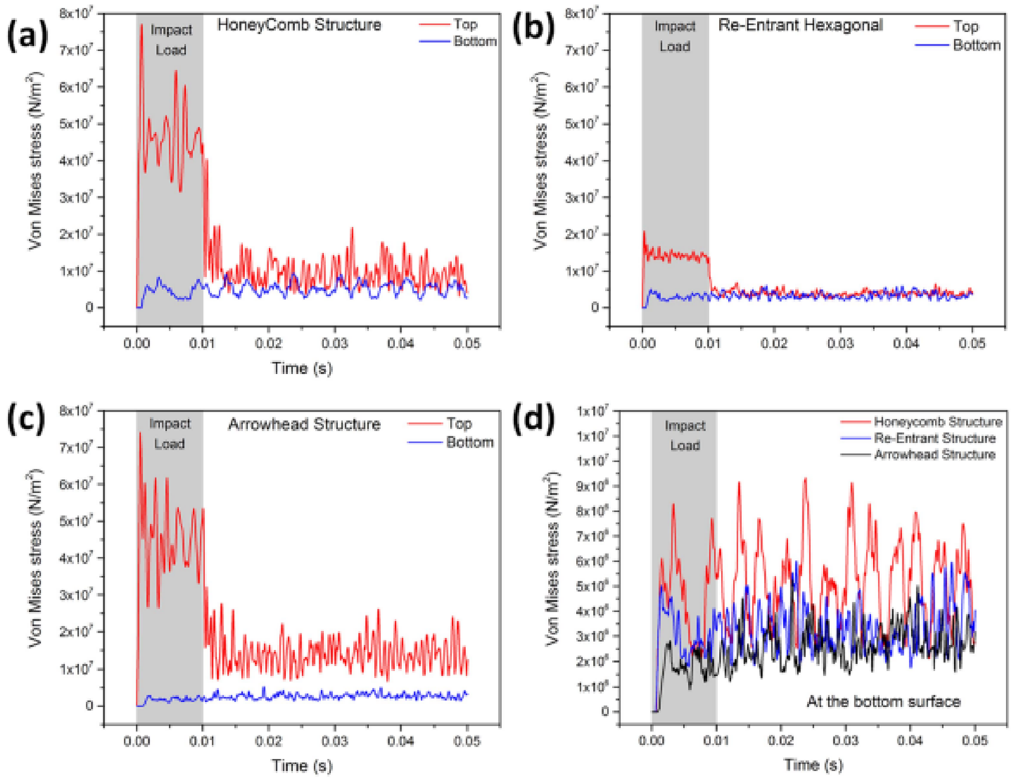

Figure 6: Yang et al. results of the FE study of auxetic (b and c) and conventional (a) materials of Von Mises stress versus time for impact loading (d) comparison of Von Mises stresses on the bottom surface of all three structures (Yang, Vora, & Chang, 2018).

Figure 7 shows the results from the experimental study by Ali et al. (2018), where 2D woven auxetics were tested using tensile testing. Looking at the definition of energy absorption, the area under the load-displacement curve will be higher for an auxetic than that of conventional material; hence, Figure 7 illustrates that auxetics have higher energy absorption.

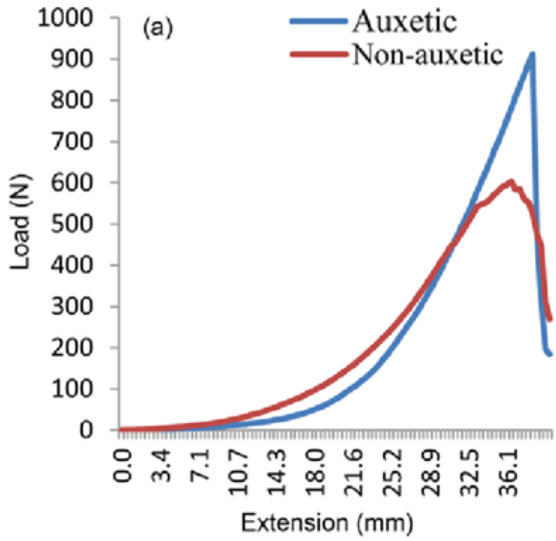

Figure 7: Load-displacement comparison of an auxetic material and conventional material (Ali, et al., 2018)

Allen et al. looked into the low-kinetic energy impact response of auxetic and conventional open-cell PU foams (Allen, et al., 2015), comparing the response of auxetic and conventional foams using the experimental approach. The impact applied was up to 4J using the drop rig and high-speed video to monitor the deformation. The set-up consisted of a flat bottom plate and a hemispherical-shaped dropper, which was dropped onto foams covered with a rigid polypropylene outer shell layer.

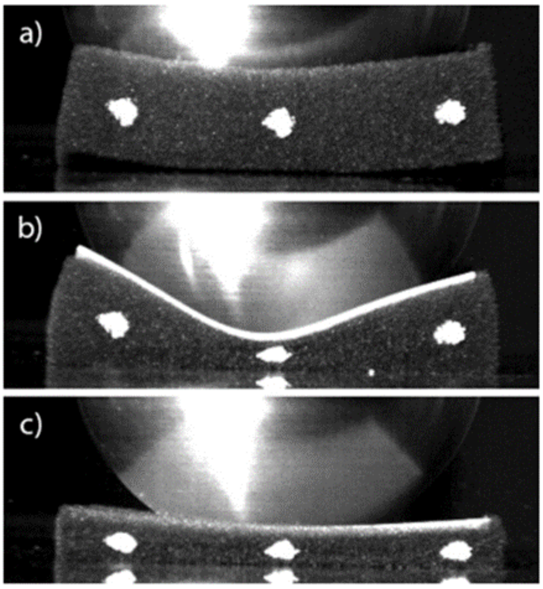

Figure 8: The maximum deformation caused by the hemispherical dropper on conventional foam, R60FR, with (a) no sheet, (b) 1 mm thick sheet and (c) 2 mm thick polypropylene sheet (Allen, et al., 2015)

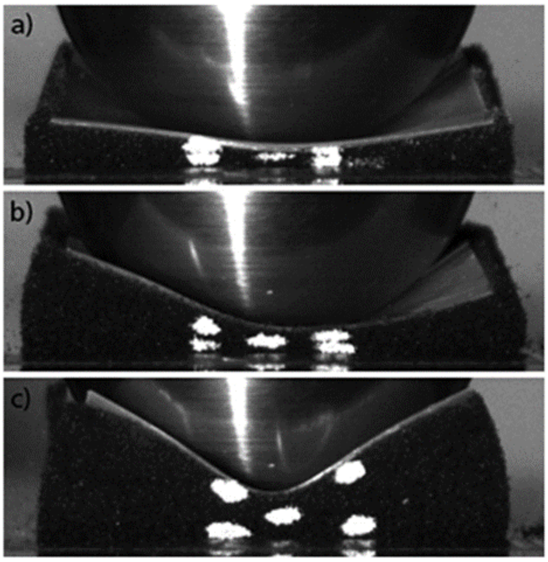

Figure 9: The maximum deformation caused by the hemispherical dropper on R45FR foam, (a) conventional at 16 ms, (b) auxetic with 0.85 Linear Compression Ratio at 17 ms, and (c) auxetic foam at 0.7 Linear Compression Ratio at 18 ms (Allen, et al., 2015)

Allen et al. found that the NPR achieved was lower in magnitude than that present in the literature. However, the effect of NPR could be observed as the auxetic foams reduced the impact peak acceleration by approximately six times in comparison to the conventional foam counterparts, proving them to have a high potential in protective sports equipment applications.

Another way to consider energy absorption is through the total strain energy equation. The strain energy per unit volume of a three-dimensional principal stress system is given by (Hearn E. , 1997):

$$U = \frac{1}{2E}[\sigma_1^2 + \sigma_2^2 + \sigma_3^2 - 2\nu(\sigma_1\sigma_2 + \sigma_2\sigma_3 + \sigma_3\sigma_1)] \qquad (9)$$

which then shows that the volumetric strain energy per unit volume is:

$$U_v = \frac{(1-2\nu)}{6E}[(\sigma_1 + \sigma_2 + \sigma_3)^2] \qquad (10)$$

The term for distortional strain energy per unit volume is

$$U_d = \frac{1+\nu}{6E}[(\sigma_1 - \sigma_2)^2 + (\sigma_2 - \sigma_3)^2 + (\sigma_3 - \sigma_1)^2]$$

(11)

Hearn (1997) notes that a uniaxial stress can be divided into dilatational (hydrostatic) and distortional (deviatoric) terms, meaning that the above can be applied to different triaxial states.

When the Poisson's ratio is 0.5, all the strain energy is distortional, resulting in $U_v = 0$; this indicates that the volume is being conserved at this value of PR.

When PR is -1.0, all of the strain is volumetric, resulting in $U_d = 0$, which aligns with the preservation of shape at this PR value.

As PR decreases from 0.5 to -1.0, the two components of strain energy, U_v and U_d, exhibit linear variations, with U_v increasing and U_d decreasing.

This is shown in Figure 10 where the correlation between the volumetric strain energy and distortional strain energy from Equation (10) and Equation (11) and Poisson's ratio were plotted.

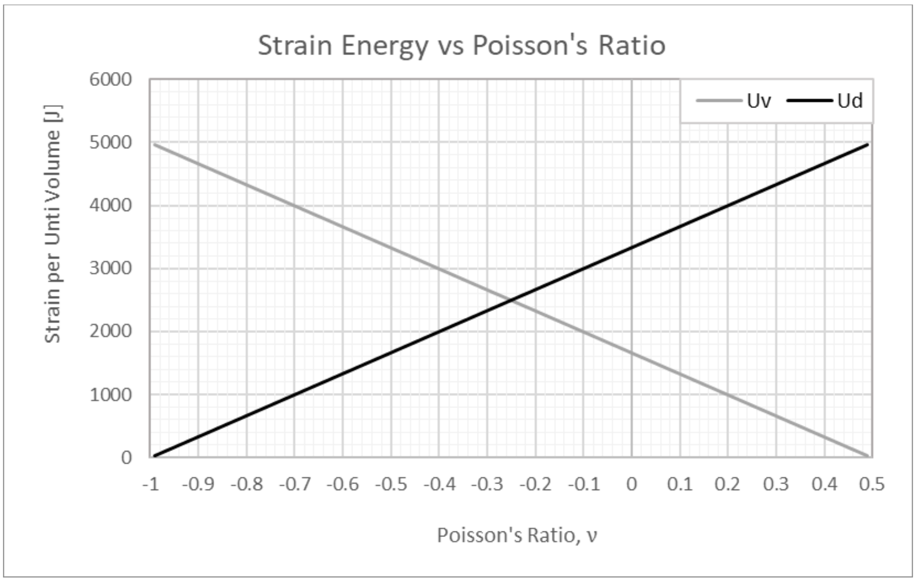

Figure 10: The plot showing the correlation between the Poisson's ratio, ν, and strain per unit volume, U_v and U_d [J].

The parameters used were Young's modulus of 100Pa and $\sigma_1 = 1$Pa, with σ_2 and σ_3 set at 0. Poisson's ratio was the only variable. As shown, the distortional strain energy is lower when the Poisson's ratio is negative. According to failure theories, alike von Mises criterion, the distortional strain energy is often the dominating factor in predicting the yielding of the material or material's failure.

Plane Strain Fracture Toughness

Plane strain fracture toughness has also been shown to improve with a negative Poisson's ratio. The value for the stress intensity factor, K_Q, is found using experimental approach and carrying out a fracture test on a specimen in accordance with BS 7448. If necessary criteria are met, as per BS7448, such as when K_{IC} isthe plane strain fracture toughness, then the following is true (British Standards Instutution, 1991):

$$K_Q = K_{IC} \tag{12}$$

The critical stress-intensity factor, K_{IC}, is the highest value of stress intensity that a material can withstand under plane strain under tensile loading. I in the subscript indicates the mode of fracture. Mode I fracture is when the fracture occurs normal to the direction of the tensile loading, as seen in Figure 11.

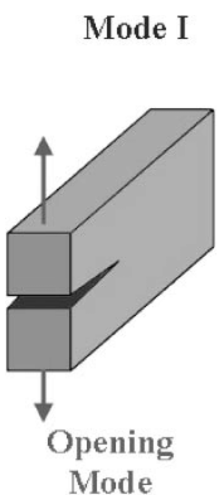

Figure 11: Mode I is the opening mode fracture (Rountree, 2002)

The stress intensity factor is given by:

$$K = Y\sigma\sqrt{\pi a}$$

(13)

where K_{IC} is the critical stress intensity factor for Mode I fracture $\left(MPa\sqrt{m}\right)$, σ is an applied stress (MPa), a is a crack size (m), and Y is a dimensionless correction factor which depends on the specimen's geometry.

Considering Griffith's criterion, fracture energy can be represented using the material constants. For the plane strain, which is defined as a two-dimensional strain where the deformation predominantly occurs on a single plane of the linear elastic materials:

$$G_{IC} = \frac{K_{IC}^2(1-\upsilon^2)}{E}$$

(14)

Hence, after rearranging, we get plane strain fracture toughness: $K_{IC} = \sqrt{\frac{G_{IC}E}{(1-\upsilon^2)}}$

(15)

Irwin extended the aforementioned Griffith's theory to ductile materials by incorporating plastic work, γ_p, at the crack tip (Sun & Jin, 2012). The energy needed to create new surfaces at the crack tip require surface energy and plastic dissipation.

Irwin proposed that the energy release rate, G, is defined as "*the decrease in potential energy per unit crack extension under constant load*". This can be shown as:

$$G = -\frac{d\Pi}{da}$$

(16)

Where $-d\Pi$ is the decrease in the potential energy, and da is the small crack extension.

The failure criterion is then defined as:

$$G = G_c = 2\gamma \tag{17}$$

Where γ is the surface energy per unit area, and G_c is the critical energy release rate. The G_c requiring 2γ is due to the plastic deformation in the crack tip contributing to the crack growth resistance.

There are a few speculations as to why auxetics have higher fracture toughness. Kolkena et al. speak in particular of a mechanism relating to the crack initiation (Kolkena, et al., 2022). When there are no defects to initiate the crack, under cyclic loading, the structure might deform in order to minimise the system's total energy. These deformations are known as persistent slip bands (PSBs), and they are usually the areas where a crack would initiate within the grains of the material, often growing in the direction perpendicular to the applied load.

Whilst studying re-entrant honeycomb structures, Kolkena et al. noted that the geometry caused the walls to touch at low strain levels, resulting in early densification of the structure, which caused an increase in the stress and strain. As a result, these structures started acting like solids and failed at much higher strain values.

Donoghue et al. studied fracture toughness in laminates and suggested that higher fracture toughness was caused by higher initial energy absorption of the auxetics (Donoghue, Alderson, & Evans, 2009).

To simply visualise the correlation between the plane strain fracture toughness, the below parameters were assumed and plotted.

Assuming Young's modulus and energy required to cause the fracture are constant and using equation (15), Figure 12 shows how plane strain fracture toughness varies with changing Poisson's ratio, showing an increased fracture toughness with negative Poisson's ratio.

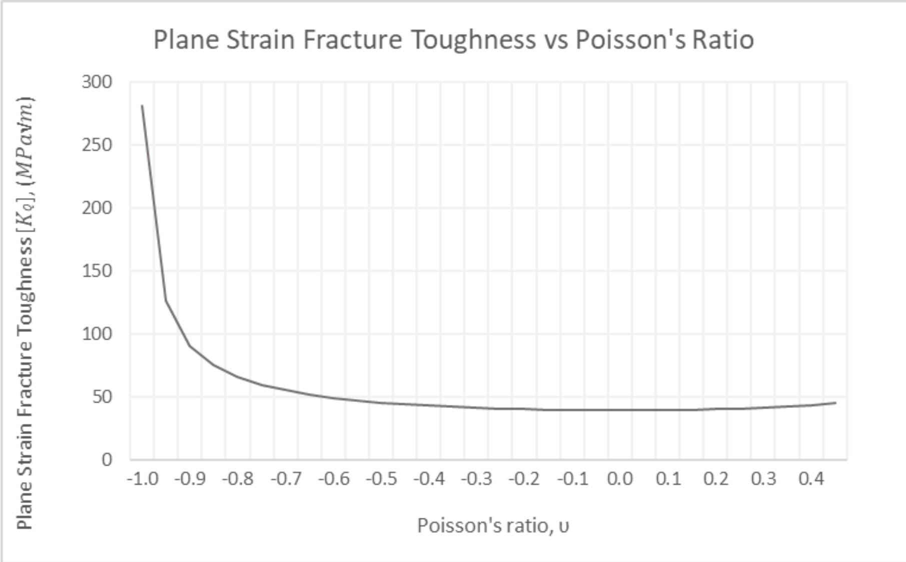

Figure 12: Plane strain fracture toughness with variable Poisson's ratio

In the case of an isotropic material with Poisson's ratio limits of $-1 \leq \upsilon \leq 0.5$, previously mentioned in section 'Shear Modulus And Bulk Modulus' on page 37, the benefit of the negative Poisson's ratio will be observed when in the range of $-1 \leq \upsilon \leq -0.5$ as the equivalent positive value is not possible.

Sound Absorption

Sound absorption is defined as the decrease of sound energy from the sound wave as it passes through the absorbent material, sound absorbers, of which there are two recognised types: porous absorbents or resonance absorbents.

Porous absorbers are either fibrous materials or foams. In a fibrous absorber, acoustic energy is transferred to heat energy when sound waves bend the fibres. In foams, besides the energy loss due to the heat, there is an additional energy loss due to the sound waves moving through the air within the cells. The energy loss equates to the reduced sound levels. Resonance absorbers are usually a form of the oscillation system made of a solid plate and air cavity behind it, which absorbs sound by targeting a particular frequency range. Resonance absorbers might have porous absorbers incorporated into the cavity to allow for a higher range of frequencies to be absorbed.

Auxetic foams have the potential to be porous sound absorbers.

The sound absorption properties are directly correlated to the material's ability to absorb energy, and auxetics are known for their higher energy absorption. Referring back to Equation (4) and the below Equation (18) for the Lamy constant, λ, and the Equation (19) for the bulk longitudinal wave modulus, S, the relationship between the Poisson's ratio and attenuation constant of acoustic waves can be derived (Luo, Li, Yan, & Zhou, 2021).

$$\lambda = \frac{E\nu}{(1+\nu)(1-2\nu)} \tag{18}$$

$$S = \lambda + 2G \tag{19}$$

In the isotropic and infinite structure, the wave velocity of longitudinal wave, c_l, is

$$c_l = \sqrt{\frac{S}{\rho}} \tag{20}$$

and the wave velocity of the shear wave, c_t , is

$$c_t = \sqrt{\frac{G}{\rho}} \tag{21}$$

where ρ is the density of the sound wave propagation material. The characteristic impedance of the material is $Z = \rho c$, where c is the speed of sound.

(22)

The changes to the PR impact the velocity of the longitudinal sound wave and the Lamy constant, in turn increasing the sound absorption coefficient of the material.

Oh et al. carried out the experimental study (2020), Figure 13, where the foam was inserted into the tube, and the sound absorption performance was measured using the two-microphone method (Oh, Kim, Hiep, & Oh, 2020).

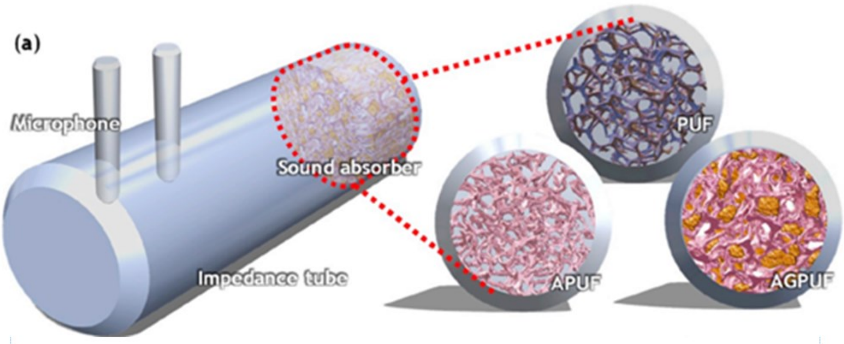

Figure 13: a diagram representing the sound absorption test using the impedance tube (Oh, Kim, Hiep, & Oh, 2020)

Oh et al. (2020) used five different samples to carry out the experiment, comparing auxetic samples to their conventional counterparts. The five samples were conventional polyurethane foam (PUF), auxetic polyurethane foam with compressibility of 10% (APUF 10%), auxetic polyurethane foam with compressibility of 20% (APUF 20%), auxetic graphene oxide-polyurethane foam with compressibility of 10% (AGPUF 10%), and auxetic graphene oxide-polyurethane foam with compressibility of 20% (AGPUF 20%). The results can be seen in Figure 14, where auxetic foams have a higher sound absorption coefficient for frequencies of up to 4000 Hz and above 5000 Hz.

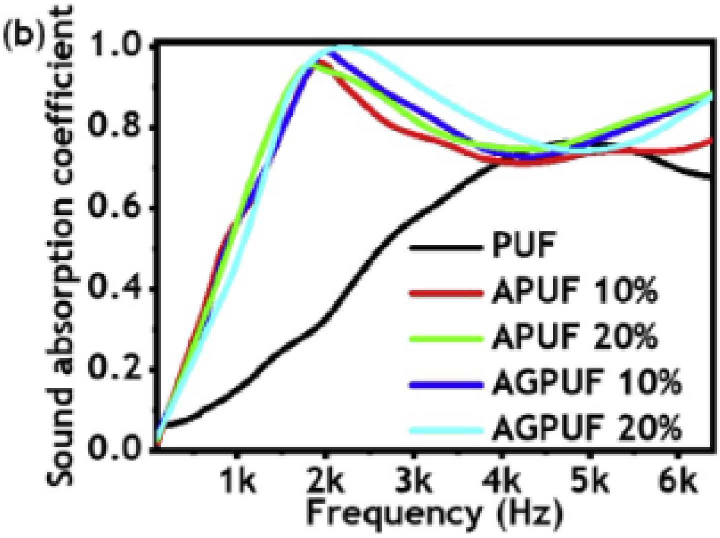

Figure 14: Sound-absorbing performance where PUF is conventional polyurethane foam, compared to auxetic foams (Oh, Kim, Hiep, & Oh, 2020)

Synclastic (Dome-Shaped) Curvature

Auxetic structures are further known to have a synclastic (dome-shaped) curvature when subjected to an out-of-plane bending (Naboni & Mirante, 2015), while conventional materials have an anticlastic deformation.

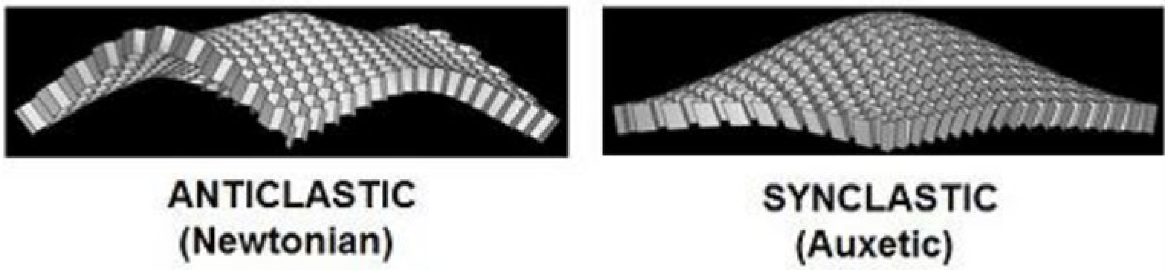

Figure 15: The curvature types showing anticlastic surface bending and synclastic where the conventional material is shown on the left and auxetic material is on the right (Panico, Langella, & Santulli, 2017)

In elastic deformation, the transverse curvature occurs due to the differential lateral contractions caused by Poisson's ratio (Wang, Wagoner, Matlock, & Barlat, 2005).

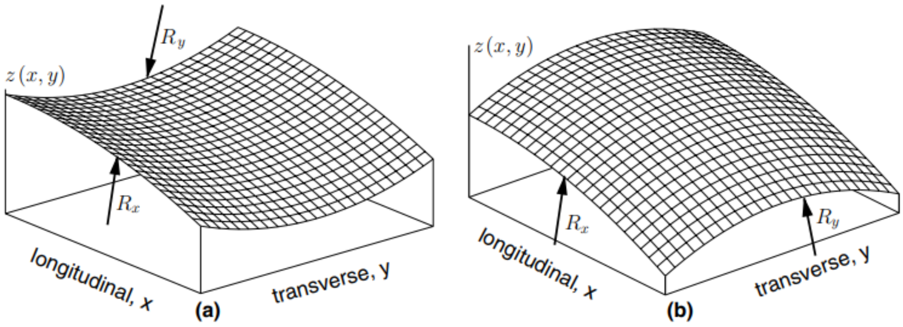

Figure 16: A plate surface after bending showing: (left) anticlastic curvature and (right) synclastic curvature (Wang, Wagoner, Matlock, & Barlat, 2005)

The curvature is given by

$$R_y = \nu R_x \tag{23}$$

and as per Equation (23), the Negative Poisson's ratio correlates to the synclastic curvature.

Applications Of Auxetic Materials

Auxetics have been researched for numerous applications, some of which are currently available commercially, including the fashion industry, sports equipment, aerospace and defence sector, as discussed in later sections.

Impact And Blast Protection

Some of the most recent works look into the impact responses of auxetics through experimentation and simulation. The literature on impact responses of auxetic materials shows a variety of impacts. An example of primarily experimental papers on the low velocity and low energy impacts are published papers by Allen et al. (2015) and Alderson & Coenen (2008). Allen et al. have been already mentioned and shown in Figure 8 and Figure 9 on page 44. Alderson & Coenen (2008) look at the auxetic carbon fibre laminates, showing that the auxetic laminates had enhanced resistance to low-velocity impacts (Alderson & Coenen, 2008).

An example of an application of the low energy impact is shown in Figure 17, which shows the use of an auxetic origami structure as a cushion in the back of the seat's headrest, which would be used to protect the passenger in the rear seat from a sudden impact, such as during sudden breaking or car collision (Tomita, et al., 2023).

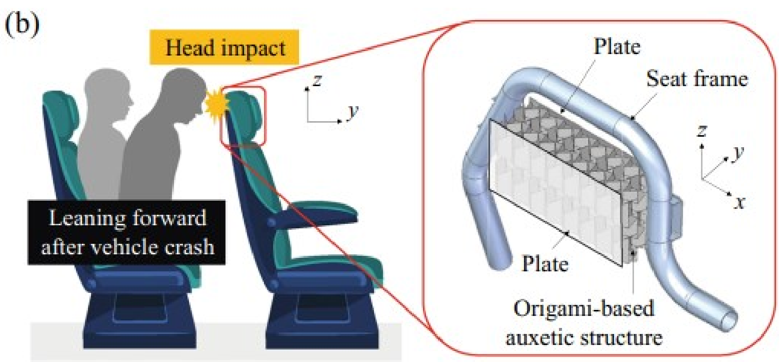

Figure 17: The application of auxetics for head protection from the collision against the seat headrest (Tomita, et al., 2023)

An application considering a much higher energy level of impact is for blast protection, which includes a blast-resistant fabric known as Zetix, which was produced by Auxetix (The Economist Group Limited, 2012) (Rodie, 2010). It utilised a helical-auxetic principle, which allowed it to increase in size when experiencing tension and resist higher-energy impacts (Gauthier, 2013). As seen in Figure 18, Zetix showed a lot of promise when compared to the conventional blast-proof fabric during the car bomb test carried out by the UK Ministry of Defence (TextileWorld, 2010), showing its capability to withstand multiple car bomb blasts without breaking (Diaz, 2007). Zetix could be used for terrorist attacks, military applications, and additional protection for the injured to allow emergency services extra time for rescue (Diaz, Zetix Blast-Proof Fabric Resists Multiple Car Bombs, Makes Our Heads Explode, 2007). With the potential to withstand multiple blasts, it makes it much more desirable for use within battle and terrorist attack scenarios where it has the potential to sustain protection, and it provides an advantage over the currently used materials and structures as they lose significant protection capability with a single blast event.

Figure 18: Comparison of Zetix blast curtain (left) with conventional blast-proof material (right) after the blast test conducted by the UK Ministry of Defence (TextileWorld, 2010)

More theoretical applications and advantages are brought on by the use of auxetic materials for blast protection. Auxetic materials and structures have mechanical properties such as higher energy absorption, which might be of interest in crash, ballistic and blast protection applications, as suggested by Novak, Vesenjak, and Ren, who have explored these applications using computational methods on sandwiched structures (Novak, Vesenjak, & Ren, 2018). Novak et al. also found during their analysis that the auxetic counterparts had a 6% mass reduction in comparison to the conventional material.

It is increasingly common to see auxetics used as a part of cladding, such as the cellular core, in order to absorb the impact and prevent any damage to the protected structure, as seen in Figure 19 (Bohara, Linforth, Nguyen, Ghazlan, & Ngo, 2023). Auxetic composite panels have been previously proposed for use in armoured vehicles to provide ballistic and impact protection, as seen in Figure 20 (Imbalzano G. , Tran, Ngo, & Lee, 2015).

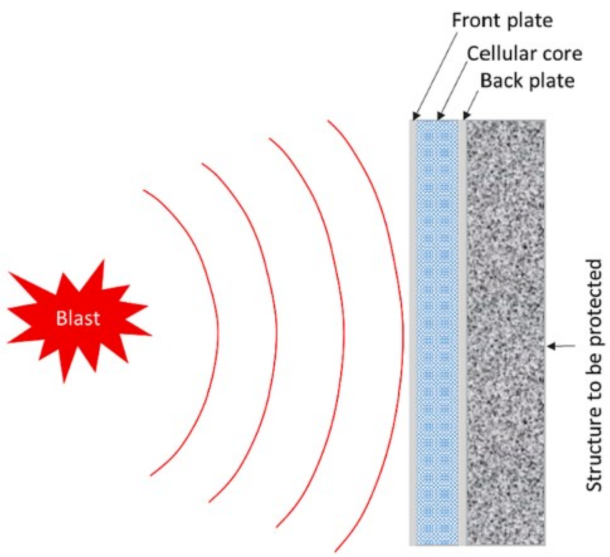

Figure 19: Example of how the auxetic cellular core can be used to protect the structure against the blast (Bohara, Linforth, Nguyen, Ghazlan, & Ngo, 2023)

Figure 20: Example of the armoured vehicle with auxetic composite panels installed (Imbalzano G. , Tran, Ngo, & Lee, 2015)

Aerospace

The use of auxetics is not new in aerospace and defence applications. However, it is possible that previously, the use of auxetics, such as the use of pyrolytic graphite, was mostly unintentional. In 1963, a paper was published describing the use of pyrolytic graphite, an auxetic, in the aircraft's thermal protection system for hypersonic vehicles (Garber, Nolan, & Scala, 1963). The pyrolytic graphite was chosen due to its thermal, aerothermochemical, and structural properties, with likely no knowledge of its auxeticity, considering that the author mentioned that the material's properties were still largely unknown and under investigation.

Another example of auxetics used in aerospace is Ni_3Al crystal alloys for engine vanes. Some of the desirable characteristics were the low-cycle fatigue of the material (Baughman, Shacklette, Zakhidov, & Stafström, 1998) (Nakamura, 1995), high melting temperature, low density, and high thermal conductivity (Darolia, Walston, & Nathal, 1996).

Wang, Zulifqar, and Hu explored more applications in 2016 (Wang, Zulifqar, & Hu, 2016). They mentioned the possibilities for incorporating auxetic materials in the wing design with a focus on energy absorption, which may provide a cushioning effect.

The cushioning effect is beneficial for the wings to be able to endure varying air pressures during flight and to dampen vibrations and shocks, especially during take-off and landing. This effect could also be utilised in other parts of the aeroplane, such as the landing gear and individual passenger seats.

Development in composites opened a lot of potential possibilities. For example, auxetic composite might be a suitable alternative for many structural applications due to increased shear modulus, desirable for an aircraft’s fuselage structure that experiences high shear forces during flight, reduced weight and improved impact resistance (Marsh, 2004).

Lastly, auxetics can be used to improve passengers’ safety and comfort when used as seatbelts that would become “fatter” by spreading the forces over the greater area while being easier to fasten due to thinner cross-sections when pulled over (US Patent No. 16592805, 2022).

Biomedical

An additional field where the applications of auxetics have been blooming in the last few years is the biomedical field. The applications of auxetics vary widely within medicine, from COVID-19 testing swabs to the development of heart valves.

In the recent event of the global COVID-19 pandemic, the importance of the development of materials like auxetics became more apparent. With fears of testing swab shortages, a 3D-printed auxetic swab was designed. The testing swab, shown in Figure 21, was designed to fit all safety criteria for biomedical uses, but also its auxeticity means it is adjustable, and hence it can be considered one-size-fits-all (Ford, 2020) (Arjunan, Zahid, Baroutaji, & Robinson, 2021). The swab can deform under axial stress to fit differently shaped nostrils to reach the nasopharyngeal, an upper part of the throat behind the nose. One of the potentials of this design is that it can be safely disinfected and re-used.

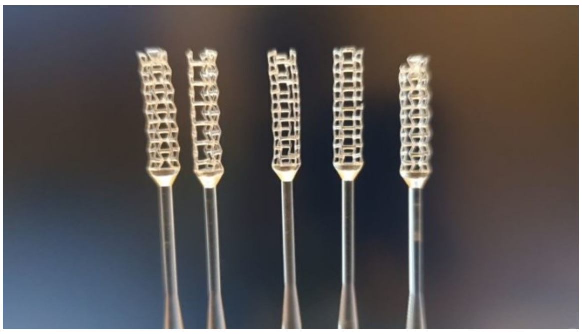

Figure 21: Open-source 3D printed Covid-19 swabs by Wolverhampton University (Ford, 2020)

A further example of auxetic in biomedicine is the project by the Complex Materials Group at ETH Zurich that looks at heart-valve replacement systems. The Complex Materials Group used 3D printing techniques and medical-grade polysiloxanes to produce patient-specific heart-valve models using the patient's CT scans. The auxetic geometry has been used for the aortic root, which makes its function similar to that of the biological heart valve, with the design expanding in two directions simultaneously (PlasticsToday, 2020).

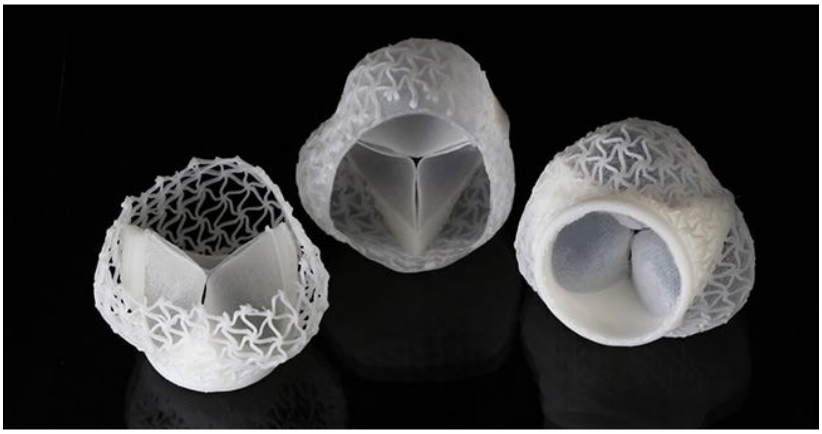

Figure 22: The 3D-printed heart-valve replacement by ViscoTec (PlasticsToday, 2020).

Future development might include introducing stem cells into the valve to match it to the patient's morphology, such as by using cell-loaded hydrogels.

The applications in biomedicine extend further, including the artificial intervertebral disc (Figure 17) (Martz, Lakes, Goel, & J.B., 2005) that could be used in support of spinal surgery (Lvov, Senatov, Veveris, Skrybykina, & Díaz Lantada, 2022). Lvov et al. further mention applications in hip replacement, fixtures for long bones, hydrogel scaffolds, and orthopaedic insoles.

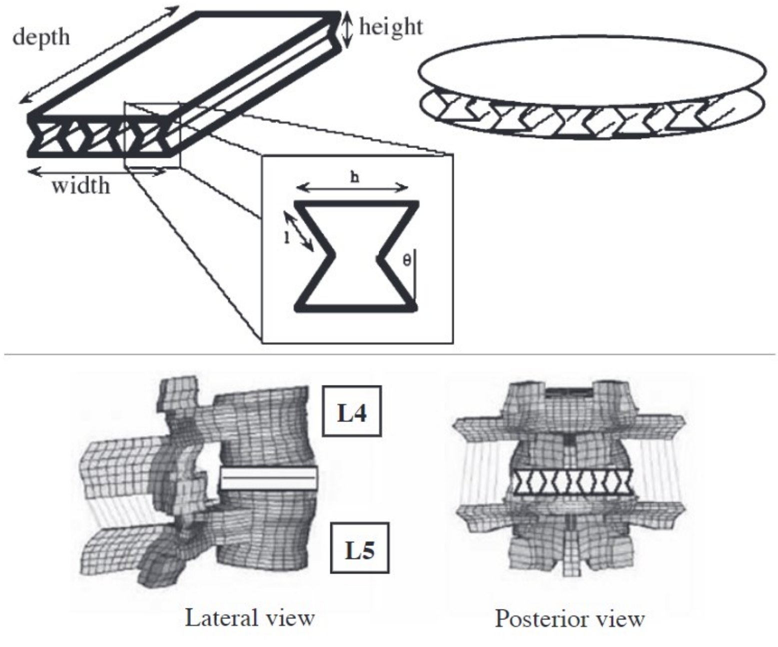

Figure 23: Proposed structure of the artificial intervertebral disc (Martz, Lakes, Goel, & J.B., 2005)

Sports

Auxetics bring many benefits to the uses in protection wear, from being more lightweight than equivalent conventional foams that can improve the users' comfort to higher impact protection, particularly sought out in contact sports.

Footwear

Starting from the commercially available wear, Nike has created the 'Nike Free series', Figure 24, where the trainer's midsole incorporates geometric shapes that exhibit auxetic behaviour, allowing deformation during the movement, improving user comfort and providing adequate support to the feet (Nike, Inc., 2016).

Figure 24: Left: Nike Free RN Flyknit auxetic sole (Nike, Inc.). Right: Under Armour Architech 3D printed performance trainers with auxetic textile design (Walker, 2016)

Under Armour 'Architech', Figure 24, is a 3D printed footwear that incorporates the variable auxetic design, 3D ClutchFit, on the upper area of the shoe, which allows a more supportive "dome" to be formed along the curvature of the foot (Walker, 2020).

PUMA XETIC, Figure 25, is another example of sports footwear with an incorporated auxetic structure (PUMA, 2020). The XETIC technology incorporates a foam-supportive structure into the sole of the shoe to enhance the rebound under the heel.

Figure 25: PUMA XETIC sneakers with the auxetic foam sole (PUMA, 2020)

Head Protection

WaveCel incorporates auxetics in the helmet's 3D structure, which consists of the double arrowhead geometry (WaveCel, 2024). The idea behind the use of this particular technology is that the auxetic structure deforms in a way that diverts the impact away from the head; the gliding of the cells aids the distribution of the rotational forces, and the cells are designed to crumple to absorb the impact energy. As a result, WaveCel claims that their helmets reduce the risk of concussion by up to 98% in comparison to the standard helmets.

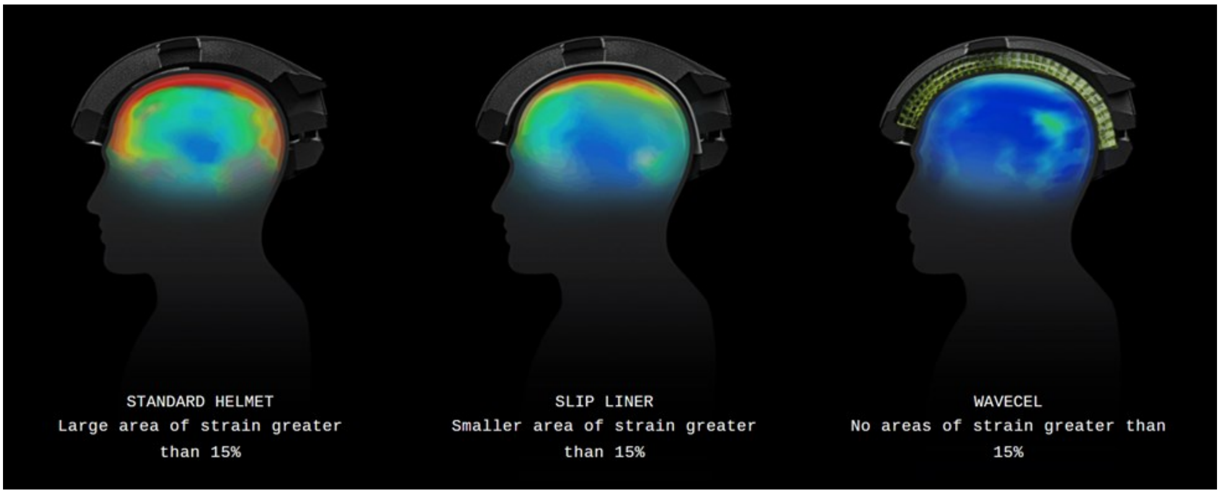

Figure 26: A comparison of the standard helmet, helmet with slip liner, and a WaveCel helmet, showing the strain on the brain during impact. The green layer in the WaveCel helmet is an auxetic double arrowhead structure (WaveCel, 2024).

Another example of head protection is the D3O's Trust Helmet with the integrated Pad System that has been commercially available as protection wear for sports like mountain biking, snow sports, American football, and ice hockey, as well as combat (D3O - Design Blue Limited, 2018). The pads are made out of gel-filled auxetic geometry, as found in Figure 27. The design provides comfort as the padding provides a better fit to the shape of the head and enhanced protection capability, which sustains consistent performance on the second impact. The auxetic geometry becomes thicker when stretched, which is perpendicular to the applied forces, hence allowing a greater deceleration of the blunt impact forces in comparison to the competitors.

Figure 27: Padding system with nine components. The inserts contain gel-filled auxetic geometry (D3O - Design Blue Limited, 2018).

Tennis Racquets

HEAD is a sports company that uses Auxetic 2.0 technology, which was developed with the support of researchers from Sheffield Hallam University, in their design of the tennis racquets, incorporating it into multiple design features such as the yoke of the racquet and the structure at the end of the handle's grip (HEAD, 2021) (Mattocks-Evans, 2021). The auxetic technology provides the tennis racquet with enhanced shock absorption but also an unexpected benefit of auxetic reaction, which, when the ball hits off-centre, it stretches some strings more than others, and the players were able to feel this reaction, giving them more control in the use of the racquet.

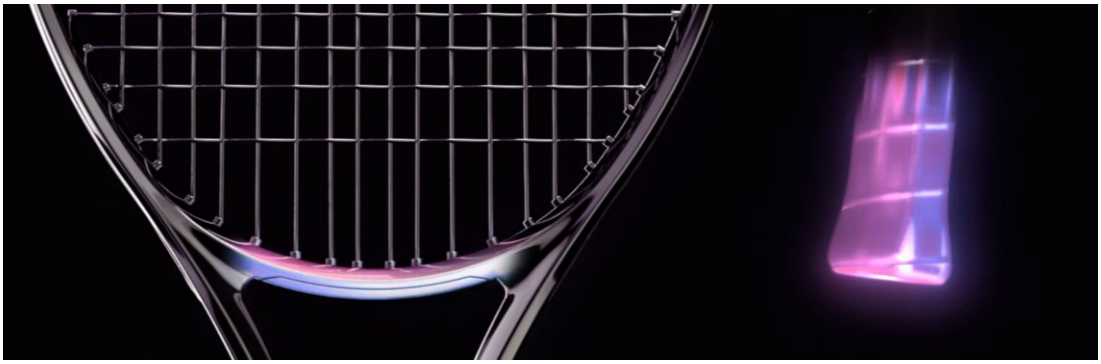

Figure 28: The HEAD tennis racquet with incorporated Auxetic 2.0 technology in its (left) yoke and (right) grip end (HEAD, 2021)

Some other suggested uses in protective wear are facemasks for outdoor sports and activities, crash mats, knee and elbow guards, vests, and outerwear (Duncan, et al., 2018). These suggestions are due to auxetic often being associated with an increase in user comfort, energy absorption, increased indentation resistance, vibration damping and shear modulus and decreased bulk modulus in comparison to the conventional counterparts.

Fashion

The fashion industry has been incorporating auxetics into novel designs. For example, Petit Pli manufactures children's suits that "grow" along with the child, Figure 29, making it a more sustainable alternative to other currently available options (Yasin, 2018) (Petit Pli, n.d.).

Figure 29: Example of the children's trousers designed by Petit Pli (Petit Pli, n.d.).

Petit Pli's range has expanded over the years and now includes maternity wear that expands to adapt to the changing body shape and expanding bags, as seen in Figure 30.

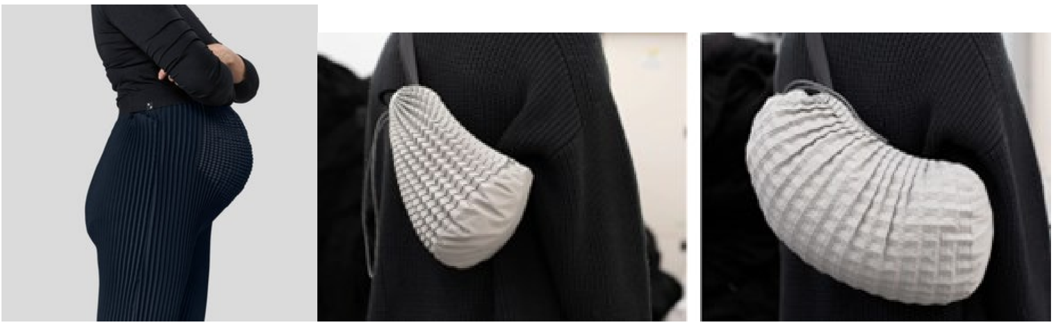

Figure 30: (Left) Maternity bottoms designed by Petit Pli (Petit Pli, n.d.); (Right) Expanding bag design by Petit Pli (Petit Pli, n.d.)

Soft Robotics

Hye Jun Youn created an interactive display using soft robotics and auxetic geometry titled “AuxeticBreath” (Han-sol, 2021), Figure 31.

Figure 31: Interactive exhibition designed by Youn (Han-sol, 2021).

Although it is an art exhibition and does not show practical use, it clearly shows that there is a potential for the use of auxetics in soft robotics. In the future, soft robotics applications might include actuator soft sleeves (Sedal, Fisher, Bishop-Moser, Wineman, & Kota, 2018) but also hints at the future where there are 3D-printed robot caregivers, Figure 24 (Martinez, et al., 2019). Auxetics should enable the expansion of the material around the joints, preventing it from breaking when the material is stretched.

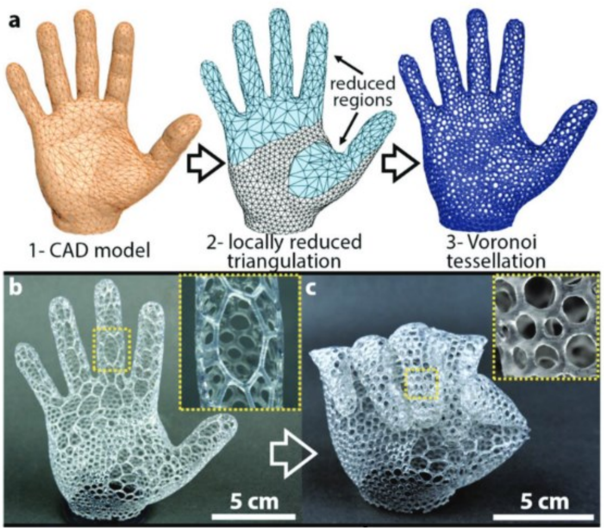

Figure 32: A CAD model of what a 3D architected soft-machine hand can look like (Martinez, et al., 2019)

Artificial Auxetics

The last few decades saw an increase in the manufacture of auxetic materials, starting with the production of open-cell foams in 1987 by Rod Lakes (Lakes, 1987). Since the first auxetic foam was made, there have been many developments in auxetic materials and structures differing in the scale (size) of the structure, the material used, and their form. Some of the examples, as well as their manufacturing methods, are discussed below, including foams, laminates and 2D and 3D lattice structures.

Composites and Laminates

Wang et al. (Wang, Zulifqar, & Hu, 2016) name a number of ways in which NPR can be achieved, including laminated angle-ply auxetic composites, composites with auxetic inclusions, auxetic composites made from preforms based on auxetic textile structures; fibres and matrix systems for auxetic composites.

Clarke et al. studied NPR in angle-ply composites through theory and experimentation (Clarke, Duckett, Hine, Hutchinson, & Ward, 1994). The composites were prepared through lamination of the unidirectional prepreg tapes of epoxy resin reinforced using carbon fibre. The NPR was achieved by tuning the layering angle and was found present between the angles of 15° and 30°. The theory reaffirmed this experimental result, and this can be seen in Figure 33.

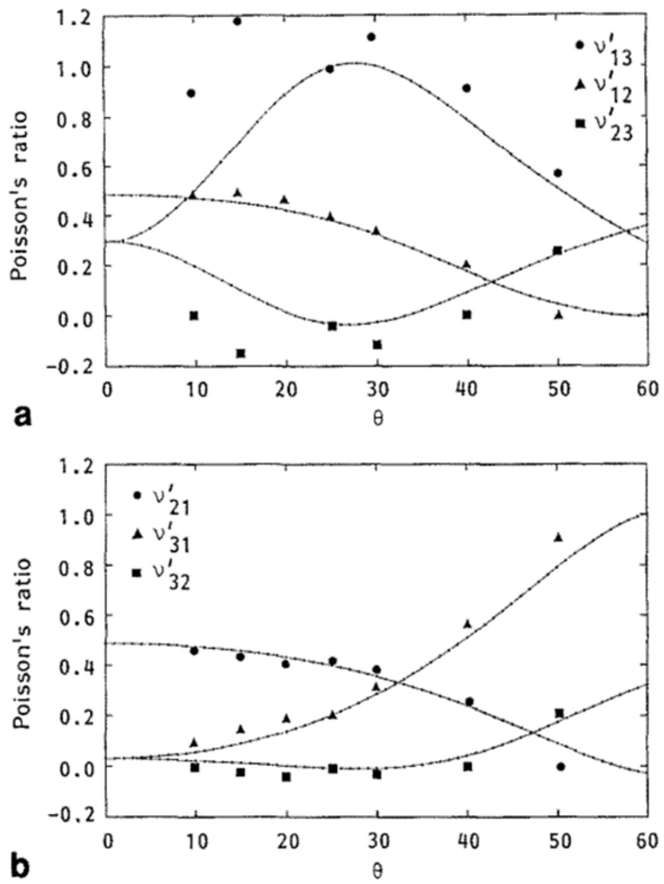

Figure 33: (solid symbols: ■▲●) the measured results; (dotted lines: --) measured results for directional Poisson's ratio. a) $v_{13} = v_{xy}$ *,* $v_{12} = v_{xz}$*,* $v_{23} = v_{zy}$ *and b)* $v_{21} = v_{zx}$ *,* $v_{31} = v_{yx}$*,* $v_{32} = v_{yz}$

More recently, McHale et al. (2024), showed experimental models consisting of the SU-8 polymer photolithographically patterned into a lattice microstructures, Figure 34. This is of interest in this research as it might be one of the avenues possible to be undertaken to manufacturability of the structures described in further sections.

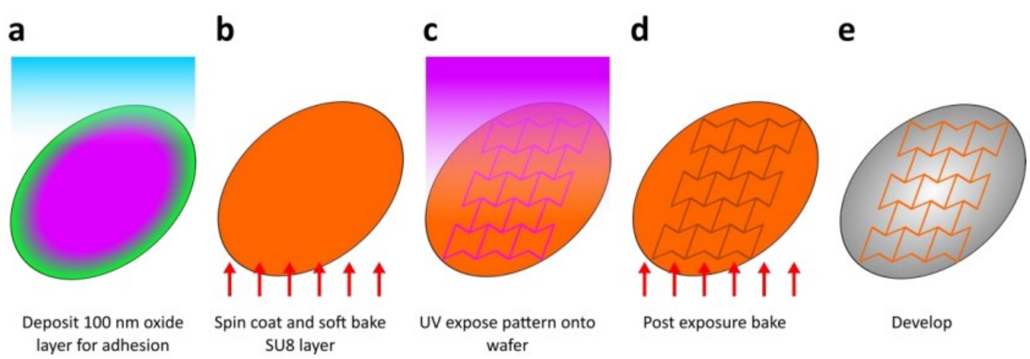

Figure 34: Fabrication process of SU-8 based model for an auxetic bow-tie lattice (McHale, et al., 2024)

Textiles and Fibres

The auxetic polymer was manufactured in the form of an anisotropic form of expanded polytetrafluoroethylene (PTFE), where the hinging of the fibrils caused the nodules to translate across, as shown in Figure 35, in turn resulting in the NPR when force was applied (Caddock & Evans, 1989). Polymers that can be manufactured into auxetic fibres are polypropylene, polyester, and nylon.

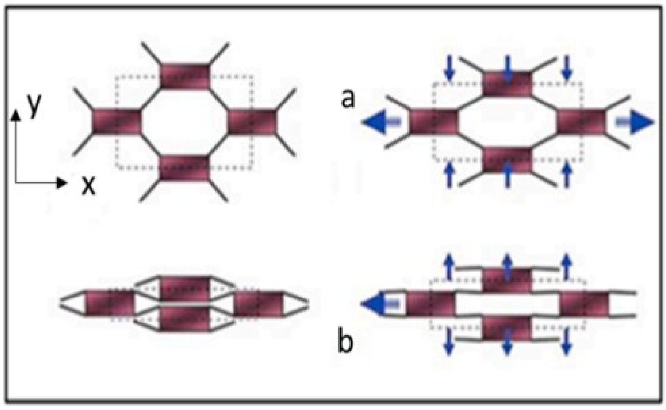

Figure 35: An illustration of the internal structure of polymer fibres where the fibrils act as hinges and cause the nodules to translate a) conventional material, b) auxetic microstructure of PTFE (Shukla & Behera, 2022)

An auxetic textile can achieve NPR by manipulating the structure of the fibrous materials or by using auxetic fibres (Shukla & Behera, 2022). These composites can be made using weaving, knitting, braiding, and nonwoven manufacturing methods, and they can be polymers, fibres, yarn, and fabrics. The same methodologies can also be applied to ceramics and metals.

Another method of achieving auxeticity within textiles is using conventional yarn and combining it in a specific way to produce helical auxetic yarns (HAY) (Patent No. KR20060009826, 2006). The thin, harder, smaller diameter yarn is wrapped around a thick, low-stiffness elastic core, as illustrated in Figure 36. When stretched, the stiffer yarn straightens, forcing the lower-stiffness yarn to wrap around it.

The elastic core becomes thinner with the elastic effect, but overall, the textile expands in the transverse. The textile can then be further arranged to enhance the auxetic property by ensuring that the yarn has an out-of-phase arrangement, as shown in Figure 36. The NPR is lower when the HAYs are in phase, as seen in Figure 36, as the individual fibres limit each other's expansion in the transverse direction.

The structure of the helical auxetic yarns (HAY), where (A) shows the unstretched HAY, and (B) shows stretched HAY

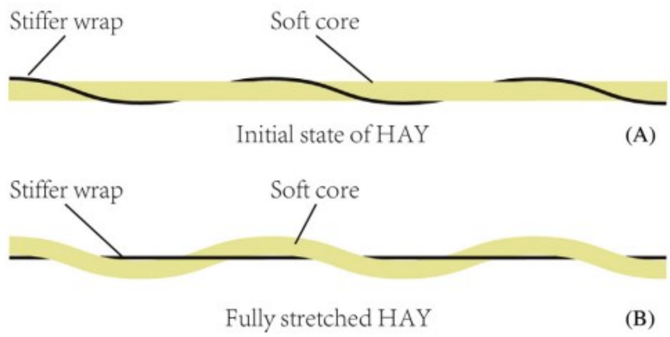

Out-of-phase arrangement of HAYs

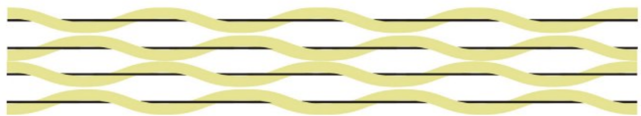

In phase arrangement of HAYs

Figure 36: The phases of HAY showing how the thin, harder, smaller diameter yarn is wrapped around a thick, low-stiffness elastic core (Hu, Zhang, & Liu, 2019)

In summary, there are many ways in which NPR was achieved within composites, from either manufacturing and using auxetic base materials for fibres or sheets to using post-production treatments to alter the internal structure. It is only appropriate to acknowledge that only the high-level overview of the methods and techniques used to produce auxetic materials artificially was provided in this section as the focus shifted to naturally occurring auxetics, discussed and reviewed in much more detail in the next section.

Foams

The auxetic foam was one of the earlier artificial auxetic structures produced. It is made by post-processing already existing conventional porous materials like Polyurethane (PU) foam, Figure 37. The first auxetic open-cell foam was fabricated using a combination of compression and thermoforming (Lakes, 1987) (Chan & Evans, 1997).

Cellular solids consist of an interconnected network of solid struts which make up the edges and plates that form the faces of the cells (Gibson & Ashby, 1988).

They are frequently mentioned within auxetic research as there have been a number of 3D cellular solids (e.g., foams) as well as 2D cellular solids (e.g., honeycombs) – designed to have a negative Poisson's ratio. Foams can be open-celled or closed-celled.

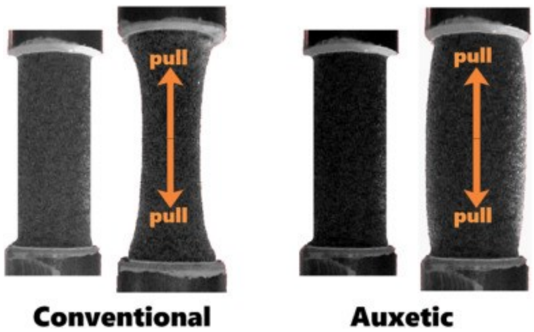

Figure 37: Comparison of conventional foam and auxetic foam whilst stretched (Jiang, et al., 2022)

The process involves off-the-shelf foam, stable compression, and a method to soften the ribs. The stable compression is applied to the foam sample using either mechanical or air pressure (Jiang, et al., 2022). This compression deforms the ribs so that they resemble re-entrant honeycomb shapes. To ensure that the ribs are deformed evenly, the pressure applied must be uniform; this can be achieved by using an appropriate mould, as seen in Figure 38.

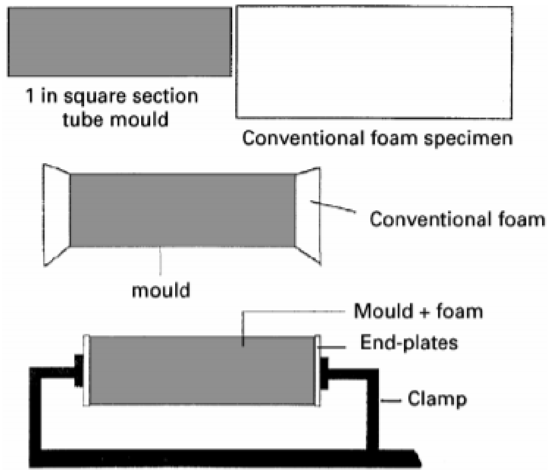

Figure 38: The diagram representing the mould and specimen set up for the auxetic foam fabrication (Chan & Evans, 1997)

Once the desired shape of the ribs is reached, they need to be softened using either heat or chemical solvents (Jiang, et al., 2022). In the case of the thermoforming process, the sample goes through annealing, a process where the material is exposed to a temperature around its softening temperature, and a cooling stage to make the rib shape permanent. Annealing and a cooling stage are not necessary with metal foams, which can have their structure altered solely via compression, which causes the foam's ribs to deform plastically.

3D Lattice Structure

Similarly to foams, 3D lattices vary in materials and manufacturing methods. However, there is a significant amount of literature on the use of additive manufacturing processes to create 3D lattices.

An example of additive manufacturing being used is in published work by Warmuth et al. (Warmuth, Osmanlic, Adler, Lodes, & Körner, 2017), who created a 3D auxetic lattice using Selective Electron Beam Melting which is categorised into powder bed fusion (PBF) in ISO52900 (Koizumi, 2020).

This method involves using the melt-a-powder bed where lattice was built vertically by creating a powder layer, then preheating it to allow for selective melting of the powder layer and building upon it. In this case, Ti_6Al_4V powder was used with particles being 45 to 105 µm and layers of 50 µm, which was controlled by lowering the table by 50 µm for each layer.

Warmuth et al. made the geometry consisting of a chiral nodes cubic unit cell built into a 3 x 3 x 5 cell lattice, as seen in Figure 39.

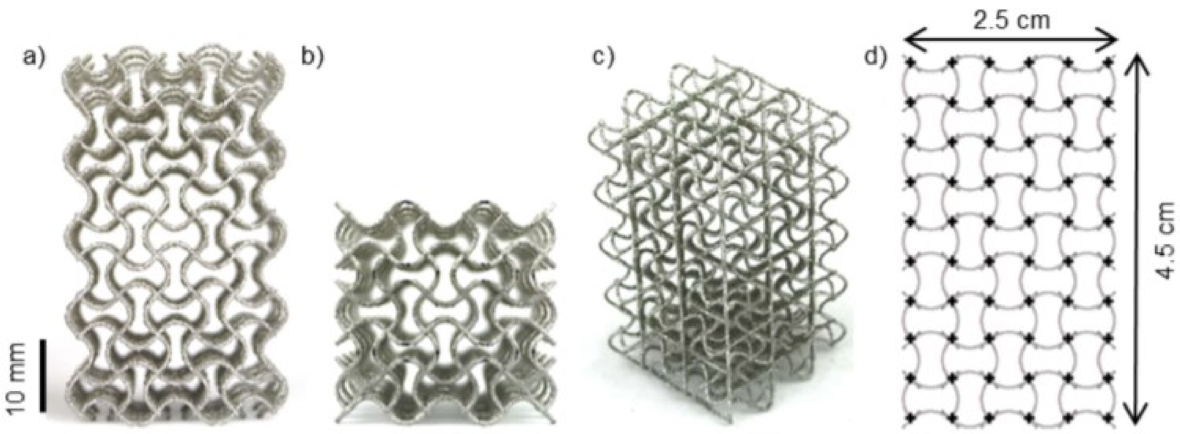

Figure 39: Samples created: a) front view, b) bottom view, c) isometric view, d) dimensions diagram (Warmuth, Osmanlic, Adler, Lodes, & Körner, 2017)

Another method of generating 3D lattices was used by the Ruiz Brothers (Ruiz Brothers, 2022), who created the lattices using 3D printing. The lattice was made using thermoplastic polyurethane (TPU), such as NinjaFlex, which, in comparison to many thermoplastics, is soft even below its glass transition temperature. NinjaFlex has been used for this purpose in several pieces of literature, including publications by Hanifpour et al. (Hanifpour, Petersen, Alava, & Zapperi, 2018) and Choi et al. (Choi, Shin, & Lee, 2022).

2D Lattice Structure

A common 2-dimensional cellular solid is a honeycomb, which consists of arrays of hexagonal polygons (Gibson & Ashby, 1988) or the auxetic equivalent – re-entrant honeycombs.

There are many examples of auxetic 2D lattice structures that have been developed over the years and are widely spread across the literature. Some examples of such structures include re-entrant honeycombs, chiral lattices, double arrowhead lattices, rotating square lattices, and rotating triangles squares. The illustration of the 2D structures from the review publication can be found in .

Gibson & Ashby mention at least four different manufacturing methods of a 2D honeycomb: sheet material is pressed into a half-hexagonal profile, and the corrugated sheets are glued together; flat sheets are glued using parallel strips, then the stack is expanded and covered in resin to harden the structure; mould casting; and extrusion.

The re-entrant honeycomb lattices are mentioned in a few further sections of this thesis.

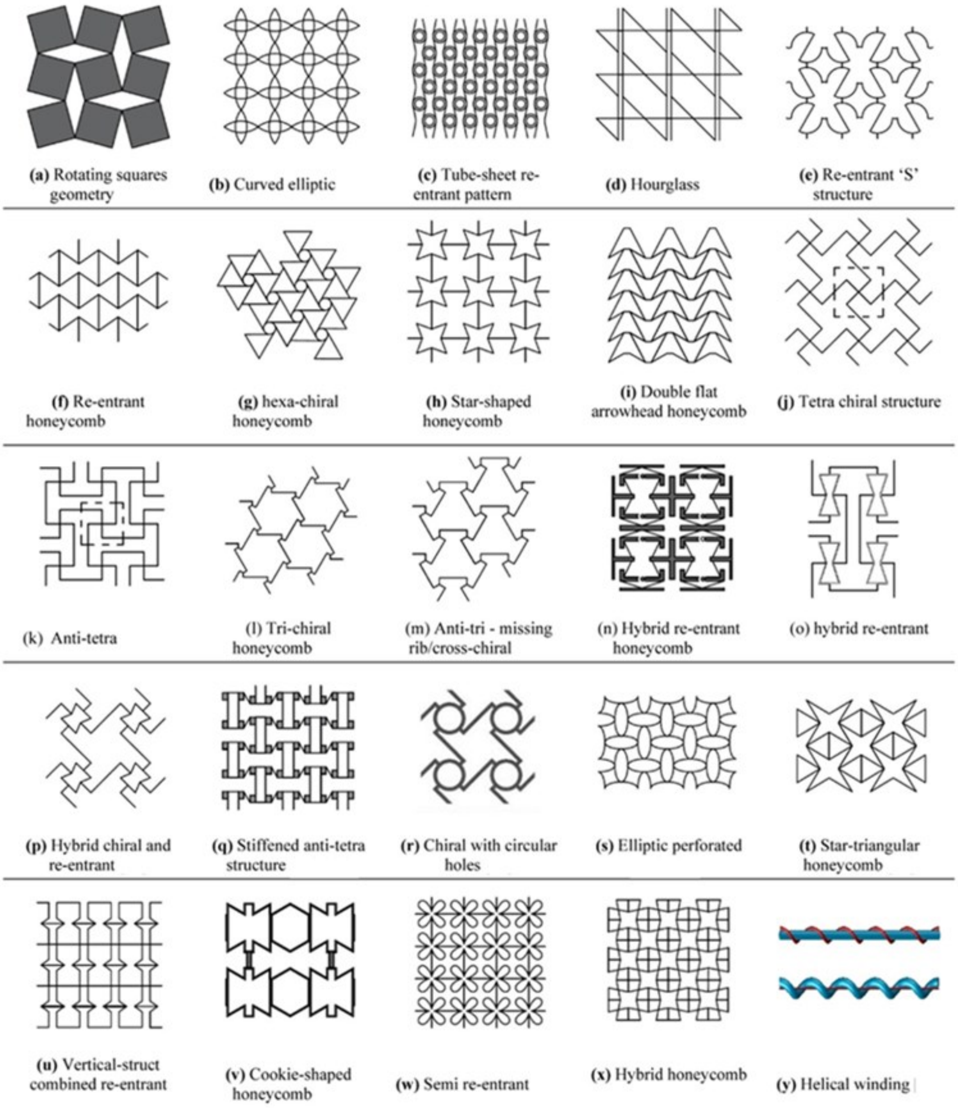

Figure 40: Examples of 2D auxetic structures, adapted from Momoh, et al., (2024)

Naturally Occurring Auxetics

There are several naturally occurring auxetic materials, from biomaterials to biominerals, with auxetic structures varying in size from as little as nano-level. Examples of naturally occurring auxetics include α-cristobalite (Yeganeh-Haeri, Weidner, & Parise, 1992), zeolites (Grima, Jackson, Alderson, & Evans, 2000), nacre (Song, Zhou, Xu, Xu, & Bai, 2008), cat skin (Veronda & Westmann, 1970), cow teat skin (Lees, Vincent, & Hillerton, 1991), embryonic stem cells (Pagliara, et al., 2014), skin of aquatic salamander (Laura A. Chernak, 2012), artery (Timmins, Wu, Yeh, Jr., & Greenwald, 2010), tendon (Gatt, et al., 2015), and cancellous bone (Williams & Lewis, 1982). This research project will focus on nacre due to the number of highly beneficial properties that could be of high importance for impact protection applications. Nacre is separately discussed in the section 'Nacre'.

α-cristobalite

α-cristobalite is known to be a naturally occurring auxetic mineral found in volcanic rock (Akhavan, 2014) that exhibits a negative Poisson's ratio (Ji, et al., 2018). Cristobalite is the low-temperature polymorph of silica and has the same molecular components as quartz silicon dioxide, SiO_2, but a different crystal structure (Anthony, Bideaux, Bladh, & Nichols, 2001).

α-cristobalite was suggested to have auxetic properties due to synchronised rotation of the SiO_4 tetrahedra but also was found to exhibit auxetic properties after dilation of the tetrahedra, which causes a variation in the tetrahedra sizes (Alderson & Evans, 2009) (Ji, et al., 2018), which can be seen in Figure 41 and Figure 42.

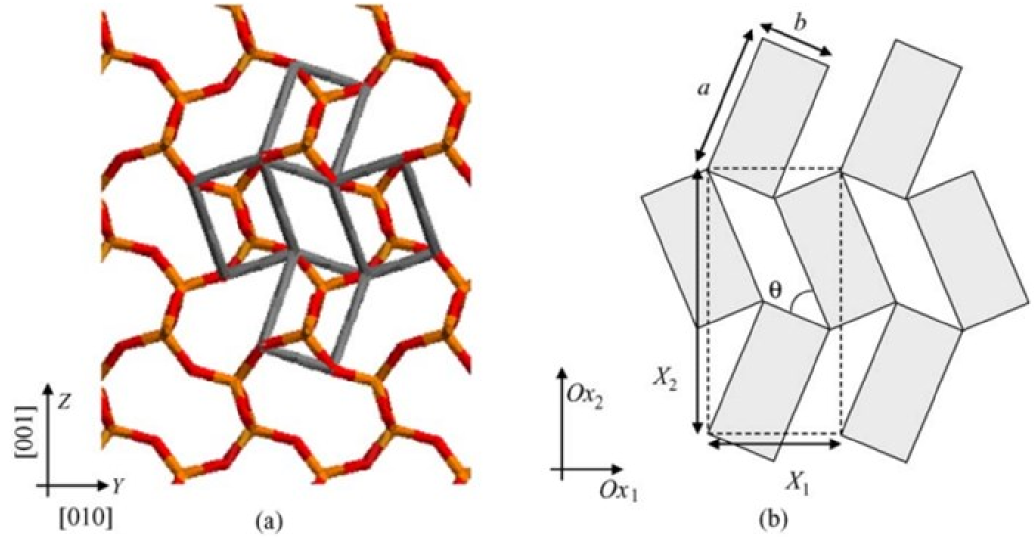

Figure 41: (a) α-cristobalite structure with the rotating rectangles in grey; (b) proposed model by Grima, Gatt, Alderson, & Evans (2006) to show how the rotating rectangles are connected (Grima, Gatt, Alderson, & Evans, 2006)

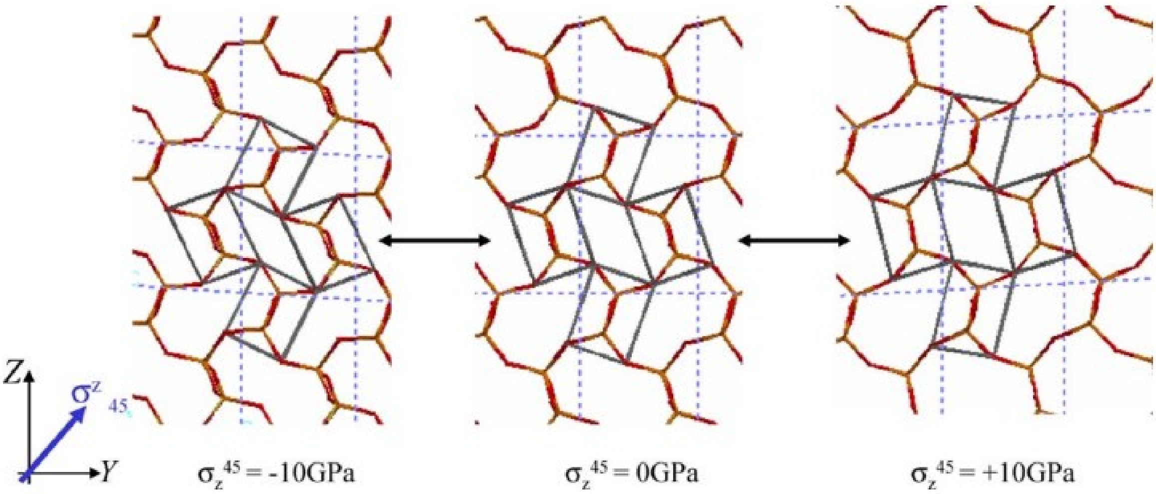

Figure 42: The diagram showing the changes to the structure of α-cristobalite under an applied load in the zy-direction (Grima, Gatt, Alderson, & Evans, 2006)

Embryonic Stem Cells

Embryonic stem cells (ESCs) can transform into different kinds of organic cells, except reproductive cells (Pagliara, et al., 2014). ESCs go through multiple states to transform into the final and irreversible state with a specific role. These states are naïve pluripotency, at least one metastable transition state, and the irreversible somatic cell. In the initial state of naïve pluripotency, EMCs can self-renew, and whilst in the metastable transition state, cells are differentiating and reprogramming into one of the somatic cells.

Pagliara et al. looked into the auxeticity of ECSs during their transition, showing that ECSs exhibit NPR properties and increased stiffness when stretched and compressed. This was shown to be caused partly by global chromatin decondensation and might be playing a crucial role in mechanotransduction, in which a cell responds to mechanical stimuli and converts them into biochemical signals, and which might be essential in the differentiation and reprogramming of the stem cells into somatic cells.

To prove that the role of the chromatin decondensation is the leading cause of auxeticity, Pagliara et al. treated the cells using 300nM of Trichostatin A (TSA), which is a histone deacetylase (HDAC) inhibitor responsible for decondensing chromatin. The changes in the relative cross-sectional area of the two types of nuclei are shown in Figure 43, and it can be seen that the TSA-treated cells are all auxetic.

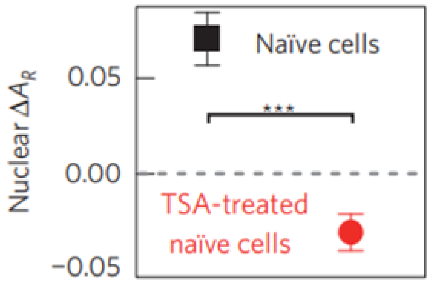

Figure 43: Relative change of cross-sectional area when nuclei are compressed. Anything below 0 is auxetic (Pagliara, et al., 2014).

Animal Tissue

A frequently mentioned example of a material with NPR is skin, with a few studies done on different animal skins, including cat, cow, pig, and aquatic salamanders. The challenge in identifying the mechanical properties of skin is that the biological tissue is non-linear, and the properties of the skin vary depending on the direction of the fibres and the force applied (Fung, 1968).

In the work by Ridge and Wright (Ridge & Wright, 1965), it was found that the skin goes through three phases when extending: an initial phase when the collagen fibres are straightening, a second phase where the oriented collagen is stiffening, and a final phase which is when the skin is yielding, and individual fibres start to break. The most significant influence on these phases and the derived constants was the condition of fibres in the meshwork and the length and area of the individual collagen fibres (Ridge & Wright, 1966).

One of the earliest quantifiable demonstrations of skin's NPR was by Veronda and Westmann, who studied cat skin under uniaxial stress to collect force-extension data (Veronda & Westmann, 1970). In their study, they analysed the data of the spinal and dorsal skin samples deformed using dead weight loadings. The results in Figure 44 show the lateral extension ratio, λ_3, and longitudinal extension ratio, λ_1, where λ_1 is defined as the ratio between principal extensions of the deformed body and the initial gauge lengths on the undeformed body. Poisson's ratio can be calculated using equation (1) and by obtaining the strains from Figure 44. The strains can be obtained by subtracting one from the extension ratios.

Lees, Vincent and Hillerton studied the uniaxial and biaxial strains of cow teat skin (Lees, Vincent, & Hillerton, 1991). Their results showed that the cow teat tissue had NPR for certain strains and over certain aspect ratios of the samples.

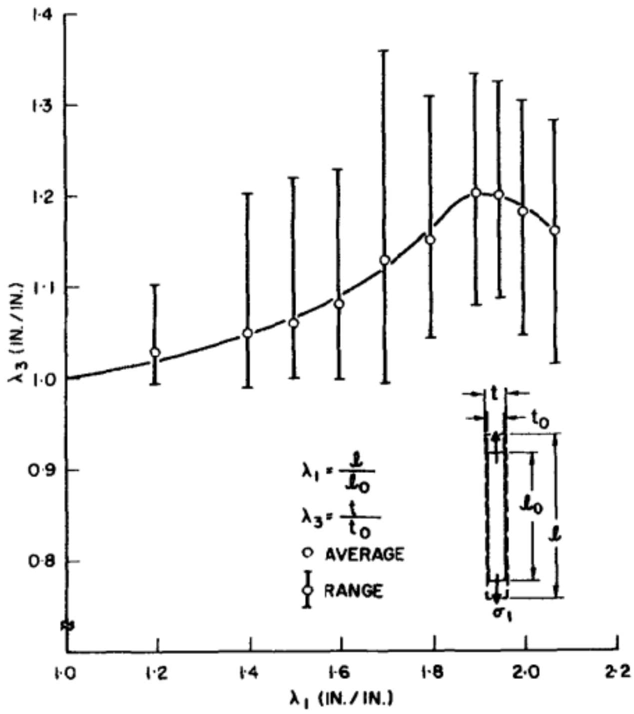

Figure 44: Lateral extension ratio, λ_3, vs longitudinal extension ratio, λ_1 (Veronda & Westmann, 1970).

A more recent study showed that pig's skin tissue has NPR, which is directional, i.e. only present when the strain was applied perpendicular to the Langer lines or skin tension lines of the tissue (Dwivedi, Lakhani, Kumar, & Kumar, 2022). The value of the Poisson's ratio found was -1.71 ± 0.29. This Poisson's ratio (the secant Poisson's ratio) was found using the True Strain:

$$\nu_{xy} = -\frac{\ln(1+\varepsilon_{xx})}{\ln(1+\varepsilon_{yy})}. \tag{24}$$

The experiments mentioned above showed a similar phenomenon where NPR was found at certain strain levels, with dependencies found in the direction of the skin fibres as well as aspect ratios of the samples used. Lees et al. suggested that fluid flow might be present within the cow teat wall, potentially introducing rheological factors and time-dependency to test.

Biomimetic materials

Biomimicry can be defined as the study of nature, its system, procedures, processes or individual elements to use as the very basis towards novel solutions (Berger, 2019). Humans drew inspiration from nature for centuries, from clothing to the technology we use. Some examples of auxetic-inspired systems were mentioned in earlier sections, but many more biomimetic inventions might be worth mentioning to recognize how far those inspirations can be drawn.

Understanding how the natural material structure is created is often the first step to mimicking it into an artificial composite, and frequently, it is the biggest challenge as the natural structure is very complex, varying across atomic, molecular, nano- and micro-scale (Sanderson, 2015).

Biomimetic textiles are a wide range of textiles that are designed for multiple purposes with natural designs as inspiration. Some beneficial properties of textiles considered are protection, self-cleaning, self-protection, and energy conservation (Maghsoudian, et al., 2022)

Camouflage is also one of the properties inspired by nature. Initially inspired by a chameleon that changes its colours, but it is also used by different animals, including butterflies, birds, frogs, and insects, where the colours of the animal allow it to blend into its environment (Maghsoudian, et al., 2022).

Camouflage developed from being a colour design feature to much more complex technology where shape optimisation, radar absorbing materials (RAM) based on conducting polymers, use of undetectable pigments, and 3D warp-knitted structure fabrics are utilised to allow soldiers to ”camouflage” even with the use of infrared (IR) or low-light surveillance technology.

Currently, colour-changing camouflage can change with changing pH, changing arrangement of bonds, oxidation, mechanochromism, and magnetic field.

Other colour-sensitive materials, for example, thermochromism (changing colour in different temperatures), photochromes (colour sensitivity in light), electrochromic (sensitive to electricity), solvatochromic (sensitive to the polarity of solvents), can be used in camouflage fabrics.

Over time the need to fabricate body armour which is hard, lightweight, and flexible, has increased (Maghsoudian, et al., 2022) (Wang, et al., 2017). These properties can be found in nature on an individual basis or within some combinations; hence, it is of high interest to understand the cause of each of those properties.

Looking at some of the strongest natural materials, most will think of the bone structures, armadillo shells, or mother-of-pearl. Each of those is made up of primarily inorganic components with a much lower amount of organic "filling", where, for example, bones are made of hydroxyapatite (inorganic) and collagen (organic) (Sanderson, 2015). Another example would be nacre, which is composed of 95% inorganic calcium carbonate in the form of aragonite and 5% organic biopolymers, β-chitin and silk fibroin proteins (Ding, et al., 2017). Separately, those materials are weak, but nature creates something strong, flexible, and self-healing from them (Sanderson, 2015).

Nacre

Nacre, also referred to as mother-of-pearl, is a natural auxetic biomineral found as an inner layer of molluscs' shells (Alderson A. , 2015). Nacre, known for its desirable properties, is an excellent inspiration for bio-inspired materials used for applications in impact protection. It is characterised by its fracture resistance, high toughness (Kakisawa & Sumitomo, 2011) (Ding, et al., 2017) (Sanderson, 2015), and relatively low weight, which is often associated with its hierarchical micro- and nanostructures (Zheng, 2019).

Nacre, which forms an inner layer of molluscs' shells, is a product of the biological mineralisation process immanent to these soft-bodied animals. Molluscs grow a hard shell for protection (Espinosa, Rim, Barthelat, & Buehler, 2009) through the complex biological mineralisation processes, which is still highly hypothetical due to a poor understanding of the biological systems (Pomar, 2020).

The shell in molluscs, including the nacreous structure, is a mechanism that is necessary to protect the molluscs against their natural predators and threats, which are very varied. These include different kinds of gastropods which drill small tapered holes in the shells to consume the mantles or some species of sponges which are capable of boring through the shell sufficiently to inhibit it, in effect, killing the mantle inside (Guida, 1976). The marine crustaceans, crabs and lobsters use their claws to break the shells to consume the mantle (Humphrey, 2008).

The organ inside the shell, the mantle, is responsible for the growth of the shell using its epithelial cells and periostracum (cross-linked protein layer). The inner structure of the mantle within the shell can be found in Figure 45.

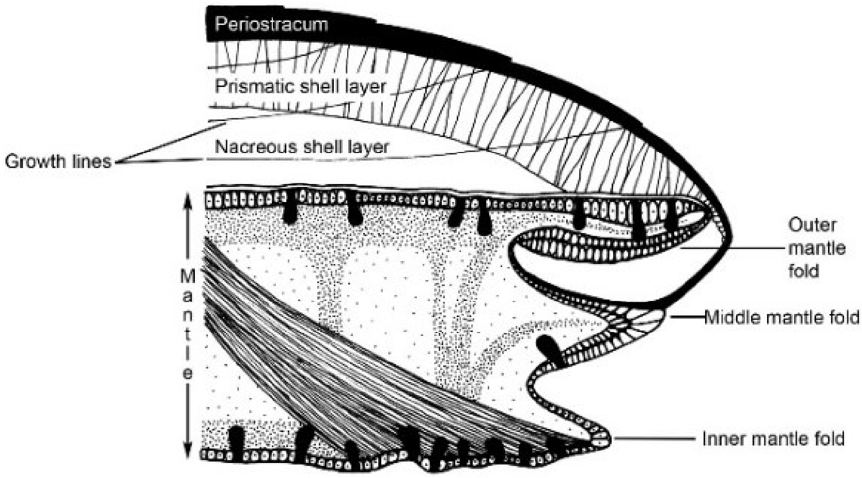

Figure 45: The diagram showing the edge of the mantle of a bivalve shell (Sobel, 2020)

On the inside of the shell, a complex matrix is responsible for the formation of $CaCO_3$ crystals, mostly aragonite (Pomar, 2020). Several types of shell structures are created through this process: nacreous, crossed lamellar, and foliated (Pomar, 2020). Nacre can be further categorised into the sheet and columnar structures (Espinosa, Rim, Barthelat, & Buehler, 2009). The common trait between all of these structures is that they contain an organic matrix that never exceeds 5% of the total volume.

Approximately 95% of the volume of the structure is composed of polygonal platelets of calcium carbonate, as seen in Figure 46, measuring approximately 0.5 μm in thickness and 5 to 8 μm in diameter. The remaining 5% of the volume is thin layers of an organic polymer matrix consisting of biopolymers of chitin and protein (Espinosa, Rim, Barthelat, & Buehler, 2009). This organic layer works as an adhesive for the structure as it holds the platelets and nanograins together. The overall structure could be compared to that of 'brick-and-mortar'. The organic layer is thought to be responsible for the nacre being 3000 times tougher and more flexible than the pure calcite (Espinosa, Rim, Barthelat, & Buehler, 2009).

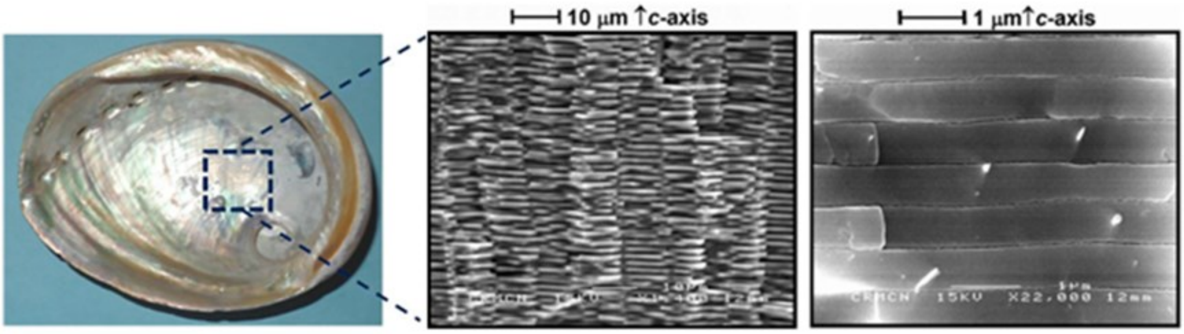

Figure 46: Photograph of nacre (Vijayan & Puglia, 2019) and SEM images of nacre's regular microstructure consisting of stacked platelets (Bruet, et al., 2005)

However, the precise mechanisms underlying the heightened properties as well as auxeticity within nacre remain unknown. There are a number of theories present in the literature that attribute these properties to either the platelets or the organic layer, but there is no consensus explanation for the behaviour present in the nacre. The various speculations by different authors will be recounted in the section "Auxetic behaviour of nacre".

Nacre's Mechanical Properties

Through mechanical testing, Currey and Taylor investigated the properties of shells of nineteen different species of molluscs, as listed in , which had different types of structures, including cross-foliated, foliated, homogeneous, crossed-lamellar, prismatic, and nacreous (Currey & Taylor, 1974). They found that cross-foliated, foliated, homogeneous, and crossed-lamellar structures did not exceed the tensile strength of 60 MPa, with the exception of a single specimen. In comparison, nacreous and prismatic structures performed much better, Figure 47, reaching higher tensile strength exceeding 120 MPa, with the exception of a single species, *Anodonta*, which has a prismatic structure (Currey & Taylor, 1974) (Öksüz & Şereflişan, 2023).

The Modulus of Rupture, M.R. shown in refers to the material property that measures maximum stress the material can withstand before it yields or breaks during the test such as the three-point bend test (Jones & Ashby, 2019). This test is often performed on brittle materials.

Class	Species		S_t [MPa]	M.R. [MPa]	E [GPa]	Structure	Orientation
Gastropoda	*Conus prometheus**	(a)	34·9 (7)	125·0 (4)	67·7 (1)	Crossed-lamellar	Parallel
	Turbo marmoratus	(b)	107·8 (4)	266·8 (4)	54·1 (4)	Columnar nacre	Normal
	Patella mexicana	(c)	33·2 (2)	171·4 (5)	60·0 (2)	Cross-foliated	Parallel
	Strombus costatus	(d)	—	58·5 (3)	48·6 (2)	Crossed-lamellar	Parallel
	Strombus gigas	(e)	6·2 (4)	73·2 (5)	40·7 (4)	Crossed-lamellar	Parallel
Cephalopoda	*Nautilus pompilius*	(g)	63·1 (3)	206·4 (6)	44·5 (6)	Mixed, mainly nacre	Various
Bivalvia	*Egeria radiata*	(i)	50·2 (5)	106·3 (4)	76·8 (2)	Fine crossed-lamellar	Parallel
	Chama lazarus	(j)	—	40·4 (1)	82·2 (1)	Complex crossed-lamellar	Parallel
	Pinctada	(k)	51·1 (1)	172·7 (1)	48·4 (1)	Sheet nacre	45°
	Atrina vexillum	(l)	60·0 (3)	139·1 (3)	39·2 (3)	Calcite simple prisms	Normal
	Atrina vexillum	(l)	89·1 (3)	172·6 (5)	57·7 (1)	Nacre	Normal
	Hyria ligatus	(m)	71·8 (2)	129·8 (1)	67·1 (1)	Columnar nacre	Parallel
	Hippopus hippopus	(o)	9·3 (1)	37·5 (1)	53·3 (1)	Crossed-lamellar	Normal
	Arctica islandica	(q)	—	48·8 (2)	65·8 (1)	Homogeneous	45°
	Anodonta cygnaea	(r)	37·8 (7)	142·3 (2)	44·0 (2)	Nacre	Parallel
	Ostrea edulis	(s)	—	72·8 (2)	47·0 (1)	Foliated	Various
	Mercenaria mercenaria	(t)	31·5 (4)	95·3 (4)	65·9 (1)	Fine crossed-lamellar to homogeneous	Parallel
	Ensis siquilla	(u)	—	123·6 (1)	54·9 (1)	Very fine crossed-lamellar	Parallel
	Pinna muricata	(v)	62·4 (1)	—	11·8 (1)	Calcite simple prisms	Normal
	Pecten maximus	(w)	42·1 (3)	110·5 (7)	30·1 (6)	Foliated	Normal
	Saccostrea cucculata	(y)	31·2 (1)	44·3 (6)	28·7 (6)	Foliated	Normal
Insecta	*Schistocerca* tibia		95	—	9·5	—	
Mammalia	*Bos* femur		190	270	18	—	

Table 1: The average mechanical properties of the shells tested, including Tensile Strength [S_t], Modulus of Rupture [M.R], Modulus of Elasticity [E] (Currey & Taylor, 1974)

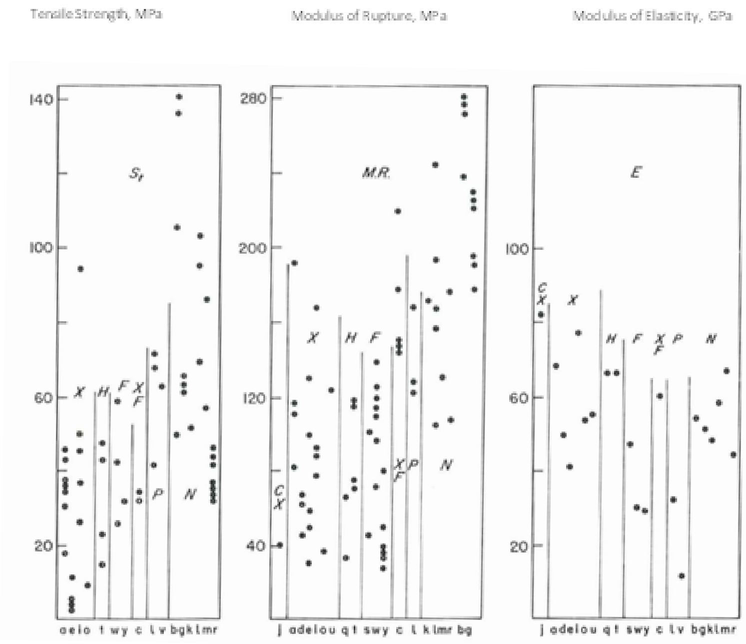

Figure 47: Mechanical properties of the individual specimens. Each column correlates to one species, as indicated in Table 1. Lines separate the specimens of different structures: H – homogenous, F – foliated, XF – cross-foliated, P – prisms, and N – nacre (Currey & Taylor, 1974).

Nacre is also known for its hardness and fracture toughness. Sun & Bhushan reviewed the literature available and found that the fracture toughness of nacre was between 3.3 and 9 $MPa\,\sqrt{m}$, which is three to nine times higher than pure aragonite, which is approximately 1 $MPa\,\sqrt{m}$ (Sun & Bhushan, 2012).

Ashby and Wegst (Wegst & Ashby, 2004) plotted nacre's toughness which they found using Charpy test against other natural materials that are often considered tough, and these are shown in Figure 48. Charpy toughness is found using Charpy impact test which allows for measuring the amount of energy absorbed by the material during fracture (Chung, 2017). Charpy toughness is not interchangeable with the fracture toughness as they are slightly different measures. Charpy toughness focuses on the energy absorption of the material before it breaks under the impact, and fracture toughness measures material's resistance to crack propagation under load (Curry, 1980).

The position of the mollusc shell on the plot indicates that it has an excellent combination of toughness and modulus relative to many other materials.

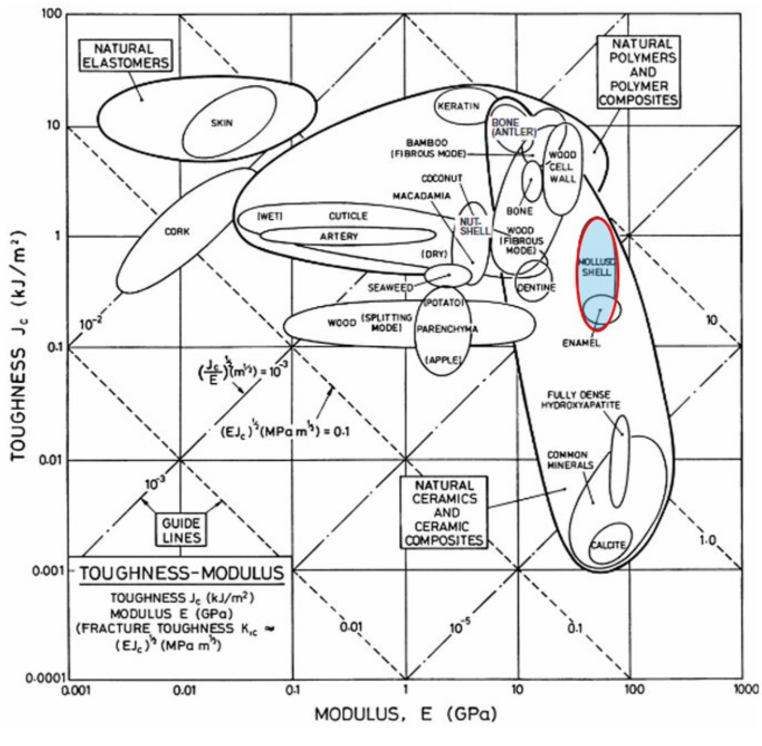

Figure 48: A chart showing the properties of natural materials and their toughness against Young's modulus (Wegst & Ashby, 2004).

Auxetic behaviour of nacre

Nacre is known to be auxetic; however, there is very little known about the origin of the auxetic response, primarily due to the scale and complexity of the structure and our inability to observe the deformation at that level. Therefore, it is possible that auxetic behaviour is to be credited for the enhanced performance of the nacre previously mentioned in the section '*Nacre's Mechanical Properties*'.

Auxeticity has been observed in the nacre through experimentation by Barthelat, et al. (2007) and Song et al. (2008).

Barthelat et al. performed tensile, shear compression and shear testing on dry and hydrated nacre specimens acquired from the red abalone shell. Their results showed that dry nacre had higher shear strength but was more brittle in comparison to the hydrated counterpart. However, more notably, the shearing test showed significant lateral expansion, which indicates that nacre has NPR (Barthelat, Tang, Zavattieri, Li, & Espinosa, 2007).

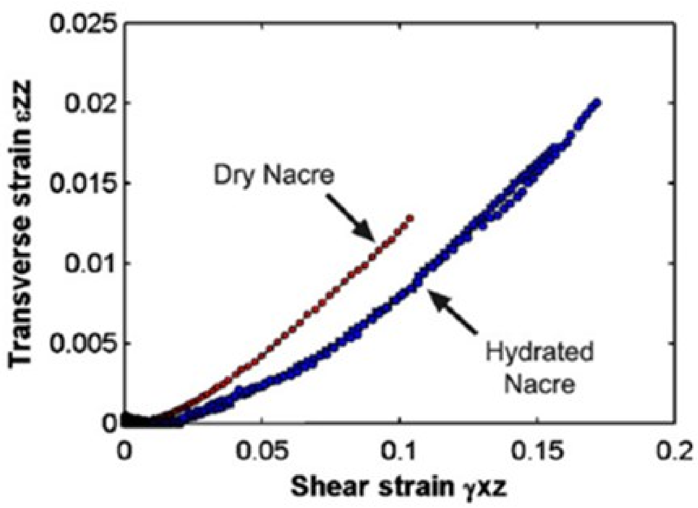

Figure 49: The results of the nacre shear test showing the positive correlation between shear strain and transverse strain, which is indicative of lateral expansion and, hence, negative Poisson's ratio (Barthelat, Tang, Zavattieri, Li, & Espinosa, 2007).

Similar results were obtained by Song et al. (2008). Song et al.'s experimental data for nacre for tensile deformation show the variations of Poisson's ratio across a range of strains, revealing NPR at certain strain levels (Song, Zhou, Xu, Xu, & Bai, 2008).

Figure 50 (a) shows the direction of the deformation applied. Across the applied longitudinal strain, the Poisson's ratio ranges from -0.38 to 0.42, as seen in Figure 50 (c).

The results showed that initially, nacre presented linear elastic behaviour up to the strain of 1.2×10^{-3}. For strains 1.2×10^{-3} to 0.01, an inelastic strain was observed, which further showed a degree of hardening and yielding as it reached its elastic limit of 70 MPa up until the point of failure.

The transverse strain was about -0.4×10^{-3} for the elastic region, which resulted in Poisson's ratio being equal to 0.32.

In the inelastic strain region, the longitudinal strain was between 1.2×10^{-3} to 4.4×10^{-3}, and transverse strain at nearly -1.71×10^{-3}, which resulted in Poisson's ratio being, on average, equal to 0.42.

For longitudinal strain between 4.4×10^{-3} and 6.1×10^{-3}, the transverse strain was consistent at near -1.71×10^{-3}, resulting in Poisson's ratio near 0.

When the longitudinal strain was increased from 6.1×10^{-3} to 9.2×10^{-3}, there was a degree of transverse expansion observed, with total transverse strain increasing from -1.71×10^{-3} to -0.54×10^{-3}, corresponding to a change in transverse strain of about 1.17×10^{-3}. This brought the Poisson's ratio to -0.38.

There was an increase in the volumetric strain energy per unit volume of the material by 1100% and a decreased deformation strain energy per unit volume by about 44%, indicating that nacre uses more energy towards the volume change than its deformation hence, it can absorb more input energy before the failure of the material.

Song et al. suggested the mechanism that might be causing the auxetic behaviour, which will be reviewed in the following section, along with other suggestions. Song et al.'s theory is referred to as Mechanism 3 for this project.

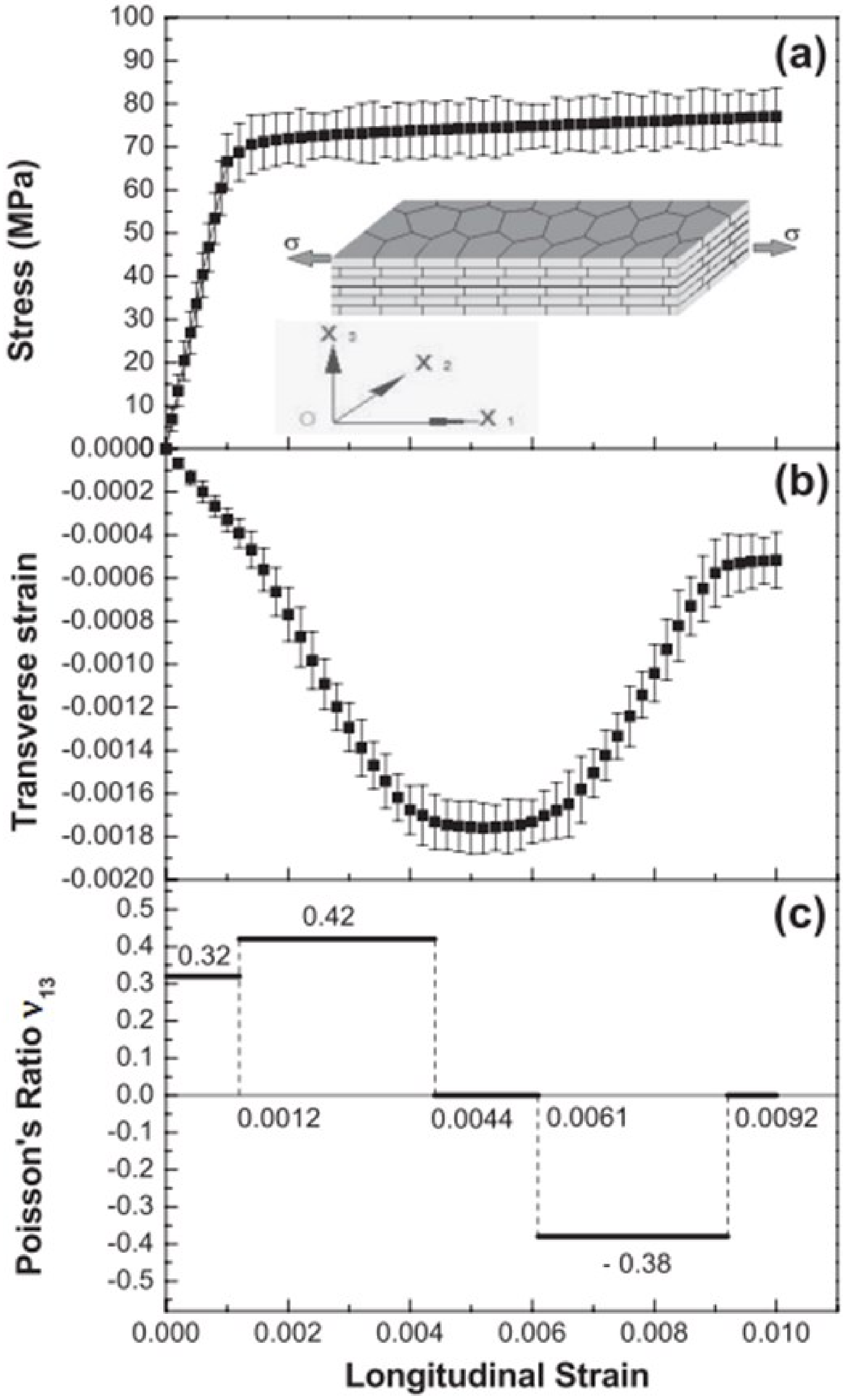

Figure 50: Results by Song et al. showing the variations in transverse strain, stress, and Poisson's ratio against a longitudinal strain of nacre (Song, Zhou, Xu, Xu, & Bai, 2008).

Auxetic Mechanisms

The auxetic behaviour within nacre is still widely unexplored, with several theories and suggestions that claim to explain the auxetic behaviour. Espinosa et al. (2011) suggested that the key to the heightened mechanical performance in nacre is the adhesion of the organic layer and waviness in the platelets, Wang & Boyce (2010) suggested that it was the shearing of the organic matrix, whilst Song et al. (2008) claimed that it was the bricks moving across the disparities caused by broken linked bridges, and lastly, Li et al. (2006) claimed that it was all caused by grain rotation within the bricks themselves.

The different theories as to how auxetic behaviour comes about in the nacre are individually explored below.

Table 2 shows a brief description of each of the theories, the author, and the reference name. For simplicity, all further references to each theory will be regarded as Mechanism 1, Mechanism 2, Mechanism 3, and Mechanism 4.

Reference	*Brief Description*	*Author*
Mechanism 1	Shearing of the organic matrix of polymeric microframes	(Wang & Boyce, 2010)
Mechanism 2	Sliding of concave bricks	(Espinosa, et al., 2011)
Mechanism 3	Brick climbing due to linked bridges causing disparities after fracture	(Song, Zhou, Xu, Xu, & Bai, 2008)
Mechanism 4	Grain rotation within aragonite	(Li, Xu, & Wang, 2006)

Table 2: Reference annotations and summary of the mechanisms used throughout this report

Mechanism 1

The model by Wang and Boyce suggests that the auxeticity is caused by the shearing of the organic matrix of polymeric microframes (Wang & Boyce, 2010).

The combination of hard and soft materials allows for the manipulation and improvement of certain mechanical properties such as stiffness, strength, impact resistance, and toughness. These properties can be further improved in the materials with micro- and nanoscale crystals as their composition allows the premature fracture to be averted by slowing down the escalation of the fracture from the initial flaw. The research showed that post-yield, plastic deformation is not incompressible, which leads to volumetric increase and, hence, to increased energy dissipation properties.

Wang et al. mention that toughness is achieved by matrix deformation and mechanical sliding, referring back to mineral bumps and bridges which are separately mentioned in **Mechanism 3**.

Their focus was on the organic layer, which has been shown to behave like highly stretched polymer fibrils or ligaments. This might suggest that either the organic matrix consists of distinct ligaments rather than a continuous material, or it breaks into such a structure during deformation. These ligaments are what likely allow the large deformations of the matrix and lead to the dissipation mechanism within the system.

The finite element analysis of the micro-mechanical composite carried out by Wang et al. was of the brick-and-mortar structure where bricks were alumina platelets, and mortar was a viscous polymer, SU-8. The model demonstrated that the microframe polymer with discrete "ligaments" leads to the transfer of the load via the shear lag mechanism, showing similarity to the continuous matrix whilst still showing improved mechanical properties like stiffness and strength.

Figure 51 shows the staggered mineral bricks with a polymer matrix layer in between, where it is clear that the matrix consists of a single layer of “X’s”.

Wang & Boyce (2010) indicated that the geometry was inspired by another study of “(3D) periodic polymer micro-frames with sub-micrometer beams” where the deformed frame microstructures are thought to resemble “the stretched matrix ligaments in the deformed nacre”.

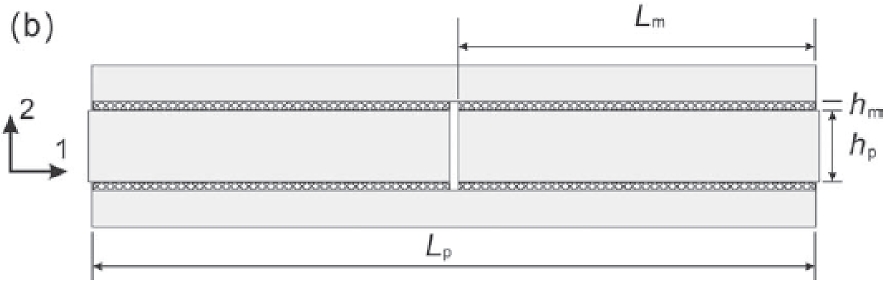

Figure 51: Representative volume element with platelet volume of 0.90 and aspect ratio equal to 10 (Wang & Boyce, 2010)

Table 3 shows the material properties used by Wang and Boyce in their analysis. Polymer’s stress-strain relationship was modelled using an elastic-viscoplastic constitutive model, and it was subjected to uniaxial tension.

Material Properties	***Mineral Brick***	***Polymer Matrix***
Poisson’s ratio	0.33	0.33
Young’s modulus	100 GPa	3.3 GPa
Yield Stress	2 GPa	100 MPa

Table 3: Material properties used for the brick-and-mortar structure (Wang & Boyce, 2010)

The range of volume fraction of platelets (V_p) analysed was from 0.50 to 0.90, or 50% to 90%, although the nacre itself is closer to the V_p of 95%. The higher volume fraction has been observed to have more desirable mechanical properties, such as higher stiffness and yield strength, but the volume fraction of nacre would be challenging to achieve within the synthetic composite.

The results in Figure 52 show incremental Poisson's ratio. The Poisson's ratio reaches the lowest magnitude for $V_p = 0.90$ value of -2.70 at a macroscopic strain of 0.006. Additionally, the plot shows the double yield. There is an instantaneous strain softening after each yielding occurrence, which is speculated to be due to microframes providing the shear lag load transfer mechanism, which is alike to the mechanism observed within the continuous matrix.

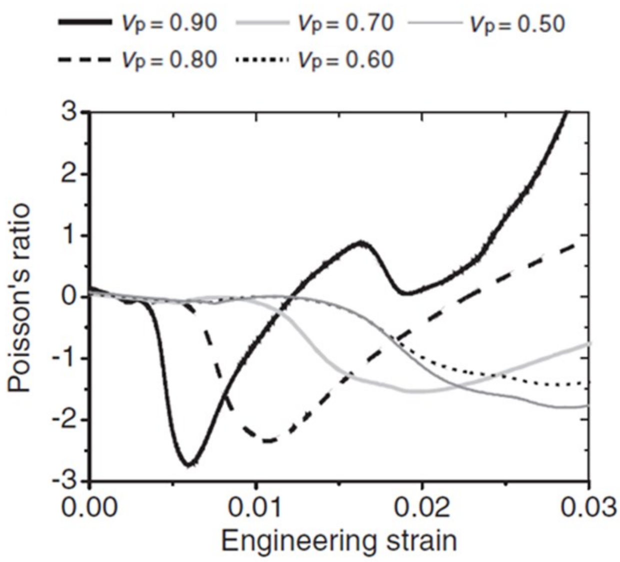

Figure 52: Comparison of Poisson's ratio versus tensile strain for different Vp ratios (Wang & Boyce, 2010).

Figure 53 (a) shows a single cell and (b) its stress-shear relation to deformation (Wang & Boyce, 2010). Strut A experiences tension, and Strut B experiences compression. At lower shear strains, lateral expansion is near zero due to the insignificant changes to normal strain. At approximately 50% shear strain, the first yielding occurs. Then, around approximately 12% of shear strain, Figure 54, the second yield point occurs when Strut A yields because of stretching. Beyond 120% of shear strain, the structure begins to expand in the normal direction when the struts rotate to allow for the negative net force to be released perpendicular to the direction of the shear. Strut B eventually buckles, which leads to the peak and then a decrease in the normal strain, and the structure's volumetric expansion decreases.

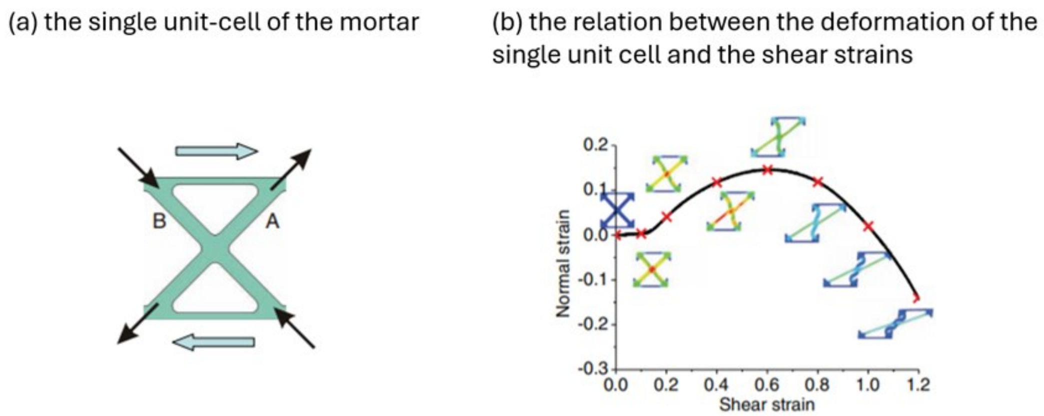

Figure 53: (a) a single unit cell; (b) a structure deformation in relation to the normal strain-shear strain (Wang & Boyce, 2010)

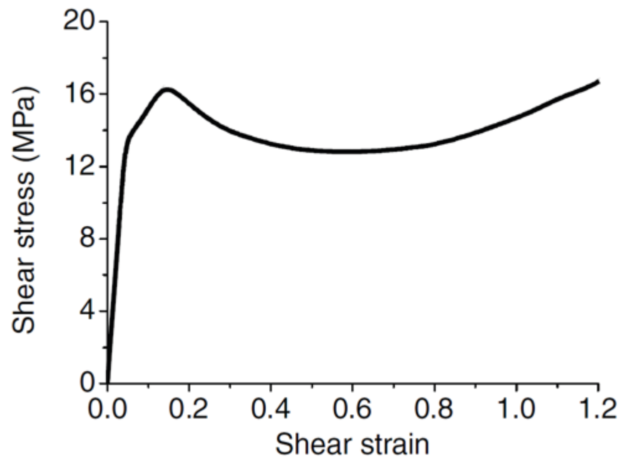

Figure 54: Shear stress (MPa) versus shear strain showing the second yield point (Wang & Boyce, 2010)

Wang and Boyce suggest that the negative Poisson's ratio observed is due to the shear behaviour of the 'mortar'. This suggests that many non-auxetic materials can be used within composites where the mechanical properties, including enhanced volume energy dissipation and higher yield strength, can be enhanced by considering the loading conditions. However, the paper does not offer any validation of the results and no comparison to the experimental data.

The X-shaped mortar not only provides some representation of stretching ligaments found in natural organic matter within nacre, but additionally, the possibility of manufacture was considered, with similar geometries already known to be manufactured by McHale et al., as described in the Supporting Information for their publication (McHale, et al., 2024).

Mechanism 2

The second model to be considered is a model presented by Espinosa et al., published in 2011 (Espinosa, et al., 2011).

The Espinosa et al. model has a similar brick-and-mortar microstructure to that previously discussed. Contrary to the model presented as 'Mechanism 1', Espinosa et al.'s model focuses on the 'brick' element of the model. Espinosa et al.'s model is based on the brick morphology, or waviness, , which leads to transverse dilation and further interfacial hardening whilst the 'bricks' are sliding under loading, propagating inelastic deformation, causing the interface hardening.

Espinosa et al. acknowledged that there are nanoscale disparities present on the surface of the bricks that interlock and increase friction during the sliding, and mineral bridges are present between adjacent tablets. These nanoscale disparities are thought to have little impact on the macroscale material behaviours; however, they potentially have an effect on minimising the propagation of any damage.

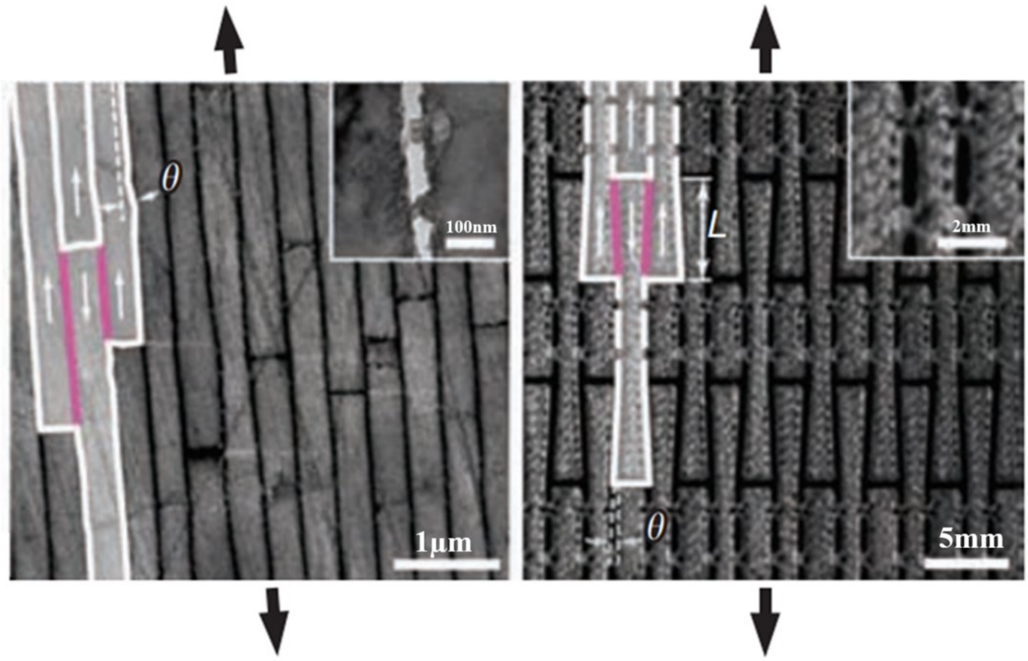

Figure 55: (left) platelet structure of natural nacre, (right) platelets of the composite inspired by nacre (Espinosa, et al., 2011)

The model presented by Espinosa et al. was reaffirmed by the experimental observation of the nacre from Red Abalone, where they studied the sliding of the 'bricks' using three-point bending and atomic force microscopy (AFM) and undertook fracture experiments with kinematic displacement field analysis using digital image correlation (DIC).

Results shown were obtained through an incremental loading process, showing deformation and crack propagation to the point of failure. They showed the relative sliding between the platelets in the overlap region with the sudden increase in lateral displacement, and otherwise, platelets deform elastically with negligible relative motion. This corresponded to the expected behaviour of the sliding of the stacks or columns.

To further demonstrate the effect of the brick morphology on the performance of the brick-and-mortar structure, Espinosa et al. developed a synthetic model that was tested to demonstrate higher energy dissipation. The scaled-up design consists of the 'bricks' made of acrylonitrile butadiene styrene (ABS) plastic with a dovetail shape and a soft epoxy 'mortar' interface, as seen in . There are bridges connecting the tablets in the transverse direction and a soft polymer interface.

The synthetic model created by Espinosa et al. has been further optimised using the parametric study considering variations of the geometry, specifically dovetail angles and dovetail overlap lengths.

The parametric study aimed to create a model that can tolerate high stresses and strains and dissipate energy. The angle of the dovetail was varied from 0 degrees to 5 degrees, and the dovetail was either 2.12mm or 5.7mm in length, with a thickness of 1.85mm. The dovetail angle of 1 degree produced the highest energy dissipation of 160kJ m $^{-3}$, which is over 100% higher than the results obtained for a 0-degree dovetail (67kJ m $^{-3}$) and approximately 50% higher than a solid ABS (110kJ m $^{-3}$).

As expected, the shorter dovetail length resulted in the platelets being pulled out at lower stresses and strains, hence resulting in lower energy dissipation.

The critical difference noted between the synthetic model, and nacre is that the platelets were made from a relatively soft polymer, ABS, rather than a ceramic, which resulted in the polymer showing some level of transverse compression strain that was also present in the ‘mortar’, lowering overall effect of the transverse displacement differences between the platelets.

The use of more brittle material for the platelets in comparison to ABS might lead to higher energy dissipation whilst maintaining the strength of the structure.

Mechanism 3

Mechanism 3 is a model by Song et al. (Song, Zhou, Xu, Xu, & Bai, 2008), consisting of a similar brick-and-mortar structure but focusing on the effect of the mineral bridges linking the bricks.

Song et al. conducted a number of experimental analyses of the nacre *Hyriopsis Schlegeli* shells that were submerged in water for three weeks prior to uniaxial tension tests, which were carried out using a scanning electron microscope (SEM) with a loading stage. The strain was applied at the rate of 0.001 s^{-1} up to the point of failure. The results have been discussed further in 'Auxetic behaviour of nacre'.

Song et al. calculated the average sliding distance of the overlap region to be approximately 80 nm and the average length of the platelets to be 8 μm, as seen in Figure 56.

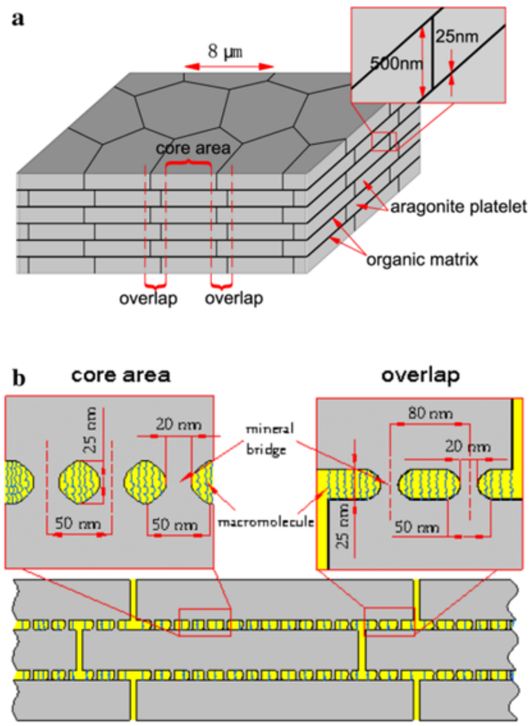

Figure 56: Diagram of the nacre structure by Song et al.; (a) illustration showing the thickness of platelet and matrix as well as the length of the platelets; (b) close-up of the repeated pattern of the structure showing the bridging between the platelets (Song, Zhou, Xu, Xu, & Bai, 2008).

It is suggested that the sliding in the matrix leads to the shear deformation and failure of the mineral bridges in the overlap region, where they eventually push against the neighbouring mineral bridge and climb on each other, as shown in Figure 57.

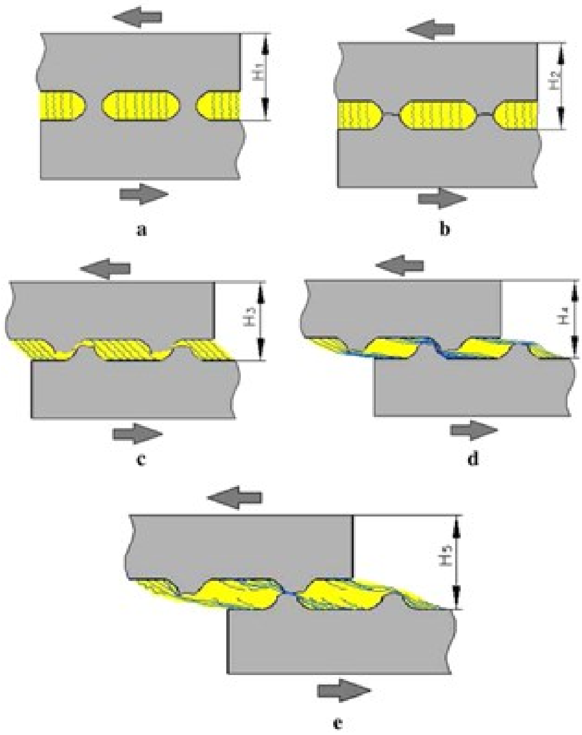

Figure 57: Platelet's transformation and climbing: (a) undeformed overlap region showing the shear stress being applied, (b) the neighbouring bricks fracture, (c) the fractured mineral bridges interpose into the organic matrix (mortar) and start sliding along, (d) the mineral neighbouring mineral bridges meet and start climbing, and (e) the mineral bridges climb one another, reaching the peak and shears to the point of fracture of the organic matrix (Song, Zhou, Xu, Xu, & Bai, 2008).

The work by Song et al. provides good experimental data for nacre, and the suggested mechanism agrees with the results. However, due to the scale at which this bridge shearing is occurring, it has not been observed directly. Hence, the described behaviour is a good proposal, but it is not a definite answer.

Furthermore, there is little proof that introducing these interlocking bridges will, indeed, enhance the mechanical properties within the synthetic materials, even if it is proposed as a guide to doing so. Also, the impact of the changing parameters of the bridges on the composite's performance is unexplored.

Mechanism 4

Mechanism 4 considers the theory by Li et al. (Li, Xu, & Wang, 2006), where the nanograin rotation and deformation in nacre are observed. Li et al. note that the laminar structure of the nacre enables the somewhat brittle material to deform inelastically, allowing stress redistribution. They also suggest that the shear loading and inter-laminar slip are not necessarily responsible for that behaviour and that previously thought aragonite is not a brittle single crystal but rather platelets that consist of millions of ductile nanosized grains with an average grain size of 32 nm. These nanograins were also found to have water content in their interfaces, which is thought to contribute significantly to their viscoelasticity (Verma, Katti, & Katti, 2006) (Mohanty, Katti, Katti, & Verma, 2006).

This has been reinforced by their experimental study of the California Red Abalone (*Haliotis rufescens*) samples using atomic force microscopy (AFM) and nanoindentation techniques, performing three-point bending and tensile tests, and through their literature review, including some of the previous work (Li, Chang, Chao, Wang, & Chang, 2004).

The indentation testing was performed until the fracture occurred and the tensile strains testing was for the range from 1% to 5%. In both cases, deformation was observed.

The tensile testing showed the increased spacing between the nanograins when higher strains were applied, as seen in Figure 58, leading to the expansion of the aragonite platelets in the direction perpendicular to the force applied. Furthermore, during the bending test, the rotation of nanograins was observed, which is believed to accommodate the bending deformation within the platelet and between the platelets, allowing for sliding to occur.

Before deformation, the adhesive biopolymer tightly holds the nanograins of irregular geometries and sizes. Once the external forces are applied, the biopolymer stretches, providing the nanograins with a sufficient amount of space to rotate, and whilst the nanograins rotate, the shear between them leads to grain deformation. Li et al. found that the width of the platelet increases with increased tensile strain up to 7% of the tensile strain. The conclusion can be drawn that aragonite nanograins are ductile rather than brittle, similar to Cu_2O nanocubes, which were previously shown to be ductile whilst brittle in bulk form (Li, Gao, Murphy, & Gou, 2004).

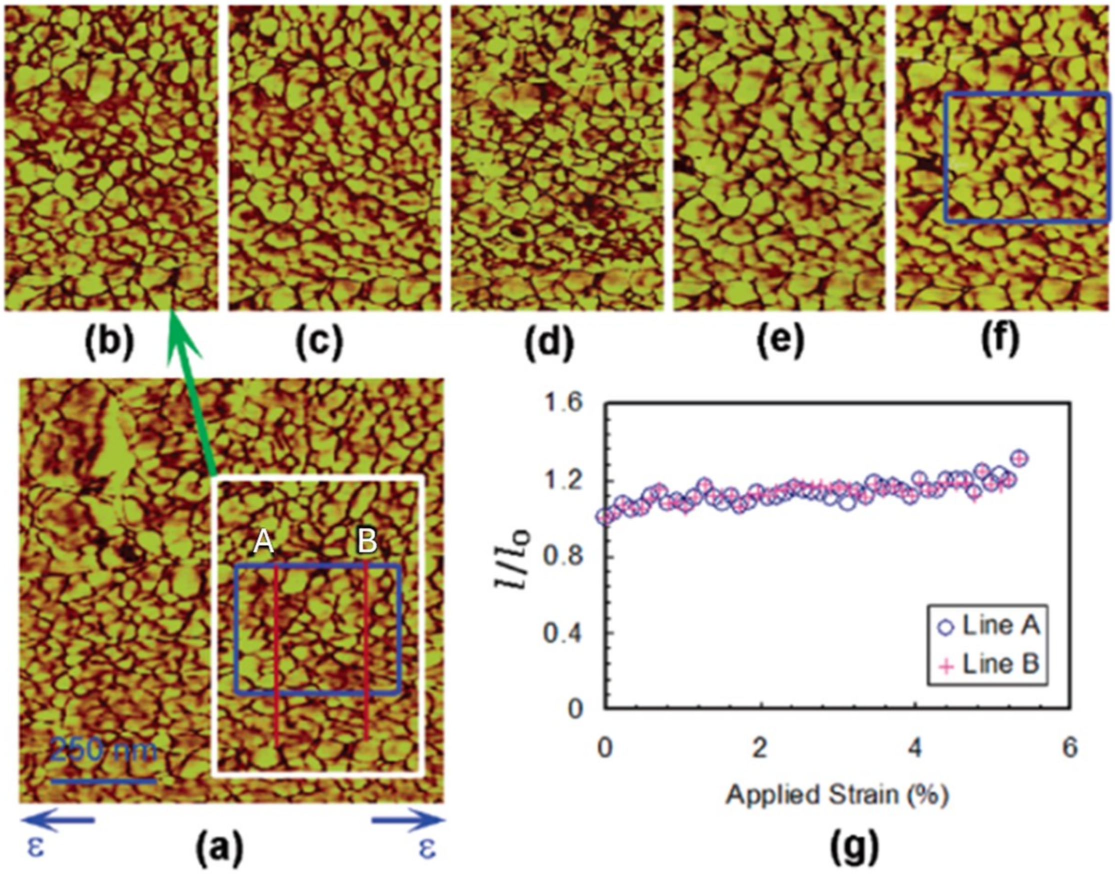

Figure 58: AFM phase images; (a) 0% tensile strain, arrows represent the direction of tensile strain applied, (b) 1% tensile strain, (c) 2% tensile strain, (d) 3% tensile strain, (e) 4% tensile strain, (f) 5% tensile strain, (g) changes in the width of the platelet at positions A and B (Li, Xu, & Wang, 2006) .

In summary, in Mechanism 4, the deformation at the nano-scale level is responsible for the auxetic behaviour, where the rotation of nanograins deforms the platelets, Figure 59 (Li, Xu, & Wang, 2006).

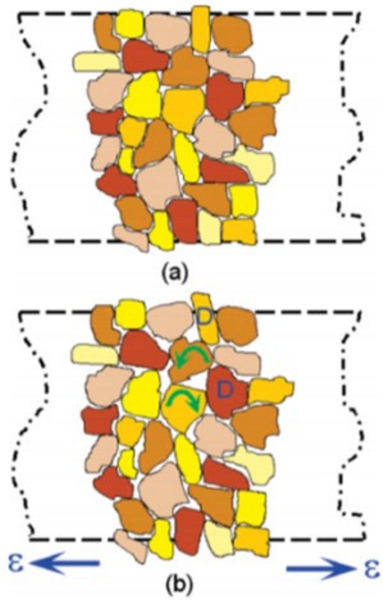

Figure 59: Grain rotation of aragonite: (a) no forces applied, (b) grain rotation and deformation with stress/strain applied (Li, Xu, & Wang, 2006).

Li et al. successfully observed the increase in spacing between the nanograins, nanograin deformation, and rotation, making this explanation very likely. This is not to disregard the influence of the mortar on the system and each element's individual contributions to the auxeticity of the nacre.

From the perspective of developing a synthetic system model, the nanograin model might be the most challenging to replicate in composites.

Auxetic Modelling And Simulation

Current advances in modelling, specifically modelling of auxetic structures, are researched to compare the results obtained and different modelling and simulation approaches. This research should lead to further investigations and develop a suitable methodology for this project.

Honeycomb models

Honeycomb structures are frequently reported in the literature. Even though a conventional hexagonal honeycomb itself is not ordinarily auxetic, a re-entrant honeycomb structure with inverted cell walls has a negative Poisson's ratio when deformation is via flexing or hinging (rotation) of the honeycomb cell walls. In addition to micro- or macro-structures, this can be achieved at a molecular level and can also be extended to disordered 3D lattices (for example, it is how PU foam can be altered to be auxetic), and can also be scaled up to create larger lattices to create structures with higher stiffness (Nkansah, Evans, & Hutchinson, 1994)

A comparison of the honeycomb and re-entrant honeycomb structures was made by Whitty et al., who studied the structures shown in Figure 60. Finite Element simulation was run using ANSYS, and it was further compared to the analytical and experimental results in terms of Poisson's ratio previously shown in Equation (1). The model size was specified by the number of unit cells, which ranged from 15x15 to 21x21 (Whitty, Nazare, & Alderson, 2002). In the latter chapters, this paper will be used to verify the methodological approach to the simulation.

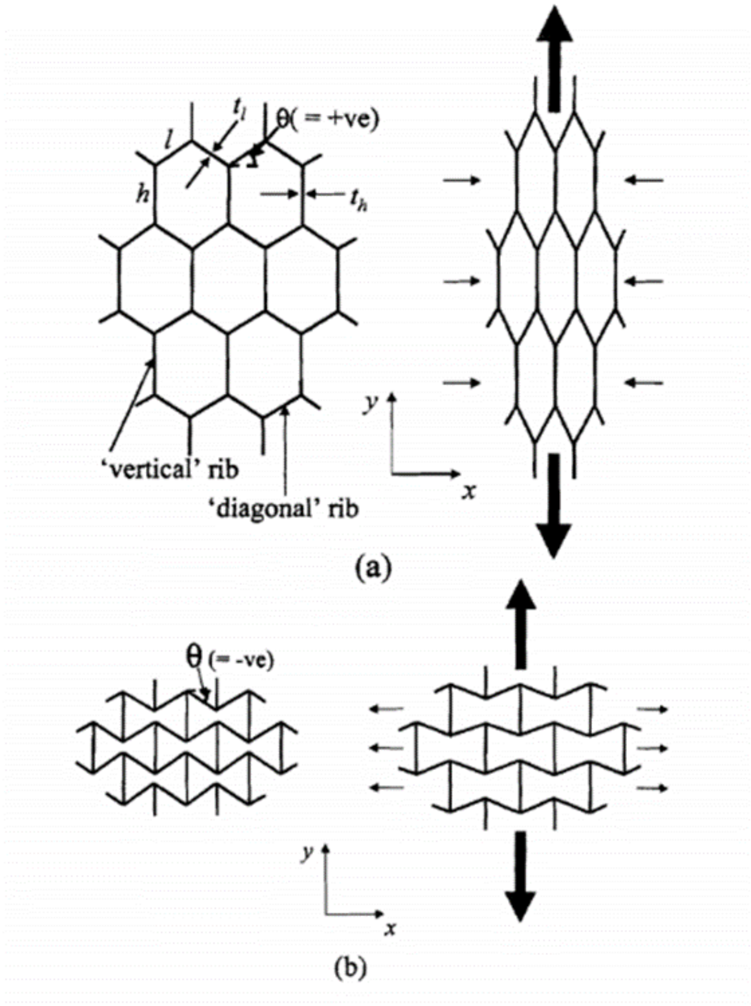

Figure 60: Deformation by the hinging of the cell walls of the (a) conventional honeycomb and (b) re-entrant honeycomb (Whitty, Nazare, & Alderson, 2002)

The structure was studied under the tensile load in the x- and y-direction with frictionless support on one edge and tensile force applied to the opposing edge, as seen in Figure 61.

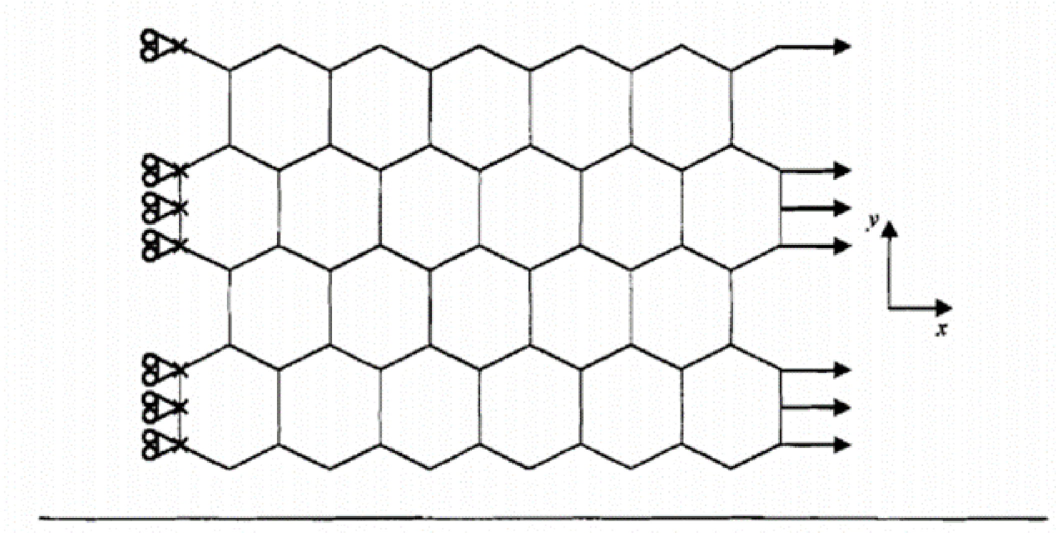

Figure 61: Set up used for the finite element simulation (Whitty, Nazare, & Alderson, 2002).

FEA Of Bio-Inspired Models

A previous study of bio-inspired models using FEA analysis was carried out by Page & Thorsteinsson (2017), where they reviewed the impact resistance of the models inspired by osteoderm (a bony plate in the skin) consisting of ABS (Acrylonitrile Butadiene Styrene) and silicone.

Their model was created using PTC Creo Parametric, and FEA was carried out using its analysis package. Each model was subjected to the force of 174 Newtons. They concluded that Model 1, see Figure 62, experienced the lowest stress of the three models considered. However, they noted that there could be errors within the process, as Model 3 showed a significantly higher maximum stress than Model 1 and Model 2 (Page & Thorsteinsson, 2017).

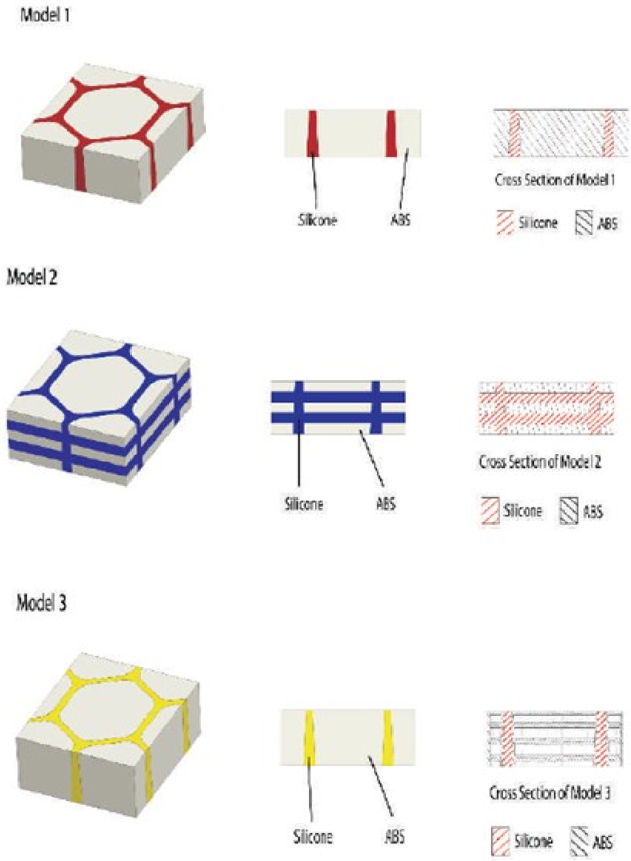

Figure 62: The figure shows three models that were created and tested as part of Page & Thorsteinsson's study (Page & Thorsteinsson, 2017)

Flores-Johnson et al. have investigated the impact behaviour of nacre-inspired aluminium composite (Flores-Johnson, Shen, Guiamatsia, & Nguyen, 2014). Their investigation consisted of creating a nacre-inspired model using aluminium-7075 in a hierarchical structure, incorporating waviness to the platelets.

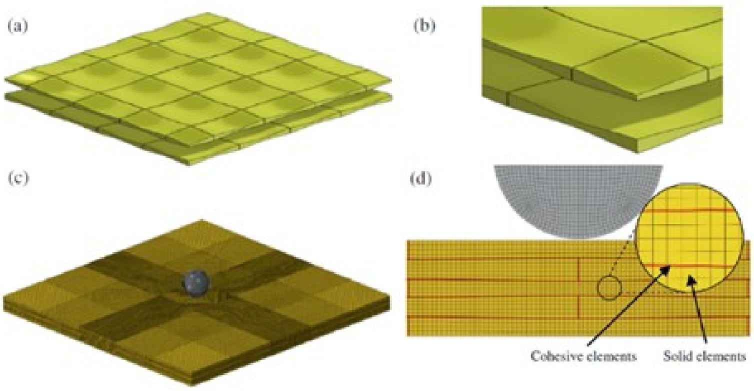

Figure 63: Model used by Flores-Johnson, (a) Solid geometry of individual layers, (b) close-up of the structure in 'a', (c) FE model of 5 layers, (d) mesh cross-section (Flores-Johnson, Shen, Guiamatsia, & Nguyen, 2014)

This model's ballistic performance was studied using Abaqus /Explicit. Impacts were by a rigid hemispherical projectile at a varied velocity of 400m/s to 900m/s.

The conclusion drawn was that the performance was improved when compared to the same thickness bulk plate, stipulating that it was due to the hierarchical structure allowing for localised energy absorption.

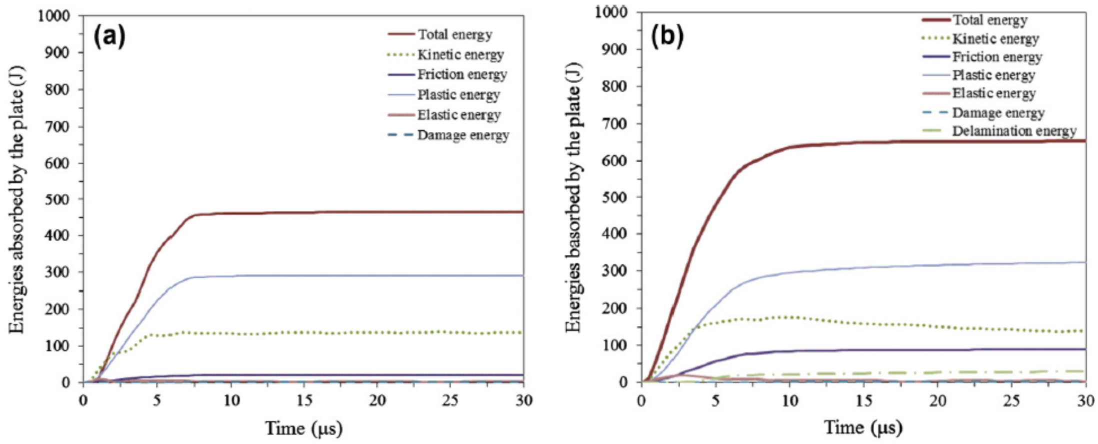

Figure 64: Energy absorption of the 5.4 mm plates, a: bulk plate b: nacre-inspired plate, at an impact of 900 m/s (Flores-Johnson, Shen, Guiamatsia, & Nguyen, 2014)

Raphel et al. created a biomimetic structure inspired by nacre and Bouligand (a layered and rotated structure resembling plywood) structures (Raphel, Jacob, & Viswanathan, 2019). FEA was carried out using SIMULIA ABAQUS Explicit (version 6.13), with a mesh of size 0.25 mm consisting of C3D8R elements and an aluminium set as a material. As a validation exercise, multiple geometries were tested using the Charpy impact test and the FEA was compared to the experimental data.

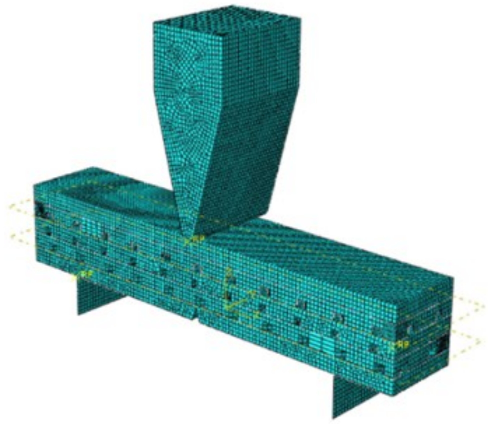

Figure 65: Assembled components in the Raphel et al. study, consisting of the specimen, the hammer tip, and the supports (Raphel, Jacob, & Viswanathan, 2019)

As a result, a number of the bio-inspired models have presented improved toughness in comparison to the bulk material, with as much as 46.15% improvement in energy absorption.

The aforementioned analyses of the nacre-inspired models omit the consideration of the effects, or even presence, of negative Poisson's ratio on the model's performance. Flores-Johnson et al. focus on the effects of the geometrical structure changes on the maximum stress of the model, which might be an indirect correlation to the effects of NPR on the behaviour of the structure.

Novak et al. performed a quasi-static crushing simulation using LS-DYNA on auxetic structures made from inverted tetrapods, Figure 66, which were then concocted from the Ti_6Al_4V powder by Selective Electron Beam Melting (SEBM) method to allow for physical loading testing.

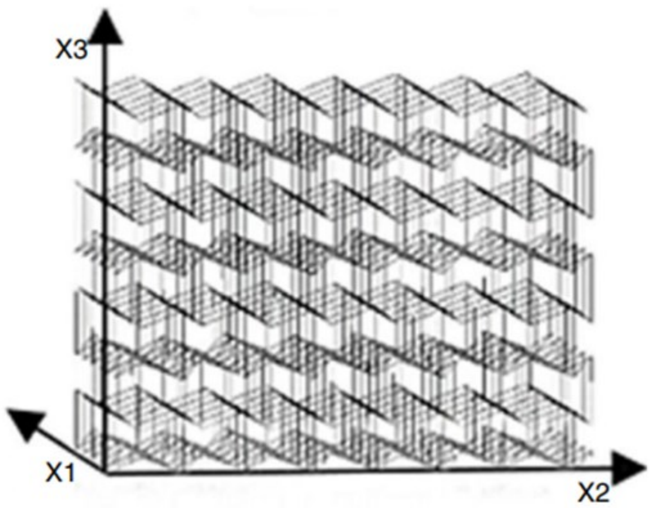

Figure 66: Geometry of the structure consisting of inverted tetrapods (Novak, Vesenjak, & Ren, 2018)

The material model used by Novak et al. was MAT_63 (ANSYS, 2002), which is designed for homogeneous crushable foams. Different loading directions were tested, Figure 67, and the energy absorption results obtained through FEA were compared to experimental data, which showed a 0.5% deviation, demonstrating the reliability of the method (Novak, Vesenjak, & Ren, 2018).

Using a similar method to the above, Novak et al. tested the monolithic steel plate. They compared it to the composite sandwich panel with an auxetic core, Figure 68, under blast loading, comparing the maximum displacement between the computational and experimental models. The steel plate was discretised using 3,125 fully integrated solid finite elements.

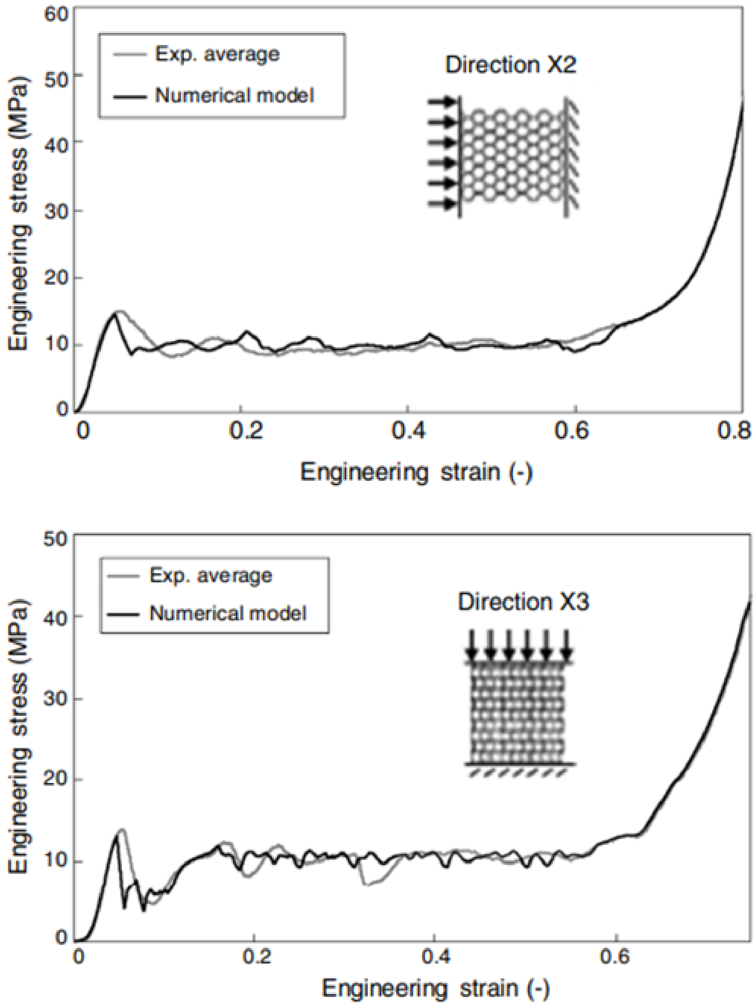

Figure 67: The results show the comparison of experimental and computational analysis in two separate directions of the structure (Novak, Vesenjak, & Ren, 2018).

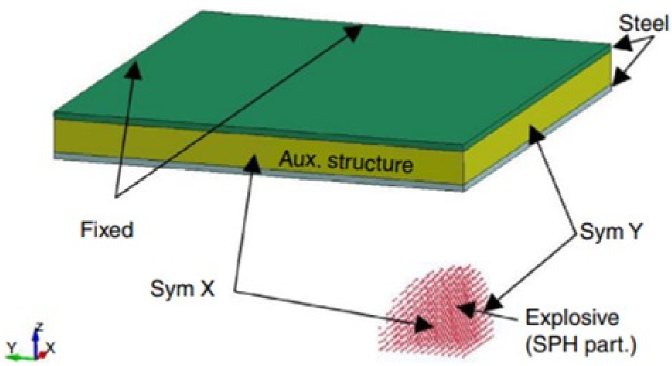

Figure 68: The set-up used for blast loading computational analysis, showing the boundary conditions used (Novak, Vesenjak, & Ren, 2018).

The results for blast loading showed that the auxetic core sandwich structure had a 33% lesser maximum displacement in comparison to the monolithic steel structure, Figure 69, and a 6% reduction in mass.

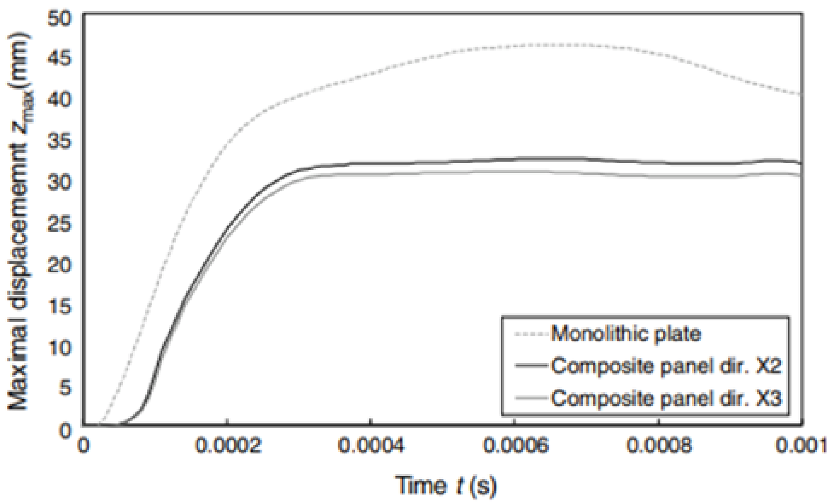

Figure 69: The results of blast loading for monolithic and auxetic core sandwich structures (Novak, Vesenjak, & Ren, 2018)

The lower maximum displacement is due to the energy absorption property of the core structure as the auxetic foam can dissipate the deformation energy, as discussed in the earlier section, 'Energy and Shock Absorption'. Novak et al. also suggested that there is a potential for further improvements in the composite's performance by introducing gradients to the foam auxetic structure. The computational challenge was also mentioned, with a suggestion that the use of the discrete modelling method rather than the homogenised computational model would produce more accurate data when studying auxetic cores with graded porosity.

Another example of impact analysis using computational modelling is the analysis carried out by Jiang et al., who looked at 3D models of multilayer orthogonal auxetic composites to see their energy absorption and impact protection capabilities using ANSYS LS-DYNA (Jiang & Hu, 2017).

The structure, as seen in Figure 70, was made out of ABS tubes, polyester filaments, and flexible PU foams as the matrix. Each model consists of 12 layers of ABS tubes to reduce the wall effect for the physical testing. For FE, the model consisted of two repeated units, resulting in the FE model being much smaller than the sample size. The diameter of the tubes is 3mm, and the wall thickness is 0.4mm.

The testing looked at low-velocity impact compression using a drop-weight. The striker weighed 6.5 kg, and its surface was a circular plate. After dropping, it hit the upper surface of the sample. The striker was modelled as a hexahedron in the FE model. The ABS tubes, polyester filaments, and PU foam were all discretised using SOLID 164 elements. SOLID 164 is commonly used for solid modelling, and it consists of eight nodes and allows for the translation, velocity, and acceleration at each node. The open-cell PU foam was modelled using the MAT_057 material model (ANSYS, 2002), which is a model designated for low-density foams.

As part of the study, Jiang and Hu looked at the mesh sizes and density, comparing the results between element sizes of 0.2 and 0.4mm. The two mesh sizes showed minor differences in Poisson's ratio, and a maximum difference of 0.28% was found; hence, 0.4mm was considered more efficient and selected as an appropriate mesh size for further investigation for the investigated model; meanwhile, the bottom plate and striker had a mesh of 1mm.

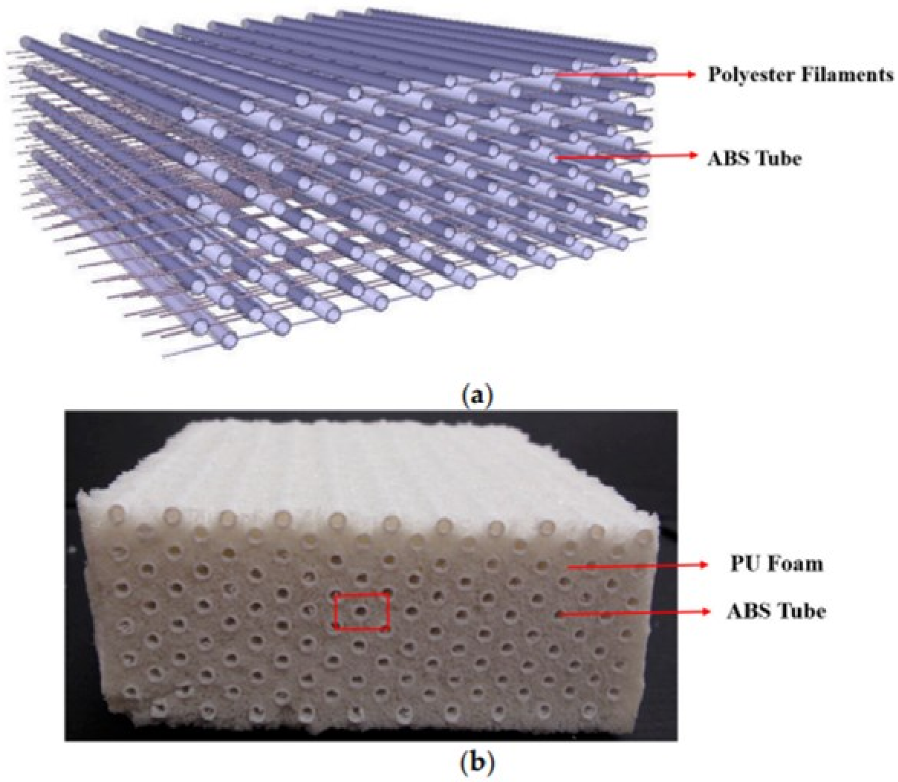

Figure 70: (a) auxetic reinforced structure; (b) red rectangle marks the repeated unit of the composite (Jiang & Hu, 2017)

The velocities investigated were 1.50 m/s, 2.05 m/s, and 2.67 m/s. The comparison between Poisson's ratio and the compressive strain was drawn, Figure 71, showing a close correlation between FE models but some deviation in comparison to the experimental data for the quasi-static compression test, which is likely due to the differences in testing scenarios. The FEA was based on the low-velocity impact scenario, and the experimental data was based on a quasi-static scenario.

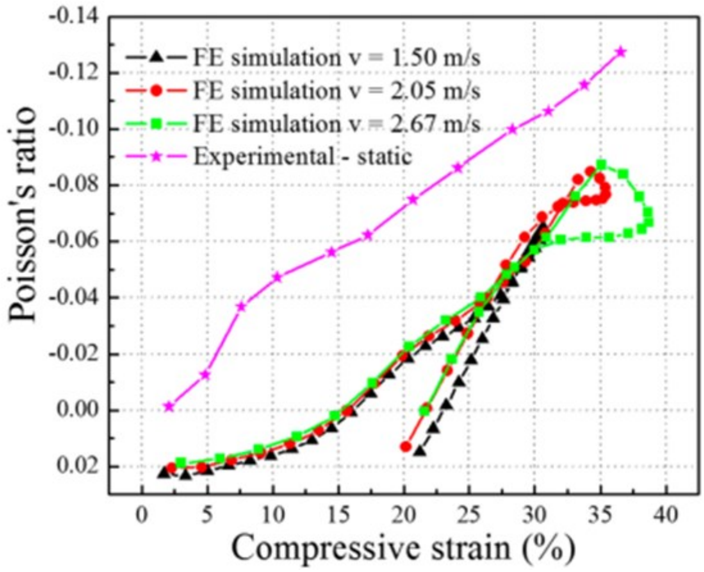

Figure 71: The Poisson's ratio versus compressive strain curves, a comparison between FE results and quasi-static experimental compression test (Jiang & Hu, 2017)

Jing and Hu found that the NPR value increased with higher velocity, with the maximum NPR found to be -0.087 at 2.67 m/s loading. The NPR value was obtained from contact stress vs compressive strain curves. The NPR values of the auxetic composite under FE impact simulation are comparatively lower than the ones obtained from static experimental testing. They also found that the results were more accurate for the first loading and later loadings affected by hysteresis and may need to be calibrated using experimental data to obtain more accurate results.

They concluded that LS-DYNA was capable of simulating complex nonlinear dynamic problems by using explicit time integration.

Summary

Auxetics are materials characterised by negative Poisson's ratio. The negative Poisson's ratio is often linked with a number of enhanced mechanical properties, such as indentation resistance, energy and shock absorption, fracture toughness, and synclastic bending behaviour, which is also why their applications are extensive. Explored separately, nacre is known for a number of desirable properties for a wide range of applications, and it has been previously used as an inspiration for composites and structures. However, the auxeticity of the nacre is still widely unexplored, and it might be the actual reason for its enhanced properties. The studies discussed show that there is no one conclusion as to what mechanism drives the auxetic behaviour in nacre. The research gap and aim of this thesis is exploring the ways in which synthetic composites can replicate the auxetic behaviour of nacre which will open the door to further research and development of synthetic composites with similar properties.

The focus of this project is to develop a synthetic system, a functional bio-inspired metamaterial, which can replicate the behaviour of nacre to find a missing link between the theory of the nacre's auxetic behaviour and practice and enhance auxetic properties within the synthetic system with the main goal of achieving NPR. Throughout the development of the model, manufacturability of the synthetic is considered with the hope that the models can be synthesised in future work.

Over the following few chapters, the knowledge gained from this literature review will be applied to the analytical and numerical models to find the governing mechanisms and key influences of geometric parameters on Poisson's ratio while applying it to the synthetic metamaterial.

The original contribution to knowledge are the development of the first complete analytical models (found in ‘Chapter 4 Analytical Models of Auxetic Systems’), and exploring their predicted mechanical properties by investigating the deformation of the nacre-inspired brick-and-mortar microstructure caused by shearing of the mortar (mechanism 1), sliding of the concave bricks (mechanism 2), and brick translation due to bridge climbing (mechanism 3). Further contributions include the associated development and application of numerical models found in section ‘Chapter 5 FE Models and Analysis 2D Models’, where novel 2D structure was presented and studied with aim to enhance NPR.

One of the biggest challenges expected in creating a novel model of nacre-inspired metamaterial is a lack of possibility to validate it against any existing data, including experimental results. This is expected to be overcome by benchmarking the method against the existing honeycomb models to verify the approach which then is applied to novel metamaterial models.

Chapter 3 Methodology, Method, and Method Verification

This section provides an analysis of the different methods used in this project and the decision-making process to obtain a suitable method. Furthermore, it builds on the content of the Literature Review to provide a more in-depth justification for the methods used. As mentioned in the previous chapter, one of the biggest challenges expected will be the inability to validate the results of the novel models due to lack of comparable resources. This is expected to be overcome by benchmarking the method against the existing honeycomb models to verify the approach which then is applied to novel metamaterial models, as shown in sub-section 'Method Verification'. Prior to this, different theorems are discussed to fully understand the underlying mathematics of any analysis carried out.

Elasticity Theory

Elasticity theory can be used to predict some of the characteristics of the material by applying Hooke's law (Meille & Garboczi, 2001). The Hooke's law describes the relationship between stress and strain in materials. When anisotropic, the material properties vary depending on the direction considered. This can be shown using the compliance coefficients matrix:

$$\begin{bmatrix} \varepsilon_{11} \\ \varepsilon_{22} \\ \varepsilon_{33} \\ \varepsilon_{23} \\ \varepsilon_{31} \\ \varepsilon_{12} \end{bmatrix} = \begin{bmatrix} S_{11,11} & S_{11,22} & S_{11,33} & S_{11,23} & S_{11,31} & S_{11,12} \\ S_{11,22} & S_{22,22} & S_{22,33} & S_{22,23} & S_{22,31} & S_{22,12} \\ S_{11,33} & S_{22,33} & S_{33,33} & S_{33,23} & S_{33,31} & S_{33,12} \\ S_{11,23} & S_{22,23} & S_{33,23} & S_{23,23} & S_{23,31} & S_{23,12} \\ S_{11,31} & S_{22,31} & S_{33,31} & S_{23,31} & S_{31,31} & S_{31,12} \\ S_{11,12} & S_{22,12} & S_{33,12} & S_{23,12} & S_{31,12} & S_{12,12} \end{bmatrix} \begin{bmatrix} \sigma_{11} \\ \sigma_{22} \\ \sigma_{33} \\ \sigma_{23} \\ \sigma_{31} \\ \sigma_{12} \end{bmatrix} \tag{25}$$

The subscripts correspond to the directions defined in Figure 72.

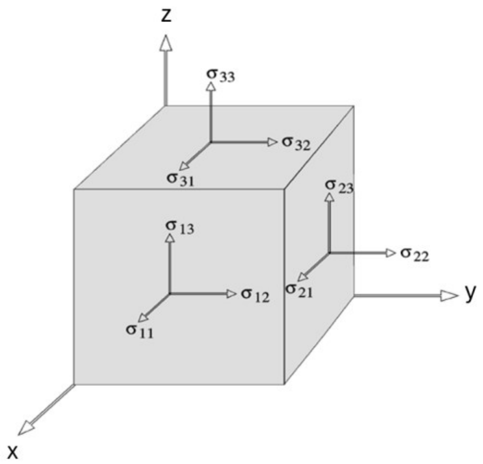

Figure 72: The diagram representing the corresponding axis, where x=1, y=2, and z=3. Adapted from Grosser & Bormann (2003).

By invoking symmetry and considering specific testing conditions, (Hearn E. J., 1997), the Hooke's law for isotropic materials can be expressed in terms of elastic constants (Young's modulus, E, shear modulus, G, and Poisson's ratio, ν), as shown in equation (26).

$$\begin{bmatrix} \varepsilon_{11} \\ \varepsilon_{22} \\ \varepsilon_{33} \\ \varepsilon_{23} \\ \varepsilon_{31} \\ \varepsilon_{12} \end{bmatrix} = \frac{1}{E} \begin{bmatrix} 1 & -\nu & -\nu & 0 & 0 & 0 \\ -\nu & 1 & -\nu & 0 & 0 & 0 \\ -\nu & -\nu & 1 & 0 & 0 & 0 \\ 0 & 0 & 0 & 2(1+\nu) & 0 & 0 \\ 0 & 0 & 0 & 0 & 2(1+\nu) & 0 \\ 0 & 0 & 0 & 0 & 0 & 2(1+\nu) \end{bmatrix} \begin{bmatrix} \sigma_{11} \\ \sigma_{22} \\ \sigma_{33} \\ \sigma_{23} \\ \sigma_{31} \\ \sigma_{12} \end{bmatrix}$$

(26)

It is from equation (26) that equation (27) and equation (25) are derived.

The generalised Hooke's law provides an equation for the total linear strain, given by:

$$\varepsilon_{11} = \frac{1}{E}[\sigma_{11} - \upsilon(\sigma_{22} + \sigma_{33})]$$

(27)

For the 3D models, isotropic strain is given by:

$$\varepsilon_{12} = \left[\frac{1+2\upsilon}{E}\right]\sigma_{12}$$

(28)

Now, considering the shear modulus, G, is equivalent to:

$$G = \frac{\sigma_{12}}{\varepsilon_{12}}$$

Substituting it into equation , equation (28) becomes:

$$\frac{\sigma_{12}}{\varepsilon_{12}} = \frac{E}{1+2\nu}$$

We obtain the previously defined equation (4): $G = \frac{E}{2(1+\upsilon)}$

Similarly, bulk modulus and Poisson's can be derived, resulting in $K = \frac{E}{3(1-\upsilon)}$ and $\upsilon = \frac{3K-2G}{2(3K+G)}$, respectively. Hence the relationship sare $\frac{9}{E} = \frac{1}{K} + \frac{3}{G}$;

To give a stable elastic system, bulk modulus (K) and shear modulus (G) must be greater than zero. For this to be the case, Poisson's ratio must be within the limits:

$$-1 < \upsilon < \frac{1}{2}$$

(29)

The same method can be applied to 2D models, where only two axis are considered.

The Hooke's law for an isotropic 2D model gives the strain:

$$\varepsilon_{12} = \left[\frac{1+2\upsilon}{E}\right]\sigma_{12}$$

(30)

As one dimension is now equivalent to 0, the compliance matrix becomes:

$$\begin{bmatrix}\varepsilon_{11}\\ \varepsilon_{22}\\ \varepsilon_{12}\end{bmatrix} = \frac{1}{E}\begin{bmatrix}1 & -\nu & 0\\ -\nu & 1 & 0\\ 0 & 0 & 2(1+\nu)\end{bmatrix}\begin{bmatrix}\sigma_{11}\\ \sigma_{22}\\ \sigma_{12}\end{bmatrix}$$

(31)

The equations can be derived in the same manner as in the previous section:

$$G = \frac{E}{2(1+\upsilon)}; \quad K = \frac{E}{2(1-\upsilon)}; \quad \text{and} \quad \upsilon = \frac{K-G}{K+G};$$

And the relationships between those equations can be shown as: $\frac{4}{E} = \frac{1}{K} + \frac{1}{G}$;

As before, to give a stable elastic system, bulk modulus (K) and shear modulus (G) must be larger than zero. For this to be the case, Poisson's ratio (ν) must be within the limits, which for the 2D model are:

$$-1 < \upsilon < 1$$

(32)

For plane strain, Young's modulus, $E_{2D} = \frac{E_{3D}}{(1-\upsilon_{3D}{}^2)}$ and Poisson's ratio, $\upsilon_{2D} = \frac{\upsilon_{3D}}{(1-\upsilon_{3D})}$

For plane stress, Young's modulus, $E_{2D} = E_{3D}$ and Poisson's ratio, $\upsilon_{2D} = \upsilon_{3D}$

Where subscript 2D refers to the 2-dimensional value, and 3D refers to 3-dimensional one.

This means that 3D elastic moduli are numerically equal to those for the 2D model, however, they do have different units. For example, the shear modulus has units of $N/_{m^2}$ for 3D model and $N/_{m}$ for 2D model (Meille & Garboczi, 2001).

Numerical Models of Auxetics

One of the ways to predict the mechanical properties of the material or metamaterial is through analytical or numerical methods, where either geometrical or mechanical properties are utilised in finding the corresponding changes in deformation. This section will look at ways in which auxetics were previously analysed, but a more in-depth evaluation of this topic can be found in Chapter 4 Analytical Models of Auxetic Systems on page 173.

Grima-Cornish, Grima, and Attard published a comprehensive article in 2021 (Grima-Cornish, Grima, & Attard, 2021) on numerical modelling of auxetic materials. The focus of the paper is on the field of thermomechanical metamaterials. They intended to represent metamaterials as mathematical models by breaking down individual mechanisms to establish mathematical relationships. Quoting a multitude of sources, Grima-Cornish et al. stated that thermo-mechanical properties can be found within auxetic structures. Although the focus of the work reported in this thesis is not on thermo-mechanical properties, the methodology used to generate mathematical models of auxetic systems is. The inspiration can be drawn from this work and applied to the analysis of four mechanisms specific to nacre, which can be found in Chapter 4.
The key equation and starting point is the equation for the Poisson's ratio,

$$\nu_{21} = -\frac{Resultant\ strain\ in\ lateral\ O_{x1} direction}{Applied\ axial\ strain\ in\ O_{x2}\ direction} = -\frac{\varepsilon_1}{\varepsilon_2} \tag{33}$$

In this scenario, O_{x1} and O_{x2} define a plane where ε_2 is a uniaxial strain applied in the O_{x2} direction, as found in Figure 73 for the case of a re-entrant honeycomb metamaterial.

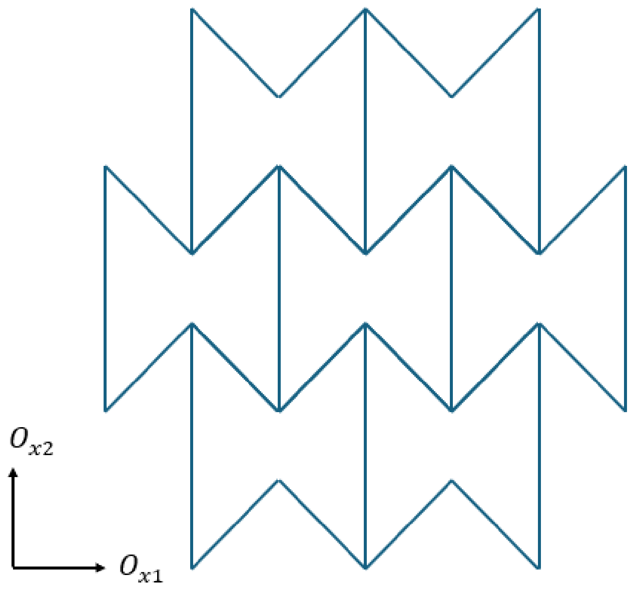

Figure 73: The system modelled by Grima et al (Grima-Cornish, Grima, & Attard, 2021).

The equation for Poisson’s ratio remains unchanged, but there are a few methods of finding the strain, for example, the engineering strain, also known as the Cauchy or the nominal strain, or the instantaneous strain, also known as incremental strain, and the true strain also often referred to as Hencky strain or logarithmic strain.

The engineering strain is defined as the extension, ΔL, over the original length, L_0, at a point k:

$$\varepsilon_{eng}[k] = \frac{\Delta L[k]}{L_0} \tag{34}$$

Whereas the instantaneous strain at a point k is found for any two successive length measurements using:

$$\delta\varepsilon[k] = \frac{L[k] - L[k-1]}{L[k-1]} = \frac{\delta L[k]}{L[k-1]} \tag{35}$$

Equation (35) can be used to express the infinitesimally small strain when the δL is infinitesimal:

$$d\varepsilon = \frac{dL}{L} = \lim_{\delta L[k] \to 0} \left(\frac{\delta L[k]}{L[k-1]} \right)$$

(36)

Lastly, the true strain at point k is defined as:

$$\varepsilon_{true}[k] = \int_{L[0]}^{L[k]} d\varepsilon = \int_{L[0]}^{L[k]} \frac{dL}{L} = [\ln(L)]_{L[0]}^{L[k]} = \ln(L[k]) - \ln(L[0]) = \ln\left(\frac{L[k]}{L[0]}\right)$$

$$= \ln\left(\frac{L[0] + \Delta L[k]}{L[0]}\right) = \ln\left(1 + \frac{\Delta L[k]}{L[0]}\right) = \ln\left(1 + \varepsilon_{eng}\right)$$

(37)

The differences in types of strains need to be considered when calculating Poisson's ratio in further sections, as well as when drawing a comparison between any of the results in this work and the existing literature.

Finite Element Analysis

Obtaining *an exact solution* is mathematically challenging and can be exceptionally computationally demanding. Hence, Finite Element Analysis (FEA) is commonly used as it provides *an approximate solution* using one of the solving methods. These methods allow the problem to be broken down into linear algebraic equations that allow for a numerical solution (Stolarski, Nakasone, & Yoshimoto, 2018).

Using FEA brings numerous benefits. It is a good approximation of the solution and can allow for a low-cost evaluation of the model without the need to create physical samples while still allowing the user to obtain representative data. It can also be more time-efficient than experimental testing. However, it also has its limitations, and these are mostly the computing/processing power and running time per model. A compromise has to be made between the highest quality mesh and reducing the processing time, as will be discussed later.

Each engineering problem is determined by a set of physical laws, which in turn can be represented through a set of Partial Differential Equations (PDEs) (Moaveni, 2015). PDEs can be used to describe various phenomena and laws of physics relevant to the model and are used to replicate real-life conditions and restraints. They can be used to obtain a solution with appropriate input information (Stolarski, Nakasone, & Yoshimoto, 2018). The input information required can be put into two categories: characteristics of the model (i.e., material properties, geometry) and external disruptions of the model, which are often referred to as boundary conditions (i.e., forces applied) (Moaveni, 2015).

Generally, the solution consists of the individual solutions for the input parameters: a homogenous solution dictated by the characteristics of the model and its natural behaviour and a particular solution for the boundary conditions. These solutions are then combined with initial conditions to obtain a global solution.

Boundary conditions often consist of conditions and restraints and might include fixation points and constraints on the degrees of freedom. The types of boundary conditions differ between different computational analyses, but considering the case of FEA of solid structures, the boundary conditions that can be applied are forces, pressure, displacements, and temperature. The boundary conditions can be applied to individual points, surfaces, edges, nodes and elements.

Additionally, there are other ways of applying the above-mentioned boundary conditions, such as applying symmetry constraints. These are particularly useful in stabilising models and reducing their size. They can be applied to cartesian and cylindrical coordinate systems by mirroring, translating and rotating around the axis.

The challenge in applying the boundary conditions is to avoid either under or over-constraining the models, which will lead to the final results being inaccurate or even being unable to converge or result in rigid body motion where the model has free translation or rotation of a body without experiencing any internal deformations.

FEA Software

This section looks at commercially available software that can be used for FEA. It compares the features and capabilities of each but also takes into consideration the user's experience and abilities, as well as licencing required. Software packages considered are ANSYS, ABAQUS, COMSOL Multiphysics, LS-DYNA, SolidWorks Simulation, and Autodesk Simulation.

Firstly, the frequency of each within the published literature was looked at to establish whether some of the software packages seem to be more popular for auxetic simulations. This was carried out by searching relevant keywords in Google Scholar, i.e. For ANSYS, the keywords chosen were ANSYS, FEA, and auxetic. "FEA" and "auxetic" were used for each software package. The number of results returned by the search engine were:

Number of search results per software package used					
ANSYS	ABAQUS	SolidWorks	COMSOL Multiphysics	LS-DYNA	Autodesk Simulation
946	1500	515	213	272	144

Table 4: Number of search results per software package used for search terms 'FEA' and 'auxetic'.

Although this is not the most reliable method to determine the most suitable software for this project, it is a good indication of what is being used by others within the area of interest.

From the above results, it can be observed that ANSYS and ABAQUS are the most popular choices for the FEA of auxetics. This activity has been repeated with the inclusion of the keyword "dynamic", and results for the top two software packages were the same, Table 5.

Number of search results per software package used for dynamic simulations					
ANSYS	ABAQUS	SolidWorks	COMSOL Multiphysics	LS-DYNA	Autodesk Simulation
666	1140	371	172	252	100

Table 5: Number of search results per software package used for search terms 'FEA', 'auxetic', and 'dynamic'

It poses a challenge to determine the most suitable commercially available software as the literature offers very little comparison between ANSYS and ABAQUS that reflects the direct needs of this project. Both software packages have varied uses and applications, and direct comparisons were drawn for other applications: thermo-structural problems, ultrasound wave propagation in laminates, and load-displacement relations for flexible beams.

Thermo-structural problems (Yamileva, Yuldashev, & Nasibullayev, 2012) where ABAQUS was found more efficient whilst using multicores and multiprocessor computers. However, in many instances, the difference could be considered negligible, especially for a higher number of nodes where computational time was 21.57 and 21.35 hours for ABAQUS and ANSYS, respectively.

Ultrasound wave propagation in laminates comparison showed that ANSYS had a closer result to the dispersion curve with a difference of 1.4%, and ABAQUS showed a deviation of around 17% (Leckey, Wheeler, Hafiychuk, Hafiychuk, & Timuçin, 2018).

Load-displacement relations for flexible beams studied by (Bai, Awtar, & Chen, 2019) showed in multiple deflections that ANSYS had a lower error percentage than ABAQUS, such as when predicting the axial elongation of the beam ANSYS was in agreement with the model, and ABAQUS yielded relatively large errors with the maximum error of 9%.

Furthermore, Magomedov and Sebaeva highlighted the capability differences between the FEA software packages in Table 6 (Magomedov & Sebaeva, 2020). These indicate that ANSYS is self-contained and unit-aware. Otherwise, its capabilities are identical to those of Abaqus.

	Abaqus (CAE)	Ansys (Mechanical)	SOLIDWORKS	Inventor (+Inventor Nastran)
Self-contained	no	yes	yes	no
Graphical geometry modeler	Includes	Includes	Includes	Includes
Graphical manual meshing	Includes	Includes	No data	Includes
CAD import	Capable	Capable	Capable	Capable
Units aware	no	yes	No data	No data
Linear static	Performs	Performs	Performs	Performs
Nonlinear - large displacements	Performs	Performs	Performs	Performs
Nonlinear - contact	Performs	Performs	Performs	Performs
Transient linear	Capable	Capable	Capable	Capable
Transient onlinear	Capable	Capable	Capable	Capable
Natural frequency	Capable	Capable	Capable	Capable
Linear buckling	Capable	Capable	Capable	Capable
Acoustic	Capable	Capable	Not Capable	Not Capable
Heat transfer	Capable	Capable	Capable	Capable
Electric/magnetic	Capable	Capable	Not Capable	Capable
Fluid flow	Capable	Capable	Not Capable	Capable
Fluid structure interaction	Capable	Capable	Not specified	No data
Solid elements	Capable	Capable	Capable	Capable
Shell elements	Capable	Capable	Capable	Capable
Price	Limited free	Limited free	Not free	both

Table 6: Comparison of FEA capability differences between commercially available software packages

ANSYS' first program was developed in 1970 as a keypunch and a time-shared mainframe (Lee, 2017). Over the years, the software's capabilities have been improved by new features being added, and ANSYS has evolved from a fixed format input to a command line-driven one. The introduction of the first Graphical User Interface (GUI) and the first pre-processor, PREP7, allowed for a model consisting of nodes and elements to be created (Lee, 2017). Nowadays, ANSYS capabilities are extensive, allowing for static, dynamic, fluid, and many more analyses. The GUI can be used to simplify the use of ANSYS, as it allows users with little to no experience with ANSYS commands to run an analysis (Moaveni, 2015).

In the literature, the results often point to ANSYS as being faster and more accurate, and Abaqus is often used to solve engineering problems. For this project, ANSYS was the software of choice due to its performance indicators, such as a lower error margin between the ANSYS analysis and the experimental data, popularity in use for the FEA of auxetics, as well as availability of licenses.

Discretisation Methods

The solution is found through the discretisation of the model, where PDEs are solved at each node. Discretisation works by dividing a large model into smaller and more manageable sections that are evaluated independently and then used to find an approximate global solution (COMSOL INC., 2018). As the solution is approximated using the nodes, generally, a higher node density or finer mesh will provide results that are closer to reality. Meshing brings a few challenges, as depending on geometry, different shapes, sizes, and densities might be required to find the most suitable discretisation method. To decide upon the most appropriate mesh, convergence might be looked at to find a point where changes to the solution become insignificant, and hence, creating a finer mesh becomes unnecessary.

There are three discretisation methods: Finite Element Method (FEM), Finite Difference Method (FDM), and Finite Volume Method. Each method breaks down a model into sections in a different manner (Dill, 2012). Understanding the differences between methods is essential when considering the meshing methods for different types of analysis, i.e. structural versus fluid dynamic. Furthermore, the software may have specific capabilities.

Finite Element Method (FEM)

The Finite Element Method (FEM) divides a model into elements which are individually analysed to obtain a global equation of equilibrium for the structure (Dill, 2012). The solution is achieved using PDEs, which should reflect the boundary conditions and reflect the laws of physics at each node of the element. As each set of PDEs is applied within the finite space, they become more straightforward functions that are often linear or quadratic polynomials with limited degrees of freedom (Sjodin, 2016).

Common element geometries can be found in Figure 74, and an in-depth analysis of each element type used during this work is in Section 'Meshing in ANSYS'. FE is flexible when it comes to discretisation in size, shape, and density; hence, the main challenge is to find suitable discretisation for the geometry analysed (COMSOL INC., 2018).

As it is an approximation, the method can be applied to many models, including complex geometries and problems; however, curves and hyperbolic equations can be challenging to solve, and the approximation might be further away from an actual value.

Finite element name	Type	Geometric Representation
One-dimensional finite element	Straight nodal lines	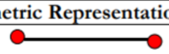
	Curved nodal lines	
Two-dimensional finite element	triangular	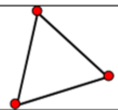
	quadrilateral	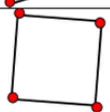
Tridimensional finite element	hexahedron	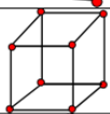
	Tetrahedron	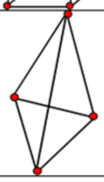

Figure 74: Types of FEM elements (Frunza, Frunză, & Luca, 2010).

Numerical Methods in FEM

ANSYS Static Structural uses FEM as the core numerical technique in solving static structural problems which is built on the two key methods mentioned: the Rayleigh-Ritz and Galerkin methods (Nakasone, Yoshimoto, & Stolarski, 2006). The numerical methods are reviewed in this section to show the impact on the approach and results obtained, however, due to the software package used, the different methods are utilised automatically without the user input required. There are ways of manipulating the software's solver, but these are out of scope of this work.

FEM fundamentally relies on the ability to solve PDEs to obtain an appropriate solution to the modelling problem. It is not always possible to use direct methods to find the exact solution unless the problem is very simple, i.e., one-dimensional.

For approximate solutions, there are two numerical methods to obtain a solution (Stolarski, Nakasone, & Yoshimoto, 2018): Rayleigh-Ritz Method and Galerkin Method. Both methods vary mathematically and produce different results.

Rayleigh-Ritz Method, often referred to as the variational method, can be applied to functionals equivalent to a differential equation. The method determines the maximum or the minimum of the function, hence its name, variational method. The minimum or maximum function is true due to the principle of the Minimum Potential Energy (MPE), defined by the equation (38).

The total potential energy of the elastic body, $\Pi =$ elastic strain energy of the body, $U -$ potential energy of the body forces, V

(38)

The MPE states that the structure will deform or displace to a position that minimises the total potential energy (Yang B. , 2005), equation (39).

$$\delta\Pi = \delta U - \delta V = 0 \tag{39}$$

Rayleigh-Ritz assumes that an approximate solution is a linear combination of trial functions containing arbitrary constants, a_i, with continuous first-order derivatives, which must satisfy the boundary conditions (Stolarski, Nakasone, & Yoshimoto, 2018). As the assumed approximate solution has maximum and minimum values and it is a stationary value within that range, it can be referred to as an admissible function. The function then can be integrated, and coefficient values can be substituted, allowing the distance between the approximate solution and the exact one to be determined,

with the goal of reducing the difference to as close to 0 as possible. Stolarski, Nakasone, and Yoshimoto (2018) provide a worked example for a boundary-value problem.

The Galerkin method, also referred to as a weighted residual method, is another method used to solve PDEs. Galerkin method does not require the derivation of the functionals, which is its advantage over the Rayleigh-Ritz method.

The function $\bar{u}$ in the method of weighted residuals is defined so that the integral of error, R, over a determined region, D, weighted by the arbitrary functions, w_i, is equal to 0.

The w_i functions are defined as:

$$w_i(x) = \begin{cases} 1 & for\ x\ inside\ region\ D \\ 0 & for\ x\ outside\ region\ D \end{cases} \tag{40}$$

The coefficients, a_i, are dictated by:

$$\int_D w_i R dD = 0 \tag{41}$$

Stolarski, Nakasone, and Yoshimoto (2018) provide a worked example for a boundary-value problem, shown as a one-dimensional differential equation.

Galerkin method can be applied in FEM as well as the Finite Volume Method (FVM), in which the exact expressions are evaluated using the average value of the solution over some volume, using this data to find an approximation within the region.

ANSYS package utilises both methods, Galerkin and Rayleigh-Ritz, but the Galerkin method is the dominant method used to solve potential differential equations.

Finite Difference Method

An alternative to FEM is a Finite Difference Method (FDM) (Key & Krieg, 1973). In FDM, the model is mapped out against the grid, which is broken down into finite mesh, as seen in Figure 75. The solution is found by finding the difference between model respective to the grid, which is made easier if uniform or cartesian grids are used. Differential equations at each node, and an exact solution is found at each node to bring a global solution. Although this method can provide an exact solution, it is not very effective for complex geometries.

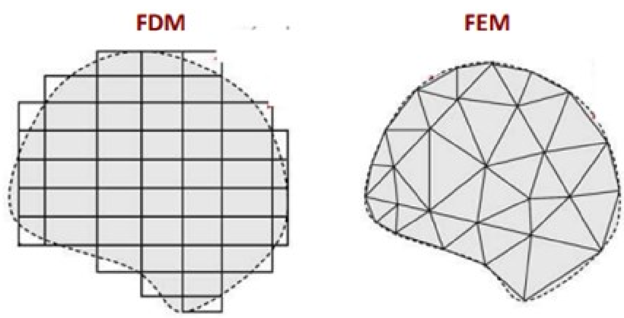

Figure 75: Comparison of discretisation methods for the Finite Difference Method (FDM) and Finite Element Method (FEM) (Polyzos, 2019)

Lastly, no commercially available software uses FDM to solve the problem at hand as it is computationally challenging to obtain the solutions in comparison to FEM.

There are many more methods to provide a solution to a numerical analysis of the models, such as the Finite Volume Method (FVM), which is often used for Computational Fluid Dynamics (CFD). However, they are not applicable to this project and, therefore, will be omitted.

Meshing in ANSYS

Meshing is a discretisation method, and it is one of the steps in 'Stage 1: pre-processing'. In this section, the 2D meshing elements used in the modelling in the latter sections are looked at and how they are used to find the solution. The 3D elements can be found in 'Appendix 1: 3D Discretisation Elements'. The information below is found in the ANSYS Theory Manual unless indicated otherwise.

2D Meshing

ANSYS Static Structural has several element options for 2D structures, which can be found in Table 7. The elements in bold were the ones chosen and used within the models described in the later section, 'Verification And Validation Of The Results' on page 143 and in Chapter 5 FE Models and Analysis 2D Modelson page 212.

Table 8 shows the elements used for the 2D model of 0.95 Volume ratio of platelets where the brick was modelled using quadrilateral elements and the mortar was modelled using solely triangles as described in section ‘Mesh’ on page 217.

PLANE42	SURF153	PLANE182	**CONTA172**	**TARGE169**	**PLANE183**
Structural Solid	Structural Surface Effect	Structural Solid	3-Node Surface-to-Surface Contact	Target Segment	8-Node Structural Solid

Table 7: 2D elements available in ANSYS as found in ANSYS Theory Manual

Element Name IDs	Material IDs	Element Type IDs	Number of Elements
TARGE169	208, 210, 212, 214, 216, ...	208, 210, 212, 214, 216, ...	14273
CONTAC172	207, 209, 211, 213, 215, ...	207, 209, 211, 213, 215, ...	14876
PLANE183	1-206	1-206	140728

Table 8: The elements used for the 2D model with the number of each element used for Mechanism 1

The PLANE42, PLANE182, and PLANE183 are elements for plane surfaces, SURF153 is for the surface model, and CONTA172 and TARGE169 are for contact and target points where the contact surface is.

The model utilises PLANE183 for the elements within the model and CONTA172 and TARGE169 for the contact region. TARGE169 and CONTA172 are associated together, as shown in Figure 76. PLANE183 was chosen as it is a quadratic element which is often considered to provide a better approximation of the curved boundaries, or in the case of the models developed, it provides a more accurate displacement of the individual element nodes which results in more accurate global view of deformation of the model than the linear element counterparts.

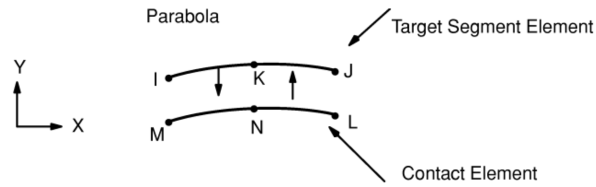

Figure 76: Target and Contact Elements interconnection

The surface of one body is taken as a contact surface, and the surface of the other body as a target surface. The contact and target elements can be assigned to rigid and flexible body combinations, such as composites. In those instances, the contact element is often assigned to the deformable (flexible) body, and the target element is assigned to the (non-deformable) rigid body. Each target segment is of a specific shape or segment type, and one target surface can consist of several target segments.

The reaction force on the target surface is a resultant force found by obtaining the sum of all the nodal forces on the associated contact elements, and it is accumulated on the pilot node. If the pilot is not defined, one of the target nodes will be used. It is usually the one with the smallest number that is chosen.

CONTA172, in particular, is a 3-node surface-to-surface contact, as shown in Figure 77.

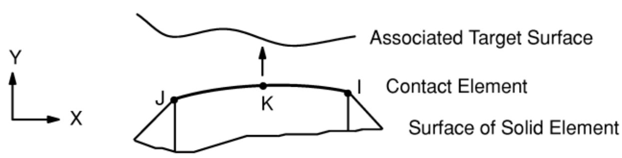

Figure 77: CONTA172 geometry consisting of 3 nodes, shown as J, K, and I.

Its stiffness matrix is integrated over the two points, and it is represented by the shape function:

$$W = C_1 + C_2x + C_3x^2 \tag{42}$$

It can be used as the contact element for either rigid-flexible or flexible-flexible surface pairs and can be applied to solid or shell bodies for either static or dynamic analysis, with or without friction. Given its potential, it is a common choice for 2D models. In the case of the modelling further on, it is used for static rigid-flexible models.

One of the challenges of the contact-target pair is that sometimes contact detection points are at Gauss points rather than nodal points, Figure 78. Gauss points are the points where the integration is performed to calculate the solution which are manipulated through meshing but not directly influenced during this work. If this occurs, the contact element can penetrate the surface, and also it can slip off the edge of the rigid surface. If a slip occurs, the contact state will be lost, and a convergence error will appear. This is managed by ensuring that different bodies do not penetrate each other. Further issues involve uniform pressures, where the equivalent forces at the nodes are not fully representative and will lead to the release at corners. This has been mentioned as an 'edge effect' in other sections and tested in section 'Test 2 – The Edge Effect Sensitivity' on page 160.

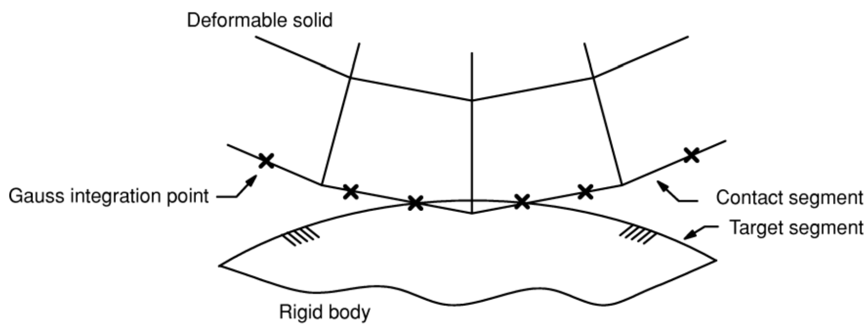

Figure 78: The Gauss Point is shown on the target-contact surface connection

The penetration is measured at normal to the contact surface at integration points. Discontinuities often cause it due to physical corners on the target surface or due to the discretisation process.

ANSYS establishes the position and motion of a contact element relative to the target surface. Contact elements have an assigned status which is denoted by: STAT=0, STAT=1, STAT=2, and STAT=3. These denote the Open far-field contact, Open near-field contact, Sliding contact, and Sticking contact, respectively.

The pinball region is centred on the integration point of the contact element, and once the contact element enters it, it is considered to be in the near field. The pinball region is key in determining the computational costs as far-field contact elements calculations are much simpler and faster in comparison. Setting the pinball region can be a useful method in reducing the computational time and brings particular benefits in convex regions, but default settings are most appropriate in other case scenarios.

The contact algorithm is for the surface-surface contact element, where the augmented Lagrangian method or the penalty method is. The augmented Lagrangian method is an iterative series that relies on penalty updates to find the exact Lagrange multipliers, also known as contact tractions. It tends to lead to better conditioning, and it is less sensitive to the magnitude of the contact penalty coefficient.

The actual surface element used within the 2D models is PLANE183. PLANE183 is an 8-Node Structural Solid, as seen in Figure 79.

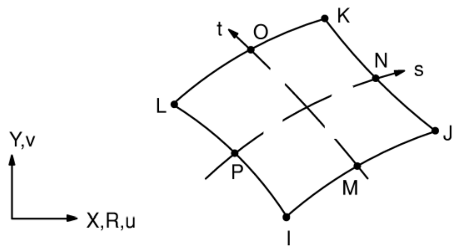

Figure 79: PLANE183 geometry showing eight nodes L, O, K, N, P, I, J and M

The main shape functions used to analyse the PLANE183 quadrilateral elements are:

$$u = \frac{1}{4}\Big(u_I(1-s)(1-t)(-s-t-1) + u_J(1+s)(1-t)(s-t-1)$$
$$+ u_K(1+s)(1+t)(s+t-1) + u_L(1-s)(1+t)(-s+t-1)\Big)$$
$$+ \frac{1}{2}\big(u_M(1-s^2)(1-t) + u_N(1+s)(1-t^2) + u_O(1-s^2)(1+t)$$
$$+ u_P(1-s)(1-t^2)\big) \tag{43}$$

$$v = \frac{1}{4}\Big(v_I(1-s)(1-t)(-s-t-1) + v_J(1+s)(1-t)(s-t-1)$$
$$+ v_K(1+s)(1+t)(s+t-1) + v_L(1-s)(1+t)(-s+t-1)\Big)$$
$$+ \frac{1}{2}\big(v_M(1-s^2)(1-t) + v_N(1+s)(1-t^2) + v_O(1-s^2)(1+t)$$
$$+ v_P(1-s)(1-t^2)\big) \tag{44}$$

The terms for these functions can be seen in Figure 79. The stiffness matrix is integrated over 2 by 2 points, and it has shape functions as defined in equations (43) and (44). The mass matrix is integrated over 3 by 3 points, and it has shape functions as defined in equations (43) and (44). The stress matrix is integrated over 2 by 2 points, and it has shape functions as defined in equations (43) and (44). The pressure load vector is specific to the face of the element and is integrated over 2 points along the face, and it has shape functions as defined in equations (43) and (44).

Convergence

The main limitations of FEA are computing/processing power and running time per model. Once the initial mesh is established using one of the discretisation methods mentioned above, convergence techniques can be applied. Convergence increases mesh density gradually and compares the results until the results become stable and any improvements are negligible. Once stable results are reached, creating any finer mesh becomes unnecessary. This also means that there is a chance for compromise between high-quality mesh and processing time, as a finer mesh with higher nodal density requires more processing.

Verification And Validation Of The Results

Validation and Verification can be used to ensure the accuracy of the models and that the models are solving appropriate problems (Srinivas, 2020). Although verify and validate are often used as synonyms in the English language. They serve a very different purpose in FEA (Roache, 2009). Verification aims to show that the solution is achieved correctly, and this can often be done by carrying out mesh refinements and converging the results. Validation ensures that the correct problem is being solved, such as that correct boundaries are set. It is a measure of certainty in the results. The best way to validate results is to compare them to experimental data. This may not always be an option, so it is good to consider other ways to verify the physical set-up of the model, such as experimental data available in the literature and mathematical analysis results (Moaveni, 2015).

Method

The method used for FEA in ANSYS follows the same sequence every time.

Stage 1: Pre-Processing

During the pre-processing stage, initial inputs are made, and the model is set up with all its boundary conditions. Geometry is generated and imported into ANSYS; in this case, DesignModeler is used to develop relevant geometries, as 2D and 3D models can be generated within the workspace with ease. The geometry is then discretised into elements and nodes, forming a mesh that represents the global problem, with element types described in the 'Meshing' section. Once these steps are completed, boundary conditions are set up to represent the physical behaviour of the object, including initial conditions and any external forces and loading.

Stage 2: Solving

ANSYS solves the equations in the background at each node to obtain the individual solutions. The solution might be the resultant stresses and strains of the model, as well as the displacement of particular sections. This step, although it does not require much user input, can take the most significant amount of time due to the required computing.

Stage 3: Post-Processing

The last stage is post-processing, when all the information is gathered, and any other information is obtained from the global solution by data manipulation. ANSYS has multiple capabilities to support this stage, from providing singular data points to tabular datasets and auto-generated reports. It is up to the user to determine the appropriate output and the format of data which will support any further analysis.

Once the data are obtained, verification is necessary to ensure the potential for errors is minimised. Common errors occurring during simulation are wrong input data, for example, material properties or dimensions of the geometry, selecting the wrong element type; poor element quality such as aspect ratio; and wrong boundary conditions and loads.

Each of those errors might slightly or significantly impact the results. In combination, they might provide results which are unrealistic and not reflective of the physical model. Hence, it is often wise to verify and validate the results to ensure the physics is correct before creating new models.

Method Verification

Method verification is carried out to ensure that the method applied to the novel metamaterial models are reliable due to inability to validate of the novel model results as there is no existing data that would be comparable. To verify the method, FEA model of the re-entrant honeycomb model is created, and the results are validated against literature consisting of analytical, finite element, and experimental data, providing a full-scope comparison. The definitions for validation and verification are in section 'Verification And Validation Of The Results'.

Whitty et al.'s models for re-entrant honeycombs (Figure 71) are considered and simulation is done using ANSYS v18.1 and v19.2 Workbench, as well as DesignModeler and Static Structural components, to create geometry and its analysis. The outputs are the deformation parameters, which are then used to calculate strains and Poisson's ratio. The aim is to achieve the results within a 5% deviation. Then, this method can be applied to novel metamaterial models with some certainty over its reliability.

Material Properties

Material properties were inputted into Engineering Data within ANSYS Workbench, as seen in Figure 80. Bulk modulus and shear modulus were automatically calculated by ANSYS using the input data for Young's modulus and Poisson's ratio, assuming isotropic rib material. Due to the limits on isotropic materials, described in the section 'Elasticity Theory' on page 120, the Poisson's ratio cannot exceed 0.5. ANSYS reinforces this limit, and only an input value of up to 0.49 is permissible. Poisson's ratio of 0.49 was used instead of 0.56, which was specified in the paper for the initial set-up, but Poisson's ratio within the literature had a tolerance of 0.10, so 0.49 PR is still within that tolerance.

Further tests included the sensitivity study of varied Poisson's ratio on the results to determine the effects of this property on the final result.

1	Property	Value	Unit
2	Material Field Variables	Table	
3	Isotropic Elasticity		
4	Derive from	Young's Modulu...	
5	Young's Modulus	4400	MPa
6	Poisson's Ratio	0.49	
7	Bulk Modulus	7.3333E+10	Pa
8	Shear Modulus	1.4765E+09	Pa

Figure 80: Engineering data used for the auxetic re-entrant honeycomb rib

Geometry

The geometry was generated using DesignModeler with the dimensions found in the paper by Whitty et al. (Whitty, Nazare, & Alderson, 2002); these can be found in Figure 81, labelled as 'Honeycomb 2 (Re-entrant)'. For 2D models, the depth, *b*, has been disregarded, but the remaining dimensions were utilised as in the 3D model.

	Honeycomb 1 (Conventional)	Honeycomb 2 (Re-entrant)
h (mm)	0.69 (0.07)	0.78 (0.03)
l (mm)	0.56 (0.02)	0.54 (0.02)
θ (°)	+23 (2)	-23 (2)
t_l (mm)	0.14 (0.03)	0.086 (0.006)
t_h (mm)	0.14 (0.03)	0.086 (0.006)
b (mm)	0.128 (0.005)	0.128 (0.005)

Figure 81: Dimensions used to create the geometry. Honeycomb 2 is being re-created (Whitty, Nazare, & Alderson, 2002)

The dimensions from Figure 81 are represented in a diagrammatic format in Figure 82.

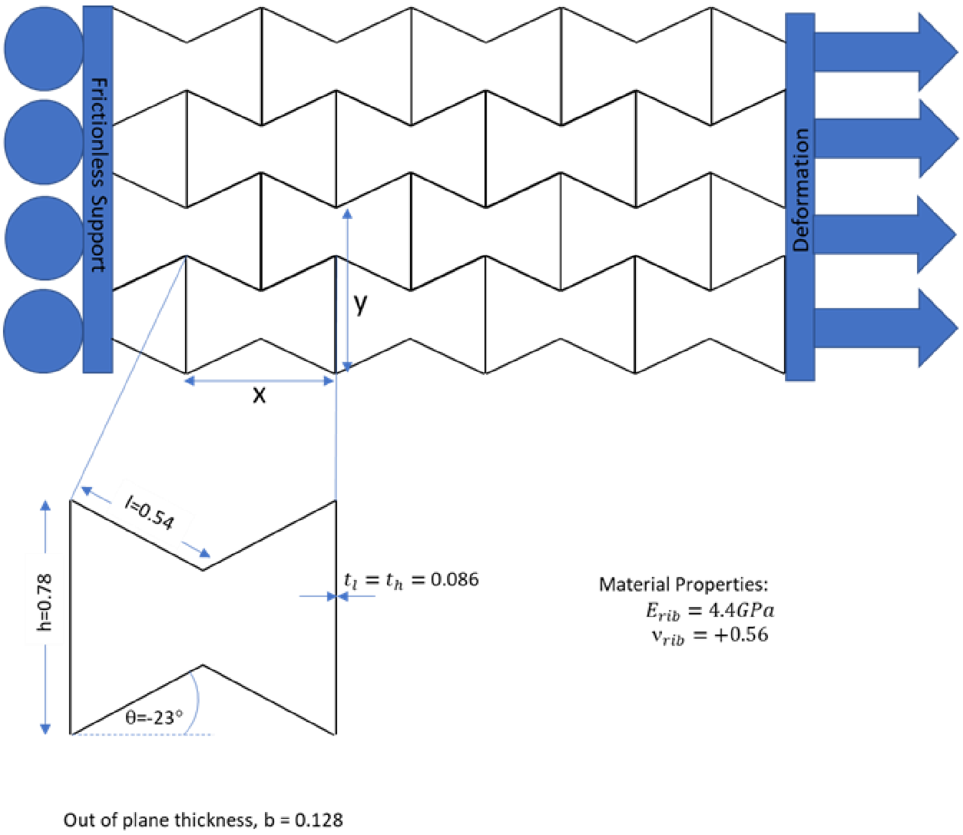

Figure 82:Diagram with relevant dimensions represented from Figure 5, showing a zoomed-in version of the repeated cell-unit

To accommodate for the single unit to be used as a repeated pattern, the thickness of 0.043 was used for individual ribs, so when combined with the adjacent thickness, they would be an expected total thickness of 0.086.

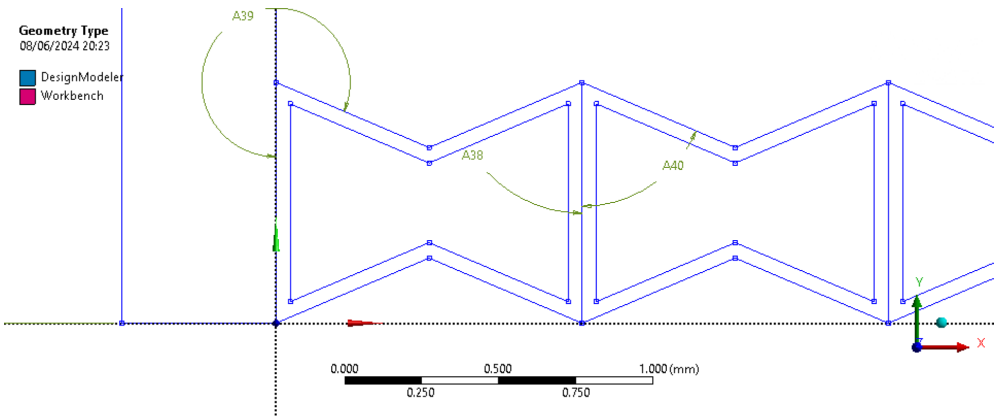

Figure 83: Sketch created in DesignModeler, which was used for creating an appropriate structure

For the 2D model, the sketch in Figure 83 was made into the surface model, which is a solid with no thickness, as shown in Figure 84.

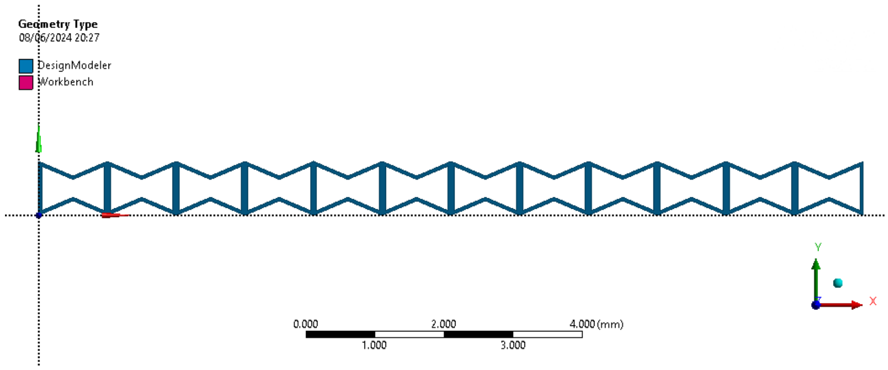

Figure 84: The surface model of the single row of repeated unit-cells

Using a small section of the model and a “pattern” tool, a bigger lattice was created. There are 24 x 24 repeated units in the lattice. To mitigate the edge effect on the lattice, solid walls were added on each side of the model. The solid walls also simplified the process of applying uniform forces when defining the boundary conditions. The final model can be seen in Figure 85.

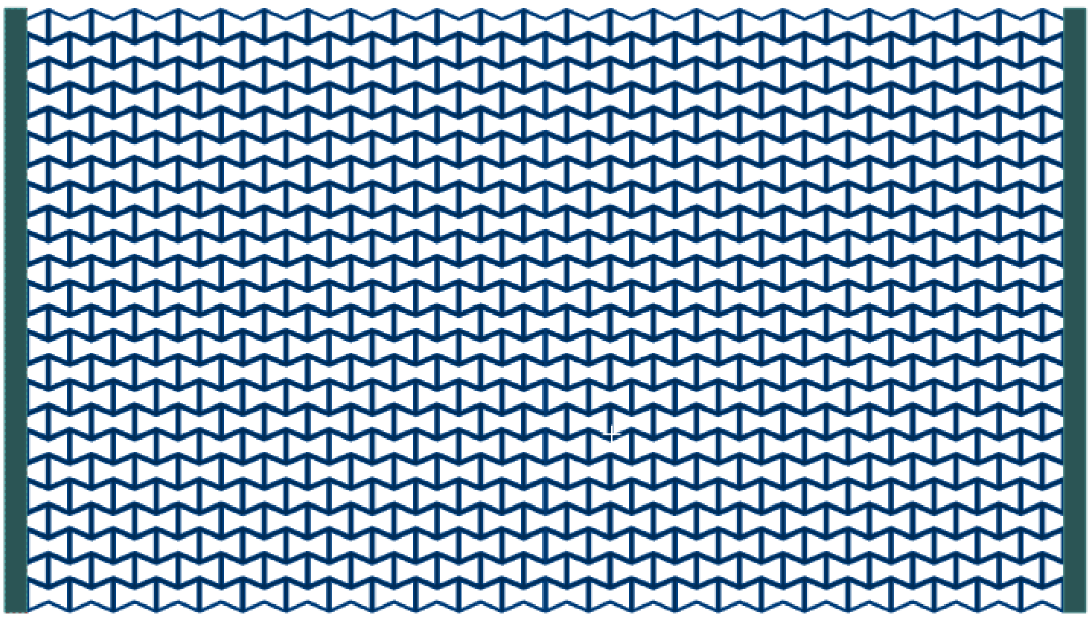

Figure 85: The entire lattice structure used for the FEA

Mesh

The unit cell was patterned and then mesh was generated with specified element size, resulting in the two triangular elements across the width of the rib when the unit cell was adjacent to another.

For the initial mesh, the element size was set to 0.05 mm, and the triangular mesh was applied to the lattice itself. The quad mesh was applied to the walls to reduce the computational time, as deformation of the walls was considered insignificant to the test. The generated mesh can be seen in Figure 86. It is recognised that two elements per width might not be sufficiently refined; hence, finer meshes were explored below.

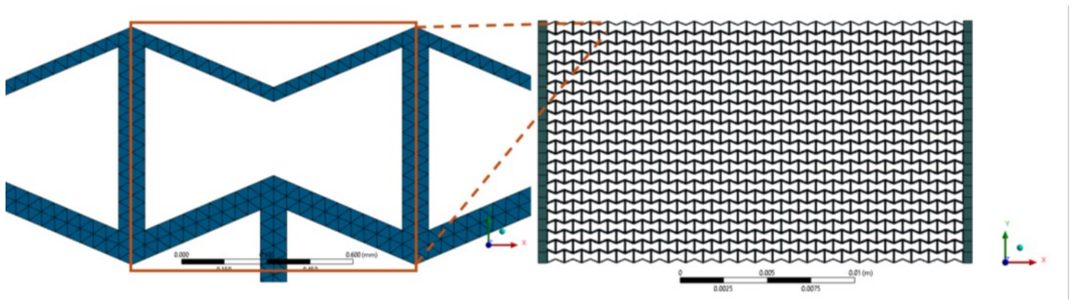

Figure 86: (Left) Zoomed-in view of the single unit cell with a generated mesh; (Right) The geometry consisting of a few rows of the repeated unit cells

The mesh shown in Figure 86 consisted of 81,480 elements and 202,236 nodes. The mesh quality, plotted in Figure 87, is between 0.89 and 1, with an average of 0.99, where the mesh quality of 1 equates to perfect triangles which is the most desirable output.

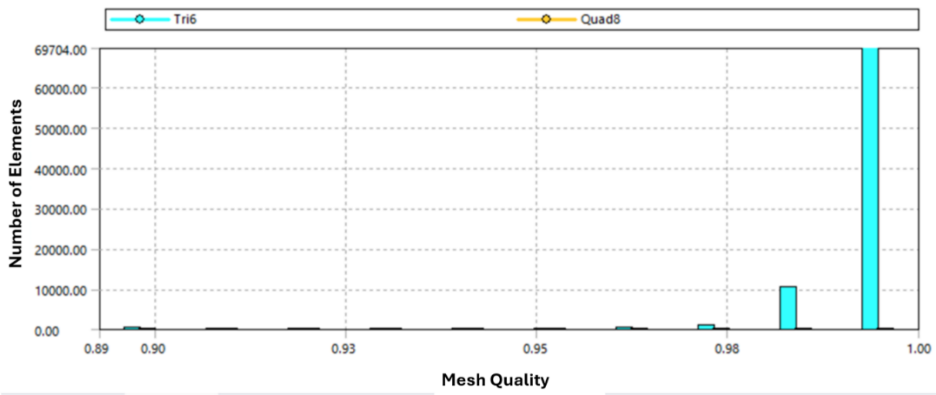

Figure 87: The mesh metrics showing the number of elements per mesh quality metrics

The aspect ratio, plotted in Figure 88, was between 1.01 and 1.43, with an average of 1.08. In the case of the triangular elements, the aspect ratio of 1 indicates an equilateral triangle which is the most desirable output.

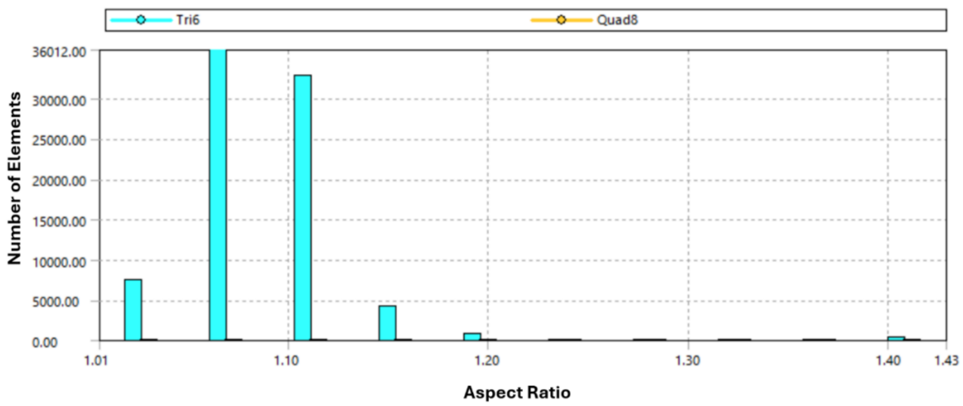

Figure 88: The mesh metrics showing the number of elements per mesh aspect ratio

The above-mentioned metrics have been measured and can be seen in Table 9. Using the refinement tool, the mesh was increasingly made finer, leading to more elements and nodes being made. It can be seen that the changes to the mesh metrics were negligible, with no improvements made after the first refinement loop. However, each refinement required a significantly longer computational time for mesh generation. It was decided that the higher mesh refinements did not bring sufficient benefits to persevere; hence, the unrefined mesh was used for further investigation.

Number of Refinement Loops	**0**	**1**	**2**	**3**
Zoomed mesh of a rib	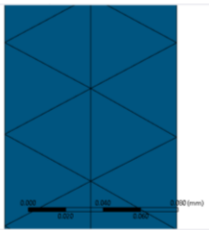	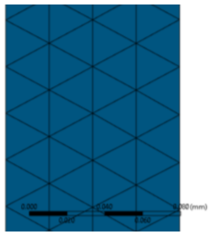	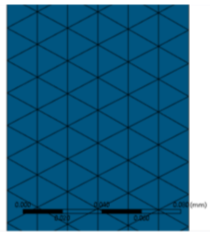	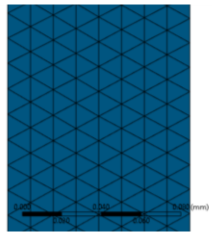
Element Quality average range	 0.99 0.89 – 1.00	 0.99 0.91 – 1.00	 0.99 0.91 – 1.00	 0.99 0.90 – 1.00
Aspect Ratio average range	 1.08 1.01 - 1.43	 1.08 1.00 – 1.37	 1.08 1.00 - 1.37	 1.08 1.00 – 1.42
Number of elements	81480	325788	732968	1303020
Elapsed Mesh Generation Time	11 seconds	4 minutes 26 seconds	28 minutes 51 seconds	1 hour 41 minutes 9 seconds
Mechanical APDL Elapsed Time (after the mesh was generated)	16 seconds	51 seconds	2 minutes 21 seconds	2 minutes 50 seconds
Mechanical APDL Memory Used	904. MB	3.3818 GB	7.5537 GB	12.419 GB
Mechanical APDL Result File Size	47.875 MB	184.25 MB	409.5 MB	723.63 MB

Table 9: The mesh metrics improvements with different number of refinement loops for the deformation of 2.39mm equating to approximately 10% tensile strain

Boundary Conditions

The generated 2D model was imported into the ANSYS Static Structural workspace, and boundary conditions were applied.

The frictionless support was applied to one side of the wall (Figure 88). Frictionless support constrains the translational movements in a normal direction to the surface to which they are applied. Frictionless support was chosen over the fixed support to allow the model to deform in the y-direction (vertically) while constraining motion in the x-direction.

A displacement was applied on the opposite wall. This was decided as an alternative to applying the force used by Whitty et al. The displacement, as shown in Figure 89 (b), was applied in the x-direction to simplify the required post-analysis. Using displacement instead of force brings the benefit of more straightforward calculations of Poisson's ratio of the structure by providing the independent variable in the x-direction (horizontal) and only requiring the measurement of displacement to be made in the y-direction.

The rotation of the model was set to 0 degrees in the z-direction to prevent any out-of-plane deformation. This is particularly important in the 2D analysis, to focus solely on in-plane deformation.

The set-up described above can be seen in Figure 89 as a diagrammatic visualisation and as the structure set up within ANSYS workspace.

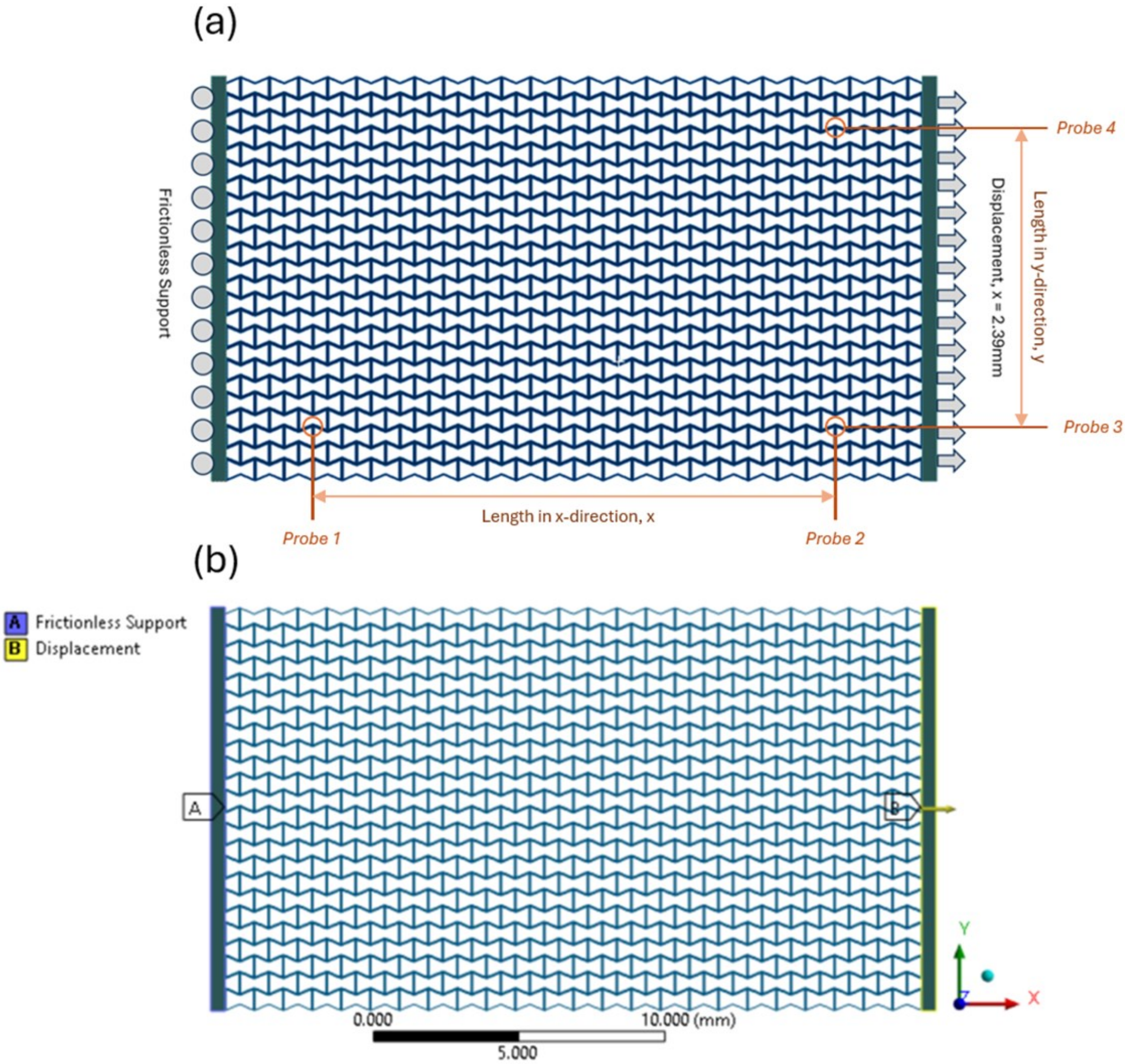

Figure 89: (a) Diagrammatic visualisation of the boundary conditions applied to the model. (b) Boundary conditions applied as seen within the Static Structural workspace

Tests

Several tests were performed to analyse the model and the dependencies on different variables. Each test was run with the same independent variable: a displacement of 2.39mm, which is equivalent to approximately 10% strain of the model. The model used in Test 1 was used as a basis for each test, with a single variable changed for each specific test. Table 10 shows what a dependent variable was and what the aim of each test was.

Test annotation (model dimensions)	Test description	Aim
1 (2D)	• Displacement in y-direction was measured using two probes along the bottom and two probes along the right-side edge. • Convergence study on the deformation	• To obtain the global Poisson's ratio of the model • To analyse the quality of the model
2 (2D)	• Displacement in y-direction was measured using probes from the centre of the lattice.	• To find out the distance from the centre of the lattice at which the edge effect influences the results

3
(2D)
	• Poisson's ratio of the rib material is varied.
	  ○ Poisson's ratio = 0.4
	  ○ Poisson's ratio = 0.2
		• To find out the effect of different Poisson's ratio of the ribs on the result of the structure

4 (3D)	• Out-of-plane thickness = 0.128mm	• To find out the effect of adding the out-of-plane thickness to the model

Table 10: The list of tests run for method validation to see the effects different variables had on the results

The purpose of this is to see whether a 2D modelling set-up will be possible and how different the results will be in comparison to the 3D model.

Test 1 – Initial Test

For this test, four probes were used, two along the x-axis and two along the y-axis. The probes are indicated in Figure 89 as Probe 1, Probe 2, Probe 3, and Probe 4.

The distance between the probes was calculated to obtain the lengths in the y- and x-directions, a few cells away from the wall, to ensure that the edge of the lattice did not affect the results. Then, the deformation was measured at each of the probes to allow for calculating the Poisson's ratio of the structure.

The mesh generated was all quadrilateral mesh for the two end walls and refined triangular mesh for the re-entrant honeycomb structure. This resulted in 730540 nodes and 325788 elements, which took 4 minutes and 18 seconds to generate. Once the mesh was generated, the solve action took 1 minute and 37 seconds.

The deformation of the model can be seen in Figure 90, where blue indicates the least deformation, which is on the left side of the model where frictionless support is applied. Red indicates the highest level of deformation, which is on the right side of the model where the displacement is applied. The deformation near the edges is slightly different than within the centre of the model, showing the edge effect – this is further explored in the next test.

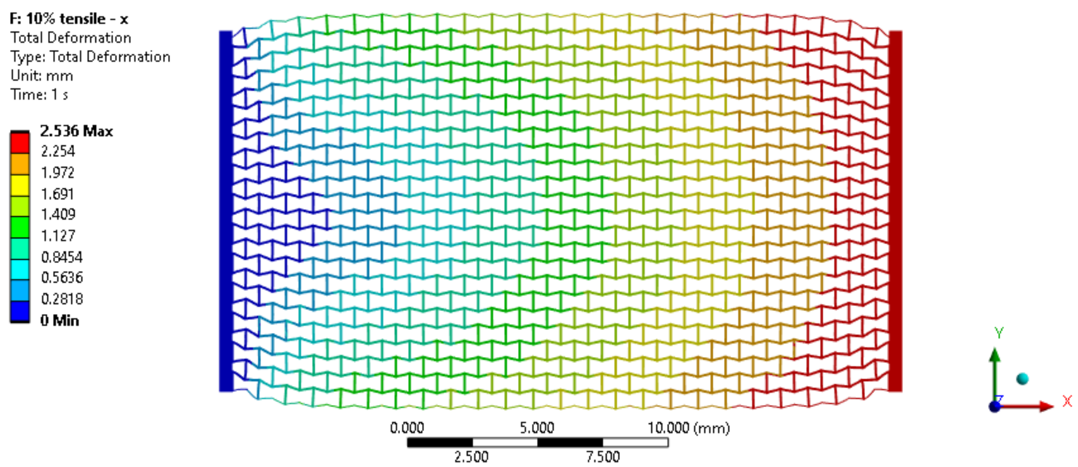

Figure 90: Total deformation of the model under approximately 10% tensile strain in the x-direction. The displacement is applied to the right side of the model; hence, the highest deformation (shown in red) is on the right.

The Equivalent (von Mises) stress of the model is shown in Figure 91, where diagram (b) shows the unit cell from the central section of the re-entrant honeycomb, which is unaffected by the edge deformation. The highest level of stress can be found around the junctions, which are likely going to be the areas that are most likely to fail first if the model exceeds the ultimate tensile strength.

Figure 91 (c) shows a zoomed-in section of the right-top corner. The red highlight indicates the highest stress within the model, which exceeds 820 MPa. As the unit cell is near the edge, the edge effect is likely affecting the result as the model cannot freely deform when attached to the solid ‘wall’.

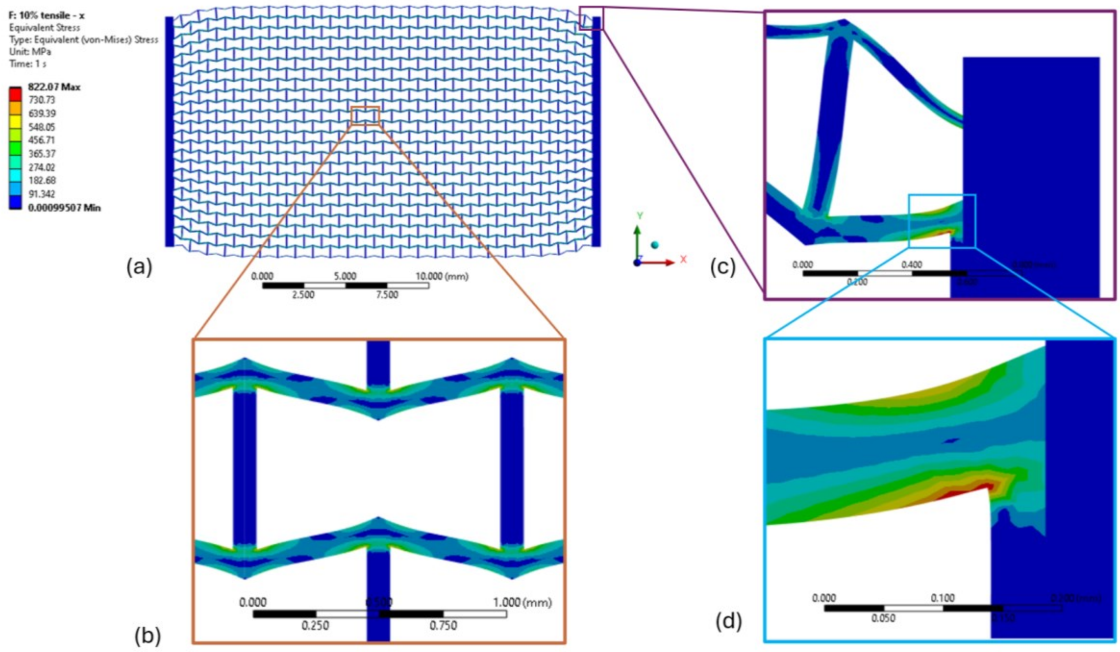

Figure 91: The Equivalent (von Mises) stress of the model under approximately 10% tensile strain in x-direction (a) the view of the entire model, (b) the zoomed-in section from within the central part of the re-entrant honeycomb showing the varying stresses within a single unit cell, (c) the zoomed-in section near the edge of the re-entrant honeycomb showing the varying stresses within a single unit cell, (d) the section showing peak stress in red

A detailed approach to finding the Poisson's ratio is outlined below.

The results were calculated using MS Excel. The original coordinates of all four probes are noted in Table 11. Probes 1 and 2 measured the deformation in the x-direction, and Probes 3 and 4 measured the deformation in the y-direction.

	Original coordinates [m]		**Deformation [m]**		**Coordinates post-deformation [m]**	
Probe number	**x**	**y**	**x**	**y**	**x**	**y**
Probe 1	0.00298		0.0002562		0.00324	
Probe 2	0.02090		0.0021338		0.02303	
Probe 3		0.00197		-0.00088		0.00109
Probe 4		0.01220		0.000781		0.01298

Table 11: The probes and their original coordinates, the deformation at each probe, and post-deformation coordinates

The coordinates in Table 11 were used to calculate the distance between the probes by simple subtraction. The undeformed lengths were found to be:

Length in x-direction, $x_{Total,0} = Probe\ 2 - Probe\ 1 = 0.0209 - \ 0.00298 = 0.01792\ m$

Length in y-direction, $y_{Total,0} = Probe\ 4 - Probe\ 3 = 0.01220 - 0.00197 = 0.01023\ m$

The deformation at each of the probes was found, as shown in Table 11.

Using the deformation results, the new coordinates were found to show where the probes were post-deformation, Table 11.

Repeating the step from earlier, the distances post-deformation are found.

Length in x-direction, $x_{Total,1} = Probe\ 2 - Probe\ 1 = 0.02303 - \ 0.00324 = 0.01980\ m$

Length in y-direction, $y_{Total,1} = Probe\ 4 - Probe\ 3 = 0.01298 - 0.00109 = 0.01189\ m$

The original distance between the probes [m]		**Distance between the probes post-deformation [m]**	
Length in x-direction, $x_{Total,0}$ (= Probe 2 – Probe 1)	0.01792	Length in x-direction, $x_{Total,1}$ (= Probe 2 – Probe 1)	0.01980
Length in y-direction, $y_{Total,0}$ (= Probe 4 – Probe 3)	0.01023	Length in y-direction, $y_{Total,1}$ (= Probe 4 – Probe 3)	0.01189

Table 12: Distance between the probes before and post-deformation

With the distance between probes before and after deformation now available, in Table 12, the change in distance can be found, which then allows for the calculation of strains in both directions.

$$\varepsilon_x = \frac{x_{Total,1} - x_{Total,0}}{x_{Total,0}} = \frac{0.01980 - 0.01792}{0.01792} = \frac{0.00188}{0.01792} = 0.1049$$

$$\varepsilon_y = \frac{y_{Total,1} - y_{Total,0}}{y_{Total,0}} = \frac{0.01189 - 0.01023}{0.01023} = \frac{0.00166}{0.01023} = 0.1623$$

At this stage, the calculation of Poisson's ratio using the definition from equation (1) is possible:

$$\upsilon = -\frac{lateral\ strain}{longitudinal\ strain} = -\frac{\varepsilon_y}{\varepsilon_x} = -\frac{0.1623}{0.1049} = -1.5472$$

The re-entrant honeycomb structure had the NPR as expected from the literature. The results are further discussed in the 'Summary of Results'.

Test 2 – The Edge Effect Sensitivity

The second test aimed to find out at which point the deformation on the edge of the lattice affects its overall properties and how significant this influence is.

The same boundary conditions were used as within Test 1, including the frictionless support on one of the walls and displacement on the other.

The main difference is the number of probes. For this test, more probes were applied, and all were set up with reference to the centre of the lattice. An observation of the edge effect on the results was made possible by the use of multiple probes.

Points distribution is shown in Figure 92, where P is the probe and P35 and P82 show the reference point, i.e. the centre of the lattice or origin. P35 and P82 will allow the calculation of the original and deformed length from the centre to the outer probes.

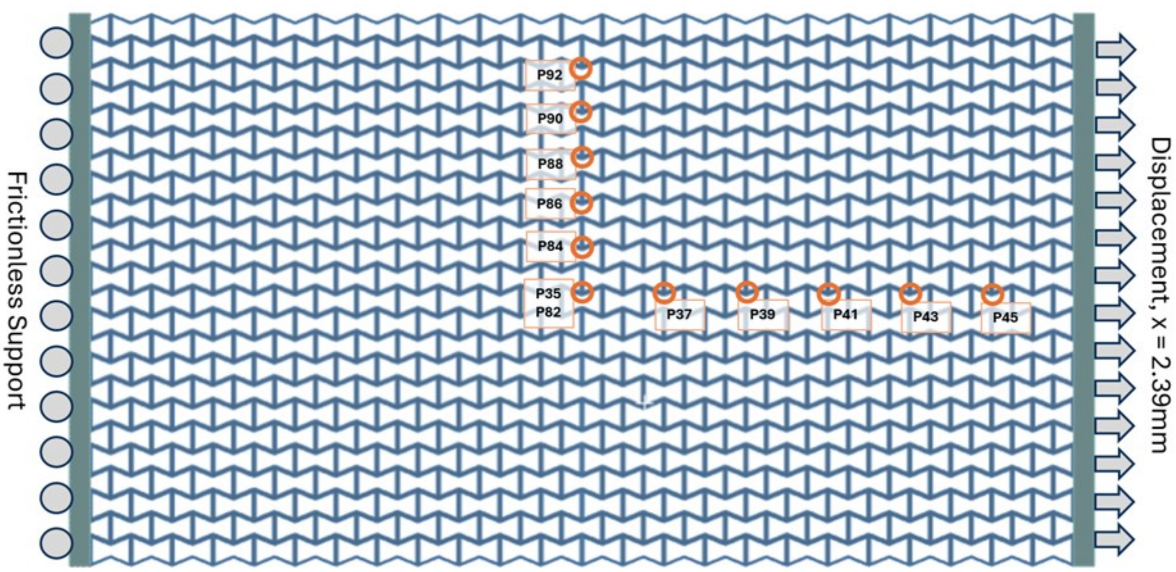

Figure 92: Set of probes used for Test 2 where P35 and P82 are reference points (P – probe)

Using a method similar to that used for Test 1, original coordinates were noted, as seen in Table 13. These coordinates were then used to find the distance between each probe and the origin. Deformation was measured at each probe, and new coordinates were found, Table 13. It is important to note that the reference points have also deformed; hence, the new P35 and P82 coordinates have to be used as origin to find the post-deformation distances between the probes. The new coordinates allowed the new distances to be calculated.

	Original coordinates [m]	Undeformed distance between the probes and the reference point [m]	Coordinates post-deformation [m]	Post-deformation distance between the probes and the reference point [m]
	x-direction			
Probe 35	0.0119	N/A	0.0131	N/A
Probe 37	0.0139	0.00199	0.0153	0.00221
Probe 39	0.0159	0.00398	0.0175	0.00442
Probe 41	0.0179	0.00597	0.0198	0.00663
Probe 43	0.0199	0.00795	0.0220	0.00883
Probe 45	0.0219	0.00994	0.0241	0.01102
	y-direction			
Probe 82	0.0068	N/A	0.0068	N/A
Probe 84	0.0079	0.00114	0.0082	0.00135
Probe 86	0.0091	0.00228	0.0095	0.0027
Probe 88	0.0102	0.00341	0.0109	0.00405
Probe 90	0.0113	0.00455	0.0122	0.0054
Probe 92	0.0125	0.00569	0.0136	0.00674

Table 13: Original coordinates for all of the probes in x- and y-direction, undeformed distances between probes, coordinates post-deformation, and distance post-deformation. Highlighted cells are the reference points.

The above-mentioned parameters allow for the changes in distance, the strains, and the Poisson's ratio to be calculated.

Probe in x-direction	Probe in y-direction	Poisson's ratio, ν
Probe 37	Probe 84	-1.69
Probe 39	Probe 86	-1.68
Probe 41	Probe 88	-1.68
Probe 43	Probe 90	-1.68
Probe 45	Probe 92	-1.70

Table 14: Poisson's ratio for each probe pair

The results for Poisson's ratio for each probe pair are in Table 14. All the results are close to each other, with the most variation being 1.6% between the highest and lowest measurements.

Test 3 – The Poisson's Ratio of the Rib Sensitivity

The material's Poisson's ratio is varied to see whether having different material properties of the ribs will affect the results. The PR used is 0.20 and 0.40, in comparison to the 0.49 used in previous tests and 0.56 used by Whitty et al., whilst keeping all other properties the same, as well as using the probe 43 and probe 90 as shown in Test 2. The engineering data used within this test can be found below in Figure 93 and Figure 94.

1	Property	Value	Unit
2	Material Field Variables	Table	
3	⊟ Isotropic Elasticity		
4	Derive from	Young's Modulus and Poisson's Ratio	
5	Young's Modulus	4400	MPa
6	Poisson's Ratio	0.4	
7	Bulk Modulus	7.3333E+09	Pa
8	Shear Modulus	1.5714E+09	Pa

Figure 93: Engineering data used for Test 3; Poisson's ratio was set to 0.4.

1	Property	Value	Unit
2	Material Field Variables	Table	
3	⊟ Isotropic Elasticity		
4	Derive from	Young's Modulus and Poisson's Ratio	
5	Young's Modulus	4400	MPa
6	Poisson's Ratio	0.2	
7	Bulk Modulus	2.4444E+09	Pa
8	Shear Modulus	1.8333E+09	Pa

Figure 94: Engineering data used for Test 3; Poisson's ratio was set to 0.2.

The same method was used to obtain the test results as previously, and the Poisson's ratio of the structure has been calculated. These results are in Table 15.

Poisson's ratio of the Rib, $\boldsymbol{\nu_{rib}}$	***Poisson's ratio of the Structure,*** $\boldsymbol{\nu}$
0.40	-1.679
0.20	-1.684

Table 15: The results for the two structures with the material's Poisson's ratio set to 0.4 and 0.2, respectively

The results obtained show little variability due to the changes in the material's Poisson's ratio and compare well with the results from Test 2. This potentially indicates that the main influence on the structure's Poisson ratio is geometry itself. However, it is acknowledged that the range of Poisson's ratio of the material is small, and the material model used remained the same.

Test 4 – The Poisson's Ratio of the 3D Structure

This test looks at the same model as Test 2, with probe 43 and probe 90 used to find the deformation. Furthermore, the structure has an added out-of-plane thickness of 0.128mm, which makes it 3D, Figure 95. The 3D model was meshed using the Hex Dominant Method with the element size of 0.05mm, which resulted in 213484 elements, or 988108 nodes. The solution was obtained in 2m 45s after the mesh was generated.

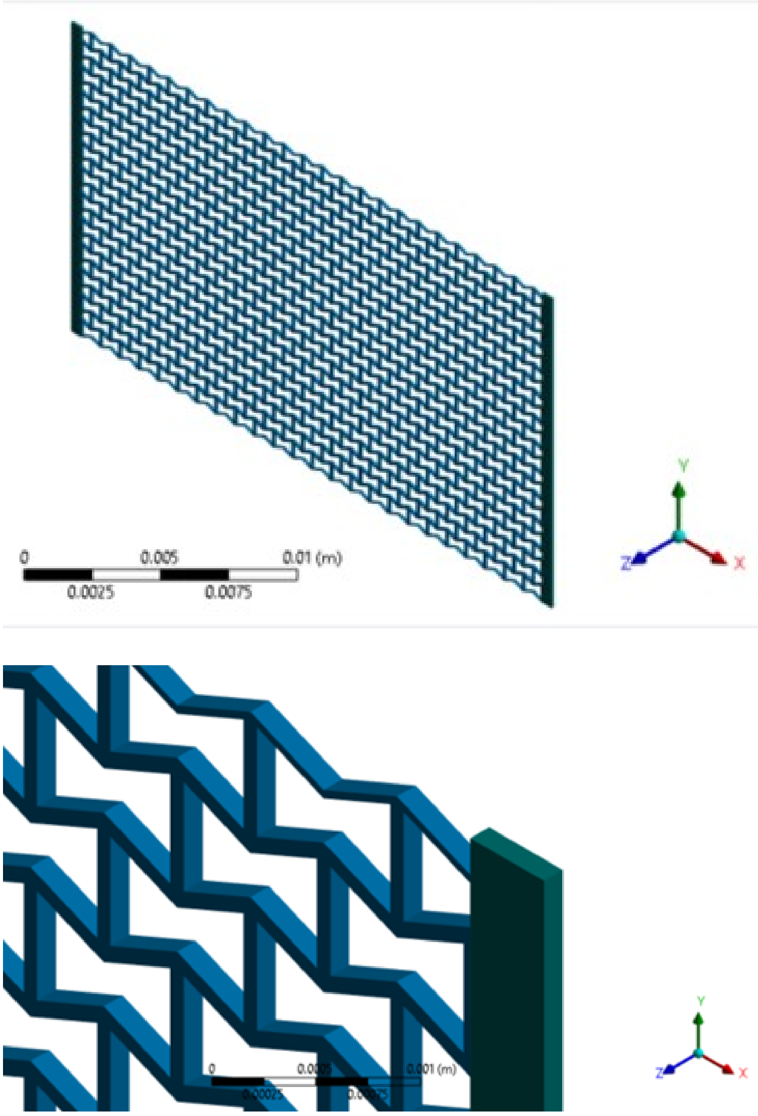

Figure 95: (Top) The 3D model of the re-entrant honeycomb structure, extruded by 0.128mm in the z-direction; (Bottom) zoomed-in section of the geometry showing its depth

The Poisson's ratio calculated was -1.708. This bears the similarity to the 2D models analysed in Test 2 and Test 3.

Re-Entrant Honeycomb Analytical Model

There are also a few analytical methods to predict the deformation of auxetic cellular structures based on hinging, flexing and stretching of the ribs. Gibson and Ashby developed a model based on rib flexing (Gibson & Ashby, 1988), and Masters and Evans developed a model containing all 3 mechanisms acting simultaneously (Masters & Evans, 1996). The Masters and Evans model expressions reduce to those of Gibson and Ashby in the cases where hinging and stretching of the ribs are not allowed. In the following, the Masters and Evans model is reviewed to demonstrate the analytical modelling approach to periodic auxetic metamaterials, which will then be employed in this project to idealise nacre structures.

Masters And Evans' Analytical Model

An analytical model by Masters and Evans enables a prediction of the elastic constants of honeycomb structures: tensile moduli, shear moduli and Poisson's ratios. These are found using the analysis of the effect of the flexure, stretching, and hinging of the cell walls (Masters & Evans, 1996).

The analysis of the re-entrant honeycomb by Masters and Evans can be found below.

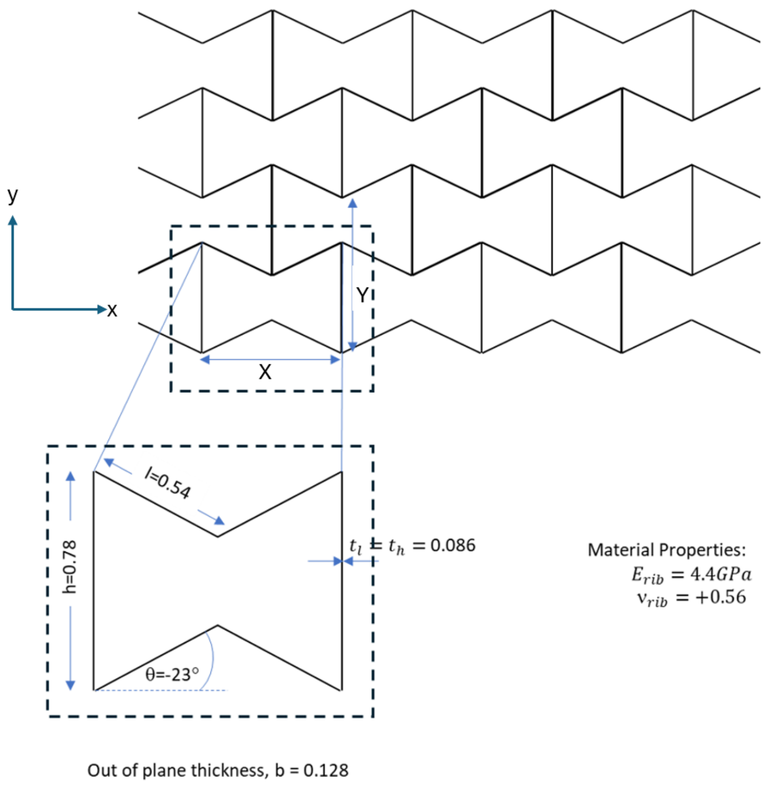

Figure 96: Representation of the re-entrant honeycomb model used to obtain an analytical solution using the Masters and Evans approach and dimensions and materials properties from Whitty et al. (Figure 82).

Figure 96 represents all the notations and dimensions used in the following derivations and calculations.

Unit-cell lengths can be found in Figure 96 and are denoted as X and Y . They are given by:

$$X = 2l \cos\theta \tag{45}$$

$$Y = 2(h + l \sin\theta) \tag{46}$$

The deformations in the x- and y- directions are given by:

$$dX = dX_f + dX_h + dX_s \tag{47}$$

$$dY = dY_f + dY_h + dY_s \tag{48}$$

Where dX_f is deformation due to flexure, dX_h is due to hinging, and dX_s is due to stretching of the ribs.

Load in y-direction

When a load is applied in the y-direction (σ_y), deformation due to flexure of the rib is given by:

$$dX_f = -\frac{Xb\sin\theta\cos\theta}{K_f}d\sigma_y \tag{49}$$

$$dY_f = \frac{Xb\cos^2\theta}{K_f}d\sigma_y \tag{50}$$

The flexure constant, K_f, is given by:

$$K_f = E_{rib}b\left(\frac{t_l}{l}\right)^3 \tag{51}$$

where E_{rib} is the Young's modulus of the rib material, which in this case is equal to 4.4 GPa, as found in Figure 96.

Deformation due to hinging of the rib is given by:

$$dX_h = -\frac{Xb \sin\theta \cos\theta}{K_h} d\sigma_y$$

(52)

$$dY_h = \frac{Xb \cos^2\theta}{K_h} d\sigma_y$$

(53)

The hinging constant, K_h, is given by:

$$K_h = G_{rib} b \left(\frac{t_l}{l}\right)$$

(54)

where G_{rib} is the shear modulus of the rib material, which can be calculated using Young's modulus and Poisson's ratio of the rib material.

Lastly, deformation due to stretching of the rib is due to the changes in the dimensions of the length of the diagonal rib, l, and vertical rib, h. These can be found in Figure 96. The deformation due to stretching is given by:

$$dX_s = 2\cos\theta\, dl$$

(55)

$$dY_s = 2\sin\theta dl + 2dh$$

(56)

The deformation of diagonal rib, l, is given by:

$$dl = \frac{Xb \sin\theta}{2K_{s,l}} d\sigma_y$$

(57)

where the stretching constant of the diagonal rib, $K_{s,l}$, is given by:

$$K_{s,l} = \frac{F}{l} = E_{rib} b \left(\frac{t_l}{l}\right)$$

(58)

The deformation of the vertical rib, h, is given by:

$$dh = \frac{Xb}{K_{s,h}} d\sigma_y$$

(59)

where the stretching constant of the vertical rib, $K_{s,h}$, is given by:

$$K_{s,h} = \frac{F}{h} = E_{rib} b \left(\frac{t_h}{h}\right)$$

(60)

Hence, from equations (55), (56), (57) and (59), the resulting stretching in the x- and y- directions are:

$$dX_s = \frac{Xb \sin\theta \cos\theta}{K_{s,l}} \, d\sigma_y$$

(61)

$$dY_s = Xb \left(\frac{\sin^2\theta}{K_{s,l}} + \frac{2}{K_{s,h}}\right) d\sigma_y$$

(62)

The total deformation is the sum of the deformation due to flexure, hinging, and stretching. The deformation along the x-direction is then determined from the equations (47), (49), (52) and (61):

$$dX = Xb \sin\theta \cos\theta \left(\frac{1}{K_{s,l}} - \frac{1}{K_f} - \frac{1}{K_h}\right) d\sigma_y$$

(63)

and along the y-direction from equations (48), (50), (52) and (62):

$$dY = Xb\left(\cos^2\theta\left(\frac{1}{K_f}+\frac{1}{K_h}\right)+\left(\frac{\sin^2\theta}{K_{s,l}}+\frac{2}{K_{s,h}}\right)\right)d\sigma_y$$

(64)

As Poisson's ratio is found using the strain, which is dependent on the change in length in the x- and y- directions, we can use the deformation found in the previous derivation to obtain the analytical model expression for Poisson's ratio:

$$\nu_{yx} = -\frac{d\varepsilon_x}{d\varepsilon_y} = -\left(\frac{dX}{X}\cdot\frac{Y}{dY}\right)$$

(65)

From equations (45), (46), (63), (64), equation (65) results in:

$$Poisson's\ Ratio,\ \nu_{yx} = \frac{\sin\theta\left(\frac{h}{l}+\sin\theta\right)\left[\frac{1}{K_f}+\frac{1}{K_h}-\frac{1}{K_{s,l}}\right]}{\cos^2\theta\left(\frac{1}{K_f}+\frac{1}{K_h}\right)+\frac{\sin^2\theta}{K_{s,l}}+\frac{2}{K_{s,h}}}$$

(66)

Young's modulus is given by:

$$E_y = \frac{d\sigma_y}{d\varepsilon_y} = \frac{d\sigma_y}{dY}\cdot Y$$

(67)

Substituting equations (45), (63) and (64) into equation (67) results in the equation for Young's modulus:

$$E_y = \frac{\frac{h}{l}+\sin\theta}{b\cos\theta\left(cos^2\theta\left(\frac{1}{K_f}+\frac{1}{K_h}\right)+\left(\frac{sin^2\theta}{K_{s,l}}+\frac{2}{K_{s,h}}\right)\right)}$$

(68)

Load in x-direction

For load in the x-direction, the same method is followed, resulting in the equation for Poisson's ratio:

$$\nu_{xy} = -\frac{d\varepsilon_y}{d\varepsilon_x} = -\left(\frac{dY}{Y} \cdot \frac{X}{dX}\right) = \frac{\sin\theta\, cos^2\,\theta\left(\frac{1}{K_f} + \frac{1}{K_h} - \frac{1}{K_{s,l}}\right)}{\left(\frac{h}{l} + \sin\theta\right)\left(sin^2\,\theta\left(\frac{1}{K_f} + \frac{1}{K_h}\right) + \frac{cos^2\,\theta}{K_{s,l}}\right)}$$

(69)

And an equation for Young's modulus:

$$E_x = \frac{\cos\theta}{b\left(\frac{h}{l} + \sin\theta\right) sin^2\,\theta\left(\frac{1}{K_f} + \frac{1}{K_h}\right) + \frac{cos^2\,\theta}{K_{s,l}}}$$

(70)

The analytical model showed a result of -1.78, which is slightly lower than the results obtained in the four tests above for the 2D and 3D FEA models.

Summary of Results

All the results are shown in Table 16. Most of the results show a slight deviation compared to the FE results obtained by Whitty et al. However, Test 1 shows the highest deviation, which is thought to be due to the edge effect, as the probes were set much closer to the edges instead of taken with respect to the centre point of the lattice. This was rectified in the following tests, where the probes used were further away from the edge.

The 3D model showed a variation of 0.04, which is within a 2.3% per cent error of the result found in the literature, which is considered a true value for this purpose.

The percentage error between 3D FEA and experimental results is 6.0%. This is slightly higher than what the findings in the literature showed.

The disparity could have many underlying causes, from the software used, mathematical models used, boundary conditions applied, or post-processing, but also within the experimental set-up and calibration. As the percentage error for the FEA was considerably lower, less than 5%, it can be justified that the method presented is reasonable for further analysis of the structures.

Results obtained during the above analysis		Literature
2D		
Test 1	-1.54	N/A
Test 2	-1.70	
Test 3	-1.71	
3D		
Test 4	-1.71	-1.75
Analytical	-1.78	-1.78
Experimental	N/A	-1.82

Table 16: All the results obtained through FE models and analytical model

Chapter 4 Analytical Models of Auxetic Systems

Nomenclature

ε	Strain
E	Young's modulus
σ	Stress
υ	Poisson's ratio
G	Shear modulus
E_{rib}	Young's modulus of the rib material
G_{rib}	The shear modulus of the rib material
S	Compliance tensor
C	Elastic moduli tensor
K	Bulk modulus
t	Thickness (in-plane)/width of the rib
h	Length of on-axis rib
l	Length of diagonal ribs
θ	Angle of rib
b	Out-of-plane thickness of the rib
x	Longitudinal direction/ horizontal
y	Lateral direction/ vertical
K_f	Flexure constant
K_h	Hinging constant
K_s	Stretching constant
F	Force

Introduction

Both analytical and numerical models can be used to predict some physical behaviours. This chapter will go over the theories that will be used to carry out the analysis of the auxetic systems. Some models rely on the elasticity theory to predict their material properties, and some use the deformation based on their geometry and trigonometrical functions to find the structure's Poisson's ratio.

This section goes over the three models as described in 'Auxetic Mechanisms'. A summary of which can be found in Table 17.

Reference	***Brief Description***	***Author***
Mechanism 1	Shearing of the organic matrix of polymeric microframes	(Wang & Boyce, 2010)
Mechanism 2	Sliding of concave bricks	(Espinosa, et al., 2011)
Mechanism 3	Brick climbing due to linked bridges causing disparities after fracture	(Song, Zhou, Xu, Xu, & Bai, 2008)

Table 17: Summary of the mechanisms analysed in this section, previously described in the Literature Review.

Mechanism 1

This model is inspired by Wang & Boyce (2010) as described in the Literature Review section titled "Auxetic Mechanisms". The focus of deformation is on the single unit cell of the mortar, Figure 97, where it can be seen that the cell is subjected to multiple forces during the deformation. There is a shear force acting on the top and bottom of the cell due to the sliding of the bricks either side of the mortar. Ligament B on the diagram is under compression.

At lower strains prior to yielding, strut A experiences elastic axial extension and bending, while strut B experiences elastic axial compression and bending.

Yielding occurs at the junction of the X-shape, which is observed at around 5% shear strain (Wang & Boyce, 2010). At this stage, it is expected that rotation about the intersection of the struts occurs alongside bending, caused by the perpendicular loading on the struts.

The strut A yields in axial tension at 12% shear strain, then as the shear strain increases further, past the yield point, it leads to the elastic axial compression and bending of strut B, plastic axial extension and bending of strut A, and plastic rotation about intersection of the struts until a next given strain of approximately 60%, at which strut B becomes unstable and deforms through buckling, as described by Wang & Boyce.

From there on, increase in shear strain continues with the strut B buckling (as described in the paper), plastic deformation of strut A, and plastic rotation of the intersection.

The buckling is more likely to occur in the structure with high slenderness ratio (Wang, He, & Xiao, 2019). Due to the lack of geometrical details within the paper, it is possible that what is observed is actually a combined bending and axial deformation where there is no instability, and which might not lead to failure as would be expected with buckling at a critical load level. This makes the analysis more challenging, but a few approaches are being considered.

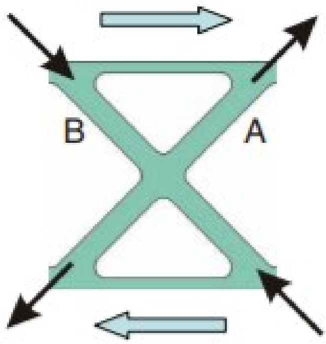

Figure 97: A single unit cell; shear force is applied at the top and bottom of the cell, resulting in compression and buckling in B-direction and tension in A-direction (Wang & Boyce, 2010).

The geometry has been idealised, as seen in Figure 98, where undeformed and deformed structures are shown. Loading in the x-direction is considered, and nomenclature and geometry from Wang and Boyce (2010) are assumed.

In the analytical model developed below, the struts are assumed to undergo a transition from elastic to plastic deformation upon yielding.

From the model presented, a few observations and assumptions can be made. The junctions connecting the mortar to the brick are fixed, considering the fact that the brick is a rigid body. This means that there is no change in distance relative to each other on the surface of a brick as the structure deforms.

The two long struts of the micro-lattice within the mortar have two very distinctive deformation profiles, as described in reference to Figure 97. From Figure 97, a strut with B experiences rotation (hinging), flexing and then buckling under large deformation and axial contraction. The other strut, A, undergoes rotation and axial stretching. To simplify the problem, only the deformation in one strut can be considered, and for simplicity, strut A is analysed. As the central junction between the struts remains mostly unchanged, this approach neglects its effect on the two struts.

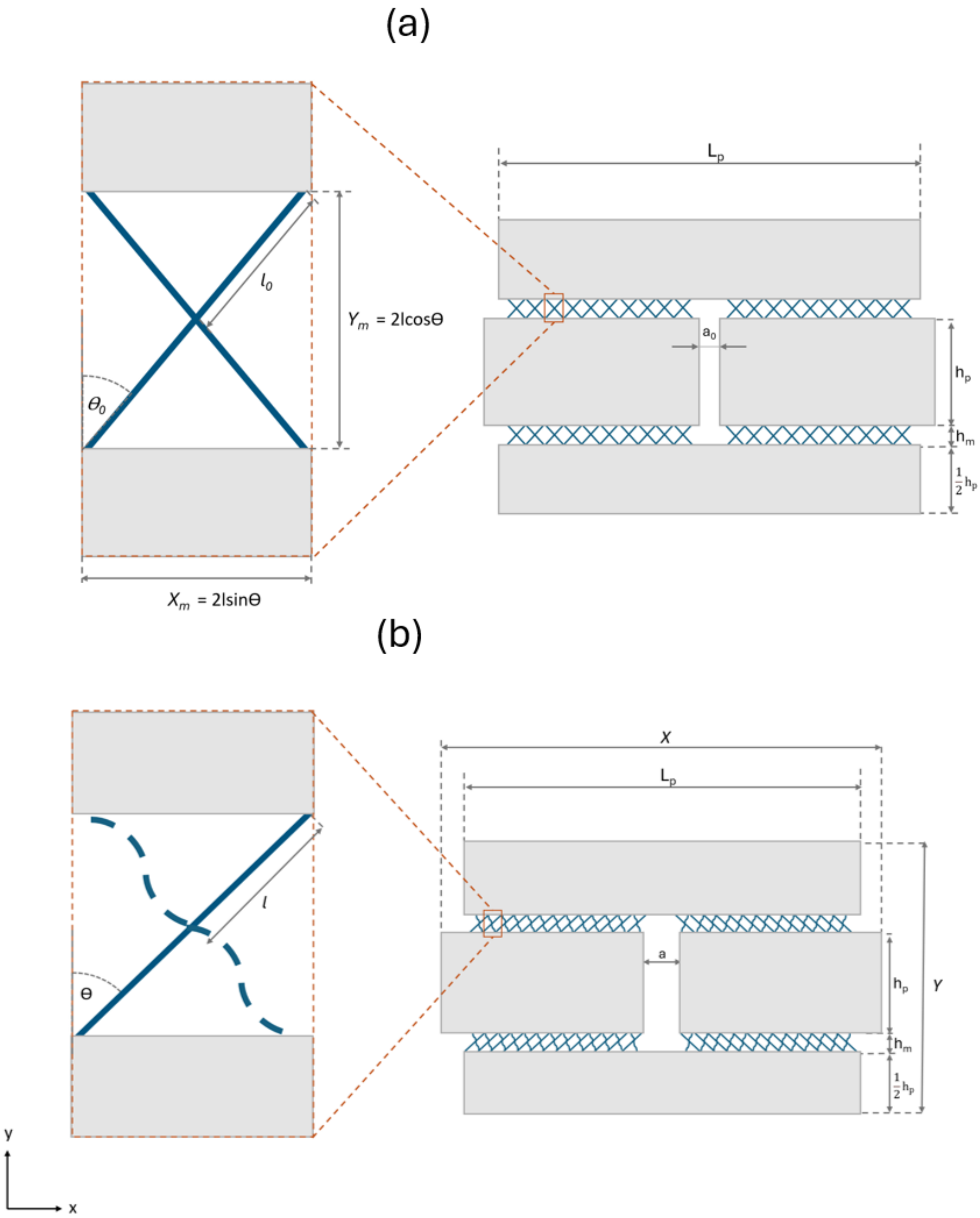

Figure 98: (a) undeformed model, and (b) deformed model. A representation of a single unit-cell of the micro-lattice with a close-up of the single unit cell of mortar, with the dimensions and their derivations used for the analytical modelling.

Now, from Figure 98, the deformation in the x-direction of the single unit of mortar is given by:

$$\Delta X_m = 2(l \sin\theta - l_0 \sin\theta_0)$$

(71)

where the terms are defined in Figure 96, and subscript zero denotes undeformed parameters.

The unit cell of the brick-and-mortar structure in the x-direction is determined as:

$$X = L_p + a = L_p + a_0 + 4(l \sin\theta - l_0 \sin\theta_0)$$

(72)

where L_p is the length of a platelet, and a is an inter-platelet gap.

The unit-cell length in the y-direction is:

$$Y = 2(h_p + h_m) = 2(h_p + 2l\cos\theta)$$

(73)

where h_p is the height of the platelet and h_m is the height of the mortar, both along the y-direction. Wang and Boyce (2010) use the instantaneous or incremental Poisson's ratio obtained from the instantaneous strain previously defined in equation (35). Wang and Boyce (2010) obtain instantaneous Poisson's ratio from the slope of the transverse stress versus axial stress data, which is equivalent to:

$$\nu_{xy} = -\frac{d\varepsilon_y}{d\varepsilon_x} = -\frac{dY/_Y}{dX/_X}$$

(74)

The instantaneous changes in unit cell lengths are caused by the deformation due to rotation (change in θ) and axial stretching (change in l) of the long strut. From equations (72) and (73), these are given by:

$$dX = 4(\sin\theta dl + l\cos\theta\, d\theta)$$

(75)

$$dY = 4(\cos\theta\, dl - l\sin\theta\, d\theta)$$

(76)

Equations (72), (73), (75) and (76) can be substituted into the equation for instantaneous Poisson's ratio:

$$\nu_{xy} = -\frac{4(\cos\theta\, dl - l\sin\theta\, d\theta) \big/ 2\left(h_p + 2l\cos\theta\right)}{4(\sin\theta dl + l\cos\theta\, d\theta) \big/ L_p + a_0 + 2(l\sin\theta - l_0\sin\theta_0)}$$

Which can be simplified to:

$$\nu_{xy} = -\frac{\left(\cos\theta\frac{dl}{d\theta} - l\sin\theta\right)}{2\left(h_p + 2l\cos\theta\right)}\frac{\left(L_p + A_0 + 4l\sin\theta\right)}{\left(\sin\theta\frac{dl}{d\theta} + l\cos\theta\right)}$$

(77)

where $A_0 = a_0 - 4l_0\sin\theta_0 = constant$

(78)

$\frac{dl}{d\theta}$ is related to the stretching and hinging force constants, K_s and K_h, respectively. These constants were previously described in the section 'Masters And Evans' Analytical Model' on page 165. These are defined for a beam of length L by:

$$F_{\parallel} = K_s dL$$

(79)

$$F_{\perp} = K_h L d\theta$$

(80)

where in our case, the length of the strut is:

$$L = 2l$$

(81)

The axial and perpendicular forces, $F_{\parallel}$ and $F_{\perp}$, shown in Figure 99, are applied to the length of the strut and cause axial extension and rotation of the long arm. They are the components of the applied shear force F and are given by:

$$F_{\parallel} = F \sin\theta$$

(82)

$$F_{\perp} = F \cos\theta$$

(83)

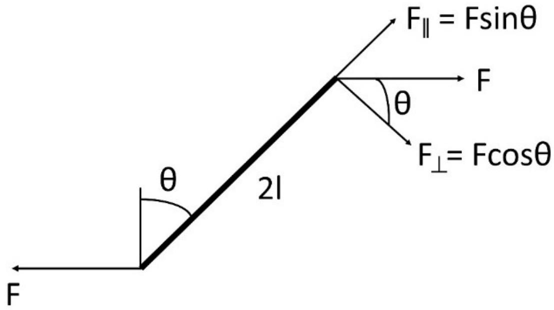

Figure 99: Force components acting on a strut due to the shear force (Alderson, 2024).

From equation (81), $dL = 2dl$.

(84)

Dividing (79) by (80)

$$\frac{F_{\parallel}}{F_{\perp}} = \frac{K_s dL}{K_h L d\theta}$$

(85)

Then substituting equations (81), (82), (83) and (84) and rearranging gives:

$$\frac{dl}{d\theta} = l\tan\theta\frac{K_h}{K_s}$$

(86)

The equation (86) shows the changes in rotational angle, Θ, corresponding to the changes in length. The incremental angle changes allow the extensions to be found which then allows for the strains to be worked out.

Substituting equation (86) into equation (77) gives the final expression for Poisson's ratio for a given geometry of the nacre-inspired metamaterial:

$$\nu_{xy} = \frac{\left(1 - \frac{K_h}{K_s}\right)}{2\left(h_p + 2l\cos\theta\right)} \frac{\left(L_p + A_0 + 4l\sin\theta\right)}{\left(\tan\theta\frac{K_h}{K_s} + \cot\theta\right)}$$

(87)

Through rearranging and integrating equation (86) to find how the strut length and angle vary with each other, variation of Poisson's ratio with strain can be found.

$$\int_{l_0}^{l}\frac{dl}{l} = \frac{K_h}{K_s}\int_{\theta_0}^{\theta}\tan\theta\, d\theta$$

(88)

which gives: $l = l_0 exp\left[\frac{K_h}{K_s}\ln\left(\frac{\cos\theta_0}{\cos\theta}\right)\right]$

(89)

The volume fraction can be used to determine the initial strut length, l_0, and this can be done as follows.

The undeformed unit-cell volume is given by: $V_0 = X_0 Y_0 b$

(90)

where b is the out-of-plane depth of the unit-cell normal to the x-y plane. The volume of platelets within the unit cell, where there are two platelets per unit cell, is:

$$V_{platelets} = 2L_p h_p b$$

(91)

From equations (72), (73), (90) and (91), the platelet volume fraction of the undeformed structure, V_p is given by:

$$V_p = \frac{V_{platelets}}{V_0} = \frac{L_p h_p}{(L_p + a_0)(h_p + 2l_0 \cos\theta_0)}$$

(92)

which, when rearranged, gives:

$$l_0 = \left[\frac{1}{V_p\left(1 + \frac{a_0}{L_p}\right)} - 1\right]\frac{h_p}{2\cos\theta_0}$$

(93)

Specifying the initial geometrical parameters of V_p, L_p, h_p, a_0 and θ_0, combined with a knowledge of K_h and K_s, allows the variation in the instantaneous Poisson's ratio with strain to be calculated. The expressions for K_h and K_s have been previously shown in equations (54) and (58) and are :

$$K_s = \frac{E_{rib} bt}{L}$$

(94)

$$K_h = \frac{G_{rib} bt}{L}$$

(95)

E_{rib} and G_{rib} are the Young's and shear moduli, respectively, of the material forming the struts of the mortar, and t is the in-plane thickness of the strut.

Where (94) and (95) are applicable, then we find:

$$\frac{K_h}{K_s} = \frac{G_{rib}}{E_{rib}}$$

(96)

The calculation of total true strains in the loading and transverse directions, ε_x and ε_y, respectively, follows the standard approach, using (72), (73) and (78):

$$\varepsilon_x = \ln\frac{X}{X_0} = \ln\left(\frac{L_p + A_0 + 4l\sin\theta}{L_p + A_0 + 4l_0\sin\theta_0}\right)$$

(97)

$$\varepsilon_y = \ln\frac{Y}{Y_0} = \ln\left(\frac{h_p + 2l\cos\theta}{h_p + 2l_0\cos\theta_0}\right)$$

(98)

Yielding of the strut can be simulated by changing the $\frac{K_h}{K_s}$ force constant ratio at the transition strain ε_x^T. The change of force constant simulates the yielding changes observed in the Wang & Boyce (2010) results found in Figure 52 correlating to the change from elastic to plastic deformation in reference to the yielding of strut (A) at the transition strain. To simulate that change, the value of the Young's modulus of the rib, E_{rib}, in equation (96) is being reduced.

There is no change required in the value of K_h when the transition is due to the strut yielding as the rotation of the strut is determined by the intersection of the struts. Hence, at the transition, K_h remains unchanged, K_s reduces, and $\frac{K_h}{K_s}$ increases overall, which was assumed to be a change of the factor of 10.

At the transition, the values of l and θ need to be recalculated for the new force constants. This is achieved following the approach of Alderson & Evans (Alderson & Evans, 1997). Rearranging equation (97) for $\varepsilon_x = \varepsilon_x^T$, and substituting (89) for l gives:

$$\sin\theta\, exp\left[\frac{K_h}{K_s}\ln\left(\frac{\cos\theta_0}{\cos\theta}\right)\right] = \frac{\left(L_p + A_0 + 4l_0\sin\theta_0\right)exp(\varepsilon_x^T) - \left(L_p + A_0\right)}{4l_0}$$

(99)

where the right side of the equation, $\frac{(L_p+A_0+4l_0\sin\theta_0)exp(\varepsilon_x^T)-(L_p+A_0)}{4l_0}$, is constant at the transition strain. The recalculated value of Θ is determined from the left side of the equation, $\sin\theta\ exp\left[\frac{K_h}{K_s}\ln\left(\frac{\cos\theta_0}{\cos\theta}\right)\right]$, for different values of $\frac{K_h}{K_s}$. This can be done using a graph, Figure 100.

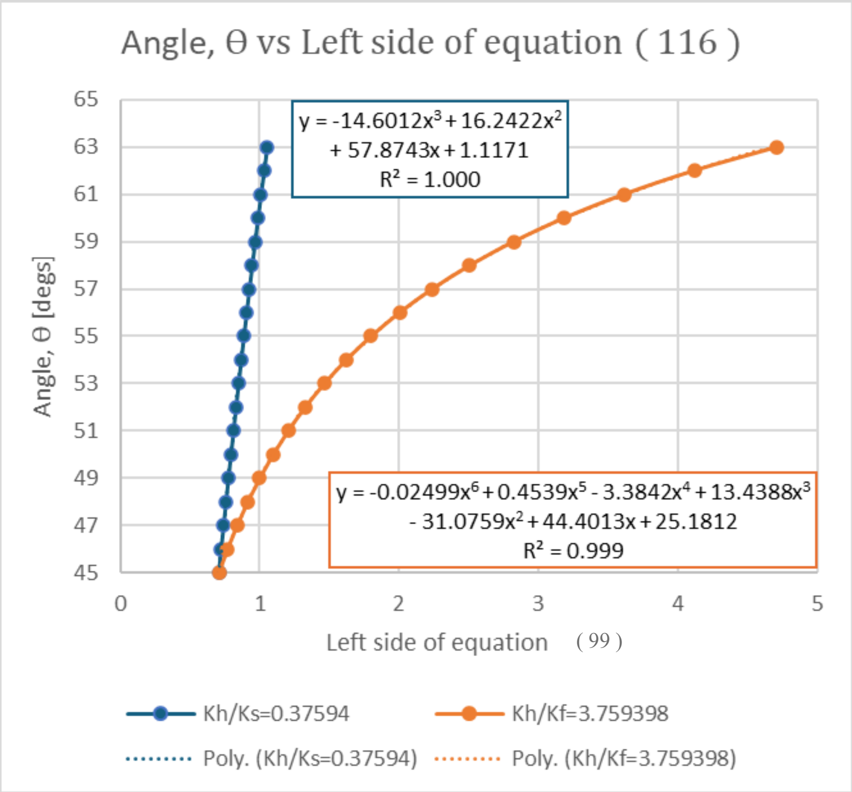

Figure 100: Angle, Θ vs the left side of Equation 116 for θ_0=45°, L_p=1, a_0 = 0.01, V_p=0.9, h_p = 0.1 and ε_x^T=0.0012. Curves shown for K_h/K_s = 0.37594 and 3.75998, corresponding to the value determined by equation 113 before yield and Ks reduced by a factor of 10 after yield, respectively, for the material considered by Wang & Boyce (Table 18).

Substituting the constant value of the right side of equation (99) for x in the polynomial best-fit curves provides the respective values of θ for the $\frac{Kh}{Ks}$ values before (= 0.37594) and after (= 3.75998) the yield transition.

The new values of θ and $\frac{Kh}{Ks}$ are then substituted into (89) to provide the recalculated value of l at the transition strain.

Equation (87) enables the parametric study to be undertaken to analyse the effect of each geometric parameter on the Poisson's ratio. The standard parameters were defined as shown in Table 18, and then L_p, $\frac{Kh}{Ks}$, θ and V_p were varied. The assumption of an isotropic material was made, which enables the shear moduli of the strut to be assumed to be $G_{rib} = \frac{\text{Erib}}{2(1+\nu_{rib})}$.

Angle, θ_0	***Platelet length in x-direction, L_p***	***The gap between the central platelets, a_0***	***Volume of the platelets, V_p***	***Height of the platelets, h_p***	***Young's modulus before yield, E_{rib}***	***Poisson's ratio before yield, ν_{rib}***
45°	1	0.01	0.90	0.1	3.3GPa	0.33

Table 18: The standard parameters set by Wang & Boyce (2010), [length in arbitrary units].

The initial parameter studies the variation of the length of the platelet and its influence on Poisson's ratio, Figure 101, for (a) $\frac{Kh}{Ks}$ = 0.37594 and (b) $\frac{Kh}{Ks}$ =3.75998.

(a)

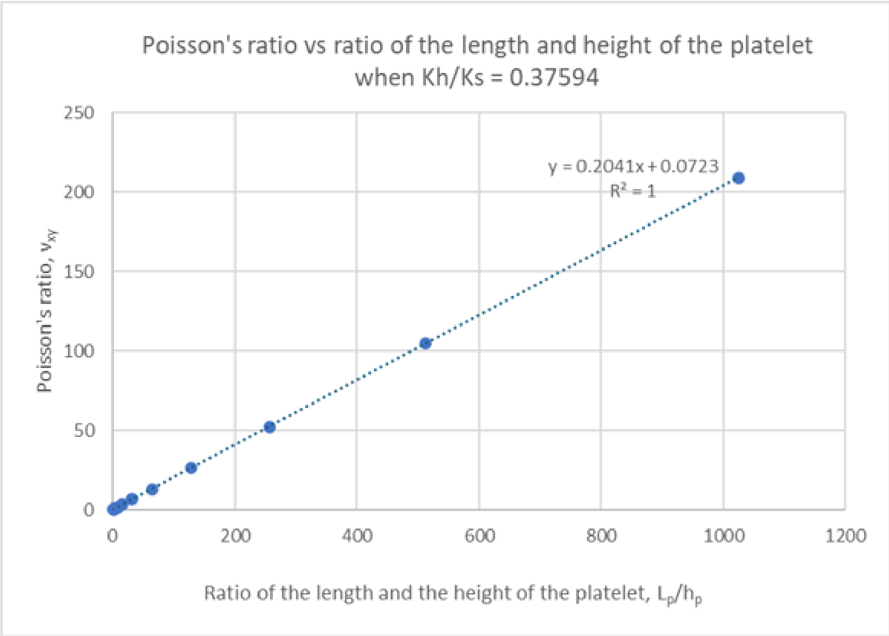

(b)

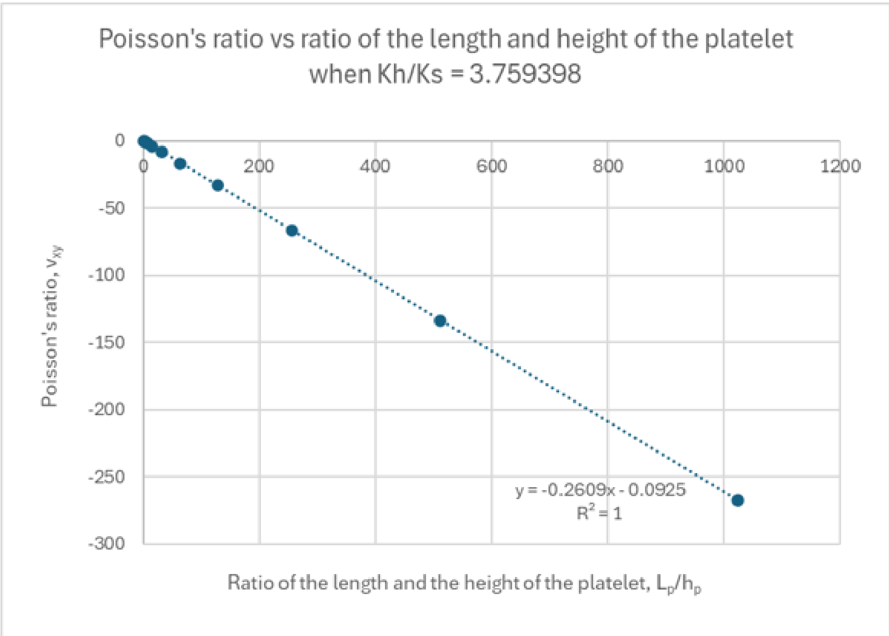

Figure 101: Poisson's ratio, v_{xy}, versus the ratio of the length and height of the platelet, Lp/hp The platelet length is varied whilst platelet height is constant. with the standard parameters set in Table 18 . (a) $\frac{Kh}{Ks}$ = 0.37594 and (b) $\frac{Kh}{Ks}$ =3.75998

The second parametric study looks at the variations of $\frac{Kh}{Ks}$ and its effect on Poisson's ratio, Figure 102. In this study, the strain remains at 0, and the focus is on the effect of varying $\frac{Kh}{Ks}$.

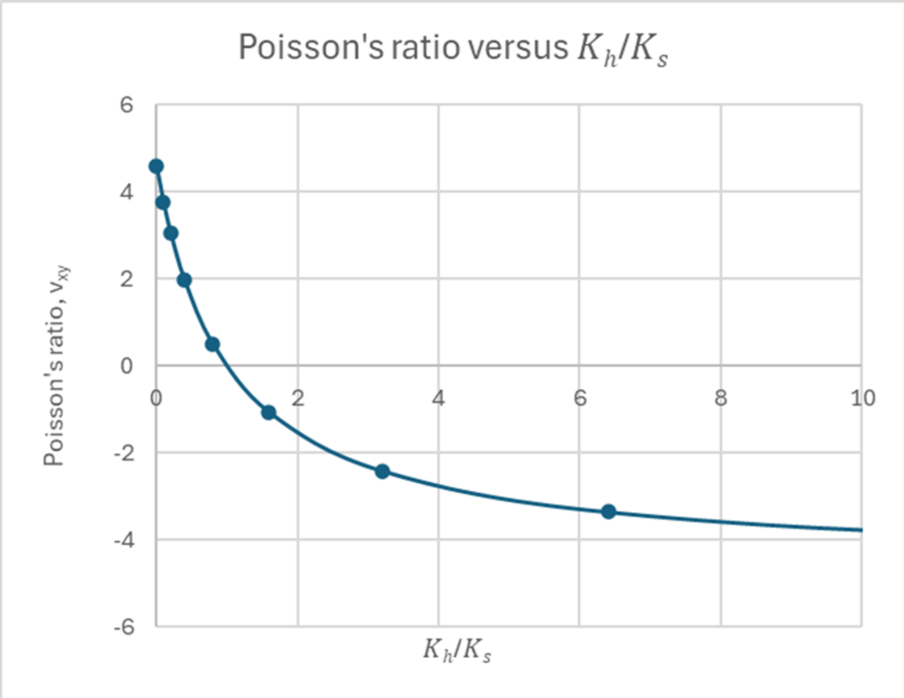

Figure 102:Poisson's ratio versus $\frac{Kh}{Ks}$ with the standard parameters set in Table 18.

Figure 103 shows the undeformed geometry as well as the changes occurring during deformation, showing that the deformation correlating to $\frac{Kh}{Ks}$ = 0.37594 results in positive Poisson's ratio, attributed to the dominant strut rotation over the strut axial extension. Once the transition occurs and $\frac{Kh}{Ks}$ =3.75998, the strut axial extension dominates over the strut rotation resulting in negative Poisson's ratio.

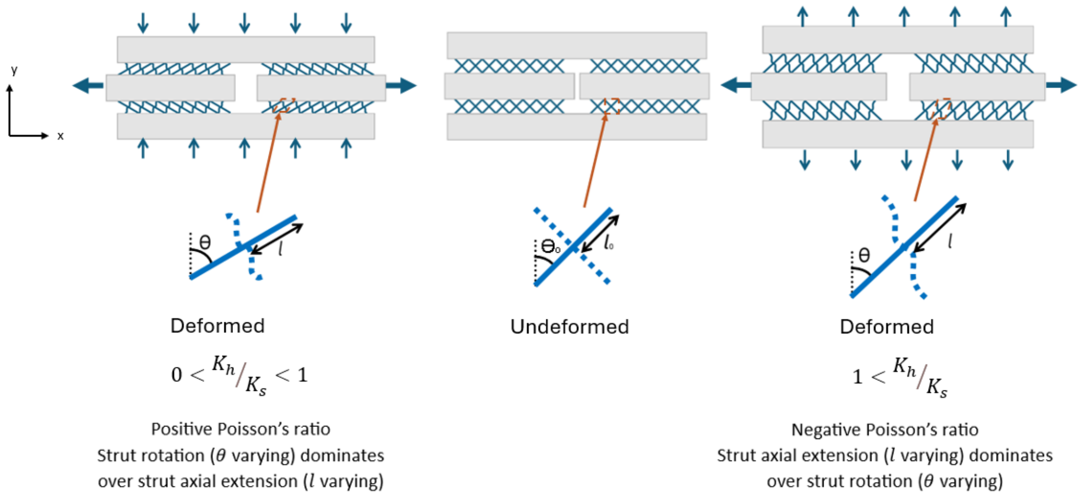

Figure 103: The undeformed geometry (middle), with shown changes when the configuration results in positive PR (left), and negative PR (right)

And the parametric study looking at the variations of angle, Θ, and its influence on Poisson's ratio, Figure 104.

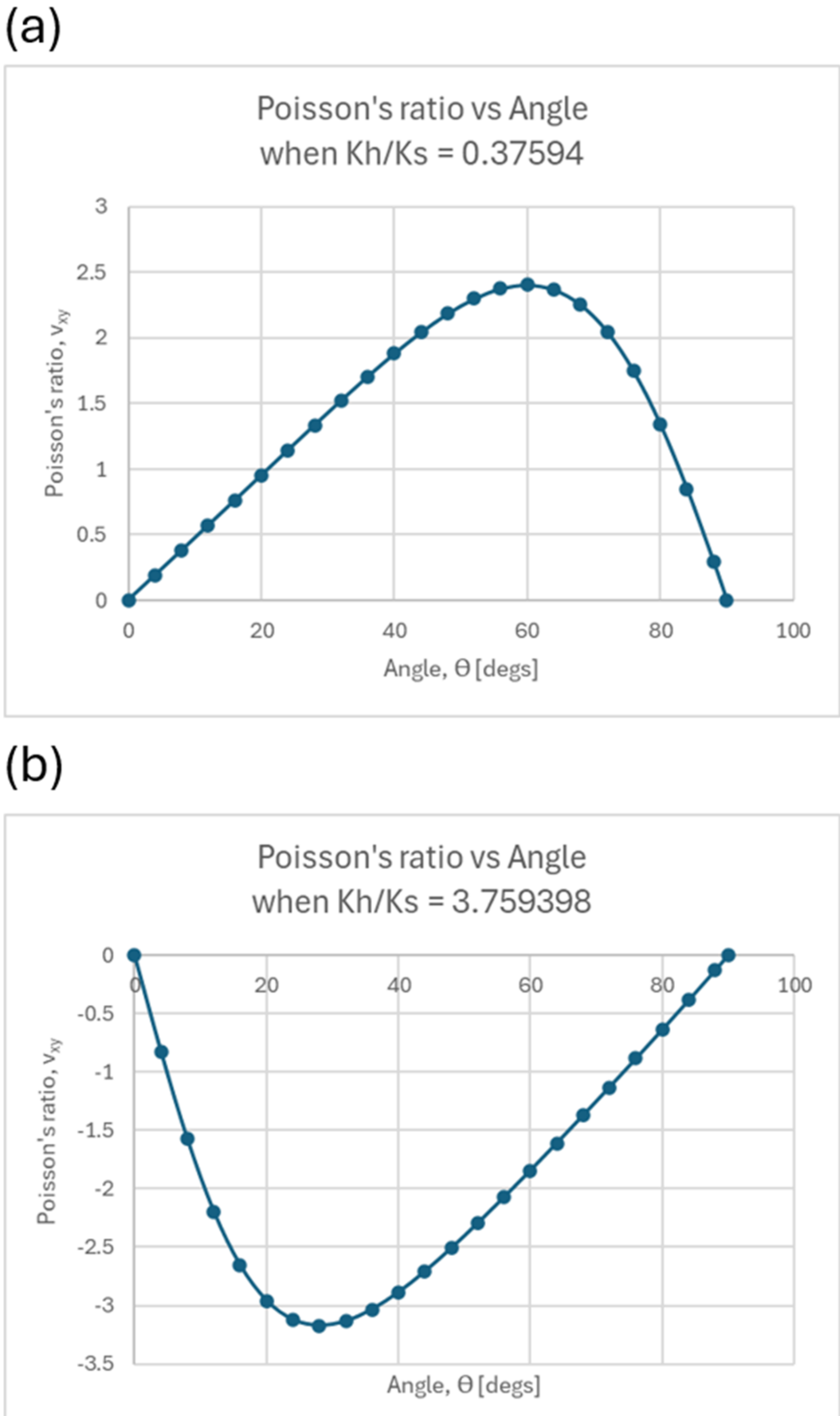

Figure 104: Poisson's ratio versus angle, with the standard parameters set in Table 18.

(a) $\frac{Kh}{Ks}$ *= 0.37594 and (b)* $\frac{Kh}{Ks}$ *=3.75998*

And lastly, the parametric study shows the effect of variable platelet volume on the Poisson's ratio, Figure 105.

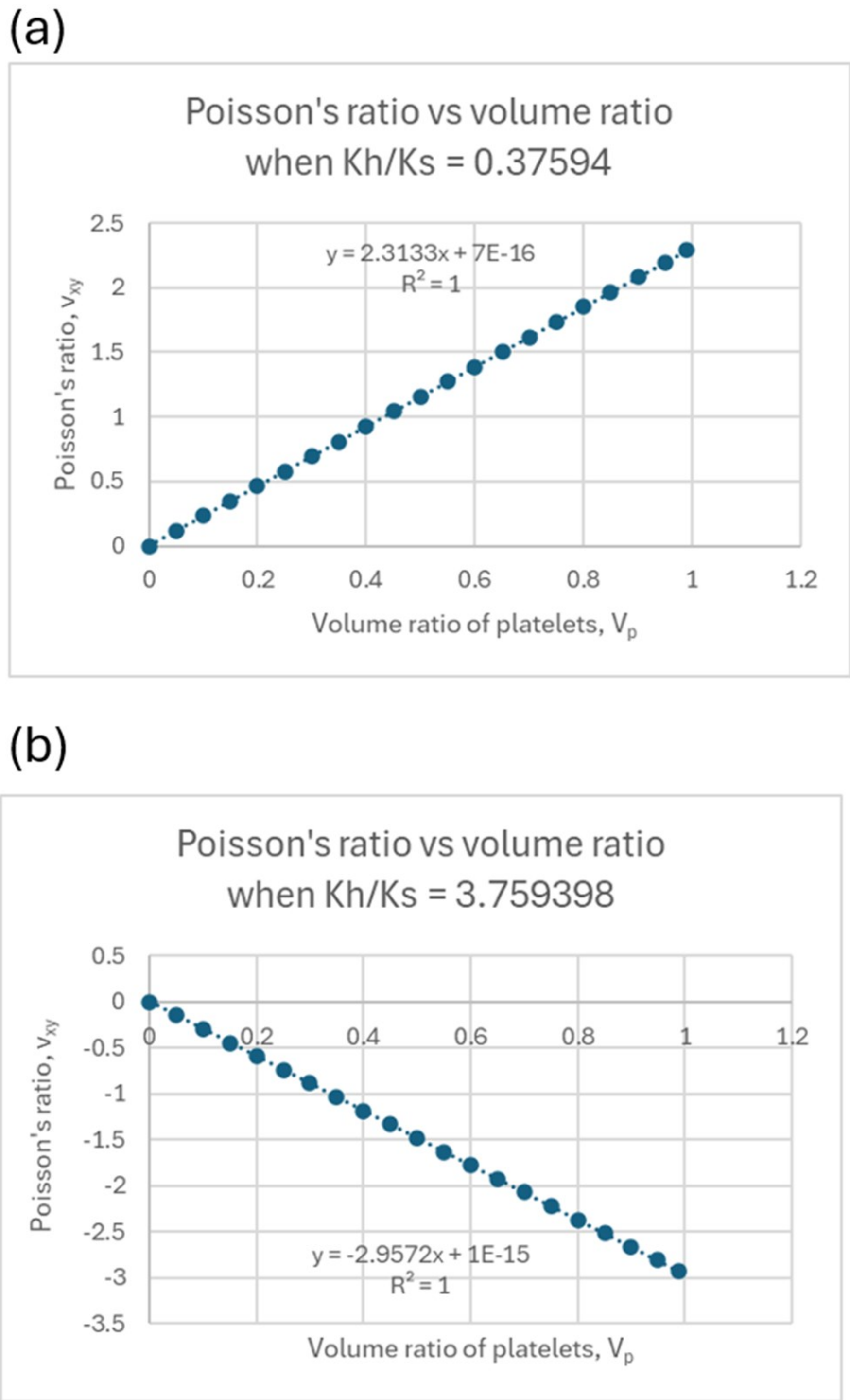

Figure 105: Poisson's ratio versus volume ratio of the platelets with the standard parameters set in Table 18.

(a) $\frac{Kh}{Ks}$ = 0.37594 and (b) $\frac{Kh}{Ks}$ =3.75998

To compare the results, longitudinal strain versus Poisson's ratio was plotted in Figure 107, and longitudinal strain versus transverse strain in Figure 106. The parameters used were from Wang & Boyce (2010), Table 18.

The assumptions made include an isotropic material so that G_{rib} can be determined from the standard expression found in equation (4), which is mentioned again at the beginning of this sub-section. The yield transition was considered to be approximately $\varepsilon_x^T \sim 0.0012$ from the experimental data of Song et al. (2008). At the yield transition, the shear modulus, $G_{rib,}$ remained constant as the pre-yield value, but Young's modulus, E_{rib}, was reduced to 0.33GPa (by a factor of 10).

Previously, the junctions connecting the mortar to the brick were assumed to be fixed, considering the fact that the brick is a rigid body. G_{rib} remaining constant reflects that. G_{rib} governs the strut's rotation and is determined by the junction between the strut and the brick. The junction can be expected to be a mixture of polymer and ceramic and to be thicker than the rib along its length. In this scenario, yielding is expected to occur along the length of the strut rather than at the junction. Consequently, the values of Kh/Ks before and after the yield transition were 0.37594 and 3.75998, respectively. The charts in Figure 106 and Figure 107 show the yield transition where Kh/Ks is 0.37594 before the yield and Kh/Ks is 3.75998 after the yield transition strain of $\varepsilon_x^T = 0.0012$.

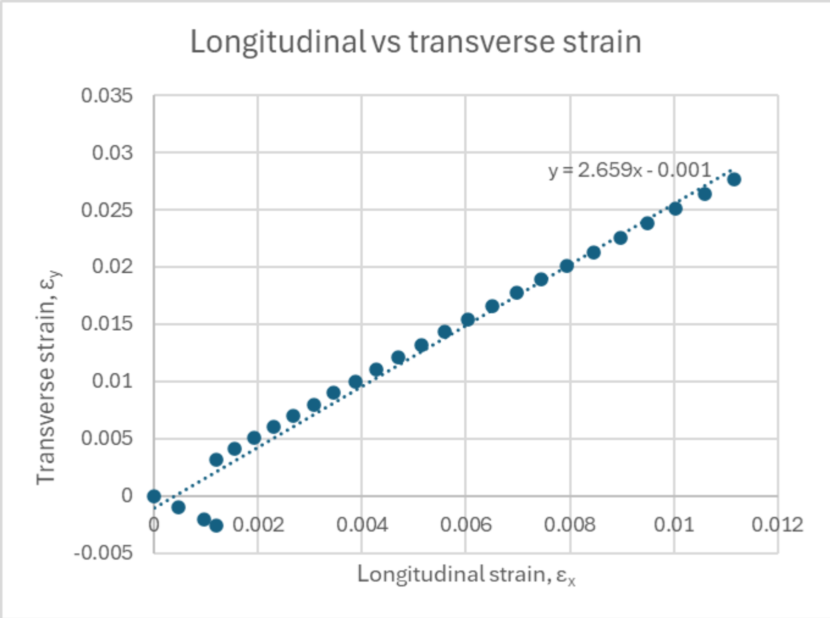

Figure 106: Transverse versus longitudinal strain, showing a transition before and after the yield at transition strain of $\varepsilon_x^T = 0.0012$.

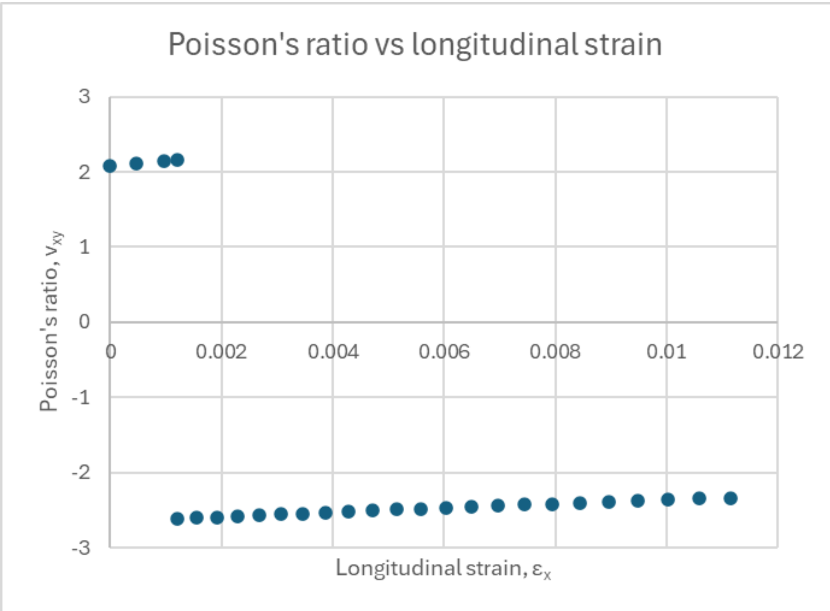

Figure 107: Poisson's ratio versus longitudinal strain, showing a transition before and after the yield at transition strain of $\varepsilon_x^T = 0.0012$.

The data plots in the figures above enable a direct comparison with the data found in the literature, and this can be seen in Figure 108.

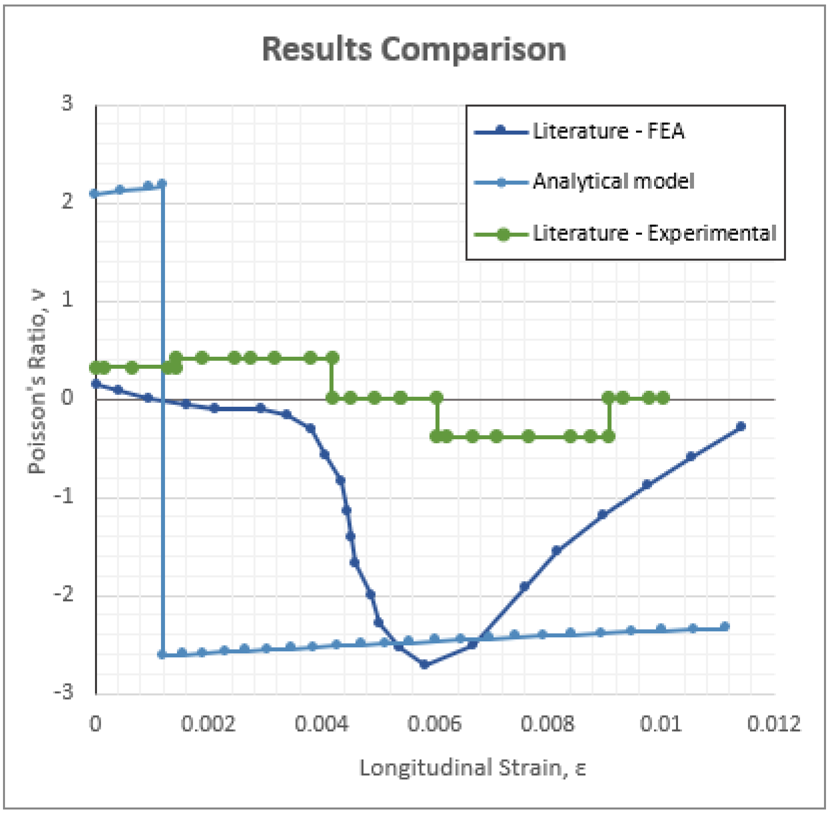

Figure 108: Comparison of data; 'Literature – Experimental' is a data by Song et al.; 'Literature – FEA' is data obtained by Wang & Boyce.

Song et al.'s data, Figure 50 on page 91, was used to obtain the yield transition strain, and it shows the reduction of Young's modulus by a factor of ~10. Figure 108 shows the Poisson's ratio versus longitudinal strain from Song et al., denoted as Literature – Experimental. This data shows that nacre has a positive Poisson's ratio for the immediate strains post-yield before it shows NPR. It then again returns to the near-zero value at higher strains.

Mechanism 1 analytical model shows the transition from the positive PR to NPR as the strain increases but associates this transition with the yield strain rather than post-yield, this corresponds to the geometry changes shown in Figure 103. The analytical model fails to predict the PR returning to near zero value at the highest strains within the range. The mechanism 1 model can predict finite positive Poisson's ratio at low strain, which is consistent with the experimental data by Song et al., whereas the Wang & Boyce models predict near-zero Poisson's ratio.

Wang and Boyce showed, Figure 52 on page 95, a correlation between the increased volume ratio of the platelets and the increase in the magnitude of maximum PR. This is consistent with the mechanism 1 model, as shown in Figure 105. The Wang & Boyce model predicts the return of Poisson's ratio towards zero at the highest strains, consistent with Song at al.'s experimental data, whereas the mechanism 1 model does not.

It is worth noting that the exact comparison cannot be made as the mechanism 1 analytical model is a two-dimensional extrusion compared to a FEA simulation which is a hypothetical structure, and experimental data which is a three-dimensional biological structure. The two data sets used for the comparison are, therefore, significantly different to the proposed topology, hence the similarity in patterns of behaviours is considered over the exact match.

Mechanism 2

Mechanism 2, also referred to as the concave model, which was inspired by Espinosa et al., is analysed below. For this analysis, its geometry was utilised, and along with trigonometry, a maximum deformation before permanent deformation and failure will occur. This was assumed to occur once the deformation in the x-direction has reached half the length of the brick or $\frac{L}{2}$ as seen in Figure 109.

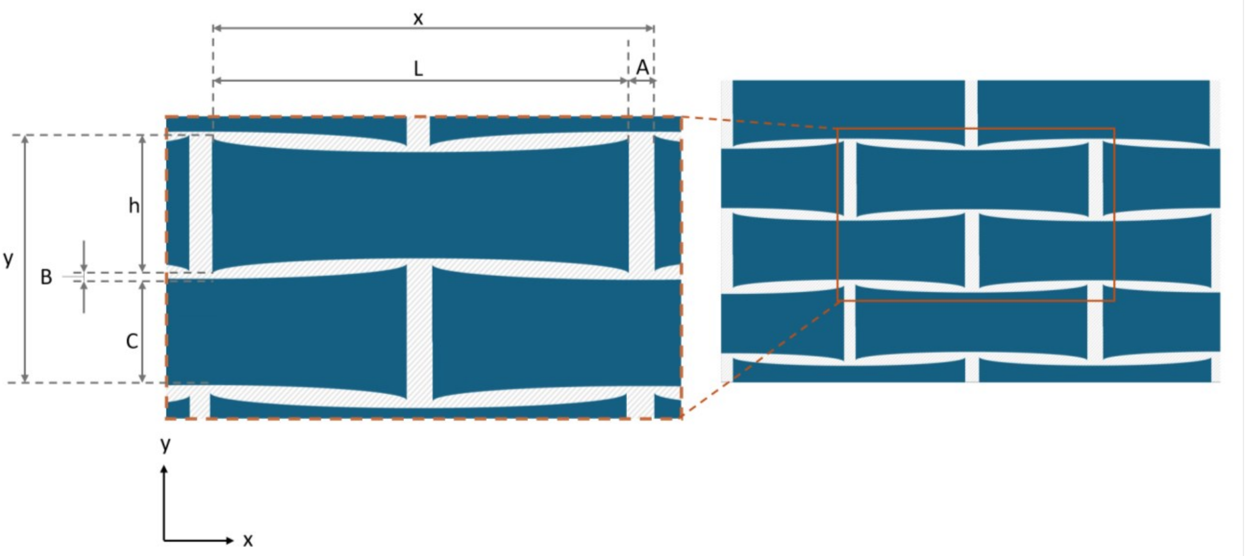

Figure 109: Diagram of the concave-shaped bricks where the gaps denoted as A and B are the polymer matrix

Unit cell length in the x-direction is given by

$$x = L + A$$

(100)

Unit cell length in the y-direction is given by

$$y = h + 2B + C$$

(101)

It is assumed that C, L and h do not deform as the brick is rigid. However, A and B will change as the polymer matrix (mortar) will deform.

The model has been simplified to assume that the gaps representing the polymer matrix do allow for frictionless deformation (A and B do not affect the deformation of the bricks).

Hence, the deformation in the x-direction is entirely dependent on the deformation of A. Strain in the x-direction, ε_x, is given by:

$$\varepsilon_x = \frac{\delta x}{x} \tag{102}$$

where we know that the change in A gives the change in x,

$$\frac{\delta x}{\delta A} = 1 \tag{103}$$

Resulting in strain in the x-direction equal to:

$$\varepsilon_x = \frac{\delta A}{L + A} \tag{104}$$

Strain in y-direction, ε_y, is given by:

$$\varepsilon_y = \frac{\delta y}{y} \tag{105}$$

Similarly to A, deformation in y-direction is solely dependent on the deformation of B:

$$\frac{\delta y}{\delta B} = 2 \tag{106}$$

which gives the strain in y-direction, ε_y, as:

$$\varepsilon_y = \frac{\delta y}{\delta B} \times \frac{\delta B}{y} = \frac{2\delta B}{h + 2B + C} \tag{107}$$

This results in the overall Poisson's ratio:

$$\upsilon_{xy} = -\frac{\varepsilon_y}{\varepsilon_x} = -\frac{\frac{2\delta B}{h + 2B + C}}{\frac{\delta A}{L + A}} = -\left(\frac{2\delta B}{h + 2B + C} \times \frac{L + A}{\delta A}\right) = -\frac{\delta B}{\delta A}\frac{2(L + A)}{(h + 2B + C)}$$

In simple terms, Poisson's ratio is: $\upsilon_{xy} = -\frac{\delta B}{\delta A}\frac{2(L+A)}{(h+2B+C)}$

(108)

The deformation is expected to occur in stages: neutral stage, where there is no change in B: $\delta B = 0$; climbing stage, when the deformation is changing, and cross-section is increasing; and maximum deformation stage when deformation in the x-direction reaches $\frac{L}{2}$ distance from a neutral position.

Fully Densified model

Another approach assumes that the model is fully densified. A and B are both equal to zero when the model is in a neutral position.

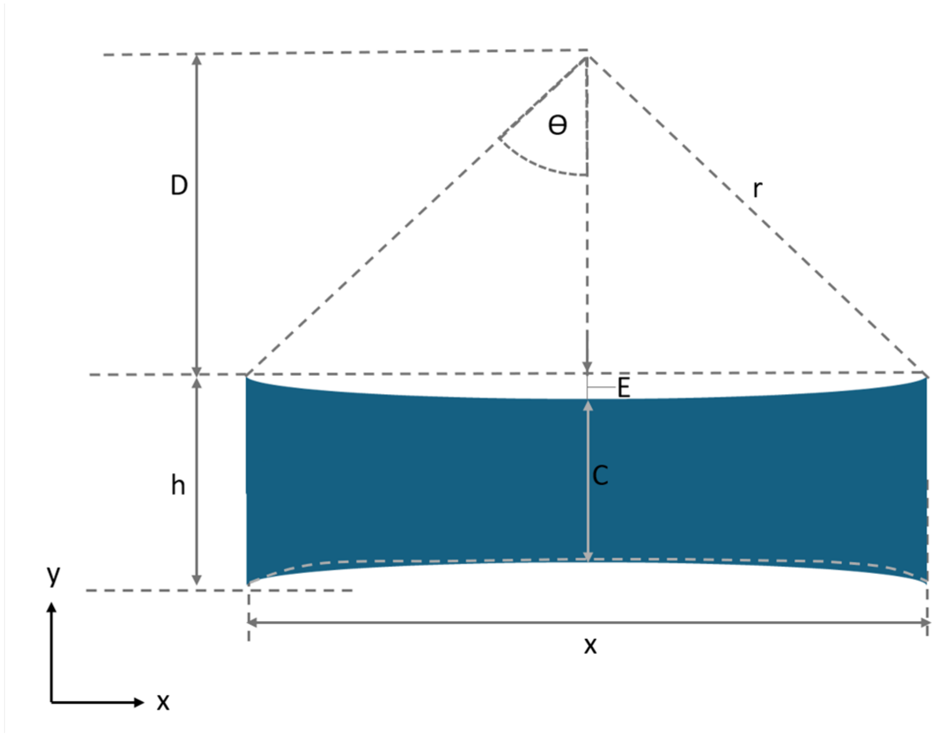

Figure 110: Parameters of the fully densified model.

In the fully densified model, we can use the curvature of the concave brick to determine the deformation.

If we assume that the curve of the concave surface is a section of a circle, then the unit length in the x-direction is equivalent to the chord length

$$x = 2(r \sin \Theta)$$

(109)

The arc length is given by: $= \left(2r\pi \frac{\theta}{180}\right)$

(110)

Unit length in the y-direction is $y = h + C$

(111)

Additional parameters are required to utilise the curvature of the concave surface using the section of the circle. D is the distance from the highest point of the concave surface to the centre of the circle in the vertical direction, which can be worked out using radius, r.

$$D = r \cos \Theta \tag{112}$$

E is the difference in length between radius and D, and also a height difference between the lowest and highest point of the concave surface, which can also be described as the maximum deformation in the y-direction.

$$E = r - D = r - r \cos \Theta \tag{113}$$

C is the cross-section of the concave brick at the centre, which is where the concave brick is the thinnest. It can be found by using the height of the brick at the thickest point (edges) and the height difference between the lowest and highest point of the concave surface, E.

$$C = h - 2E = h - 2(r - r \cos \Theta) \tag{114}$$

Therefore, the unit length in the y-direction is given by

$$y = h + h - 2(r - r \cos \Theta)$$

Which can be simplified to

$$y = 2(h + r \cos \Theta - r) \tag{115}$$

For the partially extended model, the unit length in the x-direction:

$$x = L + A$$

(116)

Unit length in y-direction:

$$y = h + C + 2B$$

(117)

As we know that $x = L + A$ as seen in equation (116), we can rearrange it to get the value of A,

$$A = 2r\sin\theta$$

(118)

And B can be determined from $y = h + C + 2B$, as seen in equation (117), to give

$$B = r(1 - \cos\theta)$$

(119)

Using the trigonometry, radius, r is given by:

$$r = \left(\frac{A}{2\sin\theta}\right)$$

(120)

Now that all the required parameters are present, variables A and B can be combined into a single equation:

$$B = \left(\frac{A}{2\sin\theta}\right)(1 - \cos\theta) = \frac{A(1 - \cos\theta)}{2\sin\theta}$$

(121)

This shows that the deformations in the x- and -y directions are dependent on each other.

Deformation in the x-direction is given by:

$$\frac{dA}{d\theta} = \frac{\partial}{\partial\theta}(2r\sin\theta) = 2r\cos\theta$$

(122)

Deformation in the y-direction is given by:

$$\frac{dB}{d\theta} = \frac{\partial}{\partial\theta}\big(r(1-\cos\theta)\big) = r\sin\theta$$

(123)

Resulting in the combined deformation of

$$\frac{dB}{dA} = \frac{dB}{d\theta} \div \frac{dA}{d\theta} = \frac{dB}{d\theta} \times \frac{d\theta}{dA} = r\sin\theta \times \frac{1}{2r\cos\theta} = \frac{r\sin\theta}{2r\cos\theta} = \frac{\tan\theta}{2}$$

(124)

We can simplify this problem by assuming that $\frac{\delta x}{\delta A} = 1$ and $\frac{\delta y}{\delta B} = 2$

This assumption gives:

$$\delta x = \delta A$$

(125)

$$\delta y = 2\delta B$$

(126)

We can use the two formulations above to create the expression which reflects changes in deformation in both the x- and y- direction in a single equation:

$$\frac{\delta y}{\delta x} = 2\frac{\tan\theta}{2}$$

Then, we can express changes in y-direction as a function of x:

$$\delta y = 2\frac{\tan\theta}{2}\delta x$$

which can be simplified to:

$$\delta y = \tan\theta\,\delta A$$

(127)

From this, we can formulate the expression for Poisson's ratio, υ_{xy} :

$$\upsilon_{xy} = -\frac{\varepsilon_y}{\varepsilon_x} = -\frac{dy}{y} \times \frac{x}{dx} = -\frac{\tan\theta\,\delta A}{y} \times \frac{x}{\delta A} = -\frac{\tan\theta\, x}{y}$$

Once simplified, it results in:

$$\upsilon_{xy} = -\frac{\tan\theta\, x}{y} \tag{128}$$

where $B = \frac{A(1-\cos\theta)}{2\sin\theta}$ and $A = 2r\sin\theta; \theta = \sin^{-1}\left(\frac{A}{2r}\right)$.

As mentioned previously, the physical limit for the angle, θ, is:

$$0 < \theta < 90°$$

As the angle tends towards the value of 90 degrees, the total value of the brick's curvature tends towards 180 degrees, which is a point after which further increase is no longer possible as it would break the physical constraints of the brick's geometry. Furthermore, as equations are a trigonometrical function of the tangent, an angle of 90 degrees will result in an infinite value. Hence, the analysis will be done with an angle of up to an angle of 90 degrees.

After a parametric study was carried out, a physical limit for A has been determined to be:

$$A_{max} = 2r\sin\theta = 2r \tag{129}$$

Results for Mechanism 2 - Parametric Analysis

A parametric study was carried out where the radius of the curvature of the concave was varied. For the analysis in this section, the control variables were the height of the brick (h), length (L), and radius (r), which are specified in Table 19.

Length, L	**Height, h**	**Radius, r**
10	*1*	*25*

Table 19: Variables that remained unchanged throughout the analysis performed to obtain results in Figure 111.

The dependent variable was the deformation in the y-direction. Furthermore, the independent variable was the angle, θ, which directly affects the deformation in the x-direction. θ was in the range $5 \leq \theta \leq 85$.

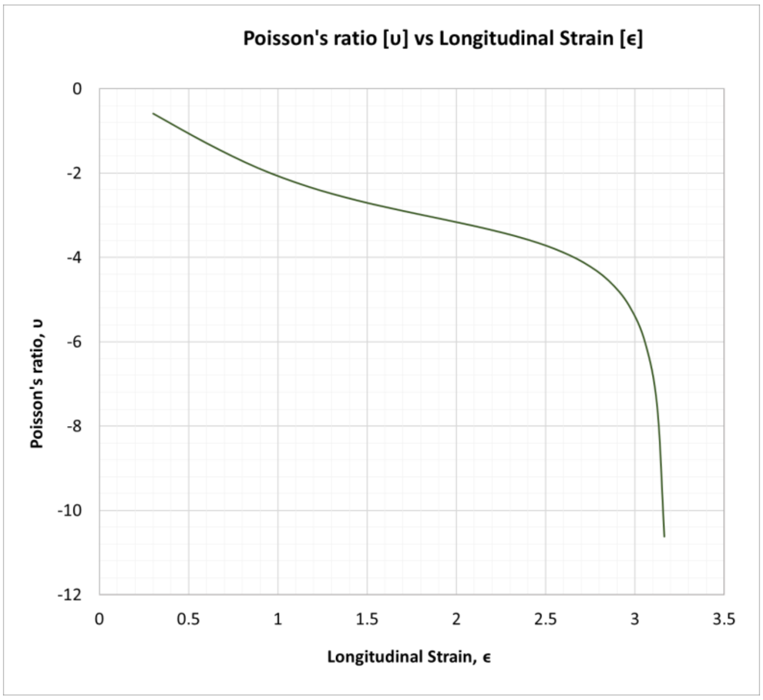

Figure 111:Results of the analysis using the variables specified in Table 19 for an angle range of 5 ≤θ ≤85

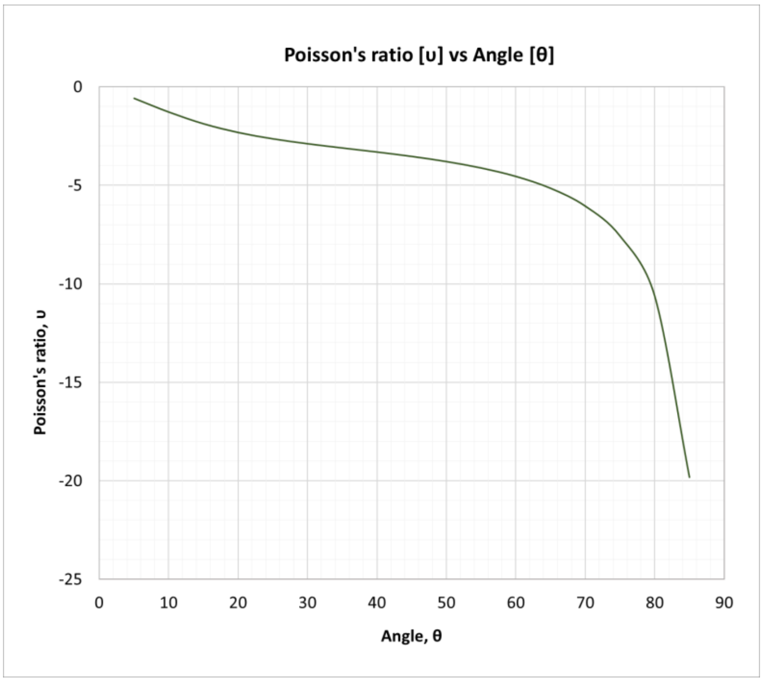

Figure 112: Results of the analysis using the variables specified in Table 19 for an angle range of 5 ≤θ ≤85

The parametric study was performed to show the dependencies between different radii and the Poisson's ratio. Figure 113 shows that the Poisson's ratio is lower for the higher radii.

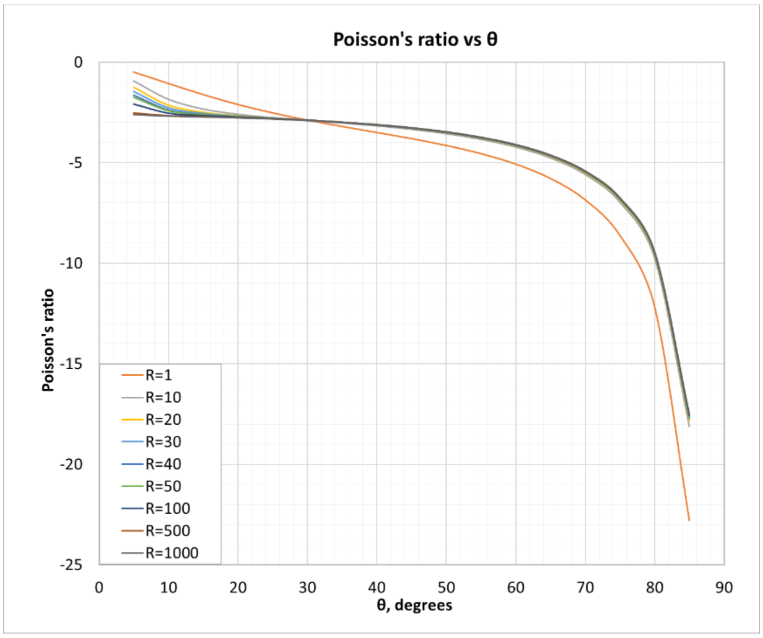

Figure 113:Comparison of the results of models with different radii for an angle range of 5 ≤θ ≤85, where h=0.1 and L=1

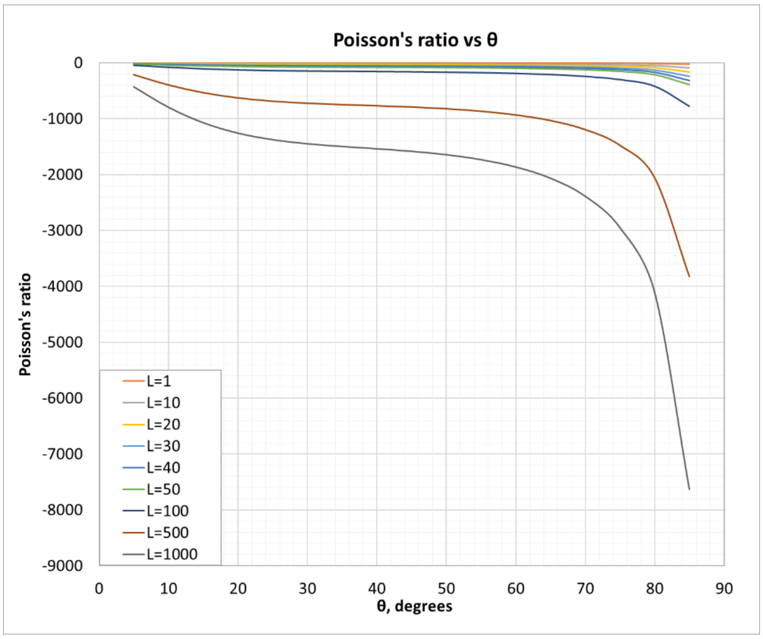

Figure 114: Comparison of the results of models with different lengths of platelet for an angle range of 5 ≤θ ≤85, where h=0.1 and r=1

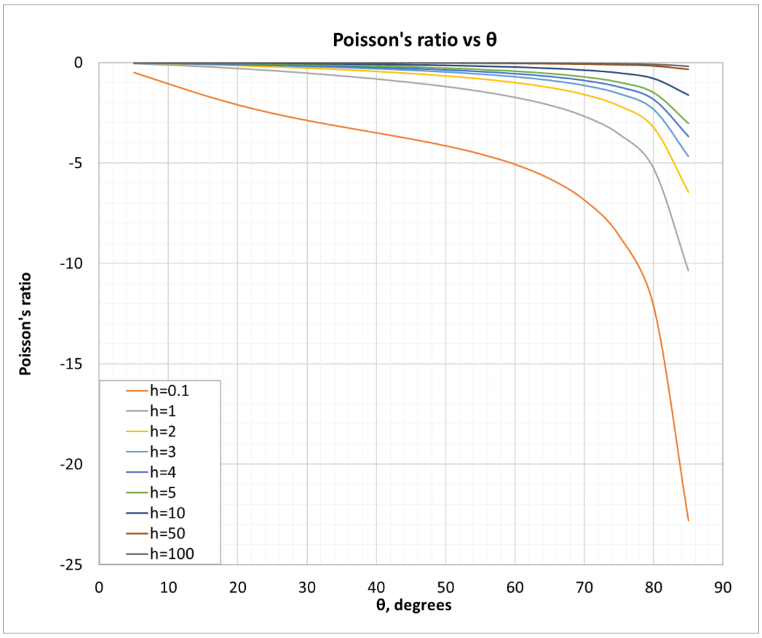

Figure 115: Comparison of the results of models with different heights of platelet for an angle range of 5 ≤θ ≤85, where L=1 and r=1

The parametric studies looked at the influence of changing the dimensions of the brick. Figure 114 and Figure 115 show the same pattern where the increase in the brick's length and height results in the decrease of Poisson's ratio with the higher angles. However, Figure 113 shows an interesting trend where all of the different radii cross each other at approximately 30 degrees. Then, the lowest radius reaches the lowest magnitude of the PR. Figure 114 shows that the higher the length of the brick, the lower the PR value. Figure 112 shows the opposite trend: the higher the height of the brick, the higher the magnitude of PR.

As perhaps expected, as the deformation starts from the neutral position of the brick and due to sustained curvature, all of the PR values are negative.

This mechanism fails to show the variability of strains present in the experimental data by Song et al., but it poses a good opportunity for enhancing NPR when considering the mechanical metamaterials.

Mechanism 3

Model inspired by Song et al. It shows a simplified version of the bridges, which are isosceles trapeziums stacked onto each other.

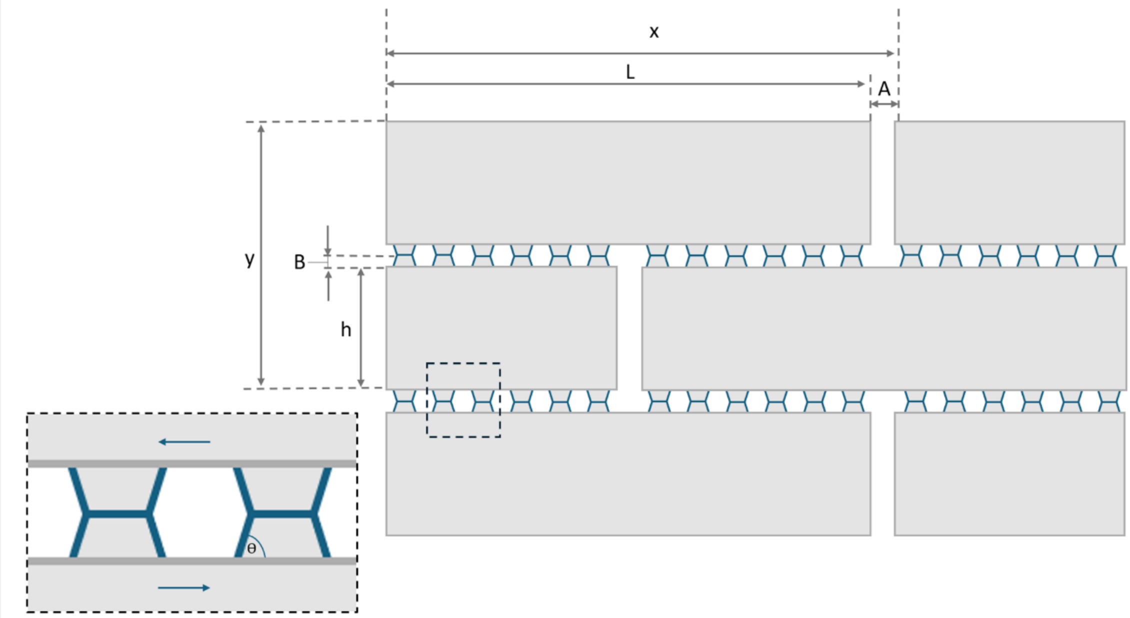

Figure 116: The figure represents a section of the brick-and-mortar structure with inter-linking mineral bridges in between the bricks

In this instance, the unit length in the x-direction is defined as the length of the brick and the gap between the bricks: $x = L + A$

(130)

The unit length in the y-direction consists of the height of two bricks and two gaps, which are made of four 'trapeziums' representing the bridges:

$$y = 2h + 4B$$

(131)

In the simplest terms, we can work out strain in x-direction with an assumption that change in x-direction is solely caused by the change in the gap width A:

$$\delta x = \delta A \text{ or } \frac{\delta x}{\delta A} = 1$$

(132)

As we know, strain in the x-direction is $\varepsilon_x = \frac{\delta x}{x}$, using previously defined values, we get $\varepsilon_x = \frac{\delta A}{L+A}$

Similarly to the above, we can use the gap in the y-direction to define that deformation, $\delta y = 4\delta B.$

Strain in y-direction is given by: $\varepsilon_y = \frac{\delta y}{y}$ which then can be re-written as $\varepsilon_y = \frac{2\delta B}{h+2B}$

Combining the two strain equations, we can find the Poisson's ratio,

$$\upsilon_{xy} = -\frac{\varepsilon_y}{\varepsilon_x} = \frac{\frac{2\delta B}{h+2B}}{\frac{\delta A}{L+A}} = -\frac{\delta B}{\delta A}\frac{2(L+A)}{(h+2B)}$$

Stages of deformation can be described as: neutral when there is no change in B for intact ridges or bridges that have failed but remain on top of each other during initial sliding: $\frac{\delta B}{\delta A} = 0$; post-breakage of the bridges and sliding of one bridge down the other when there is an initial reduction in cross-section: $\frac{\delta B}{\delta A} = -\tan\theta$; minimum deformation when the cross-section reaches a minimum and the bridges slide against the adjacent brick surface: $\frac{\delta B}{\delta A} = 0$; and increase in cross-section when there is Climbing over the broken bridges (disparities): $\frac{\delta B}{\delta A} = \tan\theta$.

These stages can be observed in Figure 117, which plots the results for the analysis, where the parameters found in Table 20 are used.

h	B	L	A	θ
0.225	0.025	2	0.015	53°

Table 20: Parameters used for the initial analytical study of Mechanism 3

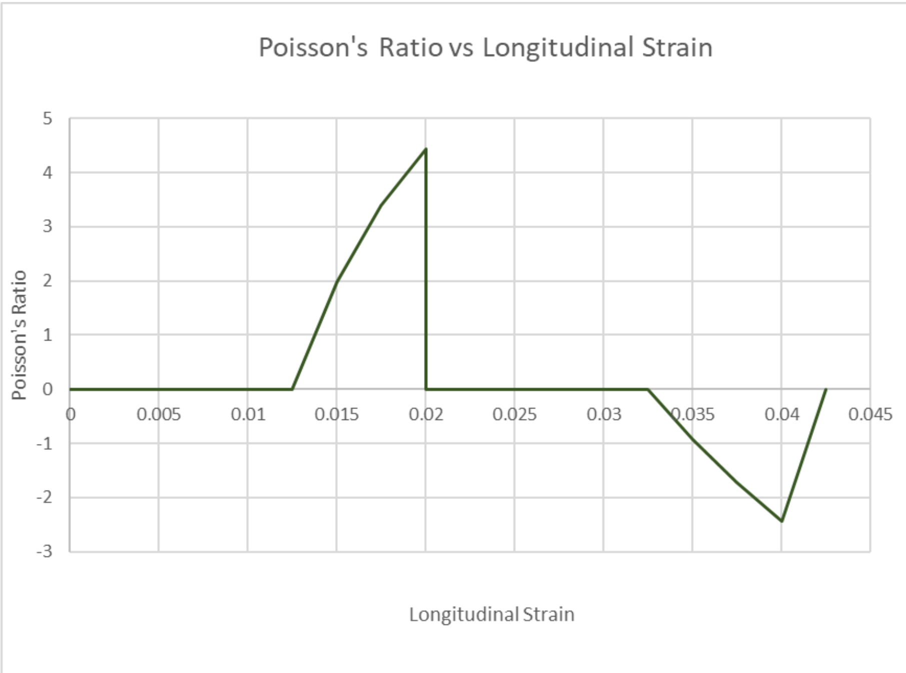

Figure 117: The results of the mechanism 3 analysis for the singular layer of the bridge when only $\frac{\delta B}{\delta A}$ is considered

Figure 118: Comparison of the results of models with different heights where L=2 and ϴ = 62

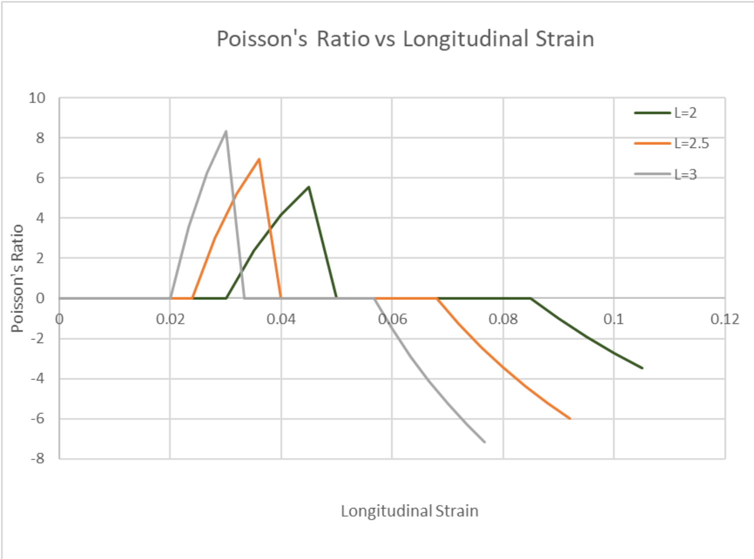

Figure 119: Comparison of the results of models with different lengths where h=0.225 and ϴ = 62

Figure 120: Comparison of the results of models with different angles where h=0.225 and L = 2

All of the parametric study results show the same trend of PR against longitudinal strain. Also, all of the studies show that if the PR has a higher positive peak, it also has a higher magnitude NPR. The shift in results in Figure 119 is due to the fact that the bridges were assumed to be in the same location and have the same width, meaning that the same amount of displacement for longer platelets resulted in lower strains; hence, the longer bricks had their peak at lower strain level.

This model replicates the Poisson's ratio moving from positive PR to NPR with the higher strains, as seen in the experimental data by Song et al. However, no yielding transition was observed. This shows the return of the NPR to positive PR at higher strains. With an assumption that the half-bridges would remain undeformed, the peak PR could likely be reached again. This mechanism poses a good opportunity for enhancing NPR when considering the mechanical metamaterials.

Chapter 5 FE Models and Analysis 2D Models

Mechanism 1

The work of Wang & Boyce inspires mechanism 1. As previously mentioned in the section on Mechanism 1 on page 93, the auxetic behaviour is said to be due to the platelets sliding and causing the shearing of organic matrices of polymeric microframes (Wang & Boyce, 2010), which can be found in Figure 121. The elastic fibre replicating that organic matrix is expected to buckle when a shear force is applied, creating an increase in the cross-section of the system over certain strains (Wang & Boyce, 2010).

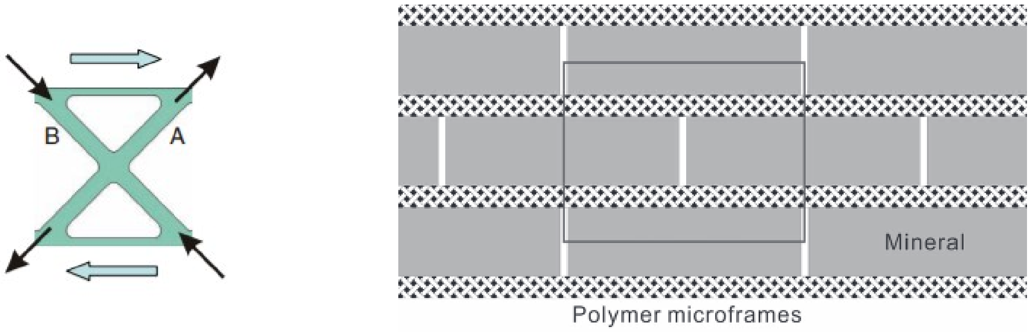

Figure 121: Left - individual unit set of the elastic matrix; Right - mineral platelet with elastic matrix in between (Wang & Boyce, 2010)

The model created and analysed in this chapter is a constituent of two materials, which, for simplicity, will be referred to as 'brick' and 'mortar'.

The Brick is a solid mineral with a high stiffness level, which, throughout the simulation, exhibits some slight deformation. The Mortar is a viscoelastic polymer, SU-8, truss microstructure, which is the leading cause of the deformation within the whole structure and hence is thought to be responsible for the Negative Poisson's ratio.

The model set-up

Material Properties

Material Properties were taken from Wang & Boyce and are presented in Table 21, and initially modelled as an elastic material. A comparison of materials can be found in 'Elastic Versus Hyperelastic Material Properties' on page 264.

	Brick	***Mortar***
Young's modulus, E (GPa)	100	3.3
Poisson's ratio, υ	0.33	0.33
Tensile yield strength, σ_{yield} (GPa)	2	0.1

Table 21: Material Properties used for the ANSYS model (Wang, Boyce, Wen, & Thomas, 2009) (Wang & Boyce, 2010)

Geometry

The Geometry was inspired by that used by Wang & Boyce from the visual standpoint. Individual dimensions and constraints were decided individually for the project. The scale was decided to represent a more accurate scale of the nacre microstructure, with an approximate unit length of the brick of 2µm with some variations to match the length of repeated units of mortar accurately. The height of the mortar was varied from 0.02µm to 0.12 µm to vary the volume ratios.

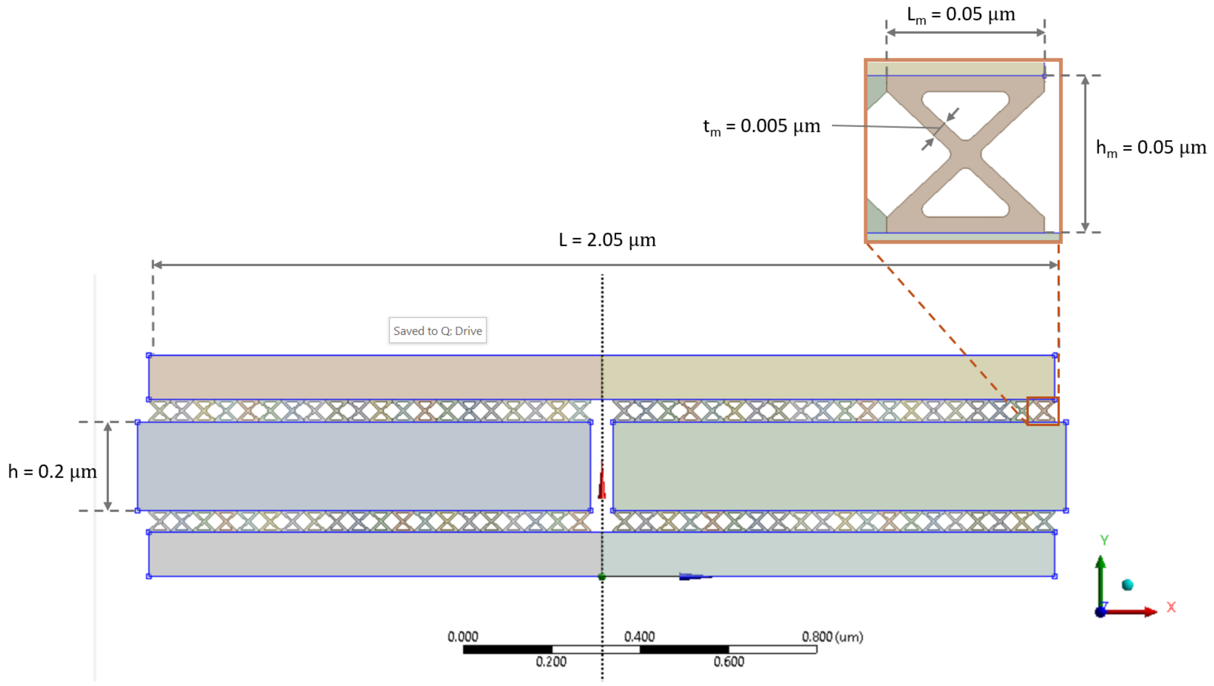

Figure 122: Geometry shown as a sketch in ANSYS DesignModeler for the structure consisting of 90% of the volume of brick (or 0.90 volume ratio).

Table 22 shows the dimensions for each volume ratio of platelets, using the same nomenclature as in Figure 122. The ratio was rounded to the nearest hundredth decimal point.

Volume Ratio, Vr	***Length of the brick, L [µm]***	***Height of the brick, h [µm]***	***Length of the unit of mortar, L_m [µm]***	***Height of the unit of mortar, h_m [µm]***
0.80	2.28	0.20	0.12	0.12
0.85	2.00	0.20	0.08	0.08
0.90	2.05	0.20	0.05	0.05
0.95	2.02	0.20	0.02	0.02

Table 22: The dimensions, as shown in Figure 122, for each volume ratio of brick-to-mortar

For the 2D model, the volume ratio was obtained using the surface areas of the bricks and the mortar:

$$Volume\ ratio, Vr = \frac{Surface\ area\ of\ the\ bricks}{Surface\ area\ of\ the\ mortar + Surface\ area\ of\ the\ bricks} \tag{133}$$

The surface area of the mortar was found using ANSYS to simplify the calculation.

The geometry was created in ANSYS DesignModeler and imported to ANSYS Static Structural. The analyses in this chapter were set to 2D using ANSYS' Advanced Geometry Options.

Connections

Once the geometry was established as described in the previous section and imported into ANSYS Static Structural, the two bodies of different materials, brick and mortar, had to be connected.

To allow for the full deformation of the mortar, the only connections put in place were the bonds at the edges directly in contact with the brick, as found in Figure 123. The bonded connection allows no sliding or separation of the faces or edges. It resembles the adhesion of the bodies as if they were glued together (ÖZGÜN, 2021). It allows for a linear solution as the contact area between the bodies will remain unchanged.

Generally, in ANSYS, a soft/fine mesh body tends to be set as a 'contact body', and a rigid/coarse mesh body tends to be set as a 'target body' (ANSYS, Inc., 1994). Due to the bonded nature of the geometry, it was considered to be negligible and the brick was set as a 'contact body', and the mortar was set as a 'target body'.

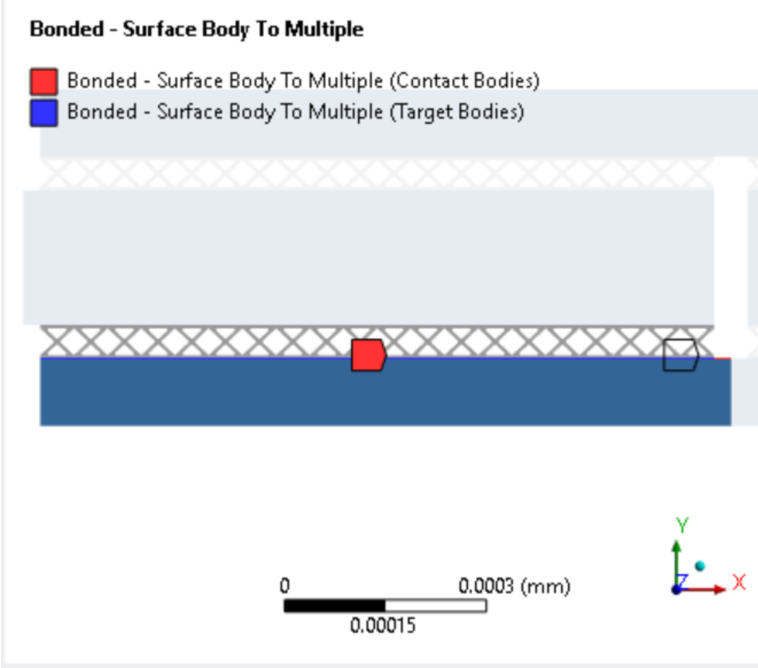

Figure 123: A section showing a bonded connection between the surfaces. Red: contact body; Blue: target body

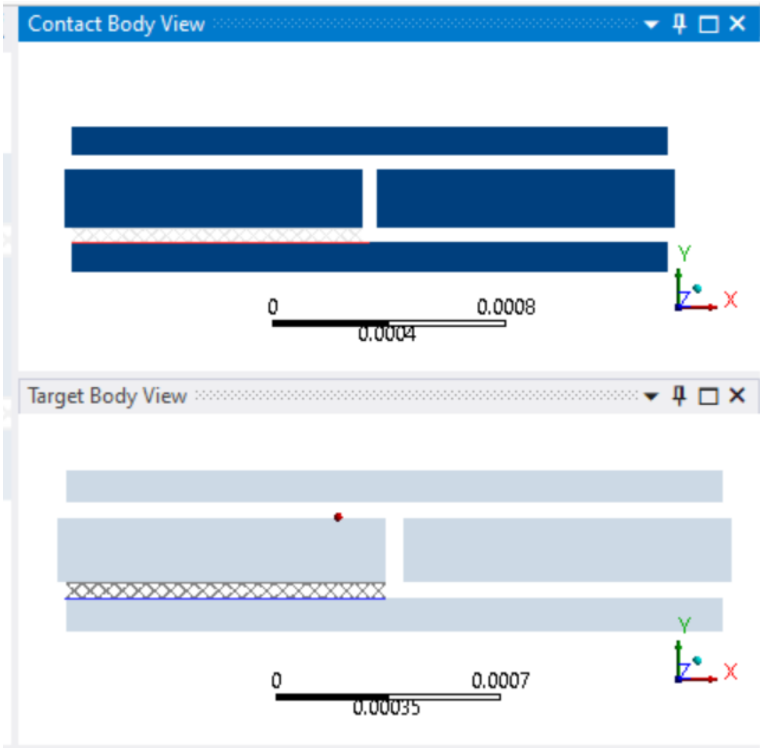

Figure 124: The two windows show the (Top) contact body, which is assigned to the brick, and the (Bottom) target body, which is assigned to the mortar.

Mesh

Individual components of the structure were set to have different meshes. The brick, which is much more rigid and is expected to have a lower level of deformation, had a larger quadrilateral mesh, whilst the mortar, which was expected to have a more significant deformation, had a smaller mesh size and triangular mesh.

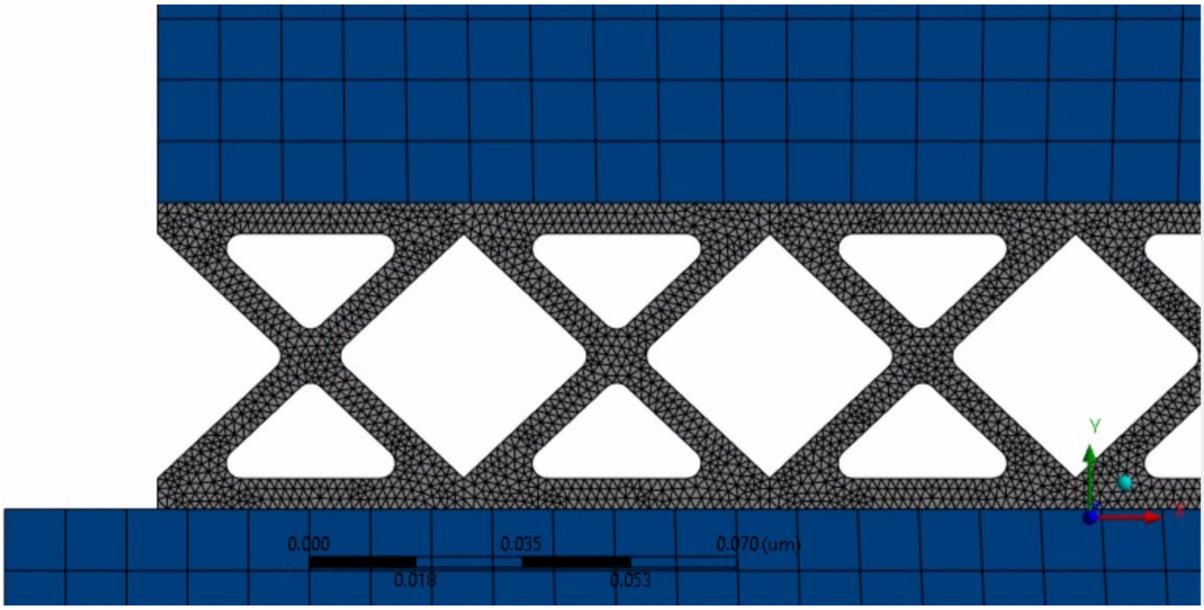

Figure 125: Mesh of the model with the 0.90 brick volume ratio; brick has a quadrilateral mesh, and mortar has a triangular meshing.

The example found in Figure 125 shows the model with the 0.90 brick volume ratio; the brick has a face quadrilateral mesh with an element sizing of 0.02µm, and the mortar has a finer triangular mesh with an element size of 0.001µm.

Table 23 shows different mesh sizes and types depending on the volume ratio. The meshing settings were intended to be kept as similar as possible throughout the different analyses, using the same element type for bricks and mortars.

Volume	Mortar Element Type	Mortar Element Size [μm]	Number of units of mortar	Brick Element Type	Brick Element Size [μm]	Total Number of Elements	Total Number of Nodes
0.80	Triangular	0.0040	36	Quadrilateral	0.005	32800	76624
0.85	Triangular	0.0025	48	Quadrilateral	0.005	36080	116664
0.90	Triangular	0.0015	80	Quadrilateral	0.010	84984	197792
0.95	Triangular	0.0008	200	Quadrilateral	0.010	140728	330632

Table 23: The summary of mesh elements and types for mortar and brick for each volume ratio, with the total number of nodes and elements

The appropriate meshing size was found during the convergence study, which is found in the section 'Mesh comparison study'. The meshing element generated was PLANE183 for the surface models, which is a 2D 6- or 8-node element for triangular and quadrilateral element types, respectively. PLANE183 elements have quadratic displacement behaviours, or in other terms, their element order is quadratic.

Contact elements were CONTAC172, and Target elements were TARGE169. All of these elements have been previously mentioned in the section '2D Meshing' on page 137.

Boundary Conditions

Three boundary conditions were set in place for the model: displacement, fixed support, and remote displacement.

Fixed support (A) on the left edge of the model and Displacement (B) in the x-direction on the right edge of the model were used to replicate the shear and tensile stress on the model, where the displacement magnitude was varied to obtain a range of results. Remote displacement (C) does not allow the central bricks to move

in the y-direction and constrains the out-of-plane rotation, ensuring that any deformation is solely 2D, Figure 126.

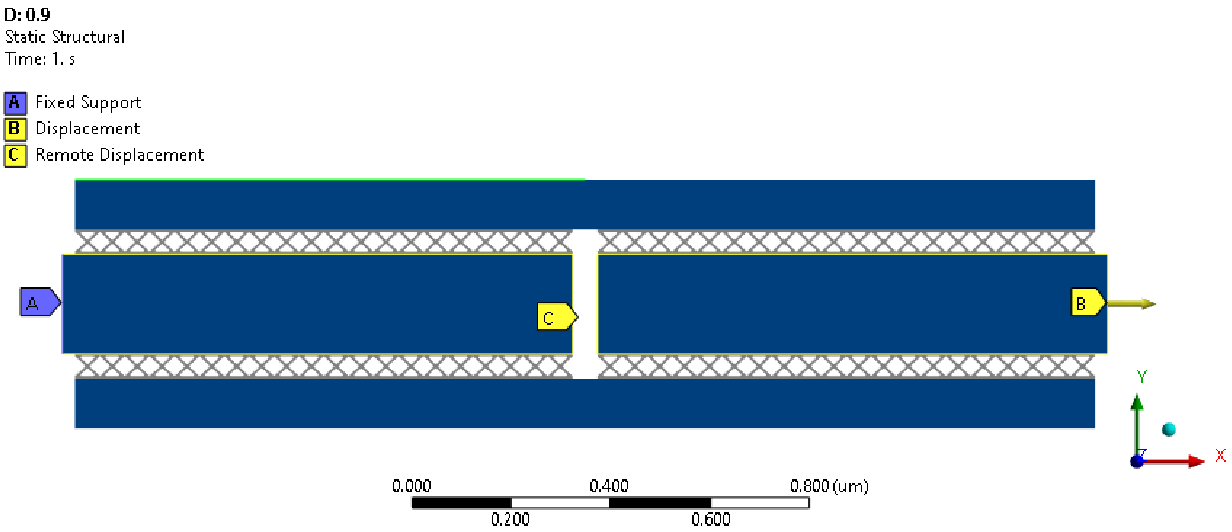

Figure 126: Boundary conditions applied to the model; (A) Fixed Support applied to the left side of the model; (B) Displacement applied to the right side of the model; (C) Remote Displacement applied to the two central bricks to constraint any rotation in out-of-plane direction and deformation in y-direction.

Solution

Analysis settings were changed to allow for large deflection.

Probes were used on each side of the model to study the deformation in the x- and y-direction. Probes 1 and 2 were used to find deformation in the y-direction, and Probes 3 and 4 were used to find deformation in the x-direction, which was equivalent to the displacement applied.

To find the results, the original coordinates were noted, and then the deformation was found through the simulation, which allowed us to obtain the new coordinates.

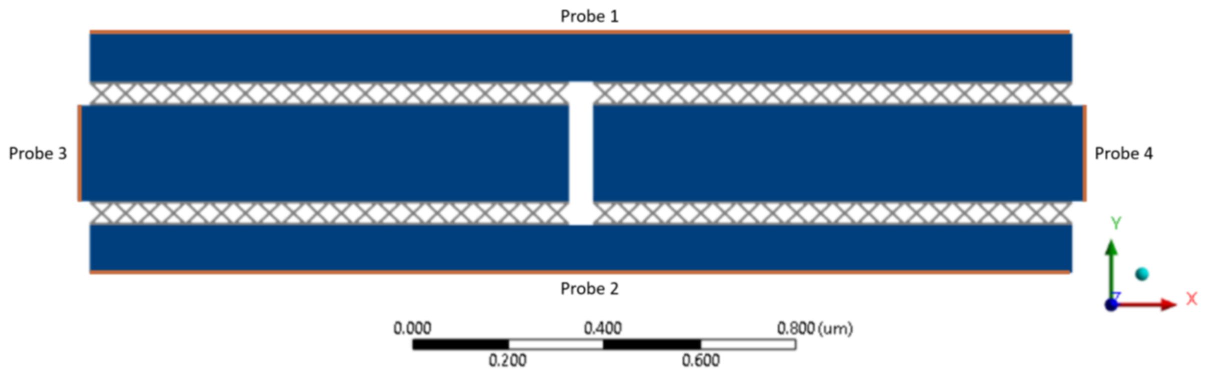

Figure 127: Probes placement on the model

Using original and new coordinates, the distance between each was found, which allowed the calculation of change in length, hence finding the value of Poisson's ratio. It is the same calculation method as previously described in Chapter 3. An example of the 0.90 volume ratio model for when approximately 0.02% strain was applied is shown below.

Step 1: Identifying original coordinates in relevant directions, as shown in Table 24.

	Original coordinates		**Deformation [µm]**		**Coordinates post-deformation**	
Probe number	**x**	**y**	**x**	**y**	**x**	**y**
Probe 1		0.500		0.000055249		0.500080626
Probe 2		0.000		0.000080626		0.000055249
Probe 3	-0.025		0.0000		-0.0250	
Probe 4	2.075		0.0005		2.0755	

Table 24: The probes and their original coordinates, the deformation at each probe, and post-deformation coordinates.

Step 2: Finding undeformed lengths of the model in x- and y-direction, as shown in Table 25.

$$Length, L_{Total,0} = Probe\ 4 - Probe\ 3 = 2.075 + 0.025 = 2.10\ \mu m$$

$$Height, h_{Total,0} = Probe\ 1 - Probe\ 2 = 0.500 - 0.000 = 0.50\ \mu m$$

Step 3: Measuring the deformation in each direction, example written in Table 24. Note that the deformation for Probe 3 remains 0 as it is a fixed support, and Probe 4 shows the applied displacement.

Step 4: Adding the deformation to the original coordinates to find post-deformation coordinates, as shown in Table 24.

Step 5: Calculating the lengths post-deformation, Table 25.

$$Length, L_{Total,1} = Probe\ 4 - Probe\ 3 = 2.0755 + 0.025 = 2.1005\ \mu m$$

$$Height, h_{Total,1} = Probe\ 1 - Probe\ 2 = 0.500080626 - 0.000055249$$
$$= 0.500025377\mu m$$

The original distance between the probes		Distance between the probes post-deformation	
Length, $L_{total,\,0}$ [μm] (= Probe 4 – Probe 3)	2.10	**Length, $L_{total,\,1}$ [μm]** (= Probe 4 – Probe 3)	2.100500000
Height, $h_{total,\,0}$ [μm] (= Probe 1 – Probe 2)	0.50	**Height, $h_{total,\,1}$ [μm]** (= Probe 1 – Probe 2)	0.500025377

Table 25: Distance between the probes before and post-deformation

Step 6: Using the original lengths and deformed lengths, strains in both directions were found

$$\varepsilon_x = \frac{L_{Total,1} - L_{Total,0}}{L_{Total,0}} = \frac{2.100500000 - 2.10}{2.10} = \frac{0.0005}{2.10} = 0.000238095$$

$$\varepsilon_y = \frac{H_{Total,1} - H_{Total,0}}{H_{Total,0}} = \frac{0.500025377 - 0.50}{0.50} = \frac{0.000025377}{0.50} = 0.000050754$$

Step 7: The strains were then used to find the Poisson's ratio of the structure

$$\nu_{xy} = -\frac{\varepsilon_y}{\varepsilon_x} = -\frac{0.000050754}{0.000238095} = -0.213$$

This method was repeated for all strains measured and for each model previously discussed.

Mechanism 1 Results

The results obtained showed a variable Poisson's ratio with increasing strains across all of the models, as seen in Figure 128. The lowest Poisson's ratio was achieved with the 0.90 volume ratio model. However, the 0.95 volume ratio model likely had similar potential due to the size of the model and its fine mesh, which accommodated a much higher number of individual mortar unit cells, making it computationally challenging to obtain accurate results. The results for the 0.95 volume ratio model above 0.01 strain failed to reach the 5% convergence limit and hence are excluded from the plots below.

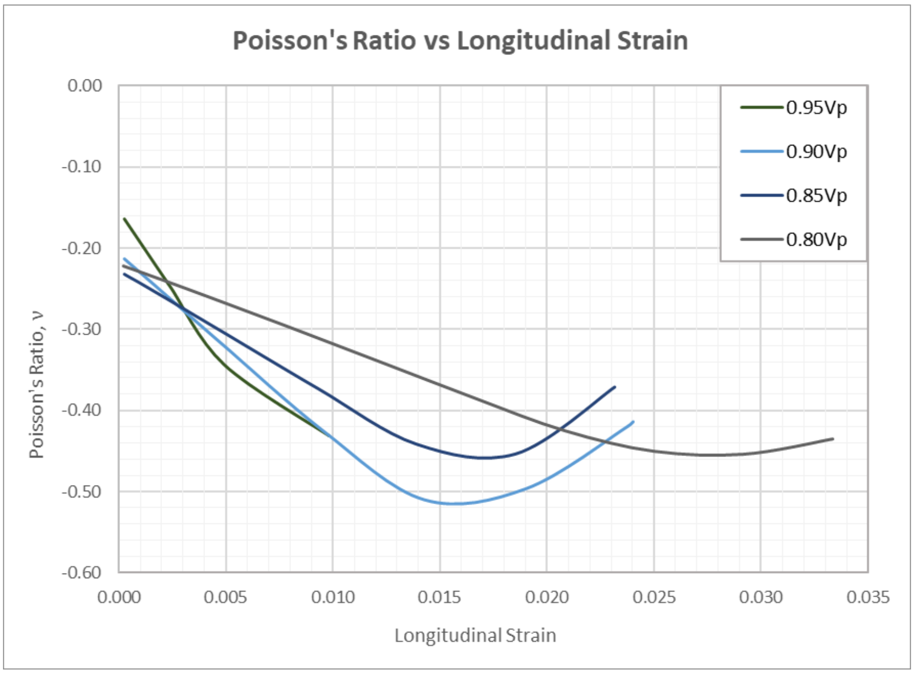

Figure 128: The results for the four models with different volume ratios showing Poisson's ratio against Longitudinal Strain

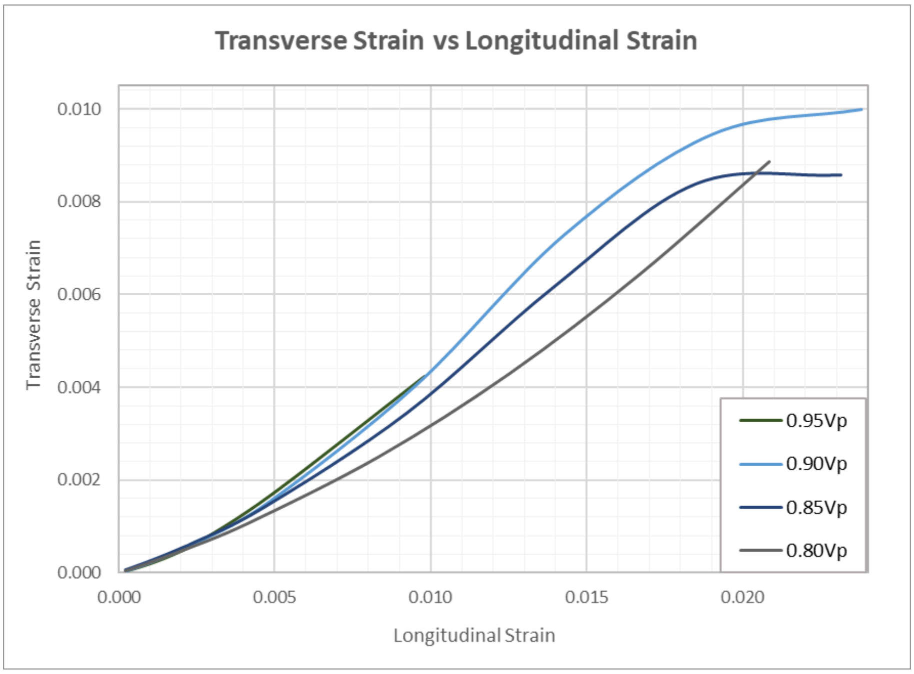

Figure 129: The results for the four models with different volume ratios showing Transverse Strain against Longitudinal Strain

Figure 130 shows the Equivalent Stress (Von Mises) result for the 0.90 volume ratio model, which had the displacement of 0.0005µm applied. This displacement is equivalent to approximately 0.02% strain. The highest stress is around the centre of the model, where the gap between the bricks is. However, the key output of interest is an observation of the struts and their deformation.

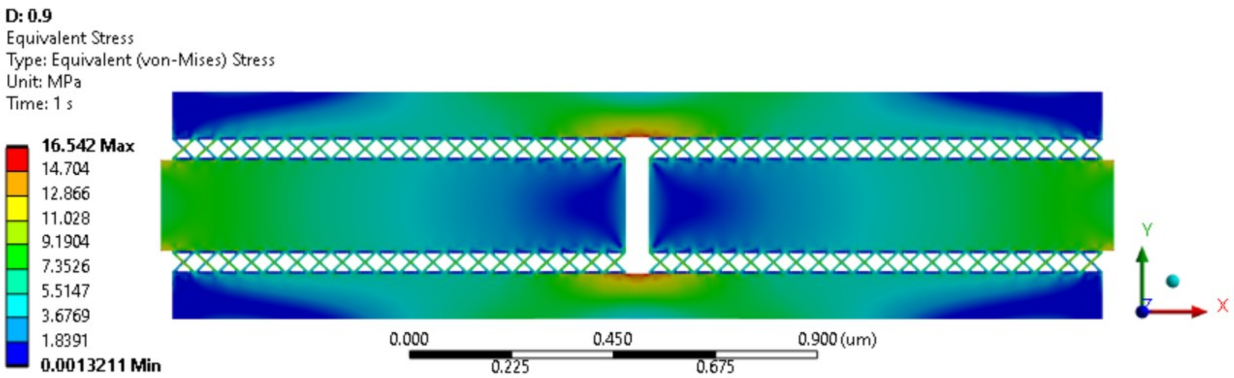

Figure 130: The Equivalent Stress (von Mises) for the displacement of 0.0005µm applied to the 0.90 volume ratio model.

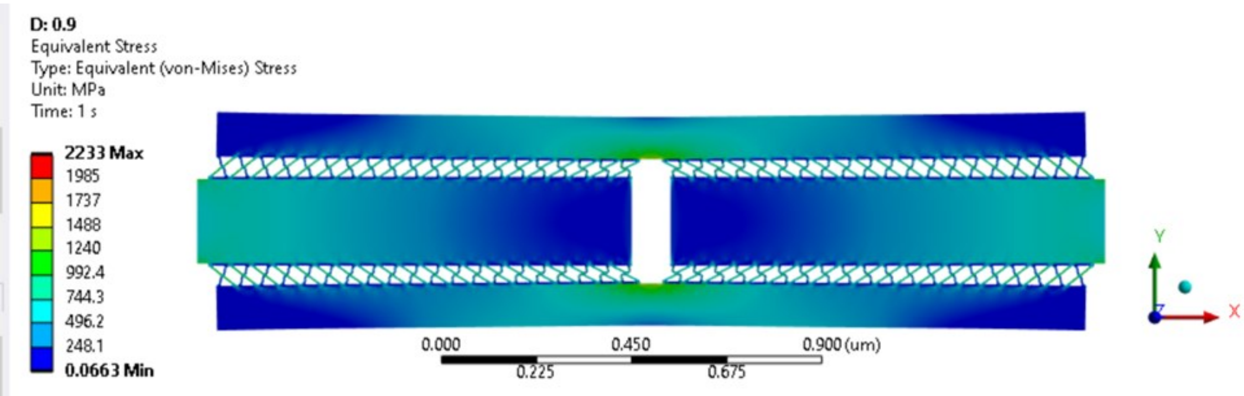

Figure 131: The Equivalent Stress (von Mises) for the displacement of 0.05µm applied to the 0.90 volume ratio model.

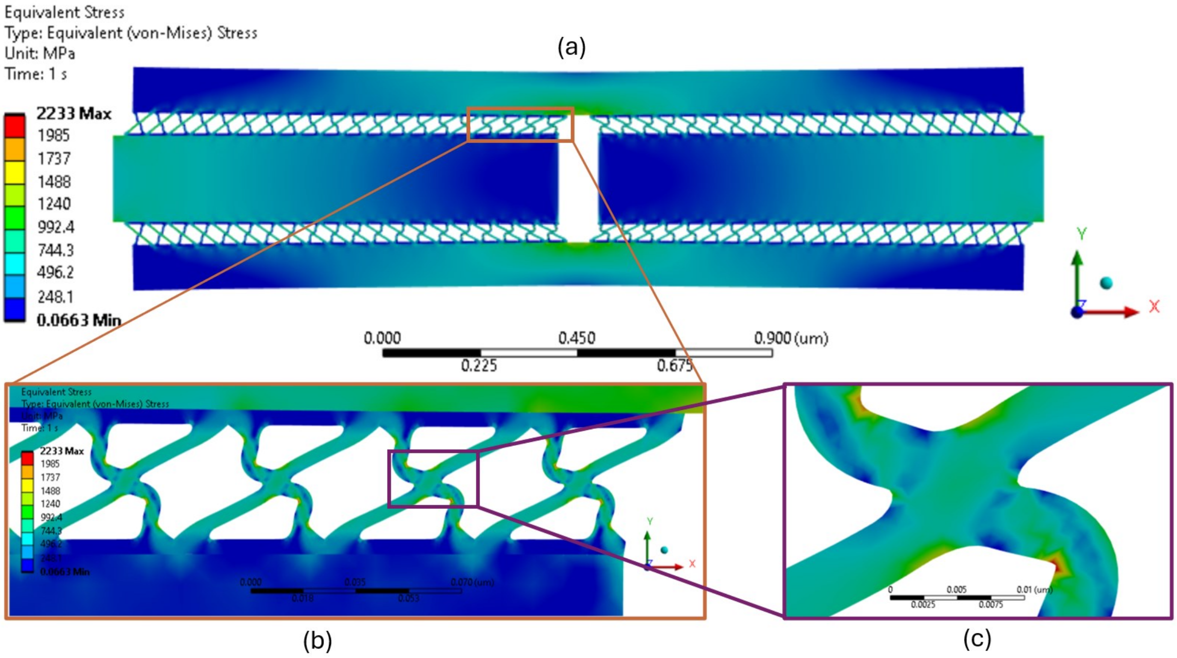

Figure 132: The zoomed-in section of the model in Figure 122 shows the Equivalent Stress (von Mises) for the displacement of 0.05μm applied to the 0.90 volume ratio model. The peak stress is shown in red in diagram (c).

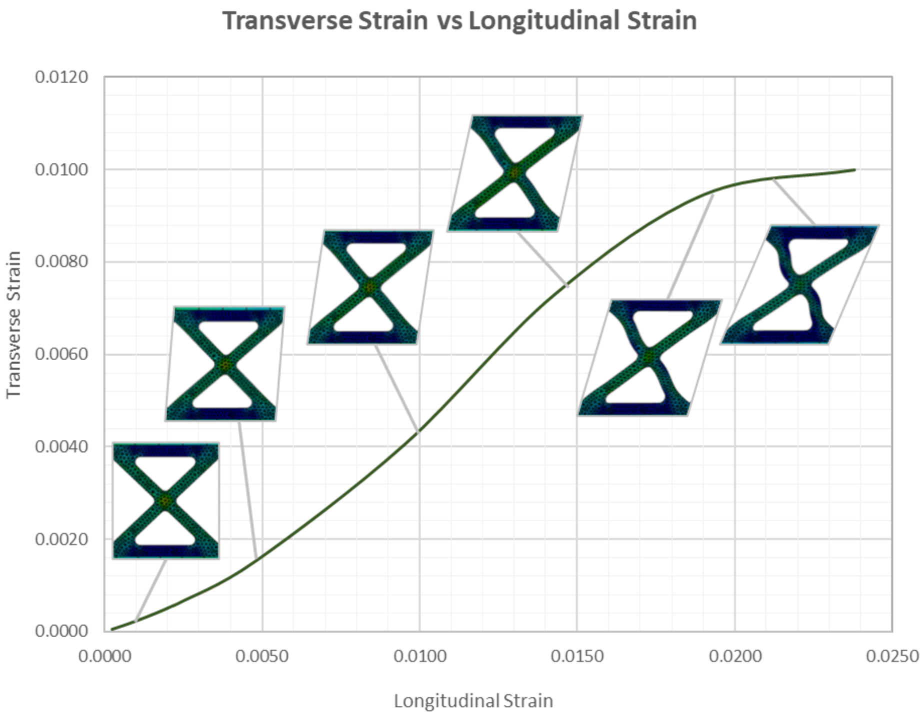

Figure 133: The plot showing transverse and longitudinal strain along with a zoomed-in unit cell of mortar showing its progressive deformation, including combined bending and fixture translation

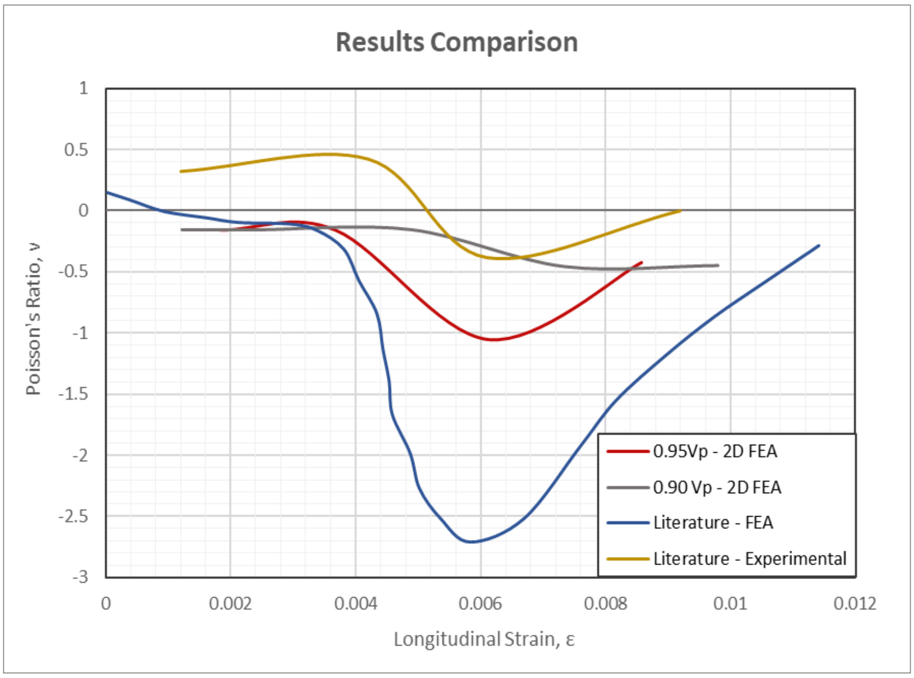

Figure 134: The results showing incremental Poisson's ratio in comparison to the FEA and experimental data found in the literature

Using the results obtained for strain in x- and y-direction, the incremental Poisson's ratio was calculated to enable the comparison to the existing literature. Figure 134 shows the incremental Poisson's ratio results for the 0.95 and 0.90 volume ratio models. Literature – FEA presents the results by Wang & Boyce, which have been previously shown in section 'Mechanism 1' on page 93.

The Literature – Experimental results have been obtained by Song et al. and are plotted as a curve. Interestingly, the 0.95 volume ratio results follow a similar pattern to the experimental data but with a lower magnitude of Poisson's ratio present. As 0.95 volume ratio is the closest in the volume to the nacre itself, the results following the similar pattern might be considered a validation, especially considering the fact that the FEA models used are made out of synthetic material and are not expected to match nacre's results but rather try to replicate some of its behaviour.

Mesh Comparison Study

For the mesh comparison study, quadrilateral and triangular meshes of mortar were compared. The mesh settings and the resulting statistics can be found in Table 26 and Table 27. The meshes generated had 1, 2, and 3 elements across the width of the rib of the mortar. The mesh study was carried out on the 0.90 volume ratio model, where the displacements were applied as previously described up to the longitudinal strain of 0.024. The geometry was similar to the 0.90 volume ratio model; however, it was noted after the initial investigation that the mortar's struts do not cross at the 90-degree angle. This was not rectified for this mesh convergence study as it was considered to have no effect on the concluding output. However, it is essential to note that Poisson's ratio obtained is not representative of the previously studied 0.90 volume ratio model. The appropriate geometry was used in all other studies described in this chapter. The results for Poisson's ratio were compared against strain to see at which point the values converged and when they might start to diverge.

Image	Mesh Settings		Statistics	
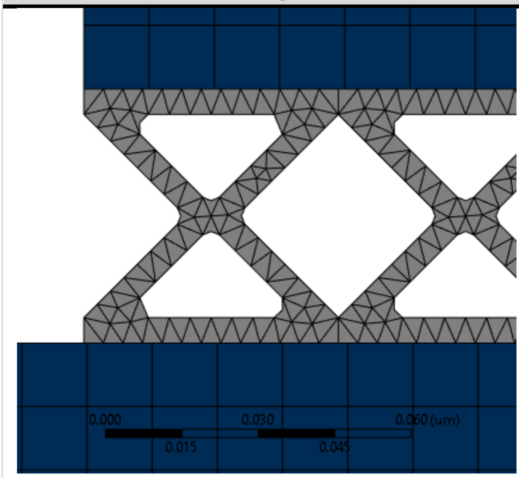	**Method (Mortar)**	All Triangles Method	**Number of Nodes**	44204
	Element Size (Mortar) [µm]	0.004	**Number of Elements**	15520
	Method (Brick)	Quadrilaterals Face Meshing	**Elapsed Time for Last Mesh Generation**	4 seconds
	Element Size (Brick) [µm]	0.02	**Elapsed Time for Last Entire Solve Action**	47 seconds
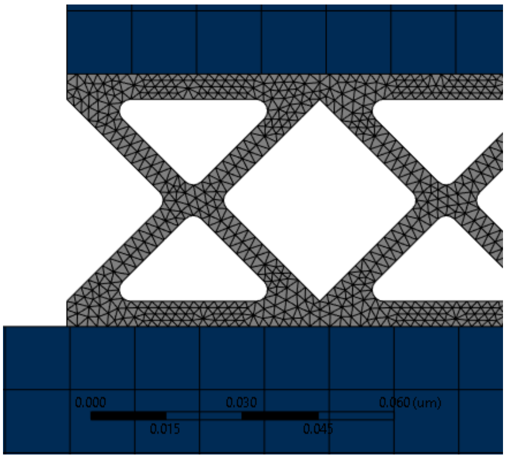	**Method (Mortar)**	All Triangles Method	**Number of Nodes**	129620
	Element Size (Mortar) [µm]	0.002	**Number of Elements**	54532
	Method (Brick)	Quadrilaterals Face Meshing	**Elapsed Time for Last Mesh Generation**	4 seconds
	Element Size (Brick) [µm]	0.02	**Elapsed Time for Last Entire Solve Action**	2 minutes 53 seconds
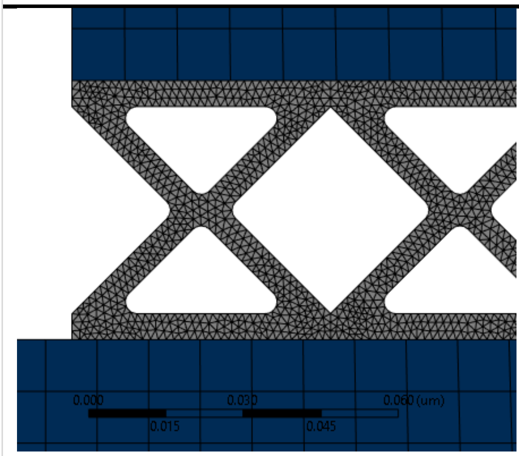	**Method (Mortar)**	All Triangles Method	**Number of Nodes**	199072
	Element Size (Mortar) [µm]	0.0015	**Number of Elements**	85484
	Method (Brick)	Quadrilaterals Face Meshing	**Elapsed Time for Last Mesh Generation**	5 seconds
	Element Size (Brick) [µm]	0.01	**Elapsed Time for Last Entire Solve Action**	4 minutes 16 seconds

Table 26: The triangular mesh settings and resulting statistics

Image	Mesh Settings		Statistics	
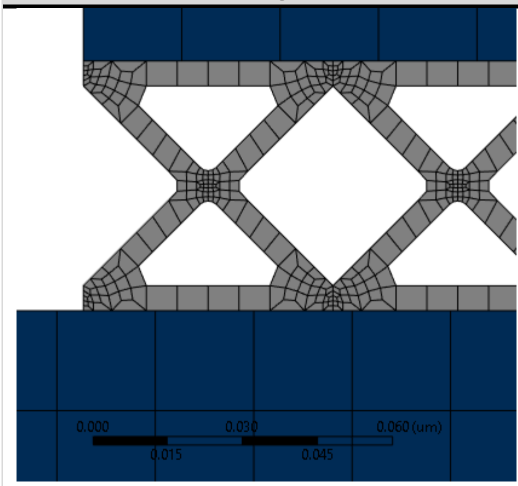	**Method (Mortar)**	MultiZone Quad/Tri: All Quad	**Number of Nodes**	20146
	Element Size (Mortar) [µm]	0.008	**Number of Elements**	16308
	Method (Brick)	Quadrilaterals Face Meshing	**Elapsed Time for Last Mesh Generation**	5 seconds
	Element Size (Brick) [µm]	0.02	**Elapsed Time for Last Entire Solve Action**	1 minute 12 seconds
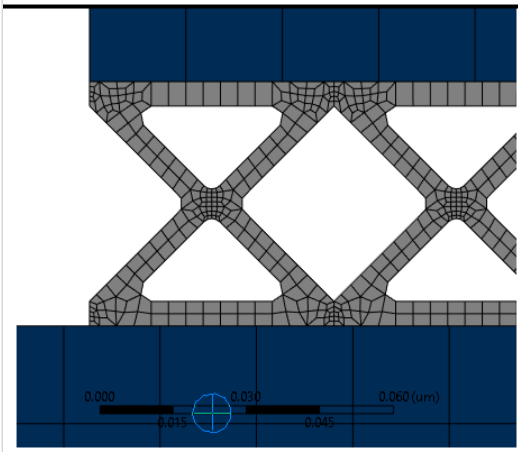	**Method (Mortar)**	MultiZone Quad/Tri: All Quad	**Number of Nodes**	24074
	Element Size (Mortar) [µm]	0.004	**Number of Elements**	19160
	Method (Brick)	Quadrilaterals Face Meshing	**Elapsed Time for Last Mesh Generation**	6 seconds
	Element Size (Brick) [µm]	0.02	**Elapsed Time for Last Entire Solve Action**	49 seconds
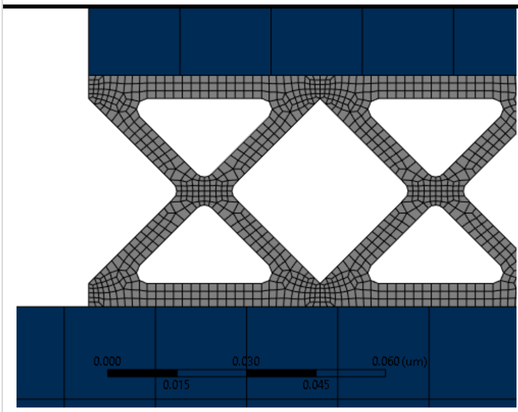	**Method (Mortar)**	MultiZone Quad/Tri: All Quad	**Number of Nodes**	46074
	Element Size (Mortar) [µm]	0.002	**Number of Elements**	37760
	Method (Brick)	Quadrilaterals Face Meshing	**Elapsed Time for Last Mesh Generation**	9 seconds
	Element Size (Brick) [µm]	0.02	**Elapsed Time for Last Entire Solve Action**	56 seconds

Table 27: The quadrilateral mesh settings and resulting statistics

Figure 135 shows a plot of longitudinal strain vs Poisson's ratio for each of the meshes type and size, that were shown in Table 26 and Table 27. From the plot, it can be deduced that lower deformations produce very similar results for all of the meshes. However, after approximately 1% strain, the results start to deviate, with the closest results being between triangular meshes of 2 and 3 elements across their width.

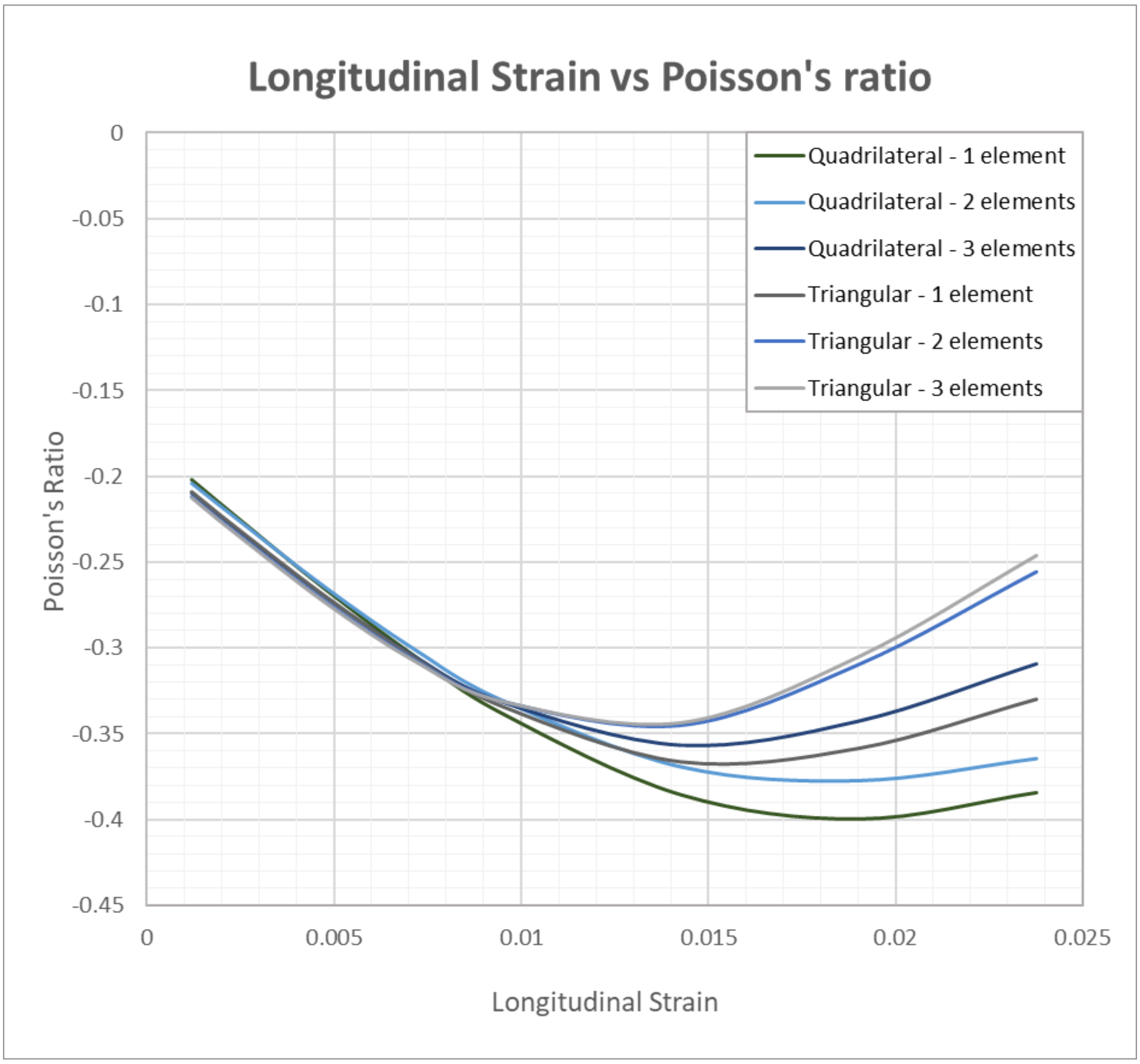

Figure 135: The results of the longitudinal strain and Poisson's ratio of the 0.90 volume ratio model with a varying mesh of the mortar

The same pattern can be observed when looking at the results of the longitudinal strain versus transverse strain plot, as found in Figure 136. To ensure the accuracy of the results, the preference is to use a triangular mesh of at least two elements across the mortar's strut's width. The triangular mesh provides more integration points, hence expected to increase the accuracy of the result. The convergence between the triangular element results is likely indicative of that.

Moreover, the standard 4-node quadrilateral elements are susceptible to shear locking when used in bending simulation. This phenomenon occurs due to the element being unable to accurately represent the strain distribution associated with bending, leading to excessive shear stresses and a stiff behaviour (ANSYS, Inc, 2023).

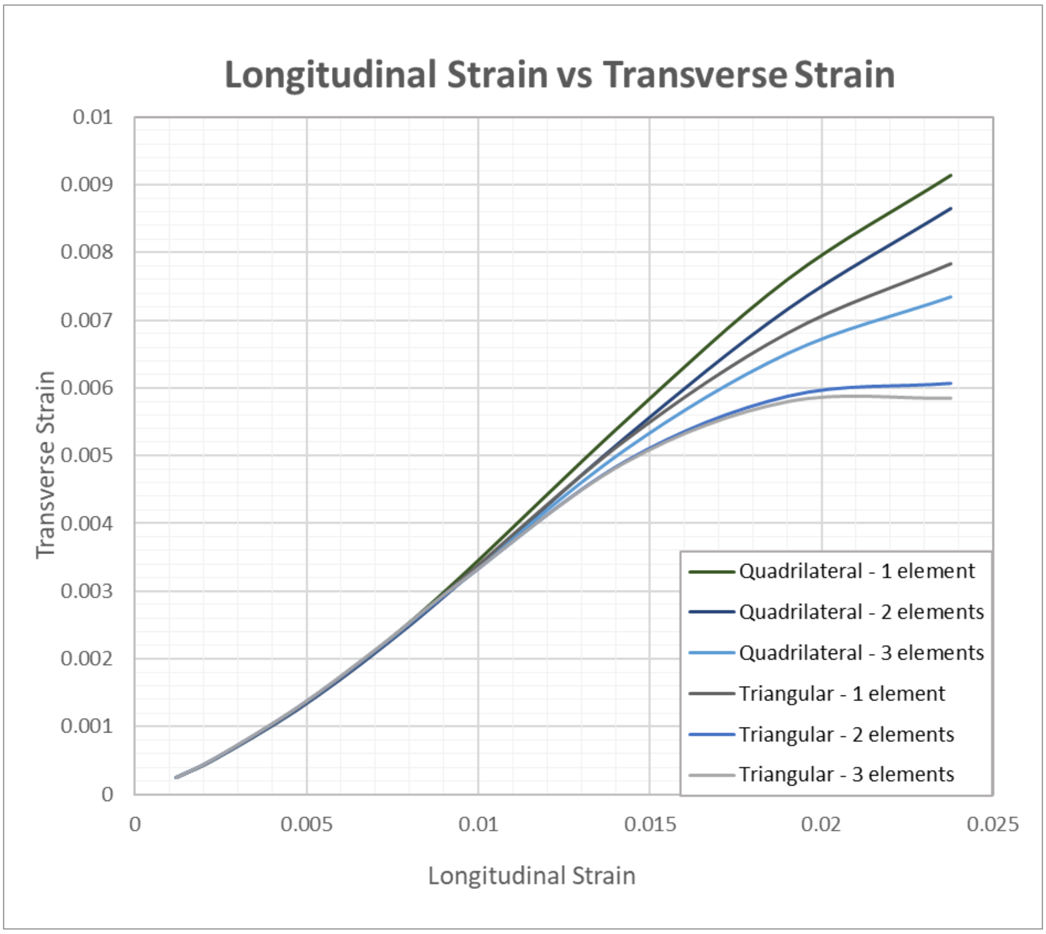

Figure 136: The results of the longitudinal strain and the transverse strain of the 0.90 volume ratio model with a varying mesh of the mortar

Convergence Study

An alternative method to determining whether the mesh is sufficient to obtain accurate results is using an in-built Convergence tool within ANSYS. The convergence tool can be applied to any of the result settings. In this scenario, they are applied to the Directional Deformation (Y-Axis) and Stress Equivalent results. The maximum convergence can be applied to the results, and the results are considered converged only if they are within the maximum tolerance. The convergence maximum was set to 5%. The convergence study was run on the 0.90 volume ratio model with the geometry and settings as previously described in the Geometry and Mesh sections of this chapter.

For the applied displacement of 0.005µm, the model required three iterations to converge the Directional Deformation and the Equivalent Stress Results, as seen in Figure 137 and Figure 138.

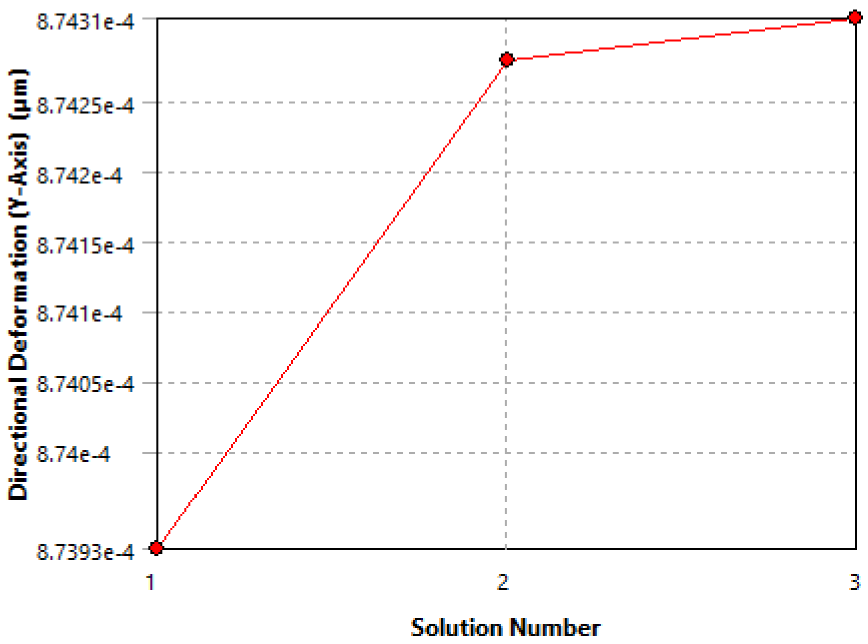

Figure 137: Convergence result for three loop iterations of the Directional Deformation [Y-Axis] of the 0.90 volume ratio model.

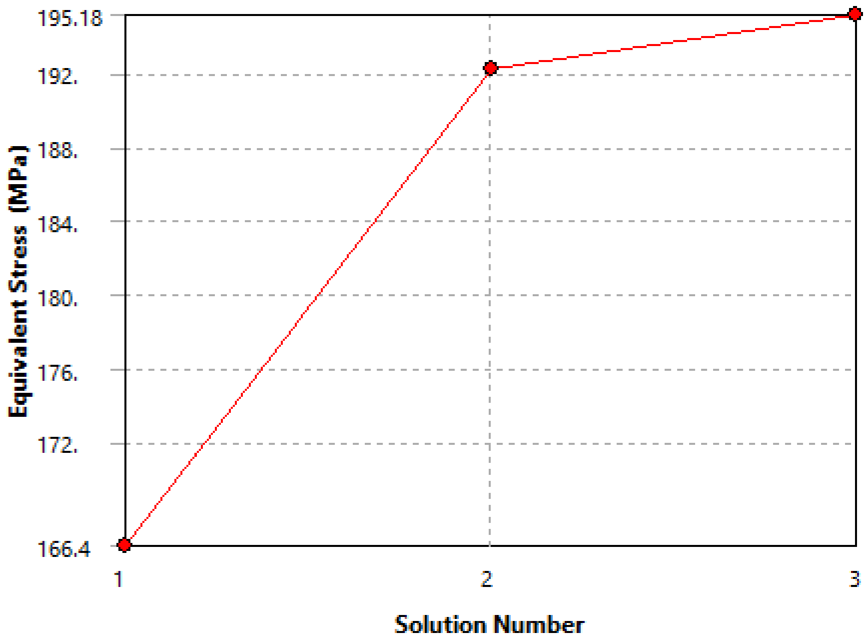

Figure 138: Convergence result for three loop iteration of the Equivalent Stress (von Mises) of the 0.90 volume ratio model.

The tabular results are shown in Table 28. The Directional Deformation converged within a single solution with less than 5% change noted between all solutions, showing that the original meshing method was suitable for the analysis. The Equivalent Stress (von Mises) converged within the three solutions, with the last iteration showing a significantly higher number of nodes and elements.

Solution Number	***Directional Deformation (Y-Axis) [µm]***	***Directional Deformation Change [%]***	***Equivalent Stress [MPa]***	***Equivalent Stress Change [%]***	***Nodes***	***Elements***
1	0.00087393	-	166.4	-	197792	84984
2	0.00087428	0.040	192.27	14.422	363033	162259
3	0.00087431	0.003	195.18	1.503	511402	230970

Table 28: The convergence results for the directional deformation and equivalent stress showing the change [%] and number of nodes

The adaptive mesh formed as a result of the convergence can be seen in Figure 139 and a zoomed-in section in Figure 140.

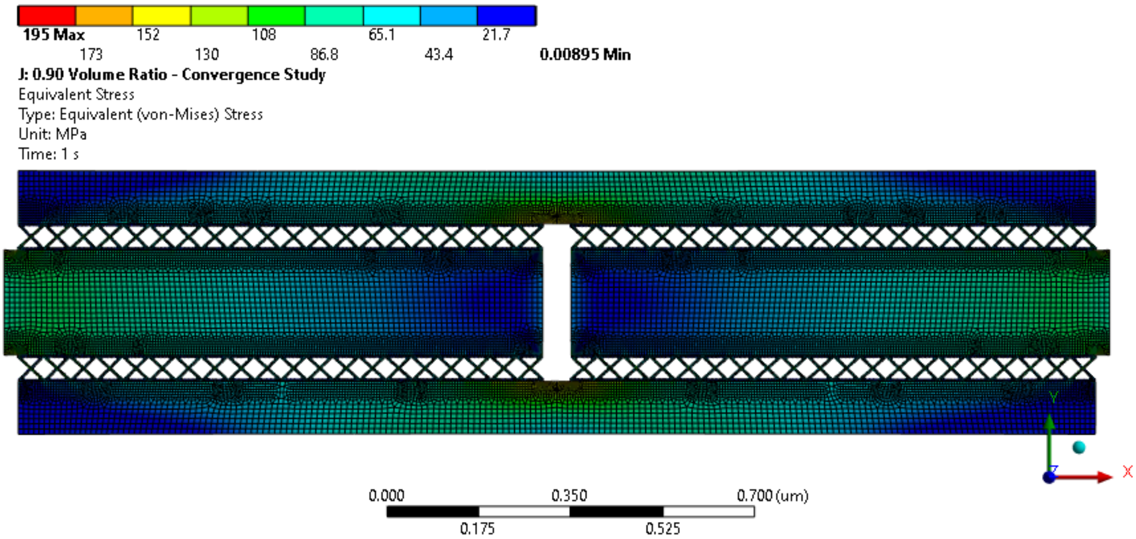

Figure 139: The Equivalent Stress (von Mises) results showing the new adaptive mesh post-convergence.

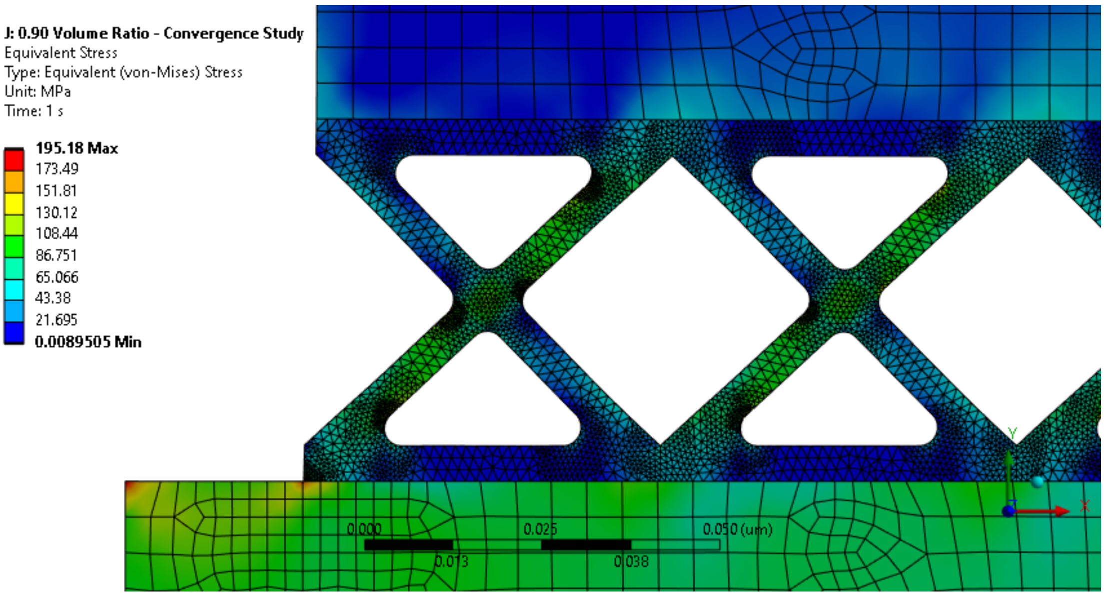

Figure 140: The Equivalent Stress (von Mises) results showing a zoomed-in section of the new adaptive mesh post-convergence.

The mesh refinement was created by the program near the contact areas between the two materials and around the radius of the fileted corners within the mortar. The results are a good indication of the areas that are particularly challenging to analyse accurately. As the key result of interest is the directional deformation of the model for the purpose of obtaining Poisson's ratio rather than the stress results, the originally proposed mesh should be sufficient to obtain accurate results. This might be reviewed again in further analysis to ensure the accuracy of the results.

Parametric Study

Mortar Geometry Variations

A parametric study was carried out to analyse the influence of individual design features within the mortar, i.e., the height of the cell, the width of the unit cell, and the width of the strut. To do this, the 0.90 volume ratio model was used as a basis, and its parameters were used as a control variable. As the parameter was changed, the new volume ratio was calculated.

Volume Ratio	***Parameter studied***	***Number of nodes***	***Number of elements***	***Height of the unit cell, H [μm]***	***Width of the unit cell, W [μm]***	***Width of the rib, W_{rib} [μm]***
0.90	Reference model	197792	84984	0.05	0.05	0.005
0.93	Height	168474	72332	0.025	0.05	0.005
0.89	Height	232376	99784	0.075	0.05	0.005
0.87	Height	259688	111204	0.1	0.05	0.005
0.88	Width	251052	109020	0.05	0.025	0.005
0.91	Width	186988	80524	0.05	0.075	0.005
0.94	Width of the rib	148392	58968	0.05	0.05	0.0025
0.87	Width of the rib	281152	127988	0.05	0.05	0.0075

Table 29: The parameters applied to see the effect of changing individual dimensions within the unit cell of mortar

The same boundary conditions were applied to the model with mesh settings that were as similar as possible, following the same method as for the initial analysis of the Mechanism 1 model, with a displacement of up to 0.05 μm being applied.

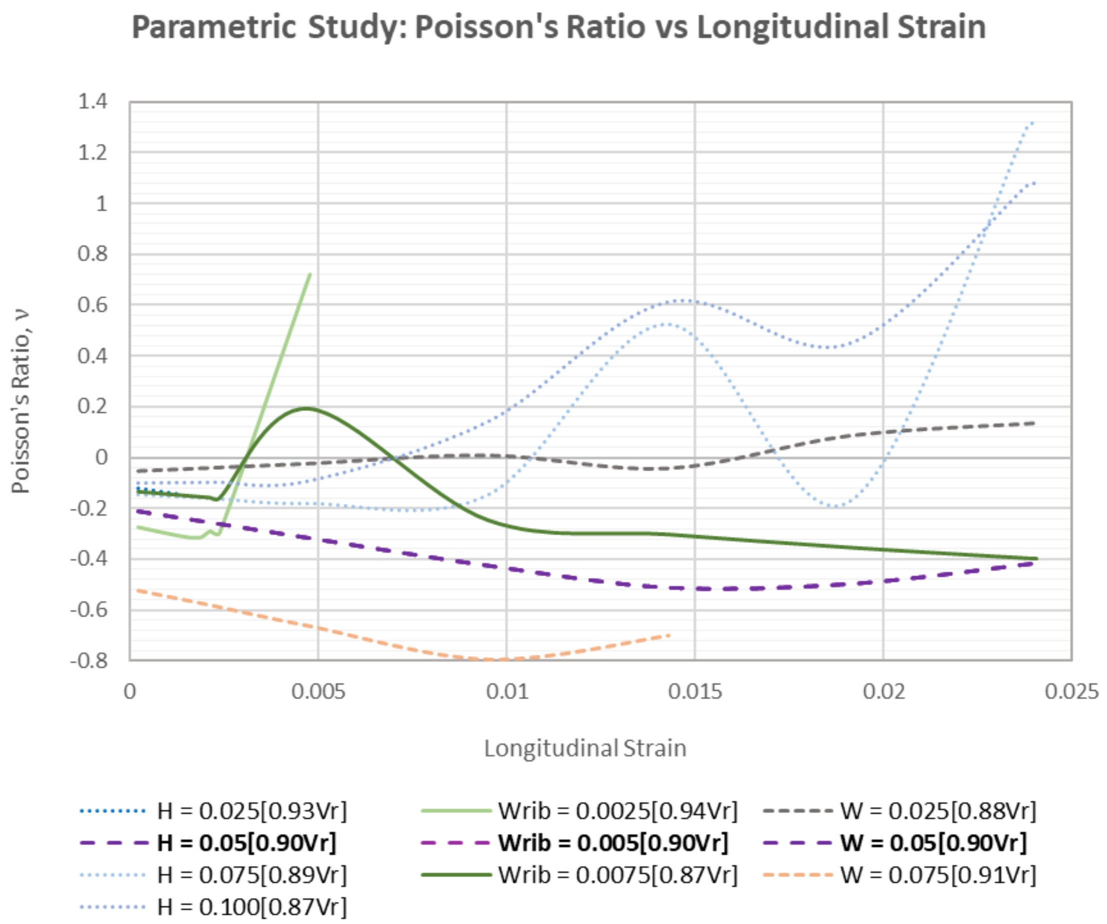

Figure 141: The results of the parametric study showing the influence of geometry on the changes of the Poisson's ratio when the force is applied

The results, Figure 141, showed that the influence of varying the geometry of the mortar on the negative Poisson's ratio is significant. This can enable the manipulation of the model to enhance the desired properties for certain applications, i.e. impact protection, but this falls out of the scope of this project.

The lowest in magnitude Poisson's ratio achieved is for the 0.91 volume ratio model (91% brick and 9% mortar), with the width of the unit cell of 0.075, shown in orange.

A few geometrical changes led to the earlier failure of the system, resulting in unconverged results and providing a limited dataset. These were: a model with the height of the unit cell equal to 0.025 μm, the model with the width of the rib of the 'X' equal to 0.0025 μm, and the model with the width of unit cell of the mortar equal to 0.075 μm, although the latter still provided a reasonable dataset to be able to observe the lowest in magnitude Poisson's ratio. The models that reached the failure mode earlier than the models with lower volume ratio were unable to converge up to the same strains as other models and showed the same behaviour pattern as the 0.95 volume ratio model described in the earlier section of this chapter, 'Geometry. Interestingly, all of these models have a commonality of having the volume ratio of the brick higher than 90%.

Looking at some of the previous results, the lower volume of brick (the higher volume of mortar) tends to be able to sustain higher strains. However, the magnitude of Poisson's ratio is lower for lower volume ratio models, i.e., the 0.80 volume ratio model, shown in Figure 128 on 223, had the highest magnitude of Poisson's ratio from the selected models.

This hints at the fact that there needs to be a balance achieved between achieving the Poisson's ratio of the lowest magnitude and the model's ability to withstand higher strains.

Further Mortar Variations

There are more possible variations within mortar that can influence the results. For example, what happens if the gap between the two central bricks is filled with mortar? These are briefly explored in this section.

Firstly, the model with the mortar introduced between the two central bricks is analysed. This is shown in Figure 142.

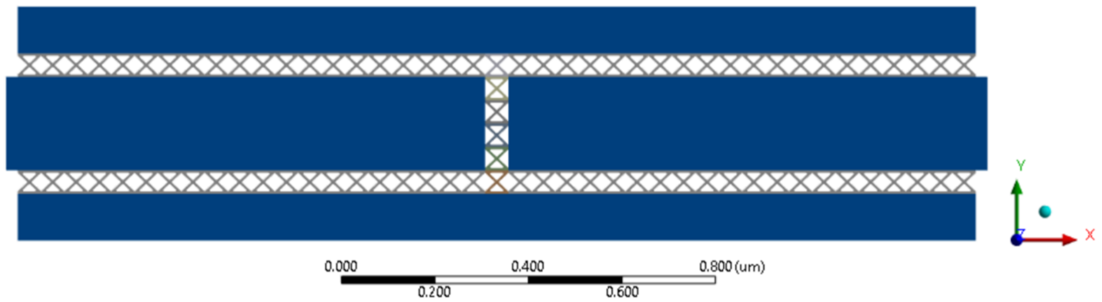

Figure 142:The model analysed with the mortar introduced in the gap between the two central bricks.

The geometry analysed was based on the 0.90 volume ratio model described in the sub-section titled ‘Geometry’ on page 213. The only difference was to add a few more repeated units of mortar into the gap between the two central bricks.

Adding the mortar in-between the bricks resulted in solely positive Poisson’s ratio and an earlier failure of the mechanism, with the results not converging past the 0.005 μm displacement. The mortar in between bricks prevents the buckling of the mortar close to the gap, resulting in a different deformation mode. The failure occurs in the brick around the corners near the central region of the model, Figure 143.

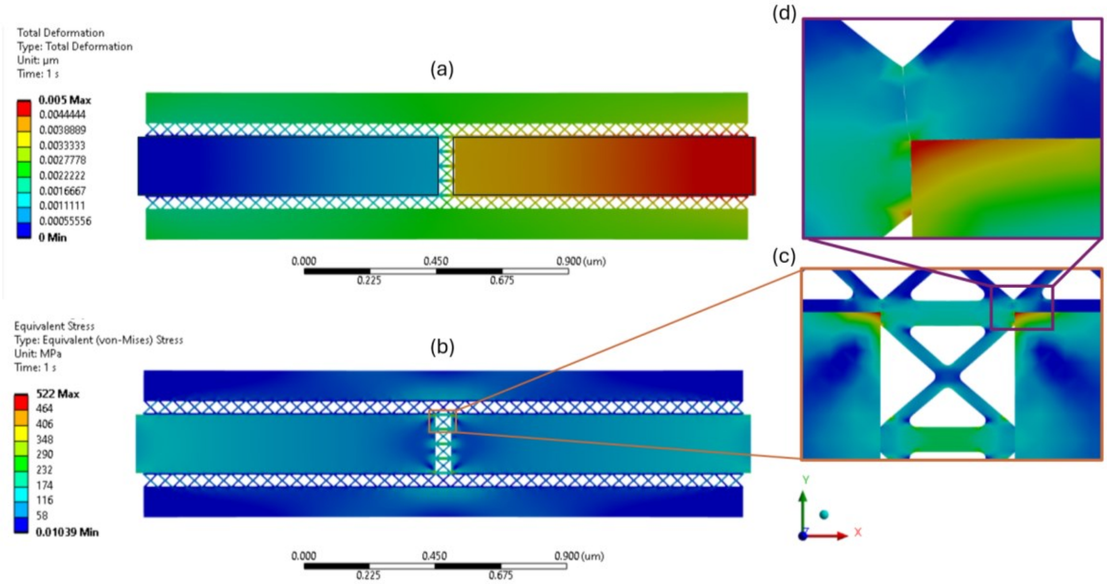

Figure 143: (a) Total deformation where the black box is the original brick size, (b) Equivalent Stress (von Mises) for the 0.005 µm, (c) peak stress found in the brick near the central region of the model, (d) area of failure occurring.

A second investigation looked at adding more than one layer of mortar in the y-direction and the influence it has on the Poisson's ratio. The geometry can be seen in Figure 144. The basis for the geometry were the parameters used to create a 0.90 volume ratio model with an additional layer of mortar.

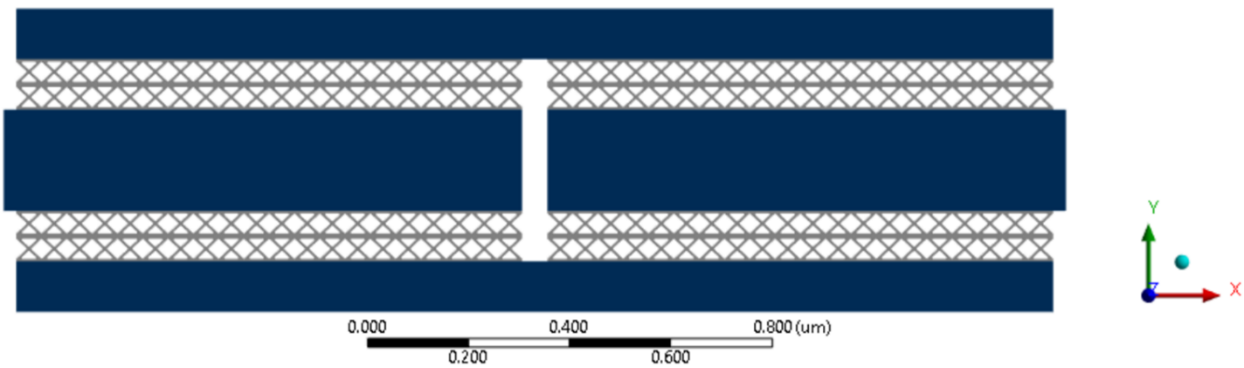

Figure 144: The geometry of the model with a doubled layer of mortar

The results for the model with two layers of mortar show that it has a slightly higher magnitude value of Poisson's ratio in comparison to the 0.90 volume ratio model but a similar behavioural pattern. This implies that the geometry of the individual X's has a more significant influence than the mortar geometry and volume as a whole. However, looking closely at the deformation of the struts within the model, Figure 146, it can be observed that the deformation is much more significant in the X's nearest to the gap, and it is not experienced uniformly throughout the mortar. This is similar in the 0.90 volume ratio mode where the peak deformation is in the X's nearest to the edges, but in that model, the deformation can be observed all the way through the layer.

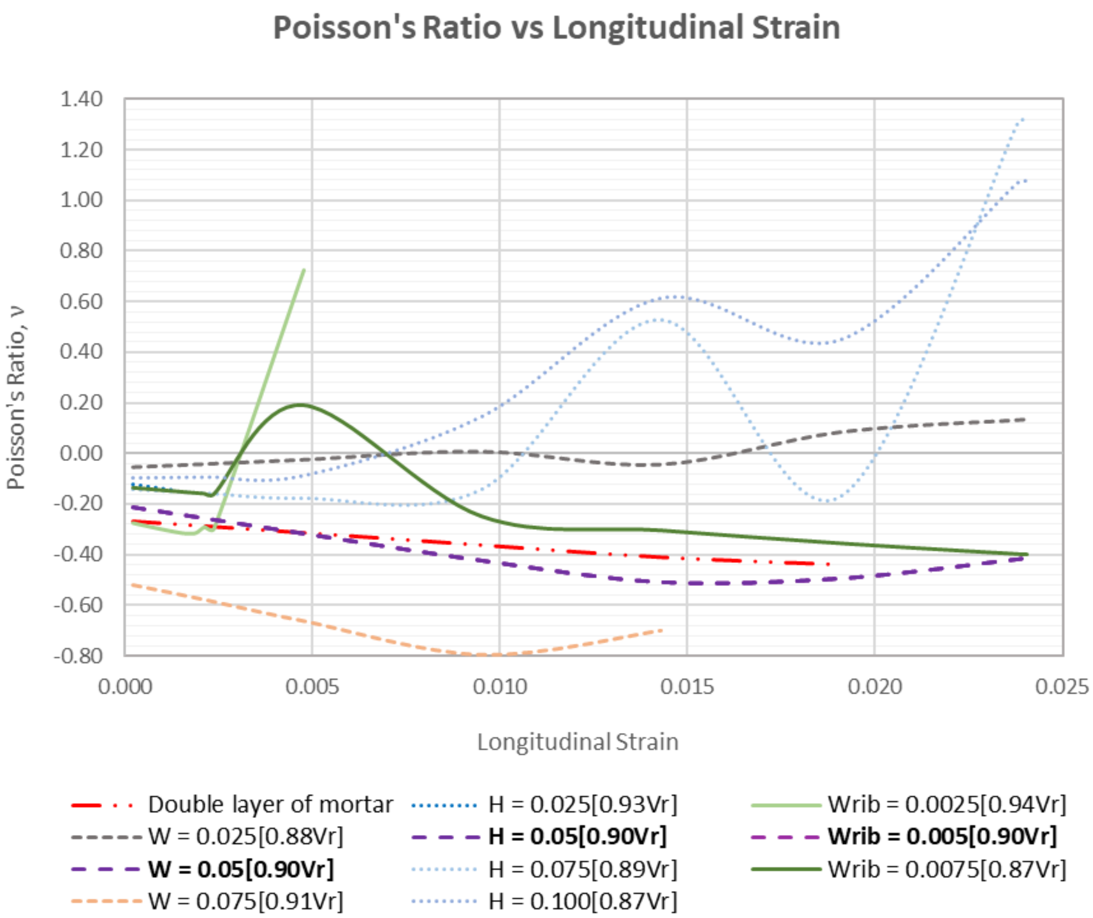

Figure 145: The results for the model with a double layer of mortar in comparison to other results from the parametric study

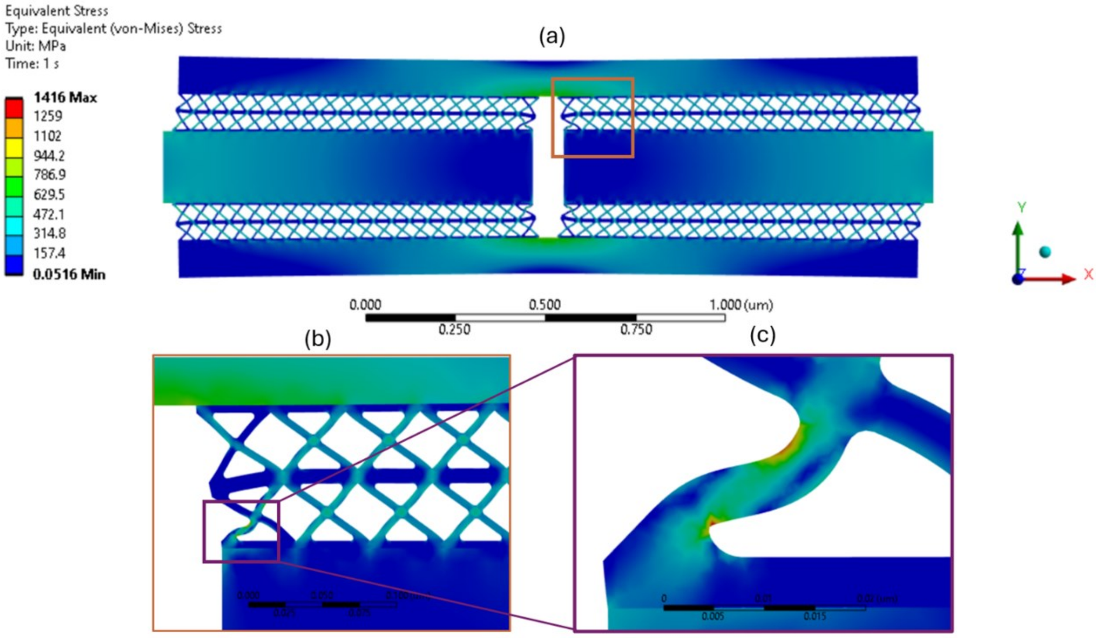

Figure 146: The Equivalent Stress (von Mises) of the model with the double layer of mortar showing (a) a full model, (b) a section with a significant level of deformation, (c) a close-up of the area with peak stress

Mechanism 2

The second model, Figure 147, currently considered, is inspired by Espinosa et al., which consists of concave-shaped bricks. This model is interesting as, in comparison to Mechanism 1, it focuses on the influence of the brick on the auxeticity of the structure.

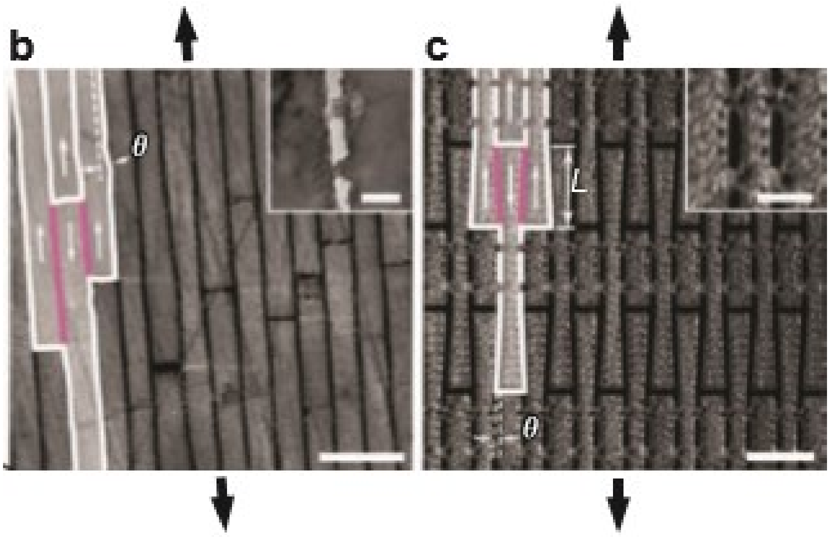

Figure 147: Espinosa et al. suggest that the increase in cross-section is due to the concave structure of the platelets (Espinosa, et al., 2011)

In theory, during deformation, due to the concave shape, the platelets are expected to climb over each other, leading to an increase in a cross-section.

The same material properties are applied as in Mechanism 1 investigation to the geometry shown in Figure 148. The key difference between the geometry in Mechanism 1 and Mechanism 2 is the added curvature to the bricks and, initially, continuous mortar without the distinctive 'X' shape that was used in Mechanism 1.

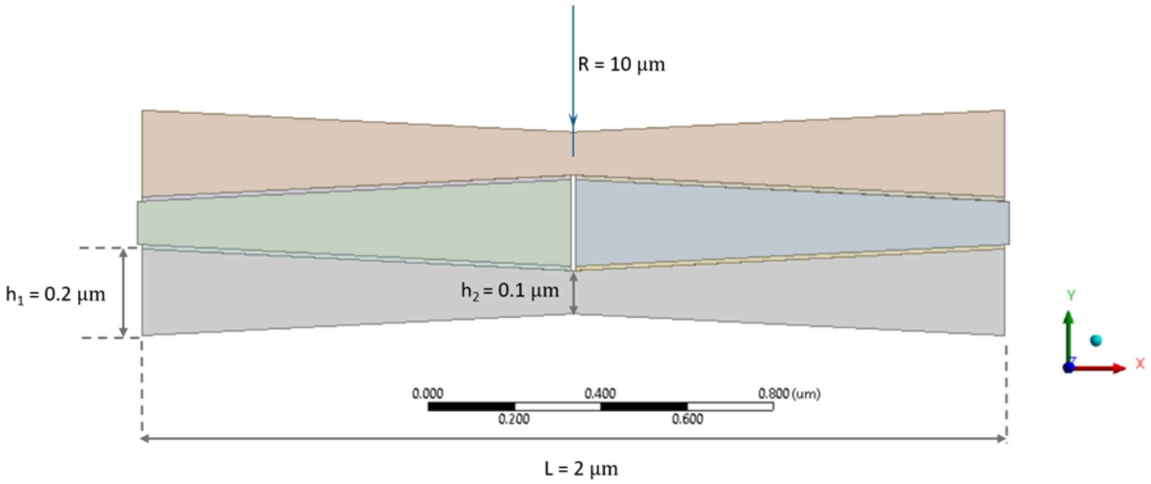

Figure 148: The geometry of the Mechanism 2 model

The volume ratio for this model was approximately 0.95 (volume of bricks), found using Equation (133) found on page 215.

The connections, i.e. contacts between the brick and mortar, were particularly challenging to establish for this model due to the nature of the deformation that needs to be observed. The brick was set as a contact body, and the mortar was set as a target body.

The mesh was generated as a Quadrilateral face mesh for the bricks with the size setting of 0.05 µm, and mortar was modelled using the All triangles method with the mesh size set to 0.01 µm. This mesh set resulted in 6597 nodes and 2573 elements, and it took approximately 4 seconds to generate it.

Two sets of connections were applied: bonded between the mortar and the top and bottom brick, and there was no separation between mortar and central bricks. This was decided so that the influence of the mortar is ignored, and the focus is on the curvature of the brick. This would mainly be the case in a densified model where the influence of mortar is disregarded. This has been modelled analytically in Chapter 4.

The boundary conditions applied were, again, more challenging, as the model had to allow for a lot of axis of freedom to show the expected translation on top of the bricks.

The remote displacement was applied to all of the models to set the out-of-plane displacement (z-direction) to 0.

The displacement was applied to the left and right bricks, pulling them in opposite directions. The bottom edge had frictionless support applied.

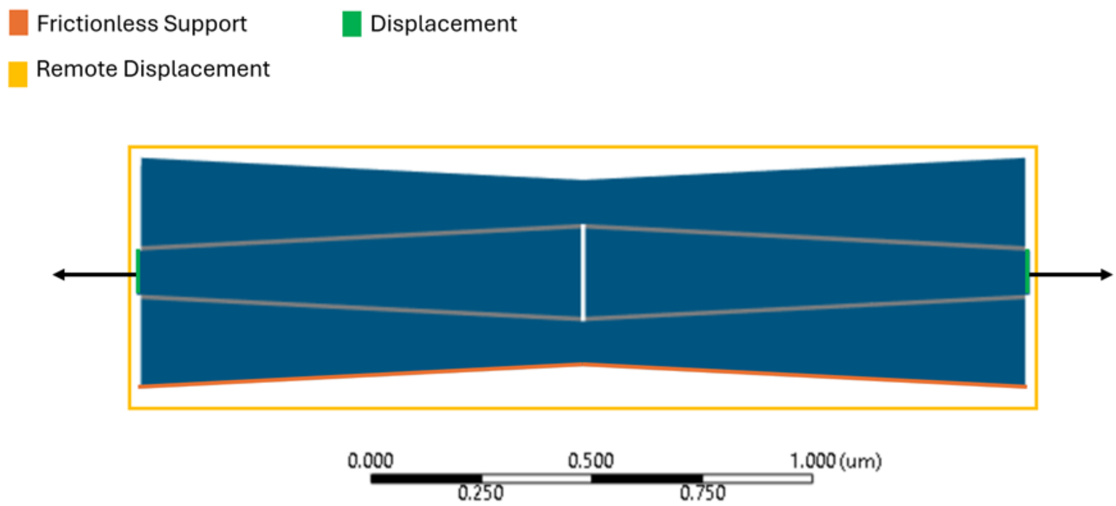

Figure 149: The diagram representing the boundary conditions applied to the model, where remote displacement is applied to the entire model to constrain its out-of-plane rotation.

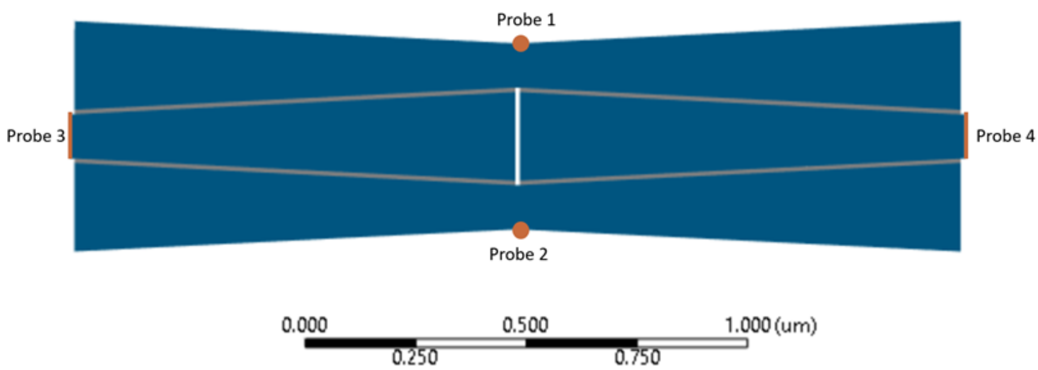

Figure 150: The probes used to measure the deformation in each direction, focusing on the deformation in the centre of the brick

The same method as for Mechanism 1 was used to obtain the results for the Poisson's ratio changes with applied strain.

Results

The results obtained in Figure 151 show that Poisson's ratio remains mostly unchanged with the applied strain. The suspected underlying reason for this is that the curvature of the brick dictates the deformation, which leads to the sustained rate of change matching the climb rate against the curve.

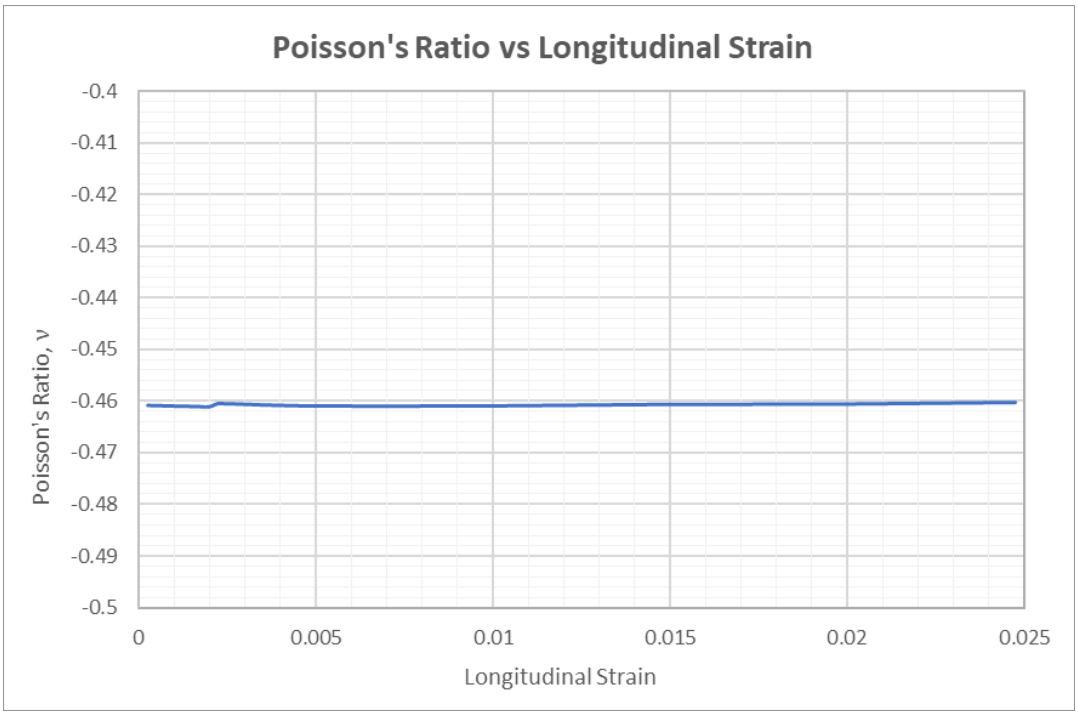

Figure 151: The results showing the Poisson's ratio versus the applied strain for the concave model of 0.94 volume ratio

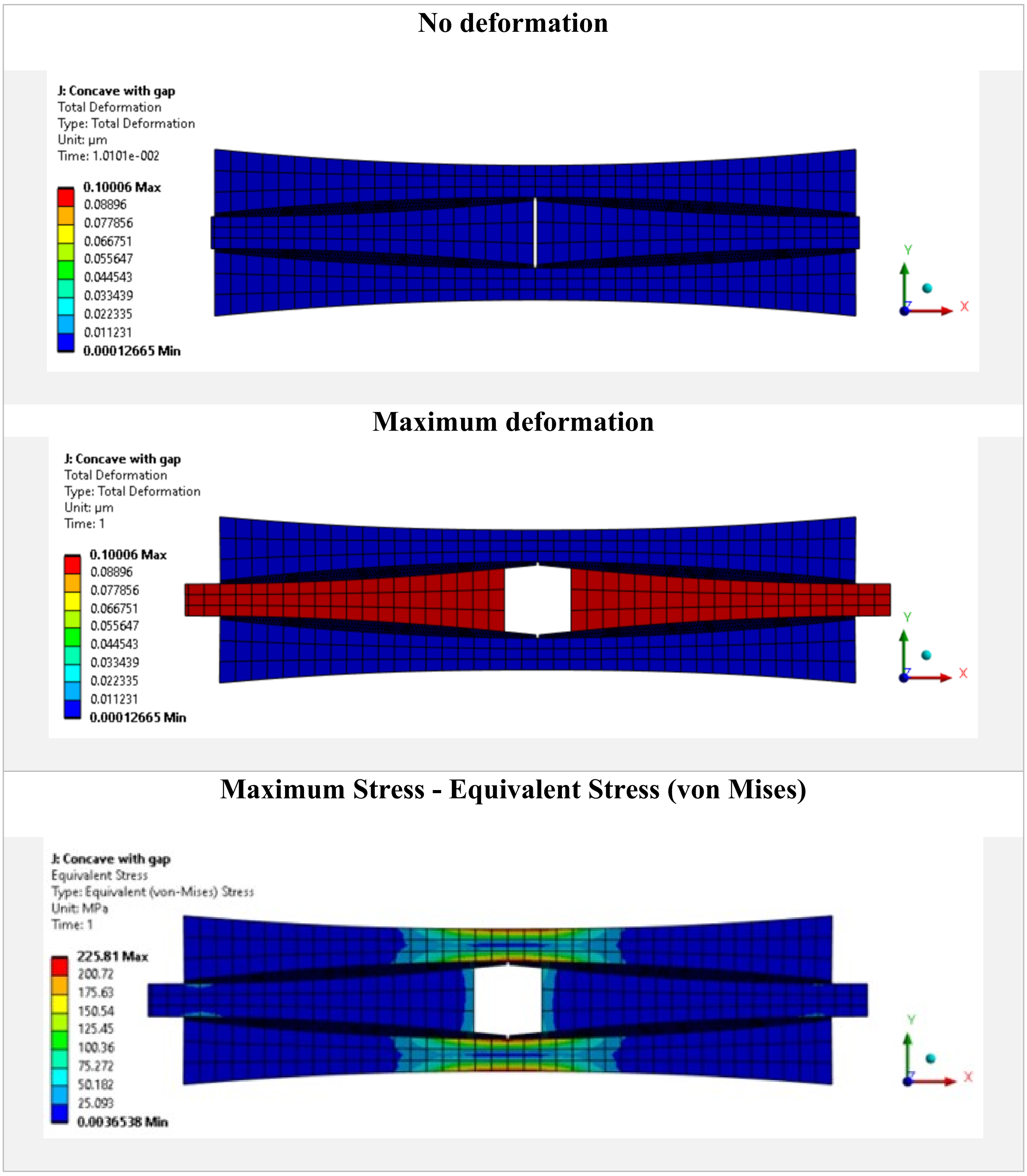

Figure 152: The results showing the changes in deformation and Equivalent Stress (von Mises) within the model when 0.02µm total displacement is applied (0.01µm in opposing directions, left and right)

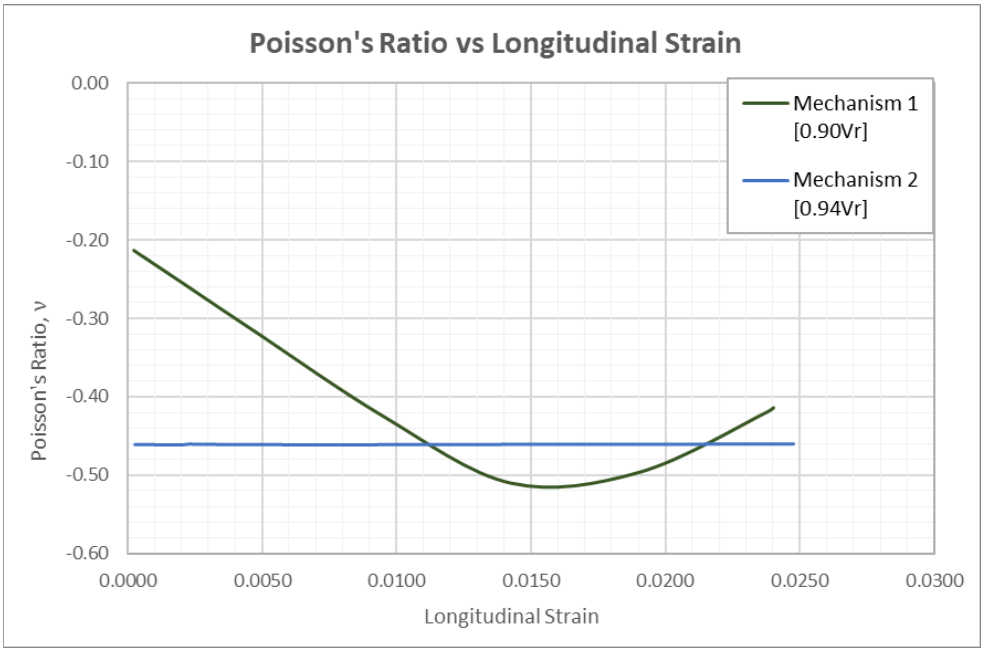

Figure 153: Comparison of results between Mechanism 1 and Mechanism 2

Figure 153 shows a comparison of the results for Mechanism 1 and Mechanism 2, showing minimal variability in Poisson's ratio of Mechanism 2. As the interest of this work lies within nacre-inspired structures, the Mechanism 2 behaviour does not replicate the behaviour shown in Figure 50 on page 91. Mechanism 2 is highly strain-independent, predicting near constant Poisson's Ratio, whereas nacre displays a clear strain-dependency.

The transition to auxetic behaviour, negative Poisson's ratio, under strain implies a response that can be utilised to improve impact protection through Poisson's ratio inspired strain energy management when required, as discussed in more detail in Characteristics of Auxetics section in Chapter 2 Literature Review.

Manufacturability was also considered, but it did not constitute the primary criterion of the decision-making.

Considering the time constraint within the PhD programme, the decision was made to focus on extending the work into three-dimensional geometry utilising mechanism 1 rather than mechanism 2.

It is important to acknowledge that the impact of the brick geometry can be significant and impactful to further enhance auxetic response in brick structures and further research can be conducted with this being a key focus, however, this feel out of scope for this work. This is reinforced by a very recent study by Peng and Bargmann (2024) (Peng & Bargmann, 2024) where the 3D brick structures were observed. The publication by Peng and Bargmann did not influence the decision to move away from Mechanism 2 as it was published very near this work's completion.

Mechanism 3

Mechanism 3 started as a replication of Mechanism 1 with the same geometry of the bricks as the 0.90 volume ratio parameters presented in Table 22 on 214. The geometry is shown in Figure 154. To enable the FEA, the analysis was run in phases of deformation, as previously described in the section Mechanism 3 on page 207.

These phases were: sliding of the bridges against each other with no deformation in the y-direction, negative deformation in the y-direction when the sliding occurring was down the slope of the bridges, sliding of the bridges against the brick with no deformation in the y-direction, and climbing of the bridges up the slope leading to an increase in cross-section in the y-direction.

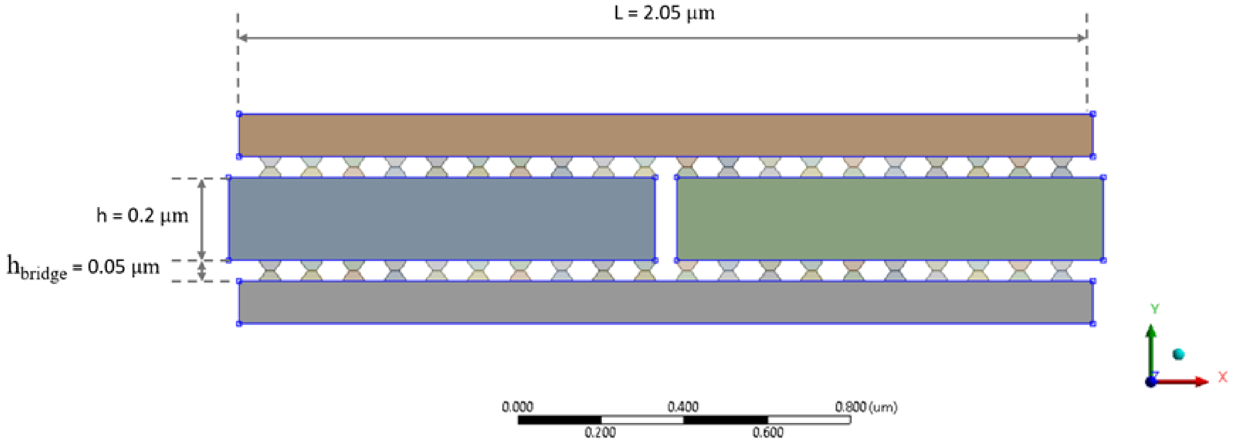

Figure 154: The diagram showing the geometry of Mechanism 3 used for the initial analysis with the relevant dimensions.

The material properties of the 'brick' were assigned to all of the components, and mortar was disregarded. This was due to an interest in the influence of the bridges on the deformation. If adequately constrained, the model should show the behaviour previously described in the section Mechanism 3 on page 101 and Mechanism 3 on page 207.

The All Triangular Mesh with the size of 0.01 µm was applied to the entire model, resulting in 39631 nodes and 18973, and it took approximately 4 seconds to generate, as shown in Figure 155. The connections applied were frictionless surface body to surface body contacts.

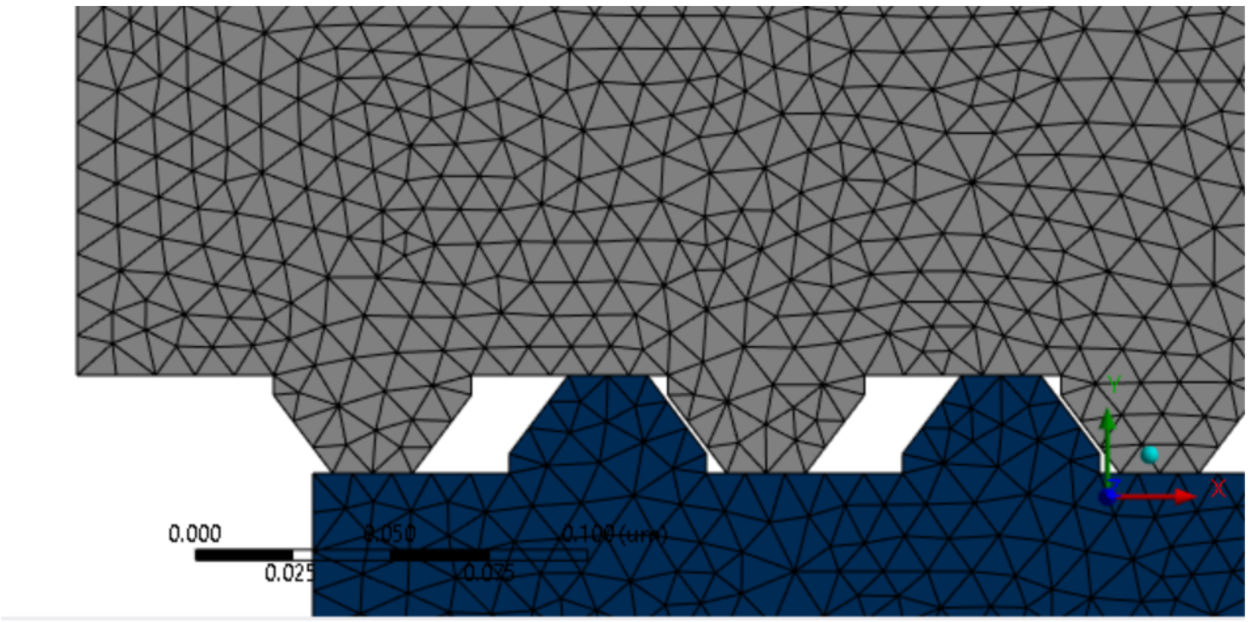

Figure 155: The zoomed-in section showing the mesh used for the analysis of Mechanism 3

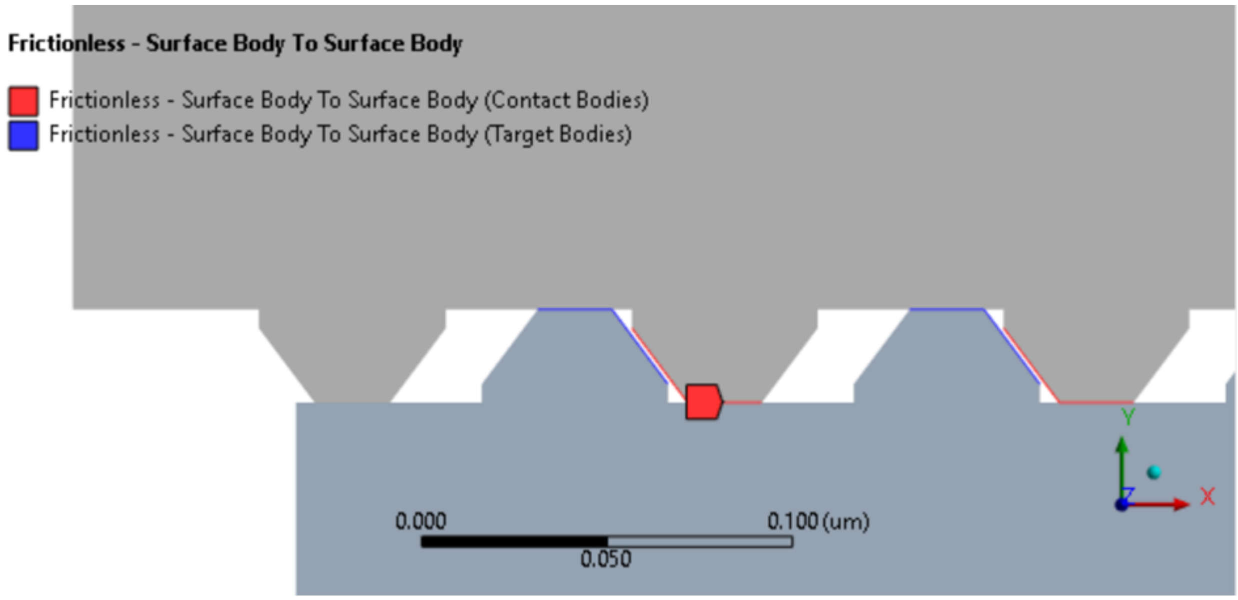

Figure 156: The zoomed-in section showing the contacts between the bridges during the 'climbing' phase

The boundary conditions were similar to the ones applied in Mechanism 2 and can be found in Figure 157. The boundary conditions applied are the remote displacement on the top brick to stop the out-of-plane displacement by setting the z-direction rotation to 0 and to stop any movement in the x-direction. Additionally, there's a fixed support on the bottom edge which ensures that the model is fully constrained. Due to the free movement of the top brick, it is still able to deform in y-direction.

The displacement is applied to the two half-bricks in the middle, set in the opposing directions along the x-axis, as shown by opposing arrows in Figure 157, to replicate the shearing strain. The displacement was applied incrementally up to the approximate distance of ~12% longitudinal strain.

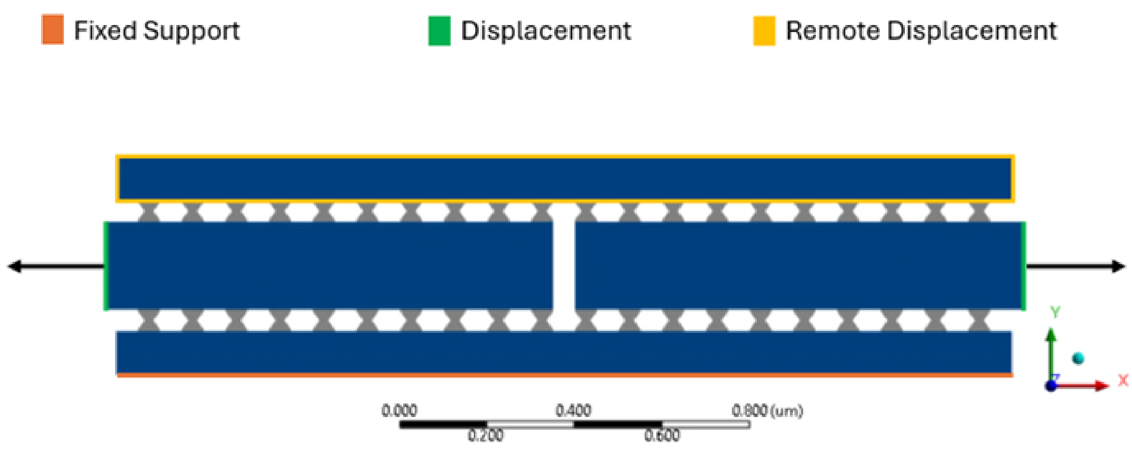

Figure 157: The boundary conditions applied to the model of Mechanism 3, showing [yellow] the remote displacement set to 0 in z-direction to ensure no out-of-plane deformation, [green] displacement applied along the x-axis in opposing directions in increments to replicate shear strain, and [orange] fixed support to fully constrain the model by fixing the bottom layer in space, but still enable deformation upwards in y-direction.

Figure 158 shows the results obtained through the FEA of Mechanism 3. In the plot, different deformation phases can be observed. As the results were obtained using the incremental displacement, the plot is not smooth. It is expected that the changes would be much more linear if smaller increments were used.

The bridges were approximately 10% of the total height of the unit cell to match the ratio found in mechanism 1, further replicating the platelets length and height. This was decided to maintain consistency among the compared mechanisms. Furthermore, this is the same order of magnitude as considered by Song et al. (2008), as shown in Figure 56.

The Poisson’s ratio achieved is very low in magnitude, reaching nearly -6. This could be an interesting geometrical feature to exploit in trying to enhance the mechanical properties with a focus on achieving the lowest magnitude of Poisson’s ratio.

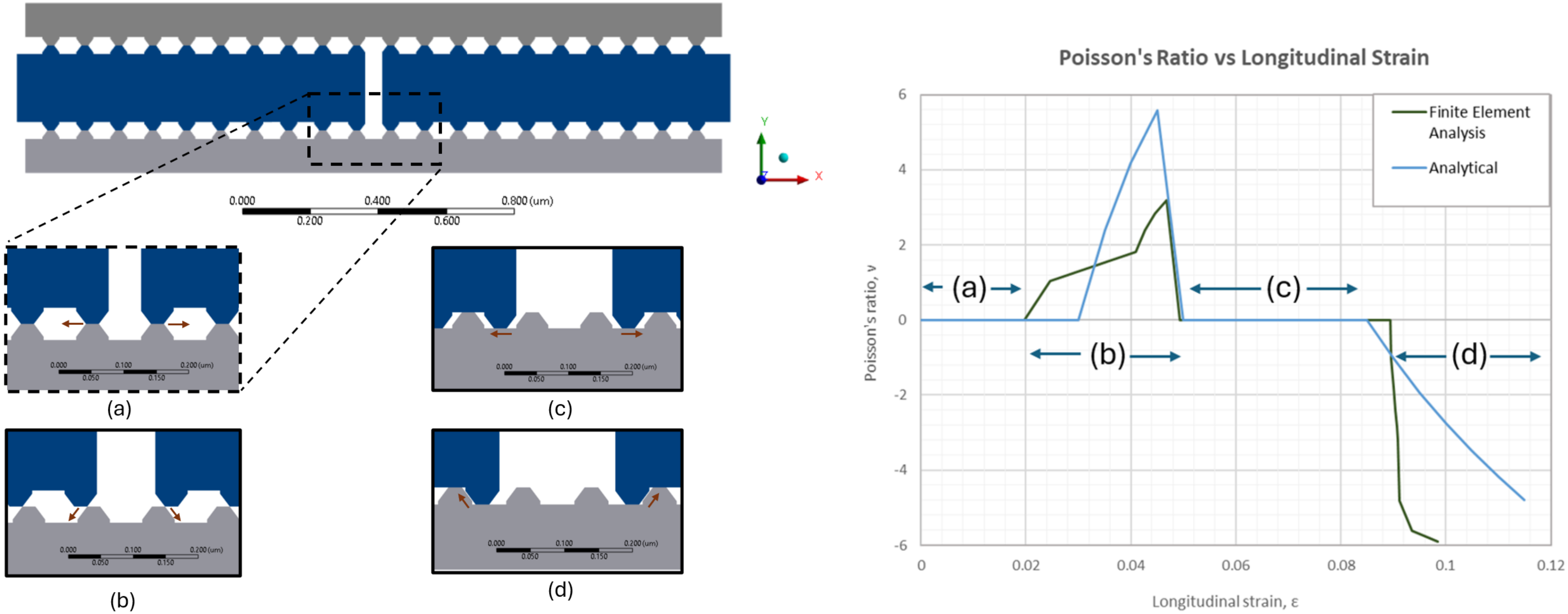

Figure 158: Left) Mechanism 3 model with different deformation phases: (a) neutral phase when there is sliding along the bridges post-fracture of the bridges, (b) the reduction in cross-section of the system when there is sliding down the slope of the bridges, (c) a neutral phase where there is sliding along the surface of a brick before (d) when the climbing over the neighbouring bridge occurs which leads to an increase in the system's cross-section. Right) A comparison of FEA and analytical model results with indicated phases in reference to the FEA results

Chapter 6 FE Models And Analysis 3D Models

Transitioning from 2D to 3D Model

As Chapter 5 showed, multiple variations of 2D models were created, analysed, and optimised. This chapter describes the development and analysis of the 3D models. This section focuses on the implicit analysis of 3D models using ANSYS Static Structural.

There are numerous challenges with transitioning from 2D to 3D models. 3D models provide a more realistic and accurate representation of real life, but the additional axis brings in additional complexity.

Developing the 3D model requires additional effort to appropriately replicate all of the dimensions and ratios of the nacre. Anisotropic materials have different properties in different directions; hence, they will behave differently in the new axis. Meshing complexity increases due to the increased volume of the geometry. The boundary conditions need to be adapted to the new axis, and new assumptions need to be made.

Lastly, computational demands mean that the analysis takes longer to complete, and therefore, it takes longer to manipulate and optimise it to achieve desirable outcomes.

Continuous Mortar Models

The first and potentially most apparent geometry adaptation is adding depth to the model through extrusion.

For the first analysis, the 0.90 volume ratio model (90% of the volume is bricks, and 10% of the volume is mortar) was solely extruded, both brick and mortar, by 0.2 µm. Material properties were unchanged between 2D and 3D models.

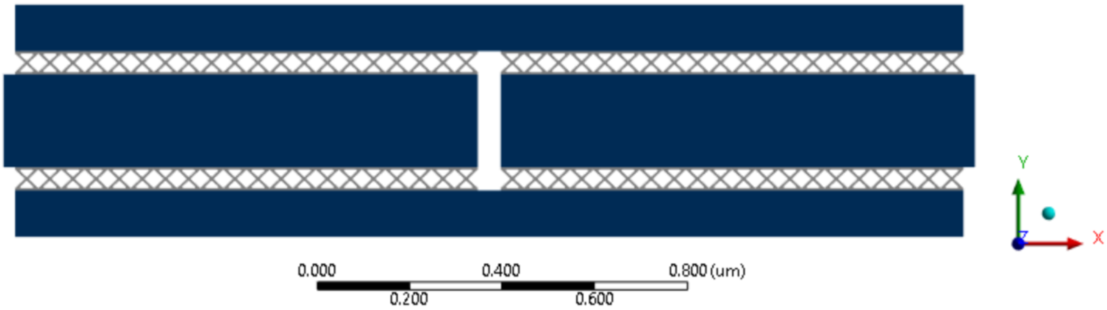

Figure 159: The front view of the 3D 0.90 volume ratio model. (Top) shows the geometry in ANSYS DesignModeler, (bottom) shows the geometry once imported into ANSYS Static Structural.

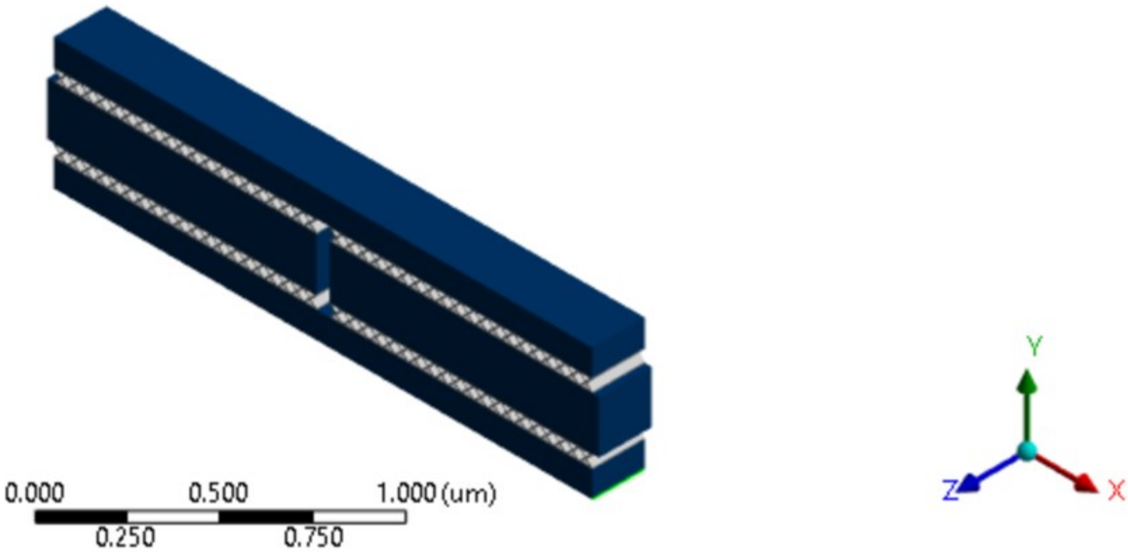

Figure 160: The isotropic view of the 3D 0.90 volume ratio model extruded by 0.2 µm

The hexahedron mesh was applied to all of the bricks with the size of elements set to 0.05 µm. The tetrahedron mesh was applied to the mortar with the element size of 0.002 µm to the front face of the mortar and 0.005 µm on the sides of the mortar. These settings resulted in 2423252 nodes and 1343720 elements, which took 30 seconds to generate.

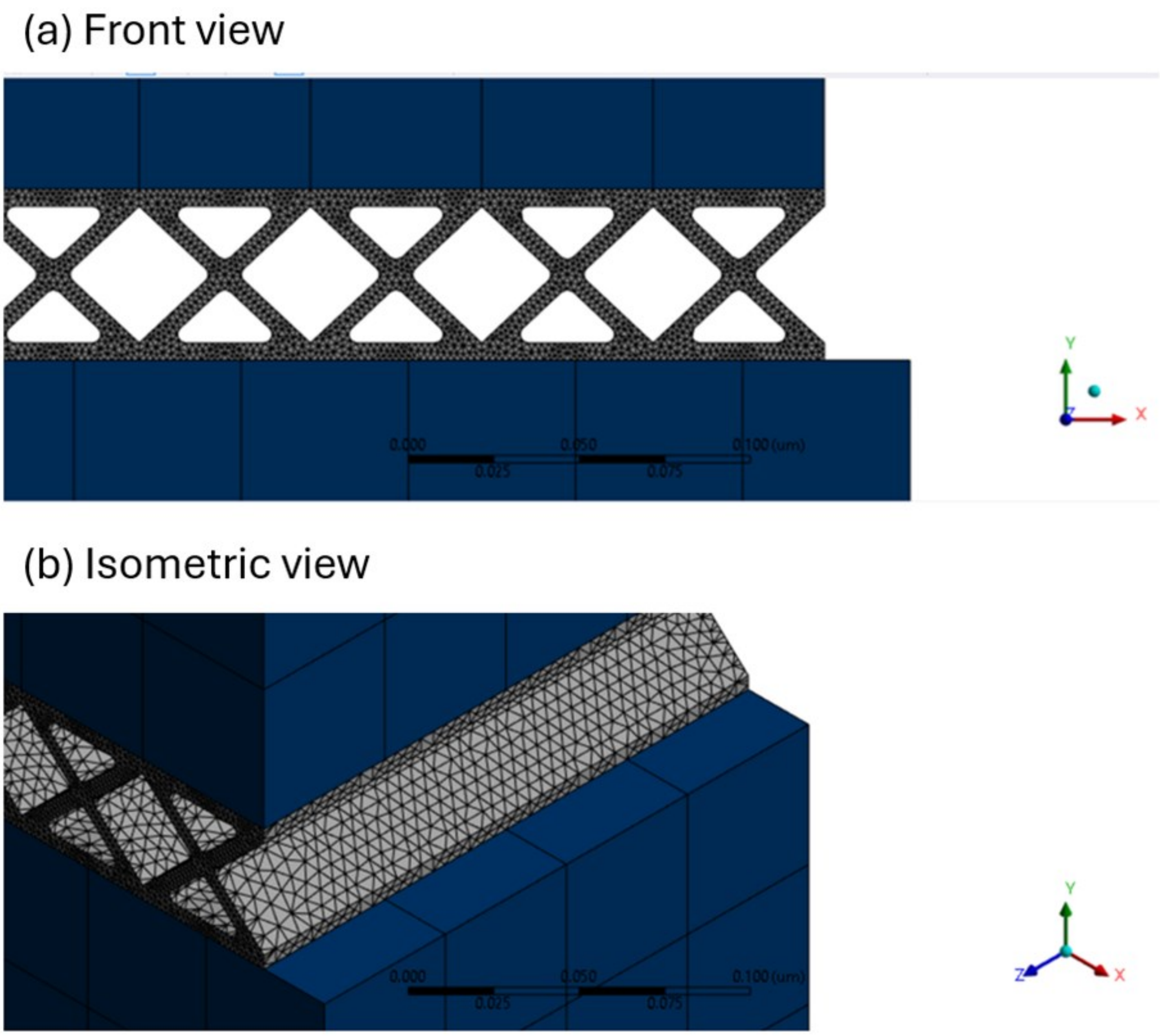

Figure 161: The zoomed-in section of the geometry showing the (a) front view of the meshed faces and (b) isometric view of the section

The boundary conditions applied were replicated from the 2D model, but instead of edges, faces were used. Fixed support (A) on the left face of the model and Displacement (B) in the x-direction on the right face of the model were used to replicate the shear and tensile stress on the model, where the displacement magnitude was varied to obtain a range of results. Remote displacement (C) does not allow the central bricks to move in the y-direction and constrains the out-of-plane rotation, ensuring that brick deformation is solely in the plane. These boundary conditions are shown in Figure 162.

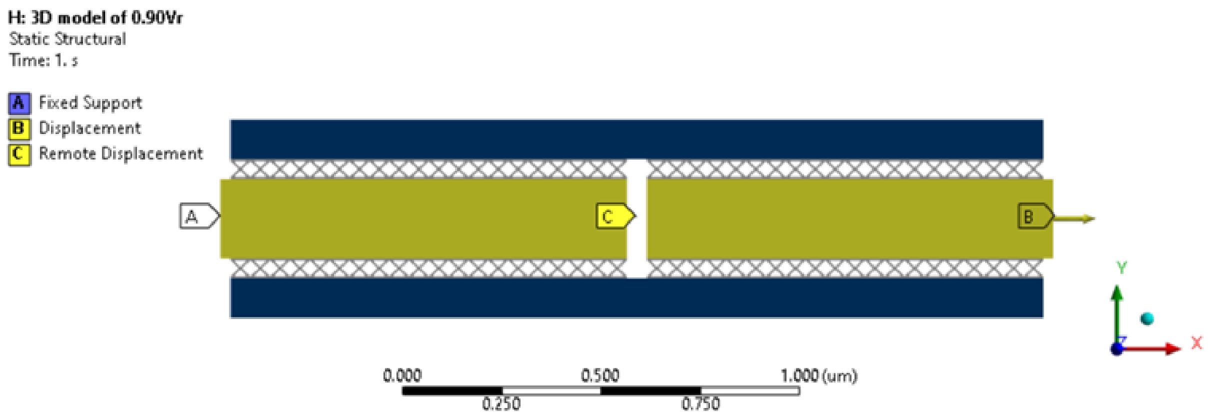

Figure 162: The boundary conditions applied to the 3D model, showing (A) Fixed support, (B) Displacement in the x-direction, and (C) Remote displacement constraining the deformation of the central bricks.

The solution took 16 minutes to generate for the highest strain applied. As mentioned in the section 'Transitioning from 2D to 3D Model', adding an additional dimension to the model increased the computational time. There are 15 increments tested for each model, which means that the entire dataset requires approximately 4 hours to obtain. This does not include any additional set-up time or meshing time.

The same range of displacements was applied to the 3D model as the 2D models, and a comparison of the results between the 2D and 3D models can be found in Figure 163. Initial results show that Poisson's ratio is significantly lower in 3D than in 2D models. It is still a negative value. It also shows that the deformation is linear and does not indicate the same variability as 2D models for the same geometric parameters and volume ratios.

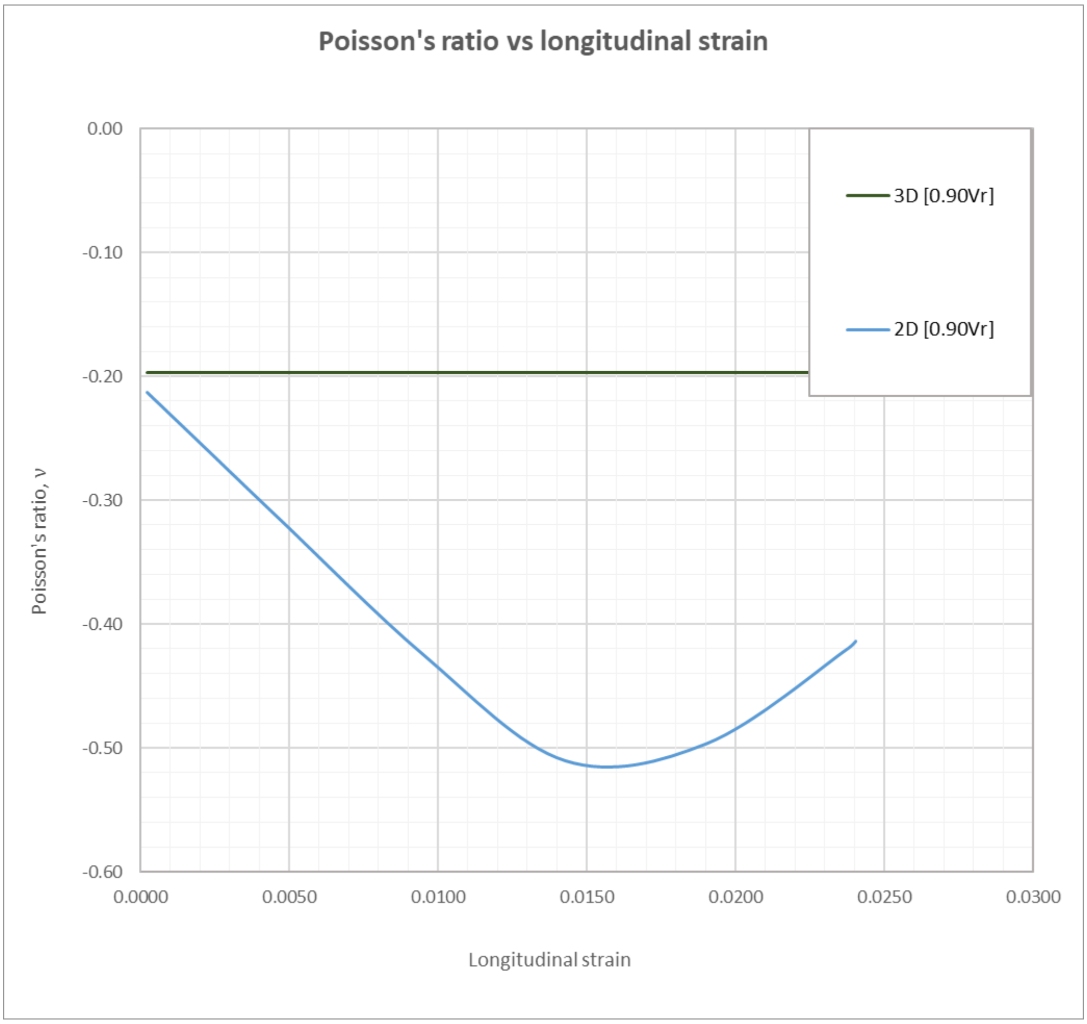

Figure 163: A comparison of 2D and 3D results for the same 0.90 volume ratio model

The results showing the Equivalent Stress (von Mises) are in Figure 164. The maximum stress appears in a region similar to the 2D model, but it is present in the central section instead of the 'rib' itself. This indicates that the deformation mechanisms are likely different between the 2D and 3D models.

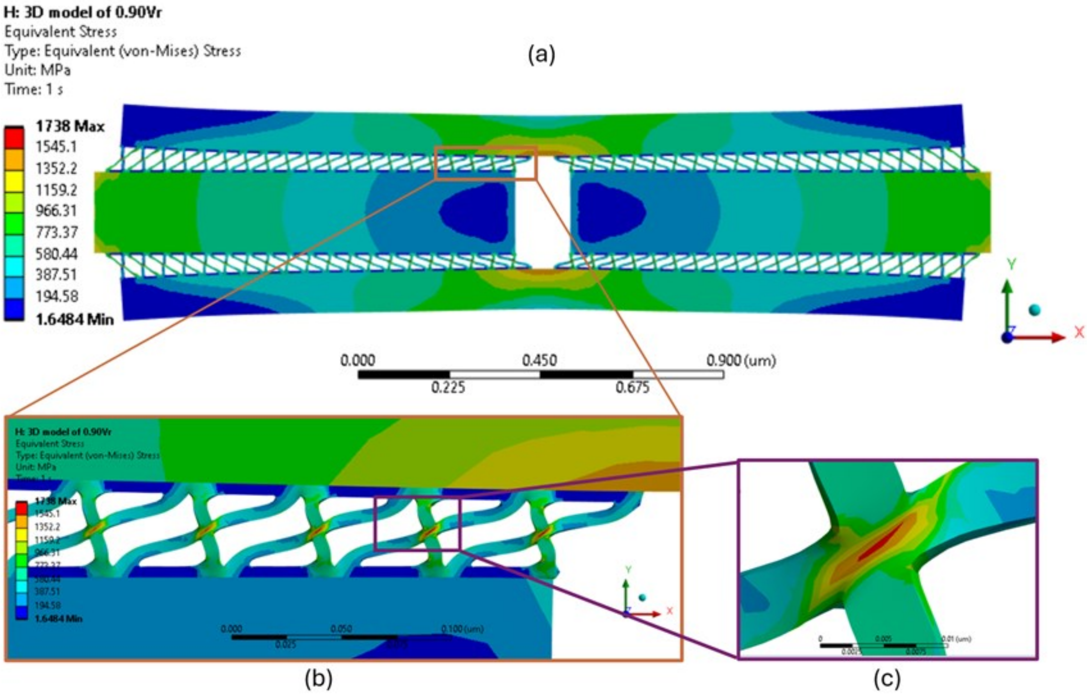

Figure 164: The results for Equivalent Stress (von Mises) of the 3D model with 0.90 volume ratio with 0.05 μm displacement applied. (a) shows the entire unit model, (b) shows a deformed section of mortar, (c) shows the peak stress within the centre of the 'X' in the mortar

The difference can be observed in Figure 165, where the peak stress is indicated in red for (a) 2D model and (b) 3D model. The two models show different deformation mechanisms. The 2D model showed bending combined with axial deformation to be the initial form of deformation, and the 3D model showed that the out-of-plane deformation might have influenced the form of deformation.

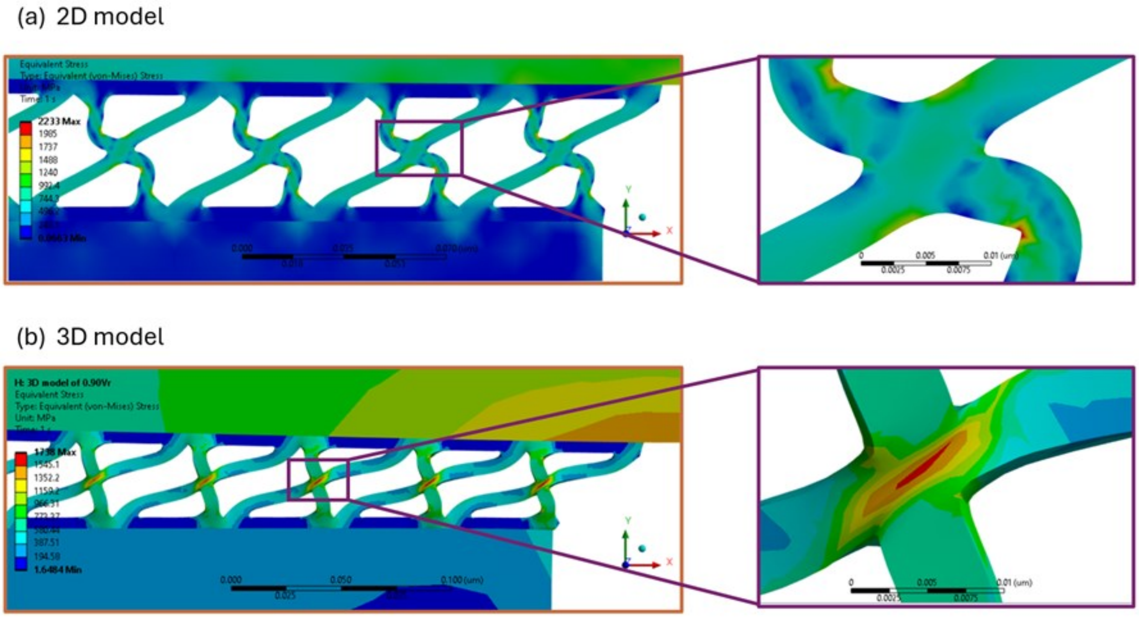

Figure 165: The Equivalent Stress (von Mises) of the (a) 2D model and (b) 3D model showing the differences in the region of the peak stress shown in red

The results show that the added axis changes the Poisson's ratio of the model. It is also likely that the fully extruded model is not optimal. Following the initial analysis, different tests were run where different element types (beams and solid elements), depths, patterns, and arrangements of the mortar were considered. This is to show the influence the mortar has on the overall deformation of the 3D system. The additional aim is to manipulate the 3D model to induce a buckling as a form of deformation mechanism to observe the variability in the Poisson's ratio that is present within the nacre.

Introducing Gaps to the Model

The first instance of manipulation is to see how the thickness of the mortar affects the results through various repetitions of the model.

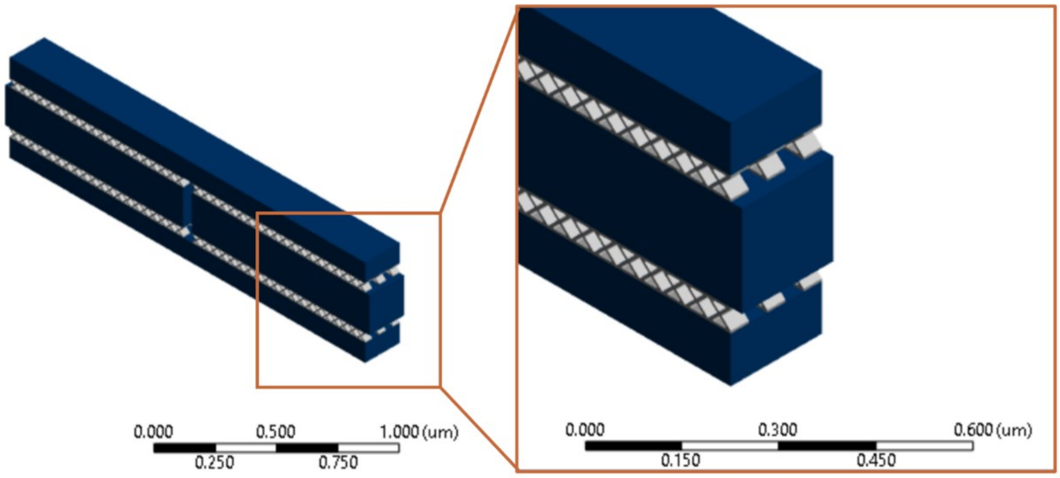

Figure 166: The 0.94 volume ratio model showing extruded layers of mortar with gaps in between the layers

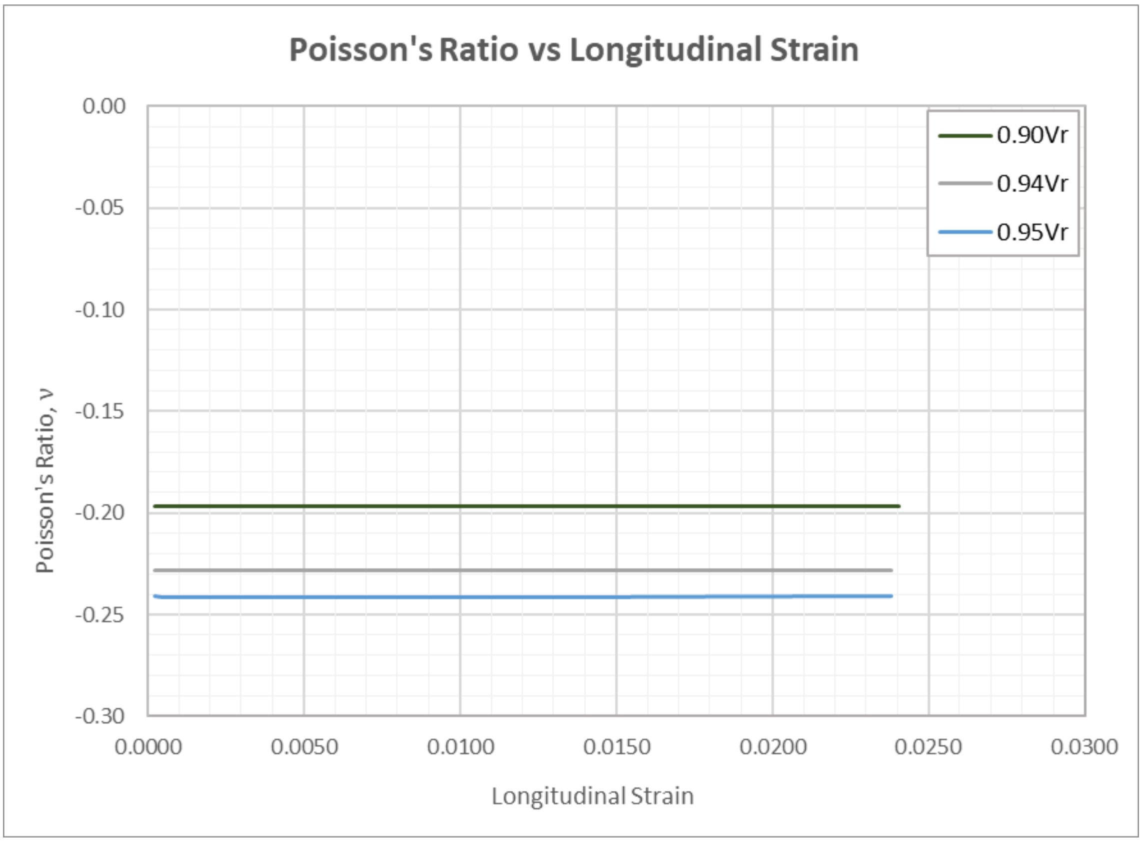

Figure 167: Comparison between different volume ratio models caused by varying gaps between the layers of mortar

The added gaps increased the volume ratio of the bricks. This has a similar effect to the 2D models, where the increased volume ratio decreases the Poisson's ratio. However, in the case of the 3D models, the deformation mechanisms do not occur in the same strain range as for the 2D models and show consistent Poisson's ratio rather than the variability observed previously. The initial speculation is that it is due to the fact that the deformation mechanism is different, the buckling does not occur as the extruded models are not slender enough to allow for it. Alternatively, this is influenced by the elastic material properties that have been used, which explains linear deformation in multiple planes. The following section looks at the effect of the changed material model on the results.

Elastic Versus Hyperelastic Material Properties

Considering the fact that Wang & Boyce (2010) used a viscoelastic material model, it was of interest to see the influence of the different material models on the Poisson's ratio.

It is expected that the changing of the material model from elastic to hyperelastic will have some effect on the FEA results, but marginal for the lower strains as the brittle properties of the elastic viscoplastic present themselves at approximately 5% strain, which is higher than most of the models analysed. However, due to the challenge of having to apply multiple loading steps if the viscoelastic model was used, hyperelastic material model was applied instead, using the experimental data. The stress-strain curve was imported into Engineering Data, which was obtained from Wang et al.'s paper (Wang, Boyce, Wen, & Thomas, 2009), Figure 169.

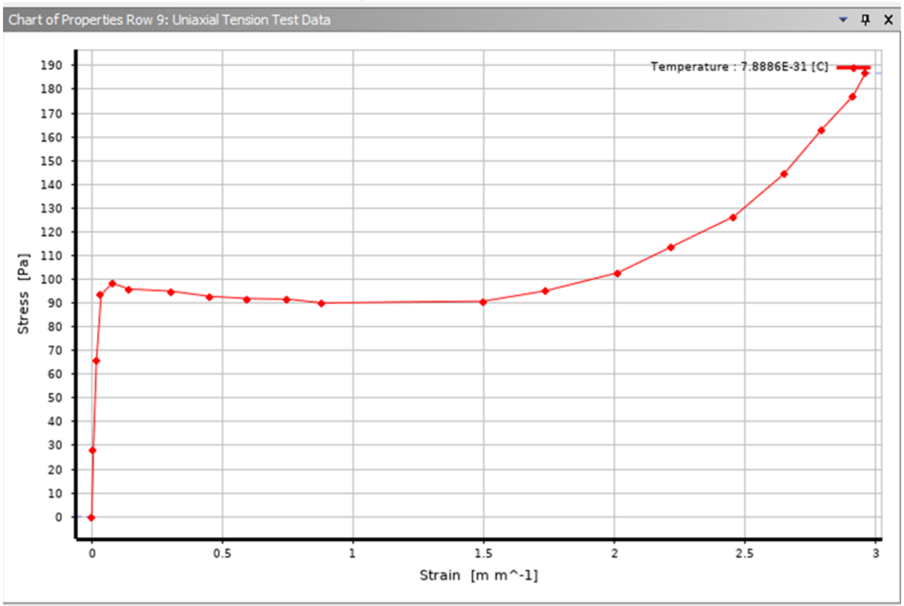

Figure 168: Strain-stress curve inputted into Engineering Data for the SU-8 material

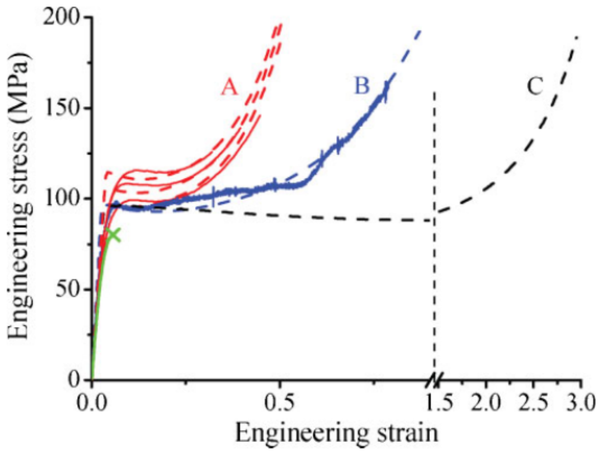

Figure 169: Engineering stress-strain behaviour of SU-8 beams under uniaxial tensions: solid lines) experimental data; dashed lines) constitutive model (Wang, Boyce, Wen, & Thomas, 2009)

All other material properties remained the same and are listed in Table 21. During this test, the fully extruded model, with the z-direction extruded by 0.5µm, was run with both sets of material properties at the same strain level. Initial results show some differences between materials. The elastic material model shows a slightly lower Poisson's ratio, which might be a good case for optimisation. A 0.004 difference in Poisson's ratio was obtained. At this stage, it is not disregarded that the different material models applied might influence Poisson's ratio versus strain correlation overall. Further comparison will be drawn when comparing the beam models in the next section.

	Elongation %	***Strain***	***Poisson's ratio***
Hyperelastic material model	0.98	0.000631	-0.064
Elastic material model	0.98	0.000670	-0.068

Table 30: Comparison of Poisson's ratio between the elastic and hyperoelastic model being used

Beams Element Mortar Model

One of the potential options that was explored is the use of beam elements instead of solid elements. This would reduce computational time significantly as beams have a lesser number of integration points, but it can also allow the exploitation of properties of a slender structure if this speculation is indeed true.

After a few initial attempts, the model shown in Figure 170 was derived using similar parameters to the 0.90 volume ratio model – the same height and width of the unit cell of mortar and the same width of the strut's width - with a very small depth of 0.0005µm applied to the model to achieve the slender structure. In this model, the bricks are made using solid elements, and the mortar consists of Xs that are built using two beams that cross each other. The beams have a circular cross-section to see if this would influence the performance of the model.

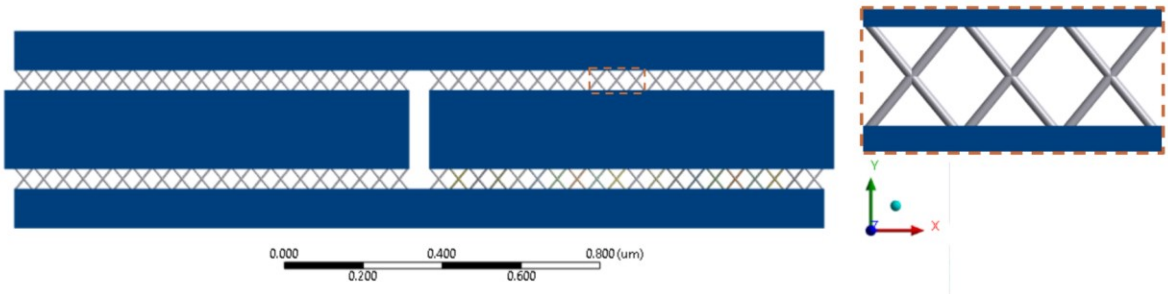

Figure 170: Left) The brick-and-mortar structure consists of bricks, which were made using solid elements and mortar, which was made using beam elements; Right)A section showing the beam elements

The combination of solid elements and beam elements was decided to retain some similarity between the models. However, as mortar brought on the highest computational demand, it was the most crucial aspect of the geometry that needed to be simplified to reduce the complexity of the analysis.

Initially, the model was very thin so that we could see the influence of the brick thickness on the results. Gradually, the thickness was added with variations of repeated units. Similarly to 2D models, the initial analysis was carried out in ANSYS Static Structural. The brick was meshed using the Hex dominant method, with the element geometry set to All Quad. The elements for the brick were sized at 0.025µm. The beams were created using the default ANSYS settings, and their edge size was set to 0.002 µm.

To ensure the structure was connected, Shared Topology was used and Merged setting was applied. BEAM188 elements were used for the mortar, as shown in "Appendix 1: 3D Discretisation Elements" which is a three-dimensional linear element.

This resulted in 22226 nodes and 7072 elements, which is a considerable reduction, even when compared to the 2D models.

The beams were manually connected to the bricks, where the bricks were target bodies, and the beams were contact bodies.

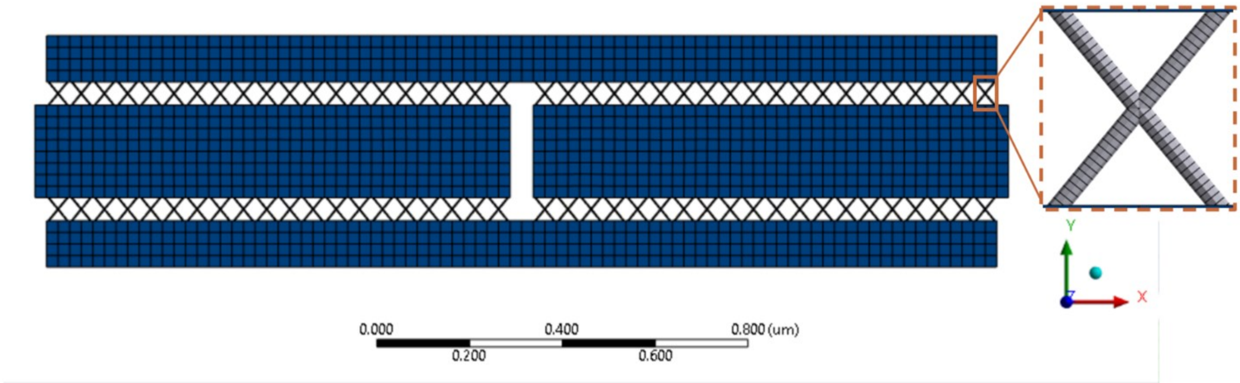

Figure 171: The mesh of the model with the solid element bricks and beam element mortar

The left side of the model was fixed. The right side was where varied displacement was applied in the x-direction, with additional input of zero displacement in y- and z-directions. The bricks were set to have no deformation and rotation in the z-direction to prevent the model from rotating out of the plane. However, mortar had an ability to deform in z-direction, while still restricted to not rotate out-of-plane, which was decided to see if the out-of-plane displacement is one of the causes of the consistent PR over the strains observed in the extruded models.

For the solution, large deformations were enabled, and deformation in the y-direction was measured using two probes on the top and bottom sides of the model. Additionally, the equivalent stress (von Mises) was measured to see the points of failure and weaknesses for potential future optimisations.

Results

These were the results obtained during the beam element analysis. The screenshots in Figure 172 and Figure 173 were from the analysis with low deformation, equating to ≈ 1.2% n and ≈ 2.4% strains. The analysis was carried out up to ≈ 4.8% strain before the deformation was too large to converge.

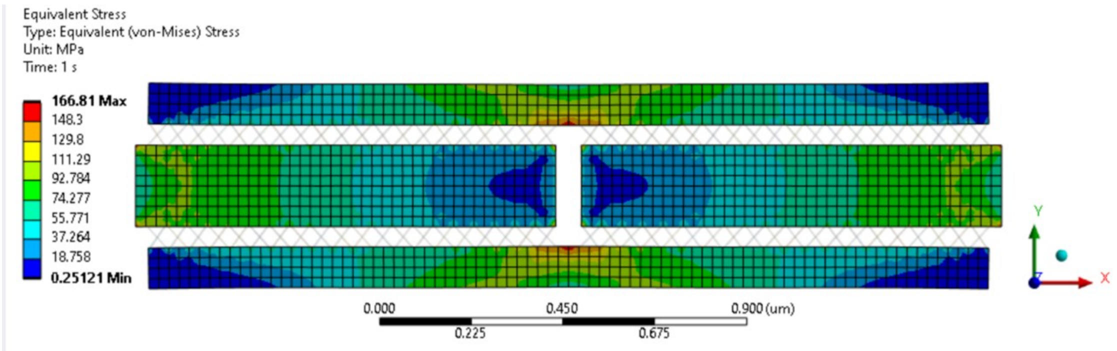

Figure 172: The results showing the equivalent stresses (von Mises) on the model at approximately 1.2% strain deformation

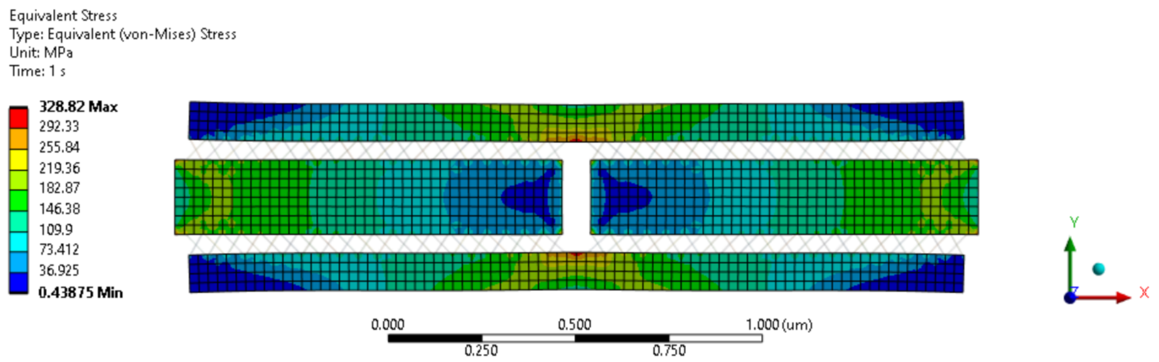

Figure 173: the results showing the equivalent stresses (von Mises) on the model at approximately 2.4% strain deformation

Figure 174 shows the axial force experienced by the beams. The beams furthest away from the centre experience the highest level of axial stretching. The different colours also indicate very clearly that one beam experiences much more axial force than another, correlating to the observations and assumptions made for the analytical model.

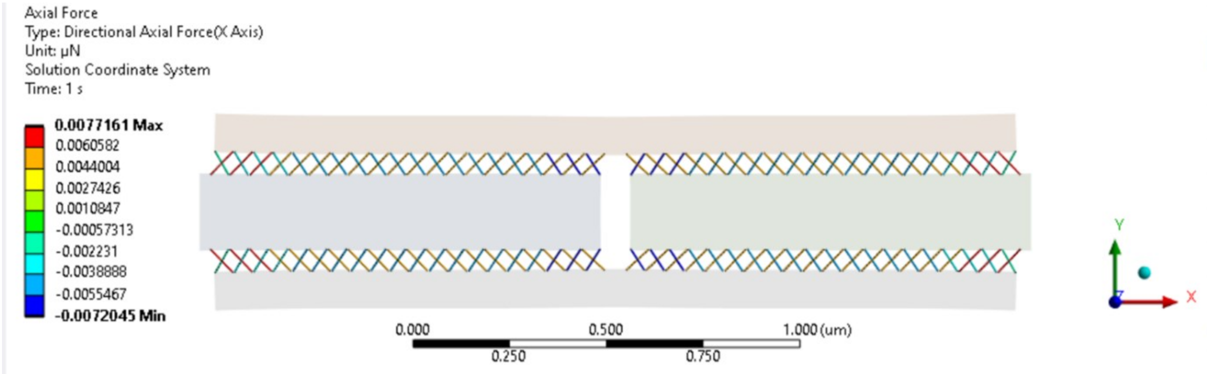

Figure 174: The axial forces on the beams at approximately 2.4% strain deformation

The plot in Figure 175 shows the results for two structures: elastic material model, and hyperelastic material model.

The thin *elastic* structure beam model with no out-of-plane deformation, the Poisson's ratio decreases with the higher strains. The boundary condition restricting the out-of-plane deformation is feasible, as in real life the continuous matrix where the repeated units are close to each other, the out-of-plane deformation will be restricted.

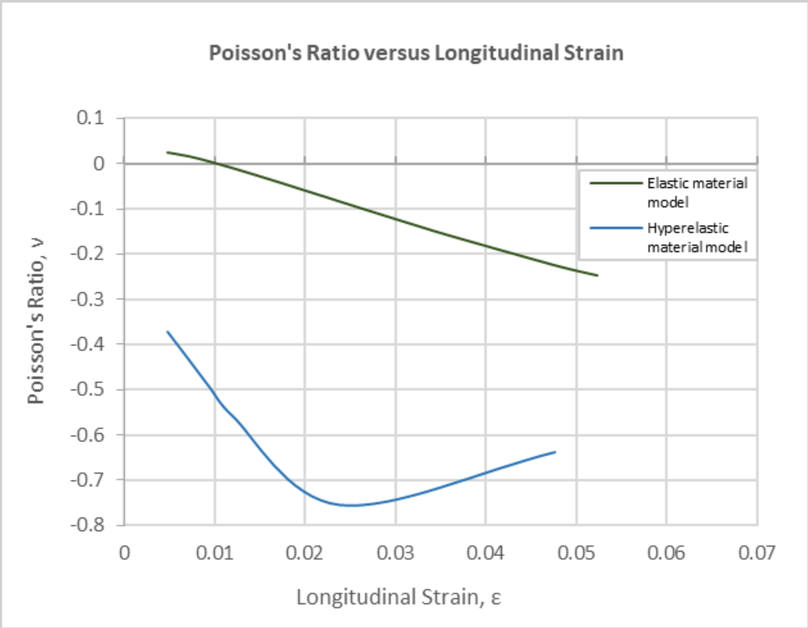

Figure 175: Results for beam element containing structure for Poisson's ratio and longitudinal strain up to approx. 4.8% for elastic and hyperelastic material models

The hyperelastic material model was applied in similar manner and the results were obtained for the quasi-static analysis. These results show that PR decreases with the strain and then starts increasing again. This is very similar to the pattern previously observed with the 2D models. Figure 176 was plotted to show the direct comparison, showing the 2D and 3D results for the parameters of the 0.90 volume ratio model being applied.

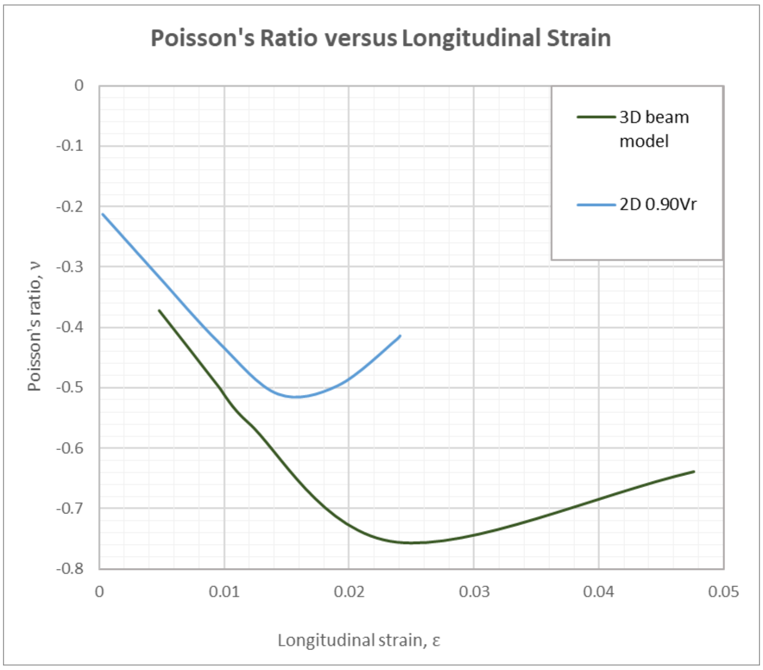

Figure 176: A comparison of the hyperelastic model's results with the previously obtained results for the 2D model with a 0.90 volume ratio

The beam model with hyperelastic material and thin structure and no out-of-plane deformation showed the behaviours previously observed in 2D models. It shows that the slender body geometries can replicate the behaviours previously observed in the 2D models with an even lower magnitude of the Poisson's ratio achieved. It is a similar behaviour that can be observed with nacre; however, it lacks the initial positive PR region. It also bears some similarity to Wang & Boyce's (2010) behaviours where the Poisson's ratio increases post yield.

This should be explored further in future work following this project, as it has a high potential for designing mechanical metamaterials.

Buckling

Following the results found, it became crucial to understand the mechanism occurring in the X-shaped mortar that could be contributing to the behaviours within the model. Wang & Boyce, as described in section Mechanism 1 in Chapter 2 Literature Review suggested that buckling might be occurring within the structure, hence this is explored in this section.

Slenderness ratio can be used to determine structure's susceptibility to buckling. Slenderness ratio is given by:

$$Slenderness\ Ratio, \lambda = \frac{KL}{r}$$

(134)

Where L is the unsupported length of the strut

And r is the radius of gyration of its cross-section

K is the column effective length factor

The effective length factor is determined by the type of fixture of the slender column, as shown in Figure 177.

(a) Pinned-pinned column	(b) Fixed-free column	(c) Fixed-fixed column	(d) Fixed-pinned column
$P_{cr} = \frac{\pi^2 EI}{L^2}$	$P_{cr} = \frac{\pi^2 EI}{4L^2}$	$P_{cr} = \frac{4\pi^2 EI}{L^2}$	$P_{cr} = \frac{2.046\,\pi^2 EI}{L^2}$
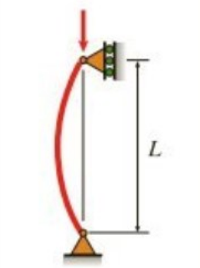	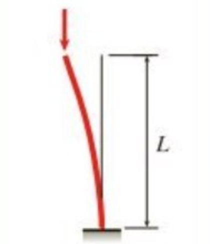	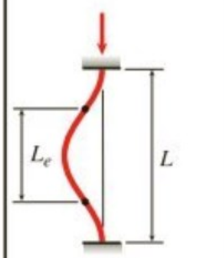	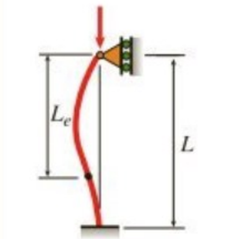
$L_e = L$	$L_e = 2L$	$L_e = 0.5L$	$L_e = 0.699L$
$K = 1$	$K = 2$	$K = 0.5$	$K = 0.699$

Figure 177: The diagram showing different fixtures and different effective length factors, where (a) shows pinned-pinned column, (b) fixed-free column, (c) fixed-fixed column, (d) fixed-pinned column (Goodno & Gere, 2018)

And radius of gyration is given by

$$Radius\ of\ gyration, r = \sqrt{\frac{I}{A}}$$

(135)

Where I is the second-area moment of inertia

And A is the cross-sectional area

The second-area moment of inertia can be found using the geometrical characteristic of the cross-section. For a square cross-section, the following equation applies:

$$\text{Second} - \text{area moment of inertia}, I = \frac{a^4}{12}$$

(136)

Where a is the width of the cross-section.

The worked example is for the 0.90 volume ratio model. The assumption was made that the strut will be treated as fixed at both ends due to its connection to the bricks on both ends. The dimensions used for the worked example are in Table 31.

Length of the strut, L	**Width of the cross-section, a**	**The column effective length factor, K**
0.0707 µm = 7.07^{-8} m	0.005 µm = 5^{-9} m	0.5

Table 31: The dimensions used for the worked example, utilising the dimensions of the 0.90 volume ratio model

The worked example starts with finding of the second-area moment of inertia. The dimensions used are converted into meters, and square cross-section is used.

$$\text{Second} - \text{area moment of inertia}, I = \frac{a^4}{12} = \frac{6.25^{-34}}{12} = 7.26^{-29}$$

.

Using the found second-moment of inertia, the radius of gyration can now be found, using equation (135).

$$Radius\ of\ gyration, r = \sqrt{\frac{I}{A}} = \sqrt{\frac{7.26^{-29}}{5^{-18}}} = 6.41^{-7}$$

Now, these can be substituted into the slenderness ratio equation (134).

$$Slenderness\ Ratio, \lambda = \frac{L}{r} = \frac{0.5 \cdot 7.07^{-8}}{6.41^{-7}} = 0.055$$

The slenderness ratio found is very low indicating that the column is unlikely to be susceptible to buckling with a more likely failure mode being crushing due to the compressive stress exceeding the material's strength.

This shows that the deformation observed is a combination of bending and axial deformation instead of buckling.

Chapter 7 – Discussion

The project has two distinctive areas that need to be investigated separately to achieve an adequate understanding of both when looking at the existing literature and research publications: the Finite Element Method and Auxetics. Understanding these areas and state-of-the-art literature was crucial before knowledge from both areas could be combined and applied confidently.

The literature review revealed areas of research around the themes mentioned above and helped to identify a research gap – nacre-inspired auxetic mechanical metamaterials. This research gap led to finding the experimental evidence that nacre is auxetic and the identification of four theorised mechanisms that might have been responsible for the auxetic behaviour.

The structure of the nacre was found to be resembling that of brick and mortar throughout, and the critical components were identified. Brick was likely a rigid and brittle body, and mortar was some form of viscoelastic matrix. Out of the four mechanisms, only one, mechanism 1, focused its speculations around the auxeticity of nacre on mortar and hence became a particular focus of this work. The remaining three mechanisms were focused on the rigid bricks or interlinking bridges – both are rigid bodies. These mechanisms can be exploited by adapting the synthetic geometries of the composites and should be considered separately. However, the mechanism 1 suggestion was fascinating in the way that it could pose an opportunity to see whether viscoelastic or elastic materials can be manipulated within composites to generate the NPR.

Through the literature review, it was shown that the nacre itself possesses a number of desirable properties, and it has been a source of inspiration for many composites. The gap was identified in trying to focus on replicating its auxeticity over other mechanical properties, which could be an actual underlying cause for other improved properties. The section ‘Characteristics of Auxetics’ showed the correlation between NPR and numerous enhanced mechanical properties.

Utilising what was learnt within Chapter 2, the methodology was posed, looking at the practicalities of FEA, the numerical models governing it, the limitations, and even considering some potential errors and ways of rectifying them, such as through validation and verification.

While preparing the method for the project, a concern arose, which was that there was no physical data available for the exact models being studied. The method was verified instead to improve the reliability of the computational models. Method verification took existing experimental data for a different auxetic model, re-entrant honeycomb, and applied boundary conditions that would be similar to the ones used for the tensile testing of the nacre-inspired models. The method was successfully verified against the FEA, experimental and analytical data found in the literature and further verified by analytical data obtained using Masters and Evans’ analytical approach to the re-entrant honeycomb. The highest disparity during the method verification was in ‘Test 1 – Initial Test’, which is mainly attributed to the edge effect and the closeness of the deformation measuring probes to the edges of the model. This issue was rectified after being investigated in ‘Test 2 – The Edge Effect Sensitivity’. Two more tests were performed using some of the probes from Test 2. ‘Test 3 – The Poisson’s Ratio of the Rib Sensitivity’ looked at the effect of material properties on the model, showing little variation in results when the re-entrant honeycomb material’s Poisson’s ratio was adjusted. ‘Test 4 – The Poisson’s Ratio of the 3D Structure’ looked at how additional plane to geometry affected the results, which showed that there was some effect, but it was not significant.

The method verification allowed an increase in awareness of the physics and setup, which can affect the results significantly with minuscule changes, but also allowed the development of the knowledge of the software used by building a familiarity with the modelling and simulation process. This method was consequently applied to the three out of four nacre mechanism models described in the previous sections, where new structures were imported and tested under the same conditions and, hence, using the same boundary conditions.

Once the method was obtained, the work moved on to developing analytical models using some of the previously existing analytical models found in the literature as the basis. Three analytical models were derived for mechanisms 1, 2 and 3. At this stage, mechanism 4 was dropped due to its nature. The nanograin rotation and deformation described in mechanism 4 were assumed to be more challenging to replicate in composites and their analytical and numerical models. Hence, the focus shifted to the remaining models.

The analytical model of mechanism 1 was inspired by the work of Master and Evans on the re-entrant honeycomb analytical model, where flexing and hinging of structural elements were utilised, and the yield transition was considered to be approximately $\varepsilon_x^T \sim 0.0012$ from experimental data of Song et al. (2008). At the yield transition, shear modulus, $G_{rib,}$ remained constant as the pre-yield value, but Young's modulus, E_{rib}, was reduced to 0.33GPa (by a factor of 10). The values of K_h/K_s before and after the yield transition were 0.37594 and 3.75998, respectively. When compared to Song et al.'s experimental data, the experimental data of nacre shows positive Poisson's ratio at immediate strains post-yield, before it shows NPR. It then again returns to the near-zero value at higher strains. The analytical model of mechanism 1 shows the transition from the positive PR to NPR as the strain increases but this transition occurs at yield rather than post-yield. Mechanism 1 fails to show positive or near zero PR at the highest strain and this is something that Wang & Boyce model predicts. The mechanism 1 model can predict finite positive Poisson's ratio at low strain which is consistent with the experimental data by Song et al. Mechanism 1 shows a correlation between increased volume ratio of the platelets and the increase in magnitude of maximum PR which agrees with the models by Wang & Boyce.

The Mechanism 2 analytical model used its geometrical shape to find the displacements in the x- and y-directions. Due to the curvature of the brick, it was treated as a section of a circle, and hence the rate of climb was calculated. The model showed a sustained rate of decrease in PR, which was related to the angle of the curvature.

Mechanism 3 was possibly the most simplified, where the interlinking bridges were modelled as isosceles trapezoids, the changes in deformation were found using the deformation phases, and the trigonometric functions determined the rate of climb.

The analytical models were used for parametric studies to improve the understanding of the importance of the geometrical properties in maximising NPR. It was also the first step in trying to understand the behaviours present in each mechanism. For example, with mechanism 2, it was essential to consider different curvature levels to see the influence of the angle and radius on NPR. Progressing from the analytical models to finite element modelling allowed more analyses to be done and more parametric studies to be carried out. Mechanism 1 became a focus very quickly due to its intriguing behaviour.

Within 2D models, mechanism 1 presented varying Poisson's ratio with increasing strains. The magnitude of the Poisson's ratio was dependent on the volume ratio of the bricks versus the platelets, as well as the geometry of the mortar, including the slenderness of the ribs of the X's. Each of those parameters was tested and compared in the 'Parametric Study' section. The FE models were investigated using other metrics as well so that the simulation could be improved. These metrics included a mesh comparison study, which was used to find the most suitable mesh size that was sufficient to provide reasonably accurate data without compromising too much on the computational time. Another study looked into convergence to determine the areas that might require a finer mesh. However, this study found that the deformation of the model was already converged within the first iteration with the triangular mesh, which was determined through a previous mesh comparison study and adaptive mesh, along with any further refinements, were not required to improve the accuracy of the data.

The developed models varied greatly in their performance, showing a vast dependency between the volume ratio of the model and Poisson's ratio and how the geometry of the bricks and mortar affected the volume ratio.

The key observations on the behaviour of Mechanism 1 are that the higher volume ratio models generally produced lower PR. However, they were likely to experience failure of the simulation (unconverged results) earlier than their lower volume ratio counterparts, and also, from a parametric study, the lowest magnitude of PR was obtained by the model with the widest unit cell, and its PR was nearly -0.80, as found in Figure 141.

The 2D models of mechanism 1 showed that the Poisson's ratio was lower in magnitude when the model was approaching the double bending deformation and then slowly levelled up when nearing the point of failure. Bending combined with axial deformation was likely a causing factor for the negative Poisson's ratio.Wang & Boyce (2010) reported buckling in their paper, however the slenderness ratio of this model and load applied show that buckling is unlikely to have occurred, as mentioned in section 'Buckling' in Chapter 6 FE Models And Analysis 3D Models.

Some research by Zhang & Ren (2020) that has not been previously discussed but is important to mention at this stage consisted of a study that investigated the utilisation of buckling in 2D auxetic models in order to enhance their NPR (Zhang &

Ren, 2020). This deformation mechanism has been showed in many 2D auxetic models. The 2D models of mechanism 1 investigated in this thesis support their findings, and it might be an interesting phenomenon to observe in the future when looking at incorporating even more geometries into the study of the mechanism 1 models, but which fell out of the scope of this work.

The last point on mechanism 1, which is likely the most critical to note, is that the behaviours of the 0.95 volume ratio model when compared to the experimental data, showed the same pattern with <u>lower</u> Poisson's ratio observed. The difference in Poisson's ratio was expected as the FEA was carried out with synthetic materials – alumina platelets and SU-8 – which have different individual material properties than nacre's aragonite and organic matrix. The lower NPR could indicate that the model had some enhanced mechanical properties. In comparison to Wang & Boyce's model, the results did not achieve quite as low PR, but there was more similarity to the nacre's experimental data than what Wang & Boyce have achieved. This could be indicative of the similar behaviour present in nacre's organic matrix itself.

When mechanism 1 was developed into a 3D system, the additional plane increased the complexity, and the deformation mechanism changed through the out-of-plane deformation that is now present. An NPR was also achieved in the extruded models, but it was constant with the increasing strains, indicating that the ratio of change remained the same in y- and x-direction. A study on two different material models was carried out to investigate the potential factors. The test showed a slight difference for the data point chosen. However, this was not entirely dismissed as a potential factor in changing behaviour.

The initial assumption was made that the fully extruded model was too thick, which led to a different deformation mechanism, which did not cause the same variability as buckling. To remedy this, gaps between the layers of mortar in the z-direction were introduced. This increased the volume ratio of the models and, interestingly, resulted in a lower magnitude Poisson's ratio. However, constant PR remained, and no buckling was observed with jamming present instead.

To introduce the elastic instability to the 3D model, beam models were created and served additional purpose. They reduced the computational time required by the solid elements. The beam models were purposefully created as a thin surface with a very slender body and were additionally constrained in the z-direction. These changes resulted in Poisson's ratio changes – now, the PR was linear but not constant. To further manipulate the model and see if the behaviours from the 2D models can be replicated, the hyperelastic material model was applied again. This time, the behaviour observed was very similar and replicable to the 2D 0.90 volume ratio model. The differences in the results between the last beam model and the 2D 0.90 volume ratio model could be attributed to many factors, including the fact that 3D beams had a circular cross-section that cannot be replicated in 2D but also due to a different element type. Most notably, the behaviour was finally replicated, although the additional constraints could be unrealistic. Removing the displacement in the z-direction hints towards another factor of consideration for the 3D models. When looking at Figure 165 on page 261, it can be observed that the area of deformation is different between the 2D and 3D models. It is assumed that the out-of-plane deformation is one of the root causes.

In 3D models, out-of-plane deformation can be harnessed to enhance the NPR, which is supported by research carried out by Li et al. (2017). Their work considered out-of-plane deformation in designing the 3D models with tuneable Poisson's ratio (Li, Hu, Chen, & Wang, 2017). This could be another avenue to explore in the future work on this topic. Both of the papers referenced in this chapter, the paper by Zhang & Ren (2020) and the paper by Li et al. (2017), suggest two different methods of tuning the PR to obtain the lowest value with 2D and 3D considerations, respectively. This reinforces the fact that there are multiple ways of achieving and enhancing NPR.

The Mechanism 2 analytical model showed a linear increase in PR in comparison to longitudinal strain. The analytical model was used for a parametric study showing the dependency between the curvature of the brick and the NPR. The curvature of the brick was adjusted through the changes in angle, radius, and length parameters. As expected, the higher level of curvature resulted in a lower magnitude of PR.

This mechanism in the 2D FE model showed constant PR of negative value, which is suspected to be due to the fact that the brick had a sloped surface with the linear profile. The slope of the brick dictated the deformation and led to the sustained rate of change matching the climb rate against the curve. This FE model was not validated against the analytical data, with likely difference that the analytical model had a curved surface rather than sloped. Also, it was not validated against the existing literature, and it was dropped at this stage. The benefits of the curvature in the metamaterials are already present in the literature, not only presented by work by Espinosa, et al. (2011) but also explored by Peng & Bargmann (2024). Hence, this was not a focus of this thesis.

The Mechanism 3 analytical model was based around the trapezoid-shaped bridges and sliding. It was a very simplified model, but it showed clearly how the bridges might affect the PR. The PR dependency was on the height of the bridge elements and the angle at which the climb occurred. The developed 2D FE models were performed in stages due to the challenging nature of the multiple phases of deformation that were difficult to replicate within ANSYS Static Structural. It is thought that the limitations within the FEA software itself make multiple constraints impossible to apply. There is too much variability between the phases to run it as a single model.

The mechanism 3 2D FE model showed a very similar pattern to the analytical model and could be considered validated.

Recommendations

It is essential to acknowledge that the work carried out in this thesis relied on computational models. The simulation has its limitations, and it often does not perfectly replicate the real world, which is filled with imperfections that cannot be fixed with a series of assumptions. And vice-versa, there are imperfections within the computational simulation that will not be observed in the real world. Although some models are considered validated, there is still scope for error.

There are a series of recommendations presented by the author that could be used to develop this work, its method and with the further exploration of the topic.

Firstly, the work explored in this thesis looked at each mechanism individually with an interest in finding a replication of the behaviour of nacre to truly enhance the mechanical properties of the synthetic material. It is possible that the combination of some or all of the mechanisms might be ideal and might produce results matching more closely those reported in actual nacre. This should be explored separately to see how the enhanced properties can be achieved by utilising the mortar shearing/buckling, concave platelets, interlinking bridges, and perhaps even the nanograin rotation.

The 3D FE models were not as widely studied as the 2D FE models. There is much potential to develop further the 3D models, such as by incorporating different known auxetic geometries into the mortar, such as re-entrant honeycomb instead of X's. The brick-and-mortar structure could be replicated as a sandwich structure.

The models could be run with different combinations of materials instead of alumina and SU-8. These were chosen for comparability to the existing literature, but other material combinations might provide much more beneficial properties for different applications. To a degree the analytical model for mechanism 1 enables this to be explored as a first approximation though varying the K_h/K_s ratio for different materials.

Further development of this analytical model would consider non-rigid and/or micro-structured platelets which would, therefore, also include mechanism 4 not studied in this project.

There is a potential for the optimisation of the models through applications of Genetic Algorithm Optimisation and which should be done to achieve ideal parameters leading to the required mechanical properties for specific applications. It could extend and provide more suitable candidate for the model than the parametric studies carried out in this thesis.

The models can also be developed and optimised for a particular application, such as to have improved impact protection capabilities that have not been explored as part of this thesis but might be assumed with the general trend of NPR correlating to the numerous properties that make auxetics desirable for those applications. Using the brick-and-mortar models developed, impact testing should be run to observe rate-dependency and compare it to a conventional system to verify this speculation.

Lastly, as manufacturing methods develop, such as that described by McHale et al. (2024), it would be hugely beneficial to see how the geometries would perform experimentally to confirm or otherwise the accuracy and usefulness of the analytical and computational models through measurements using physical samples.

Conclusions

The literature review identified a research gap in nacre-inspired auxetic mechanical metamaterials, leading to the exploration of four mechanisms that were theorised to be an explanation of nacre's auxetic properties. The methodology was established and verified using existing data for re-entrant honeycomb models.

Analytical models were derived for mechanisms 1, 2, and 3, with parametric studies highlighting the geometric influences on NPR. Transitioning to finite element models revealed further insights into the mechanisms' behaviours. Focus was given to mechanism 1, which speculated on the role of the elastic mortar in nacre's auxeticity. Mechanisms 2 and 3 were explored, focussing on the role of brick morphology and connectivity. The FE models showed dependency on volume ratio and geometrical properties.

The 2D FE model of the 0.95 volume ratio exhibited similar behaviour to the experimental data of nacre, showing that mechanism 1 predicted behaviour closest to that of nacre, hence achieving the main goal of this project.

Most importantly, the mechanisms present during the deformation can be manipulated within the computational space to enhance the NPR, with other potential benefits being brought by this. The work shows many potentials of fine-tuning Poisson's ratio of the mechanical metamaterials.

This research opens up many new avenues to further the knowledge of nature-inspired auxetic metamaterials.

References

Ahmad, Z., & Rad, M. S. (2014). Poisson's Ratio and Energy Absorption of Auxetic Foam under Dynamic Loading. *Journal of Advanced Research in Materials Science, 1*(1), 28-35. Retrieved September 10, 2021, from https://www.akademiabaru.com/doc/ARMSV1_N1_P28_35.pdf

Akhavan, A. (2014, January 12). *The Silica Group*. Retrieved from The Quartz Page: http://www.quartzpage.de/gen_mod.html#cristobalite

Alderson, A. (2015, May 22). *The seashell-inspired material inspiring a new wave of safety gear in sport*. Retrieved January 29, 2018, from THE CONVERSATION: http://theconversation.com/the-seashell-inspired-material-inspiring-a-new-wave-of-safety-gear-in-sport-42092

Alderson, A., & Evans, K. (2009). Deformation mechanisms leading to auxetic behaviour in the α-cristobalite and α-quartz structures of both silica and germania. *Journal of Physics: Condensed Matter*(21).

Alderson, A., & Evans, K. E. (1997). Modelling concurrent deformation mechanisms in auxetic microporous polymers. *Journal of Materials Science, 32*, 2797–2809. doi:10.1023/A:1018660130501

Alderson, K. L., & Coenen, V. L. (2008, February 7). The low velocity impact response of auxetic carbon fibre laminates. *Physica Status Solidi B, 245*(3), 489 - 496.

Alderson, K. L., Pickles, A. P., P.J, N., & Evans, K. (1994, July). Auxetic Polyethylene: The Effect of a Negative Poisson's Ratio on Hardness. *Acta Metallurgica et Materialia, 42*(7), 2261-2266. doi:https://doi.org/10.1016/0956-7151(94)90304-2

Ali, M., Zeeshan, M., Qadir, M. B., Riaz, R., Ahmad, S., & Nawab, Y. (2018, Vovember 26). Development and Mechanical Characterization of Weave Design

Based 2D Woven Auxetic Fabrics for Protective Textiles. *Fibers and Polymers, 19*, 2431-2438. doi:https://doi.org/10.1007/s12221-018-8627-8

Allen, T., Shepherd, J., Hewage, T., Senior, T., L.Foster, & Alderson, A. (2015). Low-kinetic energy impact response of auxetic and conventional open-cell polyurethane foams. *Physica Status Solidi B, 252*(7), 1631-1639. doi:10.1002/pssb.201451715

Alomarah, A., Xu, S., S. H., & Ruan, D. (2020). Dynamic performance of auxetic structures: experiments and simulation. *Smart Materials and Structures, 29*(5). doi:https://doi.org/10.1088/1361-665X/ab79bb

ANSYS. (2002). *LS-DYNA® KEYWORD USER'S MANUAL; VOLUME II Material Models.*

ANSYS, Inc. (©2020). *ANSYS Meshing Solutions*. Retrieved from ANSYS: https://www.ansys.com/products/platform/ansys-meshing

ANSYS, Inc. (2023). *Locking in a quadrilateral element*. Retrieved from ANSYS/ LS-DYNA: https://lsdyna.ansys.com/locking-in-a-quadrilateral-element/

ANSYS, Inc. (1994). *ANSYS Theory Reference - Eleventh Edition.* (P. Peter Kohnke, Ed.)

Anthony, J. W., Bideaux, R. A., Bladh, K. W., & Nichols, M. C. (2001). Volume II: Silica, Silicates. In *Handbook of Mineralogy* (Vol. II). Mineral Data Publishing. Retrieved November 13, 2018, from http://www.handbookofmineralogy.com

Arjunan, A., Zahid, S., Baroutaji, A., & Robinson, J. (2021). 3D printed auxetic nasopharyngeal swabs for COVID-19 sample collection. *Journal of the Mechanical Behavior of Biomedical Materials*. doi:10.1016/j.jmbbm.2020.104175

Arjunan, A., Zahid, S., Baroutaji, A., & Robinson, J. (2021). 3D printed auxetic nasopharyngeal swabs for COVID-19 sample collection. *Journal of the*

Mechanical Behavior of Biomedical Materials, 114. doi:104175

Auxetix, L. (2007). Comparison of Zetix with conventional blast-proof materials. Retrieved from http://www.auxetix.com/science.htm

Bai, R., Awtar, S., & Chen, G. (2019). A closed-form model for nonlinear spatial deflections of rectangular beams in intermediate range. *International journal of mechanical sciences, 160*, 229-240. doi:10.1016/j.ijmecsci.2019.06.042

Barthelat, F., Tang, H., Zavattieri, P. D., Li, C. M., & Espinosa, H. D. (2007, February). On the mechanics of mother-of-pearl: A key feature in the material hierarchical structure. *Journal of the Mechanics and Physics of Solids, 55*(2), 306-337. doi:10.1016/j.jmps.2006.07.007

Baughman, R. H. (2003, October 16). Avoiding the shrink. *Nature, 425*(6959), 667.

Baughman, R. H., Shacklette, J. M., Zakhidov, A. A., & Stafström, S. (1998). Negative Poisson's ratios as a common feature of cubic metals. *Nature, 392*, 362-365. doi:https://doi.org/10.1038/32842

Baumgart, F. (2000, May). Stiffness - an unknown world of mechanical science? *Injury, 31*(2), 14-23. doi:https://doi.org/10.1016/S0020-1383(00)80040-6

Berger, A. (2019, March 12). *Biomimicry: technology inspired by nature*. Retrieved from The Ecologist: https://theecologist.org/2019/mar/12/biomimicry-technology-inspired-nature#:~:text=Biomimicry%20%2D%20or%20biomimetics%20%2D%20is%20the,in%20which%20they%20are%20facing.

Bi, Z. (2018). Applications—Solid Mechanics Problems. In Z. Bi, *Finite Element Analysis Applications: A Systematic and Practical Approach* (pp. 281-339). Academic Press. doi:https://doi.org/10.1016/B978-0-12-809952-0.00008-X

Bohara, R. P., Linforth, S., Nguyen, T., Ghazlan, A., & Ngo, T. (2023). Anti-blast and -impact performances of auxetic structures: A review of structures, materials, methods, and fabrications. *Engineering Structures, 276*, 115377. doi:https://doi.org/10.1016/j.engstruct.2022.115377

Bozkurt, Ö. Y., Özbek, Ö., & Abdo, A. R. (2017, October). The effects of nanosilica on charpy impact behavior of glass/epoxy fiber reinforced composite laminates. *Periodicals of Engineering and Natural Sciences , 5*(3), 322-327.

British Standards Instutution. (1991). *BS 7448-1:1991 Fracture mechanics toughness tests.*

Bruet, B., Qi, H., Boyce, M., Panas, R., Tai, K., Frick, L., & Ortiz, C. (2005). Nanoscale Morphology and Indentation of Individual Nacre Tablets from the Gastropod Mollusc Trochus Niloticus. *Journal of Materials Research, 20*(9), 2400-2419.

Caddock, B. D., & Evans, K. E. (1989). Microporous materials with negative Poisson's ratios. I. Microstructure and mechanical properties. *Journal of physics. D, Applied physics, 22*(12), 1877-1882. doi:10.1088/0022-3727/22/12/012

Chan, N., & Evans, K. E. (1997). Fabrication methods for auxetic foams. *Journal of Materials Science, 32*(22), 5945-5953. Retrieved 12 3, 2018, from https://link.springer.com/article/10.1023/a:1018606926094

Chellam, A., Velayudhan, T. S., Dharmaraj, S., Victor, A. C., & Gandhi, A. D. (1983). A note on the predation on pearl oyster Pinctada fucata (Gould) by some gastropods. *Indian Journal of Fisheries, 30*(2), 337-339.

Cheng, X., Zhang, Y., Ren, X., Han, D., Jiang, W., Zhang, X. G., . . . Xie, Y. M. (2022, June). Design and mechanical characteristics of auxetic metamaterial with tunable stiffness. *International Journal of Mechanical Sciences, 223*.

Choi, H. Y., Shin, E. J., & Lee, S. H. (2022). Design and evaluation of 3D-printed auxetic structures coated by CWPU/graphene as strain sensor. *Scientific reports, 12*(1), 7780. doi:10.1038/s41598-022-11540-x

Choi, J. B., & Lakes, R. S. (1991). Design of a fastener based on negative Poisson's ratio foam. *Cellular Polymers, 10*(3), 205-212.

Chung, D. D. (2017). 4 - Polymer-Matrix Composites: Mechanical Properties and Thermal Performance. In D. D. Chung, & Second (Ed.), *Carbon Composites (Second Edition): Composites with Carbon Fibers, Nanofibers and Nanotubes* (pp. 218-255).

Clarke, J., Duckett, R., Hine, P., Hutchinson, I., & Ward, I. (1994). Negative Poisson's ratios in angle-ply laminates: theory and experiment. *Composites, 25*(9), 863-868. doi:10.1016/0010-4361(94)90027-2

COMSOL INC. (2018). *The Finite Element Method (FEM)*. Retrieved January 29, 2018, from multiphysics CYCLOPEDIA: https://www.comsol.com/multiphysics/finite-element-method

COMSOL, Inc. (©2020). *Finite Element Mesh Refinement*. Retrieved from COMSOL: https://www.comsol.com/multiphysics/mesh-refinement

crystallography365 project. (2014, May 25). *Same… but different. The structure of beta–cristobalite.* Retrieved from Crystallography365: https://crystallography365.wordpress.com/2014/05/25/same-but-different-the-structure-of%EF%80%A0-beta-cristobalite/

Currey, J. D., & Taylor, J. D. (1974). The Mechanical Behavior of Some Molluscan Hard Tissues. *Journal of Zoology, 173*(3), 395-406.

Curry, D. (1980, July). The relationship between fracture toughness and Charpy impact transition temperatures in mild steel. *Materials Science and Engineering, 44*(2), 285-290. doi:10.1016/0025-5416(80)90128-7

D3O - Design Blue Limited. (2018). *TRUST STEALTH HELMET PAD SYSTEM*. Retrieved from D3O: https://www.d3o.com/partner-support/products/trust-stealth-helmet-pad-system/

Darolia, R., Walston, W. S., & Nathal, M. (1996). NiAl Alloys for Turbine Airfoils.

Superalloys, 561-570. doi:10.7449/1996/SUPERALLOYS_1996_561_570

Diaz, J. (2007, December 6). *Zetix Blast-Proof Fabric Resists Multiple Car Bombs, Makes Our Heads Explode*. Retrieved from Gizmodo: https://gizmodo.com/zetix-blast-proof-fabric-resists-multiple-car-bombs-ma-330343

Diaz, J. (2007, June 12). *Zetix Blast-Proof Fabric Resists Multiple Car Bombs, Makes Our Heads Explode*. Retrieved from Gizmodo: https://gizmodo.com/zetix-blast-proof-fabric-resists-multiple-car-bombs-ma-330343

Dill, E. H. (2012). *The Finite Element Method for Mechanics of Solids with ANSYS Applications.* Boca Raton: CRC Press.

Ding, F., Liu, J., Zeng, S., Xia, Y., Wells, K. M., Nieh, M.-P., & Sun, L. (2017, July 19). Biomimetic nanocoatings with exceptional mechanical, barrier, and flame-retardant properties from large-scale one-step coassembly. *Science Advances, 3*.

Donoghue, J. P., Alderson, K. L., & Evans, K. E. (2009, September). The fracture toughness of composite laminates with a negative Poisson's ratio. *physica status solidi (b), 246*(9).

Duncan, O., Shepherd, T., Moroney, C., Foster, L., Venkatraman, P. D., Winwood, K., . . . Alderson, A. (2018). Review of Auxetic Materials for Sports Applications: Expanding Options in Comfort and Protection. *Applied Sciences, 8*(941). doi:10.3390/app8060941

Dwivedi, K. K., Lakhani, P., Kumar, S., & Kumar, N. (2022, March). Effect of collagen fibre orientation on the Poisson's ratio and stress relaxation of skin: an ex vivo and in vivo study. *Royal Society Open Science, 9*(3). doi:10.1098/rsos.211301

Engineering Core Courses. (2016). *C5.1 Euler's Buckling Formula*. Retrieved from Engineering Core Courses: http://www.engineeringcorecourses.com/solidmechanics2/C5-buckling/C5.1-

eulers-buckling-formula/theory/

Engineering ToolBox. (2008). *Stiffness*. Retrieved September 6, 2021, from Engineering ToolBox: https://www.engineeringtoolbox.com/stiffness-d_1396.html

Espacenet. (n.d.). Retrieved July 20, 2021, from https://worldwide.espacenet.com/

Espinosa, H. D., Juster, A. L., Latourte, F., Loh, O. Y., Grégoire, D., & Zavattieri, P. D. (2011). Tablet-level origin of toughening in abalone shells and translation to synthetic composite materials. *Nature Communications, 2*(1), 173. Retrieved 12 3, 2018, from https://nature.com/articles/ncomms1172.pdf

Espinosa, H. D., Rim, J. E., Barthelat, F., & Buehler, M. J. (2009). Merger of structure and material in nacre and bone – Perspectives on de novo biomimetic materials. *Progress in Materials Science, 54*(8), 1059-1100. doi:https://doi.org/10.1016/j.pmatsci.2009.05.001.

Evans, K. E. (1991). Auxetic polymers: a new range of materials. *Endeavour, 15*(4), 170-174. Retrieved November 12, 2018, from https://www.sciencedirect.com/science/article/pii/016093279190123S

Evans, K., Nkansah, M., Hutchinson, I., & Rogers, S. (1991). Molecular network design. *Nature, 353*(6340), 124.

Fazita, M. N., Khalil, H. A., Izzati, A. N., & Rizal, S. (2019). 3 - Effects of strain rate on failure mechanisms and energy absorption in polymer composites. In M. Jawaid, M. Thariq, & N. Saba (Eds.), *Failure Analysis in Biocomposites, Fibre-Reinforced Composites and Hybrid Composites* (pp. 51-78). In Woodhead Publishing Series in Composites Science and Engineering. doi:10.1016/B978-0-08-102293-1.00003-6

Flimlin, G., & Beal, B. F. (1993). Major Predators of Cultured Shellfish. *Northeastern Regional Aquaculture Center Bulletin*(180).

Flores-Johnson, E., Shen, L., Guiamatsia, I., & Nguyen, G. D. (2014). Numerical investigation of the impact behaviour of bioinspired nacre-like aluminium composite plates. *Composites Science and Technology, 96*, 13-22. doi:https://doi.org/10.1016/j.compscitech.2014.03.001

Ford, J. (2020, September 9). *TheEngineer*. Retrieved March 9, 2021, from 3D printed smart swab could alleviate COVID-19 test concerns: https://www.theengineer.co.uk/3d-printed-smart-swab-covid-19-tests/

Fracture Toughness: Measurement, Types and Typical Values. (n.d.). Retrieved from MatMatch: https://matmatch.com/learn/property/fracture-toughness

Francesconi, A., Pavarin, D., Bettella, A., & Angrilli, F. (2008, December). A special design condition to increase the performance of two-stage light-gas guns. *International Journal of Impact Engineering, 35*(12), 1510-1515. doi:https://doi.org/10.1016/j.ijimpeng.2008.07.035

Frunza, M. C., Frunză, G., & Luca, R. (2010). The Use of Numerical Applications in the Study of Dental Contacts. *Applied Medical Informatics, 26*(2), June.

Fung, Y. C. (1968). Biomechanics: Its Scope, History, and Some Problems of Continuum Mechanics in Physiology. *Applied Mechanics Reviews, 21*, 1-20.

Gad, A. F. (2024). *pygad Module.* Retrieved July 10, 2024, from PyGAD: https://pygad.readthedocs.io/en/latest/pygad.html

Garber, A. M., Nolan, E. J., & Scala, S. (1963). *PYROLYTIC GRAPHITE - A STATUS REPORT.* Space Sciences Laboratory: Missile and Space Division. General Electric.

Gatt, R., Wood, M. V., Gatt, A., Zarb, F., Formosa, C., Azzopardi, K. M., . . . Grima, J. N. (2015). Negative Poisson's ratios in tendons: An unexpected mechanical response. *Acta Biomaterialia, 24*, 201-208. doi:10.1016/j.actbio.2015.06.018

Gauthier, S. (2013, May 9). *Four explosion-resistant materials that may save your* *future self*. Retrieved from the john hopkins News-Letter: https://www.jhunewsletter.com/article/2013/05/four-explosion-resistant-materials-that-may-save-your-future-self-18131

Gen, M., & Cheng, R. (1997). *Genetic Algorithm And Engineering Design.* John Wiley.

Gibson, L. J., & Ashby, M. F. (1988). *Cellular Solids: Structure & Properties.* Cambridge: Pergamon Press. Retrieved July 31, 2019

Goodno, B., & Gere, J. (2018). Chapter 11 Columns. In B. Goodno, J. Gere, & 9. Edition (Ed.), *Mechanics of Materials, SI Edition* (p. 988).

Green Mechanic [Contributors: Ullah Atta; Talha Atta]. (2014, April 20).

Grima, J., Gatt, R., Alderson, A., & Evans, K. (2006). An alternative explanation for the negative Poisson's ratios in α-cristobalite. *Materials Science and Engineering: A, 423*(1-2), 219-224. doi:10.1016/j.msea.2005.08.230

Grima, J., Jackson, R., Alderson, A., & Evans, K. (2000, December 15). Do zeolites have negative Poisson's ratios? *Advanced Materials, 12*(24), 1912 - 1918.

Grima-Cornish, J. N., Grima, J. N., & Attard, D. (2021). Mathematical modeling of auxetic systems: bridging the gap between analytical models and observation. *International Journal of Mechanical and Materials Engineering, 16*(4). doi:10.1186/s40712-020-00125-z

Grosser, H., & Bormann, P. (2003). Theoretical source representation. doi:10.2312/GFZ.NMSOP-2_IS_3.1

Guida, V. G. (1976, December 1). Sponge predation in the oyster reef community as demonstrated with Cliona celata Grant. *Journal of Experimental Marine Biology and Ecology, 25*(2), 109-122. doi:https://doi.org/10.1016/0022-0981(76)90012-5

Haecker, C.-J., Garboczi, E. J., Bullard, J. W., Bohn, R., Sun, Z., Shah, S. P., & Voigt, T. (2005). Modeling the Linear Elastic Properties of Portland Cement Paste. *Cement and Concrete Research, 35*(10), 1948-1960. Retrieved 11 12, 2018, from https://sciencedirect.com/science/article/pii/s0008884605001201

Hanifpour, M., Petersen, C. F., Alava, M. J., & Zapperi, S. (2018). Mechanics of disordered auxetic metamaterials. *The European Physical Journal. B: Condensed Matter Physics, 91*(11). doi:10.1140/epjb/e2018-90073-1

Han-sol, P. (2021, February 17). *TheKoreaTimes*. Retrieved from Exploring pandemic psyche in art: When you breathe out, people are frightened: https://www.koreatimes.co.kr/www/culture/2021/02/145_304195.html

HEAD. (2021). *AUXETIC 2.0 - THE SCIENCE BEHIND THE SENSATIONAL FEEL*. Retrieved from HEAD: https://www.head.com/en_SK/rs/stories/auxetic-the-science-behind-the-sensational-feel

Hearn, E. (1997). Chapter 11 Strain Energy. In E. Hearn, & 3rd (Ed.), *Mechanics of Materials 1: An Introduction to the Mechanics of Elastic and Plastic Deformation of Solids and Structural Materials* (pp. 254-296). doi:10.1016/B978-075063265-2/50012-8

Hearn, E. J. (1997). Chapter 14 Complex Strain and the Elastic Constants. In E. J. Hearn, *Mechanics of materials 1: An introduction of the mechanics of elastic and plastic deformation of solids and structural materials* (pp. 361-362).

Hook, P., Evans, K. E., Hannington, J., Hartmann-Thompson, C., & Bunce, T. (2006). *Patent No. KR20060009826.*

Horwood, A., & Chockalingam, N. (2023). Principles of materials science. In A. Horwood, & N. Chockalingam, *Clinical Biomechanics in Human Locomotion* (p. 123). doi:10.1016/B978-0-323-85212-8.00002-X

Hu, H., Zhang, M., & Liu, Y. (2019). 4 - Auxetic fibres and yarns. In *Auxetic Textiles.* doi:https://doi.org/10.1016/C2016-0-04399-1

Huai-Ling Gao, S.-M. C.-B.-Q.-B.-S.-F.-H. (2017). Mass production of bulk artificial nacre with excellent mechanical properties. *Nature Communications, 8*.

Hufenbach, W., Ibraim, F. M., Langkamp, A., Böhm, R., & Hornig, A. (2008). Charpy impact tests on composite structures – An experimental and numerical investigation. *Composites science and technology, 68*(12), 2391-2400. doi:10.1016/j.compscitech.2007.10.008

Humphrey, J. D. (2008). Disease and Predation. In P. C. Southgate, & J. S. Lucas, *The Pearl Oyster: A Beginner's Guide to Programming Images, Animation, and Interaction* (pp. 367-435). Elsevier Science. doi:https://doi.org/10.1016/B978-0-444-52976-3.X0001-0

Imbalzano, G., Tran, P., Ngo, T. D., & Lee, P. V. (2015). Three-dimensional modelling of auxetic sandwich panels for localised impact resistance. *Journal of Sandwich Structures & Materials, 19*(3), 291-316. doi:10.1177/1099636215618539

Imbalzano, G., Tran, P., Ngo, T. D., & Lee, P. V. (2017). Three-dimensional modelling of auxetic sandwich panels for localised impact resistance. *Journal of Sandwich Structures & Materials, 19*(3), 291–316. doi:10.1177/1099636215618539

Imbalzano, G., Tran, P., Ngo, T., & Lee, P. V. (2016). A numerical study of auxetic composite panels under blast loadings. *Composite Structures, 135*, 339-352. Retrieved 10 22, 2018, from http://sciencedirect.com/science/article/pii/s0263822315008843

Instron. (n.d.). *Instron*. Retrieved July 03, 2023, from https://www.instron.com/en-gb/resources/glossary/p/poissons-ratio#:~:text=Cork%2C%20however%2C%20has%20a%20Poisson's,candidate%20for%20sealing%20wine%20bottles.

International Organization for Standardization [ISO]. (2016). *Metallic materials — Charpy pendulum impact test [ISO 148-1].*

International Organization for Standardization [ISO]. (2020). *Plastics — Determination of Charpy impact properties [ISO 179-2].*

International Organization for Standardization [ISO]. (2023). *Plastics — Determination of Izod impact strength [ISO-180].*

International Organization for Standardization [ISO]. (2023). *Plastics — Determination of tensile-impact strength [ISO-8256].*

Irisarri, F.-X., Laurin, F., Leroy, F.-H., & Maire, J.-F. (2011, February). Computational strategy for multiobjective optimization of composite stiffened panels. *Composite Structures, 93*(3), 1158-1167. doi:https://doi.org/10.1016/j.compstruct.2010.10.005

J. L. Williams, J. L. (1982, February). Properties and an Anisotropic Model of Cancellous Bone From the Proximal Tibial Epiphysis. *Journal of Biomechanical Engineering, 104*(1). doi:10.1115/1.3138303

Jackson, A. P., Vincent, J. F., & Turner, R. M. (1988). The mechanical design of nacre. *Proceedings of the Royal Society of London. Series B, Containing papers of a Biological character*, 415-440.

Jawaid, M., Thariq, M., & Saba, N. (2019). *Failure Analysis in Biocomposites, Fibre-Reinforced Composites and Hybrid Composites.* Woodhead Publishing. doi:https://doi.org/10.1016/C2016-0-04423-6

Jayasuriya, M. A., Mccoy, R. W., & Lippman, M. A. (2022, January 11). *US Patent No. 16592805.* Retrieved from https://www.patentguru.com/US11220765B2; https://worldwide.espacenet.com/publicationDetails/biblio?CC=US&NR=11220765B2&KC=B2&FT=D

Jean Mercier, G. Z. (2003). Elastic behaviour of solids. In *Introduction to Materials Science* (pp. 121-150). Elsevier Science. doi:https://doi.org/10.1016/C2009-0-29148-3

Ji, S., Li, L., Motra, H. B., Wuttke, F., Sun, S., Michibayashi, K., & Salisbury, M. H. (2018, February). Poisson's Ratio and Auxetic Properties of Natural Rocks.

Journal of Geophysical Research: Solid Earth, 123(2), 1161-1185. Retrieved November 12, 2018, from https://onlinelibrary.wiley.com/doi/10.1002/2017JB014606

Jiang, L., & Hu, H. (2017). Finite Element Modeling of Multilayer Orthogonal Auxetic Composited under Low-Velocity Impact. *Materials, 10*(908). doi:10.3390 / ma10080908

Jiang, L., & Hu, H. (2017). Finite Element Modeling of Multilayer Orthogonal Auxetic Composites under Low-Velocity Impact. *Materials, 10*(908). doi:10.3390/ma10080908

Jiang, W., Ren, X., Wang, S. L., Zhang, X. G., Zhang, X. Y., Luo, C., . . . Evans, K. E. (2022). Manufacturing, characteristics and applications of auxetic foams: A state-of-the-art review. *Composites Part B: Engineering, 235*(109733). doi:https://doi.org/10.1016/j.compositesb.2022.109733

Jones, D. R., & Ashby, M. F. (2019). Chapter 16 - Fracture Probability of Brittle Materials. In D. R. Jones, M. F. Ashby, & Fifth (Ed.), *Engineering Materials 1: An Introduction to Properties, Applications and Design* (pp. 247-259).

Joseph, A. (2017). Chapter 9 - Oceans: Abode of Nutraceuticals, Pharmaceuticals, and Biotoxins. In A. Joseph, *Investigating Seafloors and Oceans* (pp. 493-554). Elsevier. doi:https://doi.org/10.1016/B978-0-12-809357-3.00009-6.

Juliana M. Harding, R. L., & Clark, V. P. (2002). Shellfish stalkers: Threats to an oyster. *VORTEX; Virginia Institute of Marine Science*.

K. E. Gunnison, M. S. (1991). Structuremechanical property relationships in a biological ceramic-polymer composite. *Materials Research Society symposia proceedings, 255*, 171-184.

Kakisawa, H., & Sumitomo, T. (2011, December). The toughening mechanism of nacre and structural materials inspired by nacre. *Science and Technology of Advanced*

Materials. doi:10.1088/1468-6996/12/6/064710

Katti, K. S., Mohanty, B., & Katti, D. R. (2006). Nanomechanical properties of nacre. *Journal of Materials Research, 21*, 1237–1242.

Key, S. W., & Krieg, R. D. (1973). Comparison of Finite-Element and Finite-Difference Methods. *Numerical and Computer Methods in Structural Mechanics*, 337-352. doi:https://doi.org/10.1016/B978-0-12-253250-4.50019-1

Koizumi, Y. (2020). Selective Electron Beam Melting. In S. Kirihara, & K. Nakata (Eds.), *Multi-dimensional Additive Manufacturing* (pp. 35-45).

Kolken, H. M., & Zadpoor, A. A. (2017). Auxetic mechanical metamaterials. *RSC Advances, 7*(9), 5111-5129. Retrieved 11 12, 2018, from https://pubs.rsc.org/en/content/articlehtml/2017/ra/c6ra27333e

Kolkena, H., Garciab, A. F., Plessisc, A. D., Meynend, A., Ranse, C., Scheysdf, L., . . . A.A.Zadpoora. (2022, January 15). Mechanisms of fatigue crack initiation and propagation in auxetic meta-biomaterials. *Acta Biomaterialia, 138*, 398-409. doi:https://doi.org/10.1016/j.actbio.2021.11.002

Lakes, R. (1987, February 27). Foam structures with a negative Poisson's ratio. *Science, 235*, 1038-1040. Retrieved November 12, 2018, from http://silver.neep.wisc.edu/~lakes/sci87.html

Laura A. Chernak, D. G. (2012). Tendon motion and strain patterns evaluated with two-dimensional ultrasound elastography. *Journal of Biomechanics, 45*(15), 2618-2623. doi:10.1016/j.jbiomech.2012.08.001.

Leckey, C. A., Wheeler, K. R., Hafiychuk, V. N., Hafiychuk, H., & Timuçin, D. A. (2018). Simulation of guided-wave ultrasound propagation in composite laminates: Benchmark comparisons of numerical codes and experiment. *Ultrasonics, 84*, 187-200. doi:10.1016/j.ultras.2017.11.002

Lee, H. (2017). *Finite Element Simulations with Ansys Workbench 17.* SDC

Publications.

Lees, C., Vincent, J. F., & Hillerton, J. E. (1991). Poisson's Ratio in Skin. *Bio-medical Materials and Engineering, 1*(1), 19-23. Retrieved 12 23, 2019, from https://content.iospress.com/articles/bio-medical-materials-and-engineering/bme1-1-04

Li, R., Chen, H., & Choi, J. H. (2021, January 5). Auxetic Two-Dimensional Nanostructures from DNA. *A Journal of the Gesellschaft Deutscher Chemiker; Angewandte Chemie (International Ed.)*. doi:10.1002/anie.202014729

Li, T., Hu, X., Chen, Y., & Wang, L. (2017, August). Harnessing out-of-plane deformation to design 3D architected lattice metamaterials with tunable Poisson's ratio. *Scientific Reports, 7*. doi:10.1038/s41598-017-09218-w

Li, X., Chang, W.-C., Chao, Y. J., Wang, R., & Chang, M. (2004). Nanoscale Structural and Mechanical Characterization of a Natural Nanocomposite Material: The Shell of Red Abalone. *Nano letters, 4*(4), 613-617. doi:10.1021/nl049962k

Li, X., Gao, H., Murphy, C. J., & Gou, L. (2004). Nanoindentation of Cu2O Nanocubes. *Nano letters, 4*(10), 1903-1907. doi:10.1021/nl048941n

Li, X., Xu, Z.-H., & Wang, R. (2006). In Situ Observation of Nanograin Rotation and Deformation in Nacre. *Nano Letters, 6*(10), 2301-2304. Retrieved 12 3, 2018, from http://pubs.acs.org/doi/abs/10.1021/nl061775u

Lim, T.-C. (2015). 5 Contact and Indentation Mechanics of Auxetic Materials. In T.-C. Lim, *Auxetic Materials and Structures* (pp. 177-199). Springer Singapore Pte. Limited. doi:10.1007/978-981-287-275-3_5

Lord, J., & Whitlatch, R. (2013, October). Impact of temperature and prey shell thickness on feeding of the oyster drill Urosalpinx cinerea Say. *Journal of Experimental Marine Biology and Ecology, 448*, 321-326. doi:https://doi.org/10.1016/j.jembe.2013.08.006

Luo, Z., Li, T., Yan, Y., & Zhou, Z. (2021). Analysis of Sound Absorption Performance of Underwater Acoustic Coating considering Different Poisson's Ratio Values. *Shock and Vibration, 4*, 1-11. doi:10.1155/2021/4861877

Lvov, V., Senatov, F., Veveris, A., Skrybykina, V., & Díaz Lantada, A. (2022). Auxetic Metamaterials for Biomedical Devices: Current Situation, Main Challenges, and Research Trends. *15*(4), 1439. doi: 10.3390/ma15041439

M. Yasrebi, G. H. (1990). Biomimetic Processing of Ceramics and Ceramic–Metal Composites. *Materials Research Society symposia proceedings, 180*, 625–636.

Ma, Y. Z., Sobernheim, D., & Garzon, J. R. (2015). In *Glossary for Unconventional Oil and Gas Resource Evaluation and Development* (p. 517). doi:10.1016/B978-0-12-802238-2.00019-5

Maghsoudian, A., Alvani, S., Moaref, R., Jamalpour, S., Tamsilian, Y., & Kiasat, A. (2022). The concept of biomimetics in the development of protective textiles. In A. Maghsoudian, S. Alvani, R. Moaref, S. Jamalpour, Y. Tamsilian, A. Kiasat, & M. I. Mondal (Ed.), *Protective Textiles from Natural Resources* (pp. 133-173). Woodhead Publishing. doi:https://doi.org/10.1016/B978-0-323-90477-3.00022-5

Maghsoudian, A., Alvani, S., R. M., S. J., Y. T., & Kiasat, A. (2022). 5 - The concept of biomimetics in the development of protective textiles. In M. I. Mondal (Ed.), *In The Textile Institute Book Series - Protective Textiles from Natural Resources* (pp. 133-173). Woodhead Publishing. doi:https://doi.org/10.1016/B978-0-323-90477-3.00022-5

Magomedov, A., & Sebaeva, Z. S. (2020). Comparative study of finite element analysis software packages. *Journal of Physics: Conference Series*. doi:10.1088/1742-6596/1515/3/032073

Marsh, G. (2004). Farnborough 2004 – good prospects for aerospace composites.

Reinforced Plastics, 48(8), 42-46. doi:https://doi.org/10.1016/S0034-3617(04)00406-0

Martinez, R., Goswami, D., Liu, S., Pal, A., Silva, L. G., & Martinez, R. V. (2019). 3D-Architected Soft Machines with Topologically Encoded Motion. *Advanced Functional Materials, 29*. doi:https://doi.org/10.1002/adfm.201808713

Martz, E., Lakes, R., Goel, V., & J.B., P. (2005). Design of an Artificial Intervertebral Disc Exhibiting a Negative Poisson's Ratio. *Cellular Polymers, 24*(3), 127-138. doi:10.1177/026248930502400302

Masters, I. G., & Evans, K. E. (1996). Models for the elastic deformation of honeycombs. *Composite Structures, 35*, 403-422. doi:10.1016/S0263-8223(96)00054-2

Mattocks-Evans, G. (2021, November 1). *Hallam helps develop new tennis racket that could transform the sport*. Retrieved from Sheffield Hallam University: https://www.shu.ac.uk/news/all-articles/latest-news/hallam-develops-tennis-racket-auxetic-material

McHale, G., Alderson, A., Armstrong, S., Mandhani, S., Meyari, M., Wells, G. G., . . . Evans, K. E. (2024, January). Transforming Auxetic Metamaterials into Superhydrophobic Surfaces. *Small Structures, 5*(4). doi:10.1002/sstr.202300458

Meille, S., & Garboczi, E. J. (2001, July 17). Linear elastic properties of 2D and 3D models of porous materials made from elongated objects. *Modelling and simulation in materials science and engineering, 9*, 371-390. doi:0965-0393/01/050371+20$30.00

Mitchell, M. (1998). *An Introduction To Genetic Algorithms.* Massachusetts: Massachusetts Institute of Technology.

Moaveni, S. (2015). *Finite Element Analysis: Theory and Application with ANSYS* (4th ed.). Pearson.

Moaveni, S. (2015). *Finite Element Analysis: Theory and Application with ANSYS.* Pearson Education Limited.

Mohanty, B., Katti, K. S., Katti, D. R., & Verma, D. (2006, August 01). Dynamic nanomechanical response of nacre. *Journal of Materials Research, 21*, 2045–2051. doi:10.1557/jmr.2006.0247

Momoh, E. O., Jayasinghe, A., Hajsadeghi, M., Vinai, R., Evans, K. E., Kripakaran, P., & Orr, J. (2024). A state-of-the-art review on the application of auxetic materials in cementitious composites. *Thin-Walled Structures, 196*. doi:10.1016/j.tws.2023.111447

Naboni, R., & Mirante, L. (2015, November). Metamaterial computation and fabrication of auxetic patterns for architecture. *Digital Manufacturing & Rapid Prototyping*, 129-136. doi:10.5151/despro-sigradi2015-30268

Nakamura, M. (1995). Fundamental Properties of Intermetallic Compounds. *MRS Bulletin, 20*(8), 33-39. doi:doi:10.1557/S0883769400045085

Nakasone, Y., Yoshimoto, S., & Stolarski, T. (2006). Chapter 1 - Basics of Finite-Element Method. In Y. Nakasone, S. Yoshimoto, & T. Stolarski, *Engineering Analysis with ANSYS Software* (pp. 1-35). doi:10.1016/B978-0-7506-6875-0.X5030-3

Nike, Inc. (2016, April 5). *The New Dimensions of Nike Free*. Retrieved from Nike: https://news.nike.com/news/nike-free-2016-running-training

Nike, Inc. (n.d.). WMNS NIKE FREE RN FLYKNIT. Retrieved December 2023, 09, from https://www.nike.com/gb/launch/t/womens-free-rn-flyknit-dynamic-movement

Nkansah, M. A., Evans, K. E., & Hutchinson, I. J. (1994). Modelling the mechanical properties of an auxetic molecular network. *Modelling and Simulation in Materials Science and Engineering, 2*(337).

Novak, N., Vesenjak, M., & Ren, Z. (2018). Crush behaviour of auxetic cellular structures. *Science and Technology of Materials, 30*(1), 4-7. Retrieved 10 22, 2018, from https://sciencedirect.com/science/article/pii/s2603636318300101

Nys, R. d., & Ison, O. (2008). Biofouling. In P. C. Southgate, & J. S. Lucas, *The Pearl Oyster: A Beginner's Guide to Programming Images, Animation, and Interaction* (pp. 527-553). Elsevier Science. doi:https://doi.org/10.1016/B978-0-444-52976-3.00015-2

Oh, J.-H., Kim, J.-S., Hiep, V., & Oh, N.-K. (2020). Auxetic graphene oxide-porous foam for acoustic wave and shock energy dissipation. *Composites Part B: Engineering, 186*(107817). doi:https://doi.org/10.1016/j.compositesb.2020.107817.

Öksüz, K. E., & Şereflişan, H. (2023, June). Investigation of the structure and hardness properties of Anodonta anatina mussel shells. *Ege Journal of Fisheries and Aquatic Sciences, 40*(2), 132-139. doi:10.12714/egejfas.40.2.07

ÖZGÜN. (2021, March 7). *Ansys Contact Types and Explanations*. Retrieved from MECHEAD: https://www.mechead.com/contact-types-and-behaviours-in-ansys/#:~:text=If%20contact%20regions%20are%20bonded,the%20application%20of%20the%20load

Page, T., & Thorsteinsson, G. (2017). An FEA study on impact resistance of bio-inspired CAD models. *Journal on Mechanical Engineering, 7*(4). Retrieved February 4, 2022

Pagliara, S., Franze, K., McClain, C. R., Wylde, G., Fisher, C. L., Franklin, R. J., . . . Chalut, a. K. (2014, June). Auxetic nuclei in embryonic stem cells exiting pluripotency. *Nature Materials, 13*(6), 638–644. doi:10.1038/nmat3943.

Panico, M., Langella, C., & Santulli, C. (2017, November). Development of a Biomedical Neckbrace through Tailored Auxetic Shapes. *talian Journal of*

Science & Engineering, 1(3), 105-117. doi:10.28991/ijse-01113

Pavarin, D., & Francesconi, A. (2003). Improvement of the CISAS high-shot-frequency light-gas gun. *International Journal of Impact Engineering, 29*(1-10), 549-562. doi:https://doi.org/10.1016/j.ijimpeng.2003.10.004

Peng, X.-L., & Bargmann, S. (2024). Nacre-inspired auxetic interlocking brick-and-mortar composites. *Composites Communications, 48*(101892), 2452-2139. doi:10.1016/j.coco.2024.101892

Petit Pli. (n.d.). Retrieved from https://www.indiegogo.com/projects/petit-pli-clothes-that-grow--3#/

Petit Pli. (n.d.). *Petit Pli*. Retrieved from Petit Pli: https://shop.petitpli.com/

PlasticsToday. (2020, October 8). *PlasticsToday*. Retrieved from Researchers 3D Print Bio-Inspired Heart Valve and Stent: https://www.plasticstoday.com/medical/researchers-3d-print-bio-inspired-heart-valve-and-stent

Pokkalla, D. K., Poh, L. H., & Quek, S. T. (2021). Isogeometric shape optimization of missing rib auxetics with prescribed negative Poisson's ratio over large strains using genetic algorithm. *International Journal of Mechanical Sciences, 193*(106169). doi:10.1016/j.ijmecsci.2020.106169

Polyzos, K. D. (2019). Detection and recognition of aerial targets via RADAR data processing, machine learning techniques and neural networks.

Pomar, L. (2020). Chapter 12 - Carbonate systems. In L. Pomar, & J. A. Nicola Scarselli (Ed.), *Regional Geology and Tectonics* (pp. 235-311). Elsevier. doi:https://doi.org/10.1016/B978-0-444-64134-2.00013-4

Ponsi, F., Bassoli, E., & Vincenzi, L. (2021, October). A multi-objective optimization approach for FE model updating based on a selection criterion of the preferred Pareto-optimal solution. *Structures, 33*, 916-934.

Porter, M. M., & Mckittrick, J. (2014). It's tough to be strong: Advances in bioinspired structural ceramicbased materials. *American Ceramic Society Bulletin, 95*(5), 18-24.

Prabhu, P., Liben, M., & Wakjira, A. (2013). Improving Fracture Toughness of Glass/Epoxy Composites by Using Rubber Particles Together with Zirconium Toughened Alumina (ZTA) Nanoparticles. *Research & Reviews: Journal of Engineering and Technology, 3*(1), 21-28. Retrieved August 26, 2021

PUMA. (2020, August 4). *PUMA ENTERS NEW ERA WITH CUSHIONING TECHNOLOGY XETIC*. Retrieved from PUMA: https://about.puma.com/en/newsroom/news/puma-enters-new-era-cushioning-technology-xetic

PUMA. (n.d.). *XETIC Halflife Men's Sneakers*. Retrieved from PUMA: https://us.puma.com/us/en/pd/xetic-halflife-mens-sneakers/195196

Rad, M. S., Prawoto, Y., & Ahmad, Z. (2014, July). Analytical solution and finite element approach to the 3D re-entrant structures of auxetic materials. *Mechanics of Materials, 74*, 76-87. doi:https://doi.org/10.1016/j.mechmat.2014.03.012

Raphel, G., Jacob, M. M., & Viswanathan, S. (2019). Bioinspired designs for shock absorption, based upon nacre and Bouligand structures. *SN Applied Sciences, 1*(9), 1-12. doi:https://doi.org/10.1007/s42452-019-1062-7

Reddy, P. R., Reddy, T. S., Srikanth, I., Madhu, V., Gogia, A., & Rao, K. V. (2016). Effect of viscoelastic behaviour of glass laminates on their energy absorption subjected to high velocity impact. *Materials & design, 98*, 272-279. doi:10.1016/j.matdes.2016.03.038

Ridge, M. D., & Wright, V. (1965, December). The rheology of skin. A bio-engineering study of the mechanical properties of human skin in relation to its structure. *British Journal of Dermatology, 77*(12), 639-649.

doi:https://doi.org/10.1111/j.1365-2133.1965.tb14595.x

Ridge, M. D., & Wright, V. (1966, September). Mechanical properties of skin: a bioengineering study of skin structure. *Journal of Applied Physiology, 21*(5), 1602-1606. doi:https://doi.org/10.1152/jappl.1966.21.5.1602

Ridge, M. D., & Wright, V. (1966, April). The directional effects of skin. *The journal of Investigative Dermatology, 46*(4), 341-346. doi:https://doi.org/10.1038/jid.1966.54

Roache, P. J. (2009). *Fundamentals of Verification and Validation.* hermosa publishers.

Rodie, J. B. (2010, May/June). The Auxetic Effect. *Textile World, 160*(3), 52. Retrieved November 5, 2018, from http://search.ebscohost.com.lcproxy.shu.ac.uk/login.aspx?direct=true&db=buh&AN=50874385&site=ehost-live

Roseke, B. (2013, December 5). *What is the Torsion Constant?* Retrieved from ProjectEngineer: https://www.projectengineer.net/what-is-the-torsion-constant/

Rountree, C. &. (2002). Atomistic Aspects of Crack Propagation in Brittle Materials: Multimillion Atom Molecular Dynamics Simulations. *Annual Review of Materials Research, 12*, 377-400. doi:doi: 10.1146/annurev.matsci.32.111201.142017

Roylance, D. (2001). Finite Element Analysis. Department of Materials Science and Engineering, Massachusetts Institute of Technology, Cambridge, MA 02139.

Ruiz Brothers. (2022, December 01). *3D Printing with NinjaFlex.*

Saba, N., Jawaid, M., & Sultan, M. (2019). 1 - An overview of mechanical and physical testing of composite materials. In M. Jawaid, M. Thariq, & N. Saba, *Mechanical and Physical Testing of Biocomposites, Fibre-Reinforced Composites and Hybrid Composites* (pp. 1-12). Woodhead Publishing Series in Composites Science and Engineering. doi:https://doi.org/10.1016/B978-0-08-102292-

4.00001-1

Safri, S., Sultan, M., Yidris, N., & Mustapha, F. (2014). Low Velocity and High Velocity Impact Test on Composite Materials – A review. *The International Journal Of Engineering And Science (IJES), 3*(9), 50-60. Retrieved from https://www.researchgate.net/publication/309457007_Low_velocity_and_high_velocity_impact_test_on_composite_materials_-_A_review

Sanderson, K. (2015, March 26). Artificial armour. *Nature, 519*, 14-15.

Sarikaya, M., Gunnison, K. E., Yasrebi, M., & Aksay, I. A. (1989, February 21). Mechanical Property-Microstructural Relationships in Abalone Shell. *MRS Online Proceedings Library, 174*, 109-116.

Schmitt, F., Piccin, O., Bayle, B., Renaud, P., & Barbé, L. (2021, January 2). Inverted Honeycomb Cell as a Reinforcement Structure for Building Soft Pneumatic Linear Actuators. *Journal of mechanisms and robotics, 13*(1). doi:10.1115/1.4048834

Sedal, A., Fisher, M., Bishop-Moser, J., Wineman, A., & Kota, S. (2018). Auxetic Sleeves for Soft Actuators with Kinematically Varied Surfaces. *International Conference on Intelligent Robots and Systems*, (pp. 464-471).

Shukla, S., & Behera, B. (2022). Auxetic fibrous structures and their composites: A review. *Composite Structures, 290*(115530). doi:https://doi.org/10.1016/j.compstruct.2022.115530.

Sina Ebnesajjad, P. R. (2005). 3 - Properties of Neat (Unfilled) and Filled Fluoropolymers. In P. R. Sina Ebnesajjad, *Fluoropolymers Applications in the Chemical Processing Industries* (pp. 5-115). William Andrew Publishing. doi:https://doi.org/10.1016/B978-081551502-9.50006-5

Sjodin, B. (2016, April 18). What's The Difference Between FEM, FDM, and FVM? *Machine Design*. Retrieved January 14, 2022, from https://hallam.idm.oclc.org/login?url=https://www.proquest.com/trade-journals/whats-difference-between-fem-fdm-fvm/docview/1835759251/se-2?accountid=13827

Sobel, C. (2020, October 30). *Class Bivalvia*. Retrieved from Digital Atlas of Ancient Life logo: https://www.digitalatlasofancientlife.org/learn/mollusca/bivalvia/

Song, F., Zhou, J., Xu, X., Xu, Y., & Bai, Y. (2008, June 20). Effect of a Negative Poisson Ratio in the Tension of Ceramics. *Physical Review Letters, 100*(24).

Srinivas, K. (2020, June 1). *Verifications and Validations in Finite Element Analysis (FEA).* Retrieved from LinkedIn: https://www.linkedin.com/pulse/verifications-validations-finite-element-analysis-fea-kartik-srinivas/

Stefaniak, L. M., McAtee, J., & Shulman, M. J. (2005, December 20). The costs of being bored: Effects of a clionid sponge on the gastropod Littorina littorea (L). *Journal of Experimental Marine Biology and Ecology, 327*(1), 103-114. doi:https://doi.org/10.1016/j.jembe.2005.06.007

Stewart, R. H., Palmer, T. S., & DuPont, B. (2021, August). A survey of multi-objective optimization methods and their applications for nuclear scientists and engineers. *Progress in Nuclear Energy, 138*, 103830. doi:https://doi.org/10.1016/j.pnucene.2021.103830

Stolarski, T., Nakasone, Y., & Yoshimoto, S. (2018). *Engineering Analysis with ANSYS Software.* Elsevier.

Stolarski, T., Nakasone, Y., & Yoshimoto, S. (2018). Fundamentals of the finite element method. In T. Stolarski, Y. Nakasone, & S. Yoshimoto, *Engineering Analysis with ANSYS Software* (pp. 1-35).

Sun, C., & Jin, Z.-H. (2012). Chapter 1 - Introduction. In C. Sun, & Z.-H. Jin, *Fracture Mechanics* (pp. 1-10). Academic Press. doi:10.1016/B978-0-12-385001-0.00001-8

Sun, J. Y., & Tong, J. (2007, March 1). Fracture toughness properties of three different biomaterials measured by nanoindentation. *Journal of Bionic Engineering, 4*, 11-17.

Sun, J., & Bhushan, B. (2012). Hierarchical structure and mechanical properties of nacre: a review. *RSC Advances, 2*, 7617–7632.

Tagawa, T., Kayamori, Y., Ohata, M., Handa, T., Kawabata, T., Yamashita, Y., . . . Hagihara, Y. (2010, January). Comparison of CTOD standards: BS 7448-Part 1 and revised ASTM E1290. *Engineering Fracture Mechanics*, 327-336.

Taraban, M., Li, Y., Joyner, K., Stains, J., & Yu, Y. (2016). Impact of Matrix Dynamic Properties on Stem Cell Viability. In S. J. Lee, J. J. Yoo, & A. Atala, *In Situ Tissue Regeneration: Host Cell Recruitment and Biomaterial Design* (p. 212). doi:https://doi.org/10.1016/C2014-0-02423-9

TextileWorld. (2010, May 18). *Quality Fabric Of The Month: The Auxetic Effect*. Retrieved from Textile World: https://www.textileworld.com/textile-world/quality-fabric-of-the-month/2010/05/the-auxetic-effect/

The Economist Group Limited. (2012, December 1). *Hook's law*. Retrieved November 5, 2018, from The Economist: https://www.economist.com/technology-quarterly/2012/12/01/hooks-law

The Engineering ToolBox. (2008). Retrieved August 24, 2021, from Stiffness: https://www.engineeringtoolbox.com/stiffness-d_1396.html

Timmins, L. H., Wu, Q., Yeh, A. T., Jr., J. E., & Greenwald, S. E. (2010, May 1). Structural inhomogeneity and fiber orientation in the inner arterial media. *American Journal of Physiology*. doi:10.1152/ajpheart.00891.2009

Tolga Kuşkun, J. S. (2021). Experimental and numerical analysis of mounting force of auxetic dowels for furniture joints. *Engineering Structures, 226*. doi:https://doi.org/10.1016/j.engstruct.2020.111351

Tomita, S., Shimanuki, K., Oyama, S., Nishigaki, H., Nakagawa, T., Tsutsui, M., . . . Umemoto, K. (2023). Transition of deformation modes from bending to auxetic compression in origami-based metamaterials for head protection from impact. *Scientific Reports, 13*, 12221. doi:https://doi.org/10.1038/s41598-023-39200-8

UK Metamaterials Network. (2024). *What are Metamaterials?* Retrieved from UK Metamaterials Network: https://metamaterials.network/what-are-metamaterials/

Verma, D., Katti, K., & Katti, D. (2006). Photoacoustic FTIR spectroscopic study of undisturbed nacre from red abalone. *Spectrochimica acta. Part A, Molecular and biomolecular spectroscopy, 64*(4), 1051-1057. doi:10.1016/j.saa.2005.09.014

Veronda, D., & Westmann, R. (1970). Mechanical characterization of skin—Finite deformations. *Journal of Biomechanics, 3*(1), 111-124. Retrieved 12 23, 2019, from https://sciencedirect.com/science/article/pii/0021929070900552

Vijayan, P. P., & Puglia, D. (2019). Biomimetic multifunctional materials: a review. *Emergent Materials*(2), 391–415.

Wahab, M. (2014). *The Mechanics of Adhesives in Composite and Metal Joints: Finite Element Analysis with Ansys.* Destech Publications Incorporated.

Walker, N. (2016, March 10). *Under Armour produces its first 3D-printed performance trainer*. Retrieved from Manufacturing Global: https://www.manufacturingglobal.com/technology/under-armour-produces-its-first-3d-printed-performance-trainer

Walker, N. (2020, May 16). *Under Armour produces its first 3D-printed performance trainer*. Retrieved from Manufacturing Global: https://manufacturingdigital.com/technology/under-armour-produces-its-first-3d-printed-performance-trainer

Wang, J., He, J., & Xiao, Y. (2019). Fire behavior and performance of concrete-filled steel tubular columns:. *Journal of Constructional Steel Research*, 23.

Wang, J., Wagoner, R., Matlock, D., & Barlat, F. (2005, March). Anticlastic curvature in draw-bend springback. *International Journal of Solids and Structures, 42*(5-6), 1287-1307. doi:10.1016/j.ijsolstr.2004.08.017

Wang, L., & Boyce, M. C. (2010). Bioinspired Structural Material Exhibiting Post-Yield Lateral Expansion and Volumetric Energy Dissipation During Tension. *Advanced Functional Materials, 20*(18), 3025-3030. Retrieved 12 3, 2018, from http://onlinelibrary.wiley.com/doi/10.1002/adfm.201000282/abstract

Wang, L., & Boyce, M. C. (2010). Bioinspired Structural Material Exhibiting Post-Yield Lateral Expansion and Volumetric Energy Dissipation During Tension. *Advanced Functional Materials, 20*(18), 3025-3030. Retrieved 10 18, 2021, from https://onlinelibrary.wiley.com/doi/full/10.1002/adfm.201000282

Wang, L., & Liu, H.-T. (2021). Parameter optimization of bidirectional re-entrant auxetic honeycomb metamaterial based on genetic algorithm. *Composite structures, 267*. doi:10.1016/j.compstruct.2021.113915

Wang, L., Boyce, M. C., Wen, C.-Y., & Thomas, E. L. (2009). Plastic Dissipation Mechanisms in Periodic Microframe-Structured Polymers. *Advanced Functional Materials, 19*(9), 1343-1350. Retrieved 10 18, 2021, from https://onlinelibrary.wiley.com/doi/abs/10.1002/adfm.200801483

Wang, S., Xuan, S., Liu, M., Bai, L., Zhang, S., Sang, M., . . . Gong, X. (2017). Smart wearable Kevlar-based safeguarding electronic textile with excellent sensing performance†. *Soft Matter*(13), 2483-2491. doi:https://doi.org/10.1039/C7SM00095B

Wang, Y. (2022). Auxetic Composite Laminates with Through-Thickness Negative Poisson’s Ratio for Mitigating Low Velocity Impact Damage: A Numerical Study. *Materials, 15*(19). doi:https://doi.org/10.3390/ma15196963

Wang, Z., Zulifqar, A., & Hu, H. (2016). 7 - Auxetic composites in aerospace engineering. In S. Rana, & R. Fangueiro (Eds.), *Advanced Composite Materials for Aerospace Engineering: Processing, Properties and Applications* (pp. 213-240). Woodhead Publishing. doi:https://doi.org/10.1016/B978-0-08-100037-3.00007-9

Wang, Z., Zulifqar, A., & Hu, H. (2016). 7 - Auxetic composites in aerospace engineering. In Z. Wang, A. Zulifqar, & H. Hu, *Advanced Composite Materials for Aerospace Engineering* (pp. 213-240). Woodhead Publishing. doi:10.1016/B978-0-08-100037-3.00007-9

Warmuth, F., Osmanlic, F., Adler, L., Lodes, M. A., & Körner, C. (2017). Fabrication and characterisation of a fully auxetic 3D lattice structure via selective electron beam melting. *Smart Materials and Structures, 26*.

WaveCel. (2024). *Technology*. Retrieved from WaveCel: https://wavecel.com/technology/

Wegst, U. G., & Ashby, M. F. (2004, February). The mechanical efficiency of natural materials. *Philosophical Magazine*, 2167-2186. doi:https://doi.org/10.1080/14786430410001680935

Wen, H. (2000). Predicting the penetration and perforation of FRP laminates struck normally by projectiles with different nose shapes. *Composite structures, 49*(3), 321-329. doi:10.1016/S0263-8223(00)00064-7

Whitty, J. P., Nazare, F., & Alderson, A. (2002). Modelling the effects of density variations on the in-plane Poisson's ratios and Young's Moduli of periodic conventional and re-entrant honeycombs - Part 1: Rib thickness variations. *Cellular Polymers, 21*(2).

Williams, J. L., & Lewis, J. L. (1982). Properties and an Anisotropic Model of Cancellous Bone From the Proximal Tibial Epiphysis. *Journal of Biomechanical*

Engineering, 104(1), 50-56. doi:10.1115/1.3138303

Yamileva, A., Yuldashev, A., & Nasibullayev, I. (2012). Comparison of the Parallelization Efficiency of a Thermo-Structural Problem Simulated in SIMULIA Abaqus and ANSYS Mechanical. *Journal of Engineering Science and Technology Review, 5*(3), 39-43. doi:10.25103/jestr.053.8

Yang, B. (2005). 15 - Static Analysis of Linearly Elastic Bodies. In B. Yang, *Stress, Strain, and Structural Dynamics: An Interactive Handbook of Formulas, Solutions, and MATLAB Toolboxes* (pp. 739-805).

Yang, C., Vora, H. D., & Chang, Y. (2018). Behavior of auxetic structures under compression and impact forces. *Smart materials and structures, 27*(2), 25012. doi:10.1088/1361-665X/aaa3cf

Yasin, R. M. (2018). Petit Pli: Clothes that Grow. *Utopian Studies, 28*(3), 576-583. Retrieved 1 2, 2020, from https://muse.jhu.edu/article/686654/pdf

Yeganeh-Haeri, A., Weidner, D., & Parise, J. (1992, July 31). Elasticity of α-Cristobalite: A Silicon Dioxide with a Negative Poisson's Ratio. *Science, 257*(5070), 650-652. doi:10.1126/science.257.5070.650

Zawistowski, M., & Poteralski, A. (2024, May 4). Parametric optimization of selected auxetic structures. *Multiscale and Multidisciplinary Modeling, Experiments and Design*. doi:10.1007/s41939-024-00452-0

Zhang, J., Lu, G., Ruan, D., & Wang, Z. (2018, February). Tensile behavior of an auxetic structure: Analytical modeling and finite element analysis. *International Journal of Mechanical Sciences, 136*, 143-154. doi:10.1016 / j.ijmecsci.2017.12.029.

Zhang, X. Y., & Ren, X. (2020, September 3). A Simple Methodology to Generate Metamaterials and Structures with Negative Poisson's Ratio. *physica status solidi b - Special Issues: Auxetics, 257*(10).

Zheng, Y. (2019). Biological design of materials. In Y. Zheng, *Bioinspired Design of Materials Surfaces* (pp. 27-97). Elsevier. doi:https://doi.org/10.1016/B978-0-12-814843-3.00002-8

Zhu, Z., Li, X., Yang, R., Xie, W., & Zhang, D. (2023). The energy dissipation mechanism of bi-metal Kevlar\titanium fiber metal laminate under high-velocity impact. *European journal of mechanics/ A, Solids, 100*, 104956. doi:10.1016/j.euromechsol.2023.104956

Appendices

Appendix 1: 3D Discretisation Elements

For 3D models, the elements used are in Table 32, and their corresponding descriptions from the ANSYS Theory Manual are in Table 33.

Element Name IDs	Material IDs	Element Type IDs	Number of Elements
TARGE170	18, 20, 22, 24, 26, 28, 30...	18, 20, 22, 24, 26, 28, 30...	32374
CONTAC174	17, 19, 21, 23, 25, 27, 29...	17, 19, 21, 23, 25, 27, 29...	32374
SOLID186	1	1-4	8450
SOLID187	5, 9-16	5-16	467288

Table 32: The elements used for 3D models that had only solid elements

TARGE170	**CONTAC174**	**SOLID186**	**SOLID187**
3D Target Segment	8-Node Surface-to-Surface Contact	20-Node Structural Solid	3D 10-Node Tetrahedral Structural Solid

Table 33: The elements used in the 3D models using solid elements and their descriptions

The target and contact elements work in the same way as described in section '2D Meshing'. The shape function relies on the same equations as in 2D with an additional axis, w, defined as:

$$
\begin{aligned}
w = \frac{1}{4}\Big(& w_I(1-s)(1-t)(-s-t-1) + w_J(1+s)(1-t)(s-t-1) \\
& + w_K(1+s)(1+t)(s+t-1) + w_L(1-s)(1+t)(-s+t-1)\Big) \\
& + \frac{1}{2}\Big(w_M(1-s^2)(1-t) + w_N(1+s)(1-t^2) + w_O(1-s^2)(1+t) \\
& + w_P(1-s)(1-t^2)\Big)
\end{aligned}
\qquad (137)
$$

The stiffness Matrix and Stress Stiffness Matrix are integrated over 2 by 2 points for quad geometry and shape functions found in equations (43), (44), and (137).

It is integrated over 3 points for triangular geometry with shape functions found in equations (43), (44), and (137).

The geometries of the elements used are shown below. SOLID186 is a 20-node Quadrilateral quadratic element with mid-points on each edge, as shown in Figure 178.

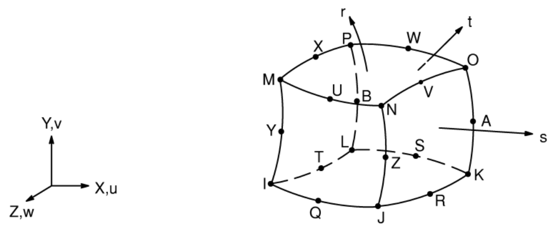

Figure 178: A diagram of SOLID186 showing its 20-Nodes as mid-nodes on each edge.

SOLID187 is a tetrahedral quadratic element with mid-points on each edge, as shown in Figure 179.

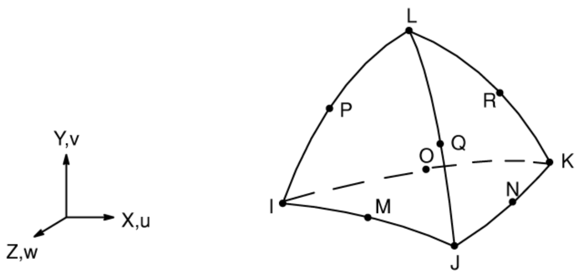

Figure 179: A diagram of SOLID187 showing its 10-Nodes as mid-nodes on each edge.

The beam models utilised the BEAM188 elements, which is a 3D finite strain linear beam.

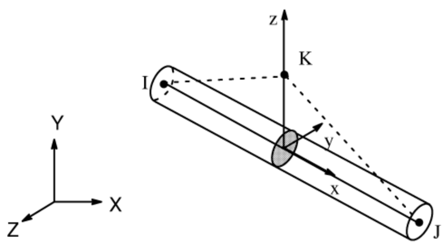

Figure 180: The diagram showing BEAM 188

Appendix 2: Worked Examples of the Analytical Models

Mechanism 1

As described in the section '', below is a worked example of the equation for the Poisson's ratio, which was previously given by equation (87):

$$\nu_{xy} = \frac{\left(1 - \frac{K_h}{K_s}\right)}{2\left(h_p + 2l\cos\theta\right)} \frac{\left(L_p + A_0 + 4l\sin\theta\right)}{\left(\tan\theta\frac{K_h}{K_s} + \cot\theta\right)}$$

The dimensions were obtained from the Wang & Boyce (2010) model, which is described in Chapter 2, with further dimensions derived in Chapter 4.

Parameter	Magnitude
Length of the platelet, L_p [μm]	1
Angle, Θ [degrees]	45
Height of the platelet, h_p [μm]	0.1
Undeformed length of the single unit of mortar, l_0 (found using trigonometry)	0.007078847
Young's modulus of the mortar' material, E_{rib}, [GPa] (post-yield)	0.33
Poisson's ratio of the mortar's material, ν_{rib} (post-yield)	0.00
The undeformed gap between the platelets, a_0	0.01
$\frac{K_h}{K_s}$	3.759398496

Table 34: Parameters used for the analysis

The parameters from Table 34 were substituted into the equations (78) and (87) for $l = 0.009600333$ which corresponded to an angle of $\theta = 49.30297974$:

Equation (78)

$$A_0 = a_0 - 4l_0 \sin\theta_0 = 0.01 - 4 \times 0.007078847 \times \sin 45 = -0.010022$$

Equations (87):

$$\nu_{xy} = \frac{(1 - 3.759398496)}{2(0.1 + 2 \times 0.009600333 \ \cos 49.30297974)} \times \frac{(1 + -0.010022 + 4 \times 0.009600333 \ \times \sin 49.30297974)}{(3.759398496 \tan 49.30297974 + \cot 49.30297974)}$$

$$= -2.388726568$$

Mechanism 2

As described in the section ‘’, below is a worked example of the equation for the Poisson’s ratio, which was previously given by

$$\upsilon_{xy} = -\frac{\tan\theta\, x}{y}$$

Or, in other terms:

$$\upsilon_{xy} = -\frac{\tan\theta\,(L + A)}{(h + 2B + C)}$$

Constant parameters were:

Parameter	***Magnitude***
L [μm]	10
h [μm]	1
r [μm]	25

Table 35: The parameters used for the worked example of mechanism 2

Then, to find individual terms for an angle of 10°:

$$A = 2r\sin\theta = 50\sin\theta = 8.6824$$

$$B = \frac{A(1 - \cos\theta)}{2\sin\theta} = 25(1 - \cos\theta) = 0.3798$$

$$C = h - 2(r - r\cos\theta) = 1 - 2(25 - 25\cos\theta) = 0.2404$$

$$\upsilon_{xy} = -\frac{\tan\theta\,(L + A)}{(h + 2B + C)} = -\frac{\tan 10\,(10 + 8.6824)}{(1 + 2\times 0.3798 + 0.2404)} = -1.64$$

To obtain the range of strains, the angle was varied from 5° to 85°.

Mechanism 3

The Poisson's ratio equation for Mechanism 3:

$$\upsilon_{xy} = -\frac{\varepsilon_y}{\varepsilon_x} = \frac{\frac{2\delta B}{h+2B}}{\frac{\delta A}{L+A}} = -\frac{\delta B}{\delta A}\frac{2(L+A)}{(h+2B)}$$

The parameters for Mechanism 3:

h	B	L	A	θ
0.225	0.025	2	0.015	53°

Table 36: The parameters used for the worked example for mechanism 3

For stage 1 of deformation: $\frac{\delta B}{\delta A} = 0$, hence $\upsilon_{xy} = 0$

For stage 2 of deformation: $\frac{\delta B}{\delta A} = -\tan\theta$, hence

$$\upsilon_{xy} = 16.12\tan 53° = 21.39$$

For stage 3 of deformation: $\frac{\delta B}{\delta A} = 0$, hence $\upsilon_{xy} = 0$

For stage 4 of deformation: $\frac{\delta B}{\delta A} = \tan\theta$, hence $\upsilon_{xy} = -16.12\tan 53° = -21.39$

Alternatively, $\frac{\delta B}{\delta A}$ can be considered alone.

For stage 1 of deformation: $\frac{\delta B}{\delta A} = 0$, hence $\upsilon_{xy} = 0$

For stage 2 of deformation: $\frac{\delta B}{\delta A} = -\tan\theta$, hence $\upsilon_{xy} = \tan 53° = 1.327$

For stage 3 of deformation: $\frac{\delta B}{\delta A} = 0$, hence $\upsilon_{xy} = 0$

For stage 4 of deformation: $\frac{\delta B}{\delta A} = \tan\theta$, hence $\upsilon_{xy} = -\tan 53° = -1.327$